MULTIBEAM ARRAY ANTENNA FOR BASE STATION IN THE FIFTH-GENERATION MOBILE COMMUNICATION SYSTEM

INTAN IZAFINA BINTI IDRUS

FACULTY OF ENGINEERING
UNIVERSITY OF MALAYA
KUALA LUMPUR

2020

MULTIBEAM ARRAY ANTENNA FOR BASE STATION IN THE FIFTH-GENERATION MOBILE COMMUNICATION SYSTEM

INTAN IZAFINA BINTI IDRUS

THESIS SUBMITTED IN FULFILMENT OF THE REQUIREMENTS FOR THE DEGREE OF DOCTOR OF PHILOSOPHY

FACULTY OF ENGINEERING
UNIVERSITY OF MALAYA
KUALA LUMPUR

2020

UNIVERSITY OF MALAYA

ORIGINAL LITERARY WORK DECLARATION

Name of Candidate: Intan Izafina binti Idrus

Matric No: 17013001/1, KHA140066

Name of Degree: Doctor of Philosophy

Title of Thesis ("this Work"): Multibeam array antenna for base station in the fifth-generation mobile communication system

Field of Study: Electromagnetic

I do solemnly and sincerely declare that:

(1) I am the sole author/writer of this Work;
(2) This Work is original;
(3) Any use of any work in which copyright exists was done by way of fair dealing and for permitted purposes and any excerpt or extract from, or reference to or reproduction of any copyright work has been disclosed expressly and sufficiently and the title of the Work and its authorship have been acknowledged in this Work;
(4) I do not have any actual knowledge nor do I ought reasonably to know that the making of this work constitutes an infringement of any copyright work;
(5) I hereby assign all and every rights in the copyright to this Work to the University of Malaya ("UM"), who henceforth shall be owner of the copyright in this Work and that any reproduction or use in any form or by any means whatsoever is prohibited without the written consent of UM having been first had and obtained;
(6) I am fully aware that if in the course of making this Work I have infringed any copyright whether intentionally or otherwise, I may be subject to legal action or any other action as may be determined by UM.

Candidate's Signature Date:

Subscribed and solemnly declared before,

Witness's Signature Date:

Name:

Designation:

MULTIBEAM ARRAY ANTENNA FOR BASE STATION IN THE FIFTH-GENERATION MOBILE COMMUNICATION SYSTEM

ABSTRACT

Research on the fifth-generation (5G) mobile communication system has been accelerated to meet the standardization of the International Telecommunications Union for higher data traffic and higher data rates. The main requirements of the 5G mobile communication systems are the utilization of millimeter waves, the deployment of small cells, and the use of multibeam array antennas for multiple-input multiple-output schemes. Multibeam array antennas play an important role in developing a new base station to enhance system capacity, improve network coverage, and reduce co-channel interference. The main objective of this thesis is to design a single-layer multibeam array antenna at 28 GHz for base station in a 5G mobile communication system. The proposed multibeam array antenna is employed with a Butler matrix, which is the most promising solution for a 5G base station antenna. However, the literature has reported issues such as high amplitude imbalance and inaccurate phase differences between the output ports of the Butler matrix that cause the radiation characteristics to show incorrect main beam directions. To overcome these issues, a Butler matrix must have highly accurate dimensions to ensure the main beams point at the desired directions. This thesis presents the design of a multibeam array antenna with eight antenna elements fed by an 8×8 Butler matrix. The Butler matrix consists of sixteen crossovers, twelve quadrature hybrids, and eight phase shifters. The optimum design of each circuit element was obtained to form the 8×8 Butler matrix. A single-element microstrip antenna was designed to operate at 28 GHz. The microstrip antenna was integrated at each output port of the Butler matrix. The complete structure of a multibeam array antenna was simulated and optimized to obtain the desired radiation characteristics. Moreover, the beam coverage of the multibeam array antenna with different antenna spacing in the vertical plane was also studied and analyzed. The results show that the beam coverage was reduced as the antenna spacing increased. Additionally, the appearances of grating lobes were observed when the antenna spacing was increased to 0.7λ. Therefore, the multibeam array antenna with an antenna spacing of 0.6λ was selected for fabrication. The multibeam array antenna was fabricated using a low dielectric constant and low tangent substrate material named NPC-F220A. The results indicate that the 8 × 8 Butler matrix achieved a low insertion loss and a low phase error with average values of 2 dB and ± 10° at 28 GHz, respectively. The return losses of the multibeam array antenna were less than −10 dB, ranging from 27 GHz to 29 GHz. The main beams of the radiation pattern were pointed at ± 6°, ± 18°, ± 30°, and ± 44° with antenna gains between 9 dBi and 14 dBi. Furthermore, the configurations of multibeam base station antennas to achieve a 360° coverage area in the horizontal plane were presented. The beam coverage designs in the horizontal and vertical sectorizations were analyzed. The findings show that the proposed design concept of multibeam base station antennas is adequate and suitable for a 5G mobile communication system.

Keywords: 5G mobile communication system; Base station; Butler matrix; Multibeam array antenna; Single-layer

SUSUNAN ANTENA BERBILANG ALUR UNTUK STESEN PANGKALAN DALAM SISTEM KOMUNIKASI BERGERAK GENERASI-KELIMA

ABSTRAK

Penyelidikan tentang sistem komunikasi bergerak generasi kelima (5G) telah meningkat pesat bagi memenuhi standard yang ditetapkan oleh *International Telecommunications Union* untuk data trafik dan kadar data yang lebih tinggi. Keperluan utama bagi sistem komunikasi bergerak 5G ialah penggunaan gelombang milimeter, pengerahan sel kecil, dan penggunaan susunan antena berbilang alur untuk skema berbilang-input berbilang-output. Susunan antena berbilang alur memainkan peranan penting dalam membangunkan stesen pangkalan yang baru untuk meningkatkan kapasiti sistem, menambahbaik liputan rangkaian, dan mengurangkan gangguan saluran-sama. Objektif utama tesis ini ialah mereka bentuk susunan antena berbilang alur lapisan tunggal pada 28 GHz untuk stesen pangkalan dalam sistem komunikasi bergerak 5G. Susunan antena berbilang alur yang dicadangkan dengan menggunakan matrik *Butler* adalah penyelesaian yang sangat baik untuk stesen pangkalan antena 5G. Walau bagaimanapun, kesusasteraan telah melaporkan isu-isu seperti ketidakseimbangan amplitud yang tinggi dan perbezaan fasa yang tidak tepat di antara port keluaran pada matriks *Butler* menyebabkan ciri-ciri radiasi menunjukkan arah rasuk utama yang tidak tepat. Untuk mengatasi masalah ini, matriks *Butler* mestilah mempunyai ketepatan dimensi yang tinggi untuk memastikan rasuk utama pada arah yang dikehendaki. Tesis ini membentangkan reka bentuk susunan antena berbilang alur dengan lapan elemen antena disuap oleh matriks *Butler* 8 × 8. Matrik *Butler* ini terdiri daripada enam belas *crossover,* dua belas *quadrature hybrid*, dan lapan *phase shifter*. Reka bentuk yang optimum bagi setiap elemen litar ini telah diperoleh bagi membentuk matriks *Butler* 8 × 8. Antena mikrojalur elemen tunggal telah direka

bentuk untuk beroperasi pada 28 GHz. Antena mikrojalur ini telah diintegrasi pada setiap port keluaran matriks *Butler*. Struktur susunan antena berbilang alur yang lengkap ini telah disimulasi dan dioptimumkan untuk mendapatkan ciri-ciri radiasi yang dikehendaki. Di samping itu, liputan rasuk untuk susunan antena berbilang alur dengan jarak antena yang berlainan pada satah tegak telah dikaji dan dianalisa. Keputusan menunjukkan liputan rasuk telah berkurang apabila jarak antena ditingkatkan. Tambahan lagi, kemunculan *grating lobe* dapat diperhatikan apabila jarak antena ditingkatkan kepada 0.7λ. Oleh itu, susunan antena berbilang alur dengan jarak antena 0.6λ telah dipilih untuk fabrikasi. Susunan antena berbilang alur telah difabrikasi dengan menggunakan bahan substrat iaitu NPC-F220A yang mempunyai pemalar dielektrik dan tangen kehilangan yang rendah. Hasil keputusan menunjukkan matriks *Butler* 8×8 ini telah mencapai kehilangan sisipan dan ralat fasa yang rendah dengan nilai purata masing-masing 2 dB dan ± 10° pada 28 GHz. Kehilangan pulangan bagi susunan antena berbilang alur adalah kurang daripada −10 dB, dari julat 27 GHz hingga 29 GHz. Rasuk utama bagi pola radiasi adalah pada arah ± 6°, ± 18°, ± 30°, dan ± 44° dengan gandaan antena di antara 9 dBi dan 14 dBi. Tambahan pula, konfigurasi stesen pangkalan antena berbilang alur untuk memperoleh kawasan liputan 360° pada satah mendatar telah dibentangkan. Reka bentuk liputan rasuk bagi sektor mendatar dan menegak telah dianalisa. Hasil kajian menunjukkan bahawa konsep reka bentuk stesen pangkalan antenna berbilang alur yang dicadangkan adalah sesuai untuk sistem komunikasi bergerak 5G.

Kata kunci: lapisan tunggal, matriks *Butler*, sistem komunikasi bergerak 5G, stesen pangkalan, susunan antena berbilang alur.

ACKNOWLEDGEMENTS

In the Name of Allah, the Most Beneficent, the Most Merciful.

First and foremost, all praise is due to Allah who has blessed me with the strength and capabilities to complete this research.

I would like to express my gratitude to my main supervisor, Associate Professor Dr. Narendra Kumar Aridas, and my co-supervisors, Dr. Tarik Abdul Latef and Dr. Mohamad Sofian Abu Talip, for their supervision and encouragement throughout this research. I really appreciate the opportunity that they have given me to broaden my knowledge in this research field.

I would also like to express my deepest appreciation to my co-researcher, Professor Dr. Yoshihide Yamada from the Malaysia-Japan International Institute of Technology, Universiti Teknologi Malaysia, for his valuable suggestions and fruitful discussions. Special thanks go to the staff at the Faculty of Engineering, University of Malaya, for their help during my doctoral study. I would like to acknowledge the Universiti Teknologi Malaysia for providing the laboratory facilities to conduct antenna measurements. I am also indebted to the Ministry of Higher Education and the University of Malaya for providing the financial support that has enabled me to conduct this research.

My sincere appreciation goes to my family, especially my mother, Azizah Buang, for her love, support, and prayers throughout my academic years. I would like to dedicate this thesis to my beloved daughter, Arina Izyan, for her boundless love and patience. Last but not least, I would like to thank everyone else who has contributed to this research.

TABLE OF CONTENTS

LIST OF FIGURES

LIST OF TABLES

LIST OF SYMBOLS

β	-	Phase difference of excitation current between adjacent antenna element
$\tan\delta$	-	Tangent loss
ε_r	-	Dielectric constant
ε_{ap}	-	Aperture efficiency
ε_{reff}	-	Effective dielectric constant
λ	-	Wavelength
λ_g	-	Wavelength in the microstrip transmission line
ϕ	-	Phase shift
ϕ_p	-	Phase differences between output port of the Butler matrix
ψ	-	Phase difference between adjacent antenna elements
Γ_e	-	Even-mode reflection coefficients for two-port networks
Γ_o	-	Odd-mode reflection coefficients for two-port networks
θ	-	Angle relative to the normal to the array
θ_G	-	Grating lobe angle
θ_p	-	Main beam angle
θ_t	-	Beam tilt angle
A	-	Compensated length for an optimal bend
A_{er}	-	Effective aperture of receiving antenna
AF	-	Array factor
B	-	Bandwidth of the channel
B_1	-	Amplitude of the quadrature hybrid at Port 1
B_2	-	Amplitude of the quadrature hybrid at Port 2
B_3	-	Amplitude of the quadrature hybrid at Port 3
B_4	-	Amplitude of the quadrature hybrid at Port 4

c	-	Speed of light in vacuum
C	-	Channel capacity
C_n	-	Number of crossover
$cos^2\phi$	-	Polarization loss factor
d	-	Antenna spacing
D	-	Diameter
D_m	-	Diagonal length of the square miter
D_t	-	Directivity of beam shaped by antenna array
f	-	Frequency
F	-	Focal length
G_m	-	Measured gain
G_s	-	Simulated gain
G_t	-	Antenna array gain
h	-	Height of the multibeam base station antenna
h_s	-	Thickness of the substrate
k	-	Wave number
l	-	Line length
L_o	-	Length of the microstrip transmission line
L_{eff}	-	Effective length of the microstrip antenna
L_p	-	Actual length of the microstrip antenna
L_{ps}	-	Length of the phase shifter
ΔL	-	Extended length of the microstrip transmission line
ΔL_p	-	Extended length on both ends of the microstrip antenna
N	-	Number of antenna elements
P_R	-	Received power
P_T	-	Transmitted power

r	-	Cell radius
S_{area}	-	Area of the antenna array
S/N	-	Signal-to-noise ratio
T_e	-	Even-mode transmission coefficients for two-port networks
T_o	-	Odd-mode transmission coefficients for two-port networks
W_o	-	Width of the microstrip transmission line
W_p	-	Width of the microstrip antenna
X	-	Diagonal length of an optimum miter
Y	-	Admittance
Z_a	-	Input impedance at the center of the microstrip antenna edge
Z_f	-	Impedance of the microstrip transmission line
Z_o	-	Characteristic impedance
Z_q	-	Impedance of the quarter wave transformer

LIST OF ABBREVIATIONS

1G	:	First-generation
2G	:	Second-generation
3G	:	Third-generation
4G	:	Fourth-generation
5G	:	Fifth-generation
6G	:	Sixth-generation
CST	:	Computer Simulation Technology
EM	:	Electromagnetic
GSM	:	Global Systems for Mobile
GMSK	:	Gaussian Minimum Shift Keying
GPRS	:	General Packet Radio Services
EDGE	:	Enhanced Data Rates for Global Evolution
HSPA	:	High Speed Packet Access
IMT	:	International Mobile Telecommunications
LTE	:	Long Term Evolution
UMTS	:	Universal Mobile Telecommunications System

LIST OF APPENDICES

CHAPTER 1: INTRODUCTION

1.1 Background of Research

The mobile communication system has evolved tremendously since the past few decades. It has become a necessity and significantly improved our daily activities. In this fast-paced world, mobile communication allows mobile users to access information anytime anywhere. This technology has also benefited various sectors such as healthcare, automotive, agriculture, education, defense, and public safety.

In the mobile communication system, the radio wave energy radiates uniformly from the base stations to mobile users and vice versa (Kyohei & James, 2008). A base station consists of transmitters, receivers, and interfaces for telephone infrastructure to allow mobile users to communicate with each other. The base station provides services to the subscribed mobile users within a coverage area that is divided into several cells. The base station will assign different frequencies for each cell. The same frequency of a cell can be reused in other cells that are separated spatially (Stutzman & Thiele, 2012). The mobile network operators deliver their services for voice and data communications to the subscribed mobile users within the defined coverage area.

The current fourth-generation (4G) mobile communication system provides services for multimedia and high-quality video streaming (Alsharif & Nordin, 2017). Incidentally, rapid increases for the demand among mobile users call for a better service quality. According to the Visual Networking Index Forecast reported by Cisco, mobile data traffic is predicted to increase up to 77 EB per month by 2022 (Cisco, 2017). Figure 1.1 presents the mobile data traffic for six years, from 2017 to 2022. It is expected that this graph will continue to increase in the coming years. Moreover, the current 4G mobile communication system is limited to the carrier frequency up to 2.6 GHz and the spectrum bandwidth is less than 780 MHz (Rappaport et al., 2013).

Therefore, new mobile technology is imperative to cater to the tremendous demands for delivering high service quality to mobile users.

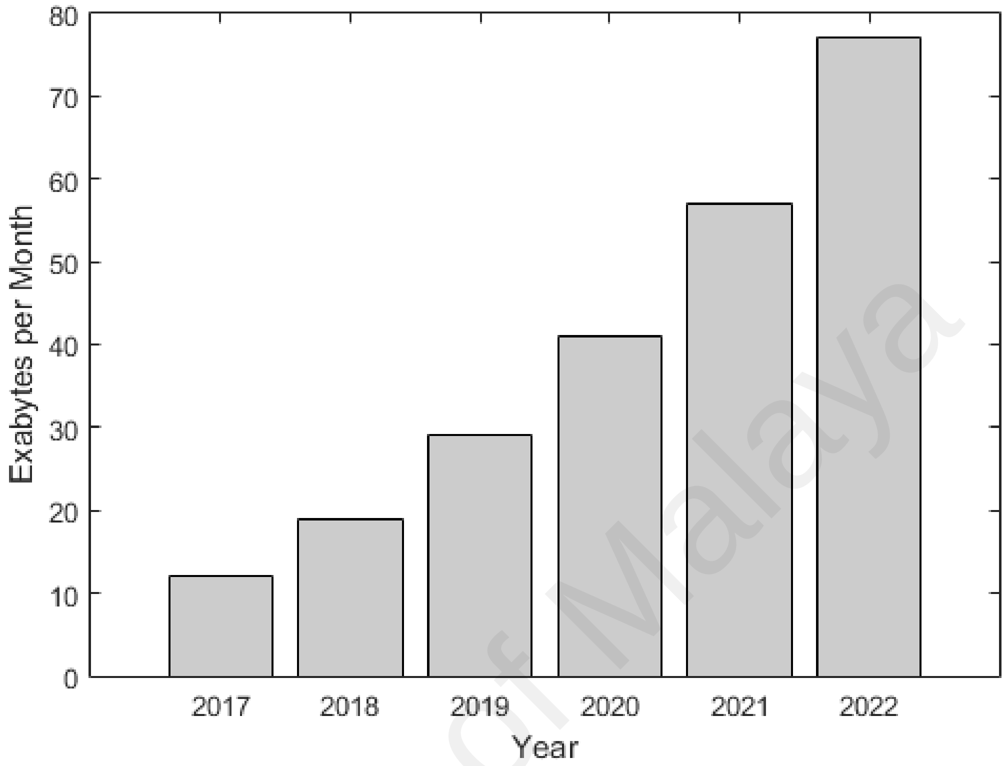

Figure 1.1: Mobile data traffic from 2017 to 2022 (Cisco, 2017)

Recently, research on the fifth-generation (5G) mobile communication system has attracted numerous interests from researchers and design engineers that wish to cater to the increasing demand for higher data traffic and higher data rates (Alnoman & Anpalagan, 2017; Gavrilovska, Rakovic, & Atanasovski, 2016; Hong et al., 2017; Rappaport et al., 2013). These efforts have been accelerated to meet the standardization of the International Telecommunications Union. The main requirements for the 5G mobile communication systems are the utilization of millimeter wave, the deployment of small cells with a cell radius of less than 200 m, and the use of a multibeam array antenna for multiple-input multiple-output schemes (Alnoman & Anpalagan, 2017; Gavrilovska et al., 2016; Hong et al., 2017; Rappaport et al., 2013). The mobile communication system will enable massive numbers of connected devices, less latency, and lower deployment costs, as compared to the current 4G mobile communication system.

Antennas are critical components in both base stations and mobile terminals. They are used to establish a radio transmission line between the radio stations. In the base station, the types of base station antennas that are commonly used are reflector antennas, lens antennas, and array antennas. Additionally, the basic requirements for a base station antenna are compact, low cost, and lightweight. Therefore, antenna design presents huge opportunities in developing a new 5G base station antenna.

1.2 Problem Statement

The advent of the mobile communication system has led to tremendous demands in developing base station antennas since the first-generation mobile communication system was introduced. The performance of the base station antennas has been significantly improved over the past years in terms of beam coverage, bandwidth, antenna gain, size, and fabrication cost. As the 5G mobile communication system is expected to deliver high service quality to mobile users, this idea will be a great opportunity for researchers and design engineers to develop a new base station antenna.

The spectrum bandwidth of less than 3 GHz has almost been fully utilized in the current 4G mobile communication system. Due to this, there is a necessity to explore the new frequency bands in millimeter waves for more channel capacity. In the 5G mobile communication system, the Federal Communications Commission (FCC) has defined that the 28 GHz band to be used. Despite this fact, the propagation can be affected by heavy rain at this frequency (Niu, Li, Jin, Su, & Vasilakos, 2015). However, studies have shown that the attenuation caused by the rain does not give any significant effect on the propagation provided that the cell radius is less than 200 m (Niu et al., 2015). Therefore, dense deployment of the base stations is crucial in the 5G mobile network to ensure continuous signal availability within the coverage area.

Base station antenna requires low profile, low cost, high antenna gain, high efficiency, and good radiation characteristics. In the 5G mobile communication system, radiation characteristics of multiple beams with narrow beamwidth are necessary. The base station can simultaneously produce beams in the horizontal and vertical sectorizations within the coverage area using the multibeam techniques. The ability to steer the beam to a specific direction can be performed by adjusting the amplitude and phase of the antenna (Kyohei & James, 2008). The advantage of using a multibeam antenna at the base station is to enhance the system's capacity. Besides that, the multibeam antenna also improves the network coverage and reduces the co-channel interference between the base stations (Hong et al., 2017; P. Yang, Liu, & Zhang, 2014)

To achieve the multibeam characteristics, the beamforming circuits such as the Butler matrix, the Blass matrix, and the Rotman lens can be fed to the array antenna (Blass, 1960; Butler, 1960; Rotman & Turner, 1963). The Butler matrix has received great attention due to its design simplicity, low power dissipation, and cost-effectiveness for large-scale production (Ali, Fonseca, Coccetti, & Aubert, 2011; Bantavis et al., 2018; Kim, Yoon, Lee, & Shin, 2019; Nedil, Denidni, & Talbi, 2006; Slomian, Wincza, Staszek, & Gruszczynski, 2017; Vallappil, Rahim, Khawaja, & Iqbal, 2020; Zhu, Sun, Ding, & Guo, 2019). On the other hand, the Blass matrix has low efficiency due to high losses associated with the structure (Bhowmik, Srivastava, & Prasad, 2014). The Rotman lens suffers from high ohmic loss, high power loss within the lens and high phase error across the aperture (Katagi, Mano, & Sato, 1984; J. J. Lee & Valentine, 1996). However, the Butler matrix has the ability of producing orthogonal beams, which improve the beam scanning coverage (Babale, Rahim, Barro, Himdi, & Khalily, 2018). Moreover, the structure of the Butler matrix is compact and suitable to be used in a space-constrained base station. Nevertheless, the main drawbacks of designing a Butler matrix in millimeter waves using microstrip technology are due to its high insertion losses and incorrect output phases at the output ports of the Butler matrix that affects the radiation characteristics. Additionally, the literature has also reported the issue of the inaccurate beam directions in the higher-order Butler matrices as the dimensions of the circuit elements are imprecise (Corona & Lancaster, 2003; Tian, Yang, & Wu, 2014; Won-Cheol, Byung-Wook, Choul-Young, Jun Chul, & Jong-Min, 2016). To overcome these issues, a Butler matrix must possess high accuracy dimensions to ensure that the radiation beams are pointing at the desired directions.

Previous studies have focused on the improvement of the circuit performance and size reduction of the Butler matrix at frequencies of less than 10 GHz by eliminating some circuit elements (Babale et al., 2018; Ben Kilani, Nedil, Kandil, & Denidni, 2012; Tian et al., 2014). Babale et al. (2018) developed a 4 × 4 Butler matrix using only modified quadrature hybrids to produce a phase difference of 45° at 6 GHz without the use of a phase shifter and a crossover. As a result, the designed Butler matrix exhibited an insertion loss and a phase error of 3 dB and 3°, respectively. Moreover, Tian et al. (2014) designed a 4 × 4 Butler matrix at 6 GHz using hybrid couplers with phase differences of −45° and −90° along with a crossover. The designed Butler matrix achieved a low insertion loss and a low phase error of 1 dB and 1°, respectively. However, the proposed hybrid couplers could not be characterized using the closed-form transmission line theory (Babale et al., 2018). Ben Kilani et al. (2012) designed a 4 × 4 Butler matrix based on conductor-backed coplanar waveguide technology at 5.8 GHz using two directional elliptic couplers, two directional slot-coupled couplers, and two phase shifters to avoid the use of a crossover. The proposed Butler matrix showed an insertion loss and a phase error of 1.5 dB and 10°, respectively. Although these research works successfully reduced the number of circuit elements, these techniques are only valid for a 4 × 4 Butler matrix and are not applicable for higher-order Butler matrices, which require a more complex structural design.

Several designs of the Butler matrices have been reported in the millimeter wave frequencies (C. Chen & Chu, 2010; Trinh-Van, Lee, Yang, Lee, & Hwang, 2019; Q. Yang, Ban, Kang, Sim, & Wu, 2016). A Butler matrix operating at higher frequencies has a reduced physical size; yet, an increased propagation loss as the wavelength is smaller compared to the lower frequencies. Chen and Chu (2010) designed a 4 × 4 Butler matrix based on a substrate integrated waveguide at 60 GHz. The Butler matrix designed in their study was formed using two crossovers, four quadrature hybrids, and four phase shifters. The quadrature hybrids and crossovers were designed using short-slot couplers. Consequently, the proposed Butler matrix achieved an insertion loss and a phase error of 2.5 dB and 12°, respectively. Q. Yang et al. (2016) reported a 4 × 4 Butler matrix based on a substrate integrated waveguide at 30 GHz. The Butler matrix designed in their study was composed of two crossovers, four quadrature hybrids, and two pairs of phase shifters. The crossover was realized by cascading two quadrature hybrids. Additionally, the phase compensation technique was employed to design 0° and 135° phase shifters. The proposed Butler matrix obtained the simulated results of an insertion loss and a phase error of 1 dB and 5°, respectively. However, the authors did not report the measured results of an insertion loss and a phase error. Furthermore, Trinh-Van et al. (2019) presented a 4 × 4 Butler matrix consisting of two crossovers, four quadrature hybrids, and two phase shifters at 27.925 GHz. The proposed Butler matrix obtained an average insertion loss and a phase error of 2 dB and 10°, respectively. In either case, these research works presented were limited to only 4 × 4

Butler matrix, and therefore is insufficient for the base station applications, as higher-order Butler matrices are required to feed the antennas at a base station.

Only a few research studies have developed the 8 × 8 Butler matrices, as the structures of these Butler matrices are more complex and difficult to design. Two main issues of designing an 8 × 8 Butler matrix are high insertion loss and high phase error, as it has more circuit elements compared to a 4 × 4 Butler matrix. Moubadir, Bayjja, Touhami, Aghoutane, and Tazon (2015) proposed an 8 × 8 Butler matrix based on a single-layer structure at 2.4 GHz for the wireless local area network using electromagnetic simulation software. The Butler matrix consisted of twelve quadrature hybrids, four crossovers, four phase shifters with a −22° phase difference, two phase shifters with a −67.5° phase difference, and two phase shifters with a −45° phase difference. However, the proposed Butler matrix was not validated via measurement. Furthermore, the circuit performances of the Butler matrix such as scattering parameters were not discussed. Zhai, Fang, Ding, and He (2014) designed an 8 × 8 Butler matrix based on a dual-layer microstrip configuration at 4.3 GHz using four phase shifters and six quadrature hybrids placed at the bottom and top layers, respectively. These layers were connected via through-holes. The Butler matrix yielded an insertion loss and a phase error of 2.5 dB and ± 15°, respectively. Moreover, Zhong et al. (2017) developed an 8 × 8 Butler matrix based on a dual-layer substrate integrated waveguide at 28 GHz to 31 GHz. The proposed Butler matrix consisted of an additional four quadrature hybrids, as compared to the conventional configuration. The simulated results showed an insertion loss and a phase error of 2 dB and 15°, respectively. However, the study did not clarify the overall losses of the fabricated Butler matrix. Besides, the air gap between substrate layers can cause additional losses and phase errors, further degrading the performance of the Butler matrix. In fact, the use of through-holes in multilayer structure increases fabrication complications. Based on the literature, these issues could be overcome using a single-layer microstrip structure that is more cost-effective and simple in design.

The main challenge of this research was to obtain high accuracy dimensions for a Butler matrix. The Butler matrix was designed at millimeter wave frequency, as the frequency increases, the wavelength becomes smaller. Therefore, if the dimensions of the designed Butler matrix are imprecise, the performance of the Butler matrix can be affected in which, high insertion loss and inconsistent transmission amplitude as well as incorrect phase difference can be observed at the output ports of the Butler matrix. This thesis presents the detailed design methodology of a multibeam array antenna fed by a Butler matrix based on a single-layer structure at 28 GHz. By utilized a three-dimensional electromagnetic simulation software, the accurate dimensions of a multibeam array antenna can be obtained. Additionally, the optimization was performed to achieve the required antenna performance. The designed multibeam array antenna was fabricated for measurements. The measured results were observed and analyzed to ensure the functionality of the proposed multibeam array antenna. Besides that, the design concept of multibeam base station antennas for the 5G mobile communication system was presented. The radiation patterns of the base station antenna were observed and analyzed in both horizontal and vertical planes. Moreover, the design of the multibeam base station antennas to achieve a 360° coverage area was shown. The beam coverage designs for horizontal and vertical sectorizations were demonstrated in this thesis.

As the 5G mobile communication system will be commercialized, research on sixth-generation (6G) mobile communication system has been started and it is predicted to deploy around 2030. The 6G mobile communication system will be operated in terahertz frequencies to provide higher data traffic, higher rates, larger bandwidth, and better service quality, as compared to the 5G mobile communication system, especially for artificial intelligence and machine learning applications (Akyildiz, Kak, & Nie, 2020; Alsharif et al., 2020; Dogra, Jha, & Jain, 2020; Z. Zhang et al., 2019). However, the design of a multibeam array antenna for base station in the 5G mobile communication system, as proposed in this thesis is still relevant in the near future since the mobile network operators will use the existing 5G mobile network to support their services to the subscribed mobile users (Ramírez-Arroyo et al., 2020; Saha, 2020; Sim, Lim, Park, Dai, & Chae, 2020)

1.3 Objectives

The main objective of this thesis is to design a multibeam array antenna based on a single-layer structure at 28 GHz for base station in a 5G mobile communication system. The proposed multibeam array antenna will produce multiple beams in different directions. The specific objectives of this thesis are listed as follows:

i. To design a beamforming circuit of a Butler matrix with a low-loss and low phase error characteristic.

ii. To identify the best antenna spacing configuration and to develop a multibeam array antenna for the base station.

iii. To propose the design concept of multibeam base station antennas.

1.4 Scope of Research

The rapid growth of the mobile communication system as a result of the increasing demand among mobile users for higher data traffic and higher data rates provides great opportunities to develop a new base station. The base station antenna for the 5G mobile communication system requires an efficient performance, low profile, lightweight, and more cost-effective for large-scale production. Thus, an array antenna is considered in this research to achieve these stringent requirements.

This thesis presents the design methodology of a multibeam array antenna fed by a Butler matrix at 28 GHz based on a single-layer structure to produce multiple beams within a coverage area. The Butler matrix was formed by the circuit elements such as the crossover, the quadrature hybrid, and the phase shifters. Furthermore, a three-dimensional electromagnetic simulation software called Computer Simulation Technology Microwave Studio was used to simulate and optimize the Butler matrix. Subsequently, the electrical performances of the circuit elements were observed and analyzed. The designed Butler matrix was fabricated using a substrate material with low loss tangent and low dielectric constant.

Moreover, a single-element microstrip antenna was designed to operate at 28 GHz. The microstrip antenna was integrated at the output ports of the Butler matrix. The complete structure of the multibeam array antenna was simulated and optimized to obtain the desired radiation characteristics using Computer Simulation Technology Microwave Studio. The radiation patterns and the antenna gains of the multibeam array antenna were observed and analyzed. Additionally, the antenna spacing of the multibeam array antenna was varied to study the beam coverage in the vertical plane. The best configuration of the antenna spacing for the multibeam array antenna was identified in this research. The proposed multibeam array antenna was fabricated using the same substrate material used to fabricate the Butler matrix. Furthermore, antenna measurements such as scattering parameters and radiation characteristics were conducted to validate the simulation results as well as to ensure the functionality of the proposed multibeam array antenna.

The design of multibeam base station antennas to achieve a 360° coverage area was presented in this thesis. The radiation patterns of the base station antenna were shown using graphical representations for the horizontal and vertical planes. Moreover, the analyses of the beam coverage designs for the base station antenna in the horizontal and vertical sectorizations were performed. The studies of the beam tilt technique in the vertical sectorizations were conducted to provide better coverage solutions to mobile users within the defined cell area.

1.5 Thesis Organization

Chapter 1 describes the background of the research including the problem statement and research motivations. The objectives of this thesis are outlined. Furthermore, the scope of the research is explained briefly in this chapter.

Chapter 2 gives an overview of mobile communication systems. The fifth-generation mobile communication system is discussed, which includes the concepts and technical requirements. The types of base station antenna are explained briefly. Moreover, the characteristics of the millimeter wave along with the limitations of the millimeter wave communications are discussed in this chapter. Apart from that, the multibeam antennas for the base station are described and the suitability of the multibeam antennas for the 5G base station antenna is discussed. The fundamental of the Butler matrix is explained in detail together with the basic operation and the design principles of the circuit elements. The microstrip antenna and linear antenna array with mathematical equations are presented.

Chapter 3 explains the research methodology of designing a multibeam array antenna for base station in the 5G mobile communication system. A flow chart is illustrated to describe the process flow beginning with the literature review, design of a Butler matrix, design of a multibeam array antenna, and design of multibeam base station antennas. The main requirements of a base station antenna for the 5G mobile communication system are addressed. Besides that, three-dimensional electromagnetic simulation software, antenna fabrication, and measurements are also explained.

Chapter 4 presents the design methodology of a single-layer Butler matrix at 28 GHz. The Butler matrix consists of circuit elements such as the crossover, the quadrature hybrid, and the phase shifters. These circuit elements were designed using three-dimensional electromagnetic simulation software. The electrical performances of the circuit elements were observed and analyzed. The 8×8 Butler matrix was formed by the integration of these circuit elements. The designed Butler matrix was fabricated using a low loss tangent and low dielectric constant substrate material. The scattering parameters measurements were conducted to ensure the actual performance of the fabricated Butler matrix. The simulation and measurement results of the Butler matrix were analyzed and discussed.

Chapter 5 elaborates on the design of a single-layer multibeam array antenna at 28 GHz. The design of a single-element microstrip antenna is presented. The performance of the single-element microstrip antenna was observed and analyzed. Furthermore, the design of a multibeam array antenna fed by an 8×8 Butler matrix is demonstrated. The beam coverage of the multibeam array antenna in the vertical plane was studied by varying the antenna spacing. The performance of the multibeam array antenna was observed and analyzed. Moreover, the designed multibeam array antenna was fabricated and measurements were conducted. The simulation and measurement results of the multibeam array antenna were analyzed and discussed.

Chapter 6 describes the proposed design concept of multibeam base station antennas for the 5G mobile communication system. The configuration of a base station antenna is explained. The radiation patterns of the base station antenna in the horizontal and vertical planes are presented. Apart from that, the design of the multibeam base station antennas to achieve a 360° coverage area in the horizontal plane is demonstrated. The analyses of beam coverage designs in the horizontal and vertical sectorizations are also presented. Furthermore, the studies of beam tilt technique in the vertical sectorization to provide beam coverage to mobile users for the inner and outer cells as well as to provide beam coverage to mobile users for high-rise building were conducted. The radiation patterns of the base station antenna were analyzed and discussed in this chapter.

Chapter 7 concludes the findings of the research works by discussing the analyses that have been conducted and the results that have been obtained. The main contributions of this thesis are highlighted in this chapter. Moreover, the recommendations for future work are also addressed.

CHAPTER 2: LITERATURE REVIEW

2.1 Introduction

This chapter presents an overview of mobile communication systems, from the first-generation (1G) to the current fourth-generation (4G) mobile communication system. The fifth-generation (5G) mobile communication system is discussed, including the concepts and technical requirements. Furthermore, this chapter explains the types of base station antennas. The current issues of the 4G base station antenna are also highlighted. Moreover, the characteristics of millimeter wave are presented in detail including the studies done on the millimeter waves, which are useful in developing a new 5G base station antenna. The limitations of millimeter wave communications are also stated in this chapter. Besides that, the types of multibeam antennas for the base station are explained along with previous studies on the development of multibeam antennas. The suitability of the multibeam antennas for the 5G base station antenna is also discussed. This chapter also describes the fundamental of a Butler matrix, including the basic operation and the design principles of the circuit elements such as the quadrature hybrid, the crossover, and the phase shifter. Apart from that, the design of a rectangular microstrip antenna is presented and the fundamental design equations are given. The configuration of a linear array antenna is also described.

2.2 Overview of Mobile Communication Systems

The mobile communication system has undergone a tremendous evolution in the past few decades. A new generation of mobile communication systems has been introduced approximately every ten years. The main purpose of introducing a new mobile communication system is to provide better service quality to mobile users.

The first-generation (1G) mobile communication system was introduced in 1981. This mobile communication system was based on an analog modulation technique and was used mainly for voice communications. The 1G mobile communication system had a data rate of up to 2.4 kbit/s and a bandwidth of 30 kHz at 800 MHz. During the deployment of the 1G mobile communication system, each country had implemented its standardizations of the mobile communication system. For example, in Japan, the 1G mobile communication system was launched by the Nippon Telephone and Telegraph. Meanwhile, the Nordic Mobile Telephone system operated in Northern European countries such as Denmark, Finland, Norway, and Sweden. In the United States, the Advanced Mobile Phone System was introduced. The 1G mobile communication system has many disadvantages such as poor security system, low service quality, limited numbers of mobile subscribers, and mobile services that were limited to voice communications only (Alsharif & Nordin, 2017; Park & Adachi, 2007).

In 1992, the second-generation (2G) mobile communication system was launched to overcome the limitations of the 1G mobile communication system. It was based on a digital modulation technique, which is known as the Global System for Mobile (GSM) communications. This system used the time division multiple access transmission and Gaussian Minimum Shift Keying (GMSK) with a data rate of 9.6 kbit/s and bandwidth of 200 kHz for voice communications. The General Packet Radio Services (GPRS) is the 2.5^{th} generation mobile communication system that uses packet switching technology, which increases the data rate up to 50 kbit/s. Furthermore, the Enhanced Data Rates for Global Evolution (EDGE) improved the data rate up to 200 kbit/s. This system employs the eight phase shift keying and GMSK modulation techniques to provide higher speed data communications to mobile users (Alsharif & Nordin, 2017).

The third-generation (3G) mobile communication system was employed in 2001. This system was the first international standard system defined by the International Telecommunication Union known as the Universal Mobile Telecommunications System

(UMTS) (Park & Adachi, 2007). This system uses the wideband code division multiple access and the High Speed Packet Access (HSPA) techniques to allow high-speed mobile access with Internet Protocol services, and improves the quality of video and audio streaming. The allocation frequency band is in the range of 1.8 GHz to 2.5 GHz with a data rate of up to 2 Mbit/s. There are two protocols used in the HSPA, which are, the high-speed downlink packet access and the high speed uplink packet access. These protocols enable mobile users to download music and video, play interactive games, send and receive high-resolution pictures and videos, as well as emails with large file attachments. Furthermore, the evolved HSPA was introduced in 2008 with a data rate of up to 42.2 Mbit/s (Alsharif & Nordin, 2017; Park & Adachi, 2007; Rappaport et al., 2013).

The current fourth-generation (4G) mobile communication system was utilized in 2011. The 4G mobile communication standardization, known as the Long Term Evolution (LTE), was developed by the 3rd Generation Partnership Project. LTE uses an orthogonal frequency division multiplexing technique based on radio access technology. In the 4G mobile communication system, the multiple-input multiple-output system improves the service quality and provides multiple stream transmission to enhance the spectrum efficiency. This system supports advanced multi-antenna transmission with a data rate of up to 100 Mbit/s and bandwidth of 20 MHz. Furthermore, the LTE-Advanced is introduced to improve the throughput rate of more than 1 Gbit/s and the bandwidth increases to 100 MHz via carrier aggregation. This system supports heterogeneous networks with existing macrocells, microcells and picocells along with wireless fidelity access points (Alsharif & Nordin, 2017; Korhonen, 2014; Rappaport et al., 2013).

The next generation of the mobile communication system is known as the fifth-generation (5G) mobile communication system. The concepts of the 5G mobile communication system have been studied for the past few years by researchers such as Gavrilovska et al. (2016), Niu et al. (2015), and (Shanzhi & Jian, 2014). Figure 2.1 presents the roadmap for the 5G mobile communication system. The initial research stage, involving the development of prototypes and evaluation trials, started in 2011. In 2015, the International Mobile Telecommunications (IMT) defined the main requirements for 5G standardizations. The product development phase will be completed by the end of 2020. It is expected that the 5G mobile communication system will be commercialized by 2021 (Le et al., 2015; Rodriguez, 2015; Xiang, Zheng, & Shen, 2016).

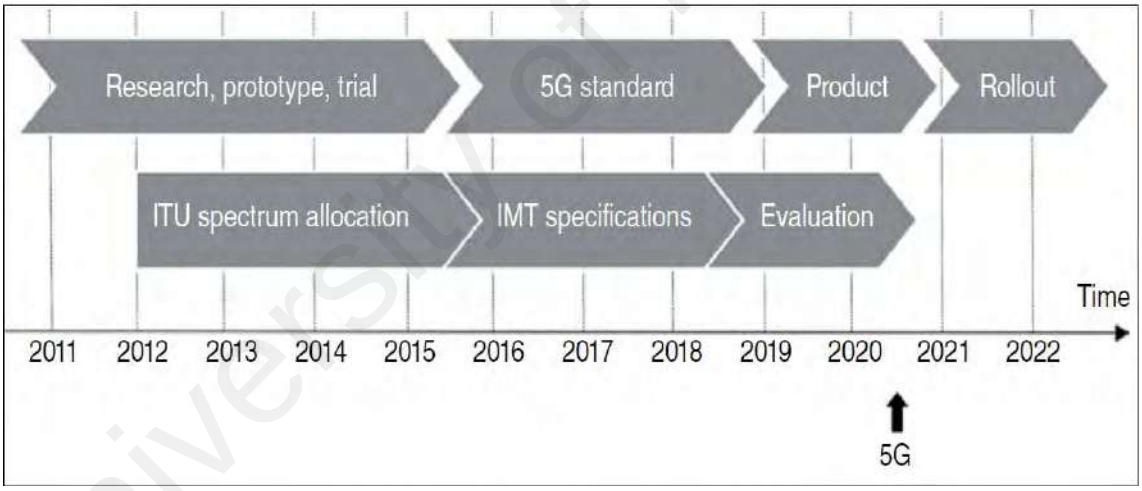

Figure 2.1: Roadmap for the 5G mobile communication system (Rodriguez, 2015)

The key requirements of the 5G mobile communication system, as compared to the current 4G mobile communication system, are illustrated in Figure 2.2. The eight key performance indicators were defined by the International Telecommunication Union, which are user experienced data rate, spectrum efficiency, mobility, latency, connection density, network energy efficiency, area traffic capacity, and peak data rate (Mumtaz, Rodriguez, & Dai, 2017). As shown in Figure 2.2, the 5G mobile communication system will support the user experience with a data rate of 100 Mbit/s in urban and suburban areas, as compared to the 4G mobile communication system, which achieved a data rate of only up to 10 Mbit/s. The spectrum efficiency of the 5G mobile communication system is expected to be three times higher than the 4G mobile communication system. Moreover, the mobility of the 5G mobile communication system is expected to achieve up to 500 km/h, whereas the 4G mobile communication system can only support up to 350 km/h, particularly in high-speed train applications. Furthermore, the latency of the 5G mobile communication system is less than 1 ms to ensure highly reliable signal connectivity. On the other hand, the latency of the 4G mobile communication system is 10 ms. In machine-to-machine communications, the 5G mobile communication system is expected to support a connection density of 10 times higher than the 4G mobile communication system, which is up to 10^6/km^2. The network energy efficiency of the 5G mobile communication system is 100 times greater than the 4G mobile communication system. Additionally, the 5G mobile communication system is expected to support area traffic capacity of 10 Mbit/s/m^2, which is 100 times higher than the 4G mobile communication system. The 5G mobile communication system will increase the peak data rate up to 20 Gbit/s, meanwhile, the 4G mobile communication system achieved the peak data rate of 1 Gbit/s (Alsharif & Nordin, 2017; Dahlman, Parkvall, Astély, & Tullberg, 2014; Gavrilovska et al., 2016; Mumtaz et al., 2017; Xiang et al., 2016). To achieve these key requirements, most of the research that has been conducted is focused on the utilization of higher frequencies in the millimeter waves, massive multiple-input multiple-output schemes, dense deployment of small cells, and development of multibeam antennas (Andrews et al., 2014; Boccardi, Heath, Lozano, Marzetta, & Popovski, 2014; Hong et al., 2017; Hwang, Tsai, & Hsiao, 2015; Rappaport et al., 2013).

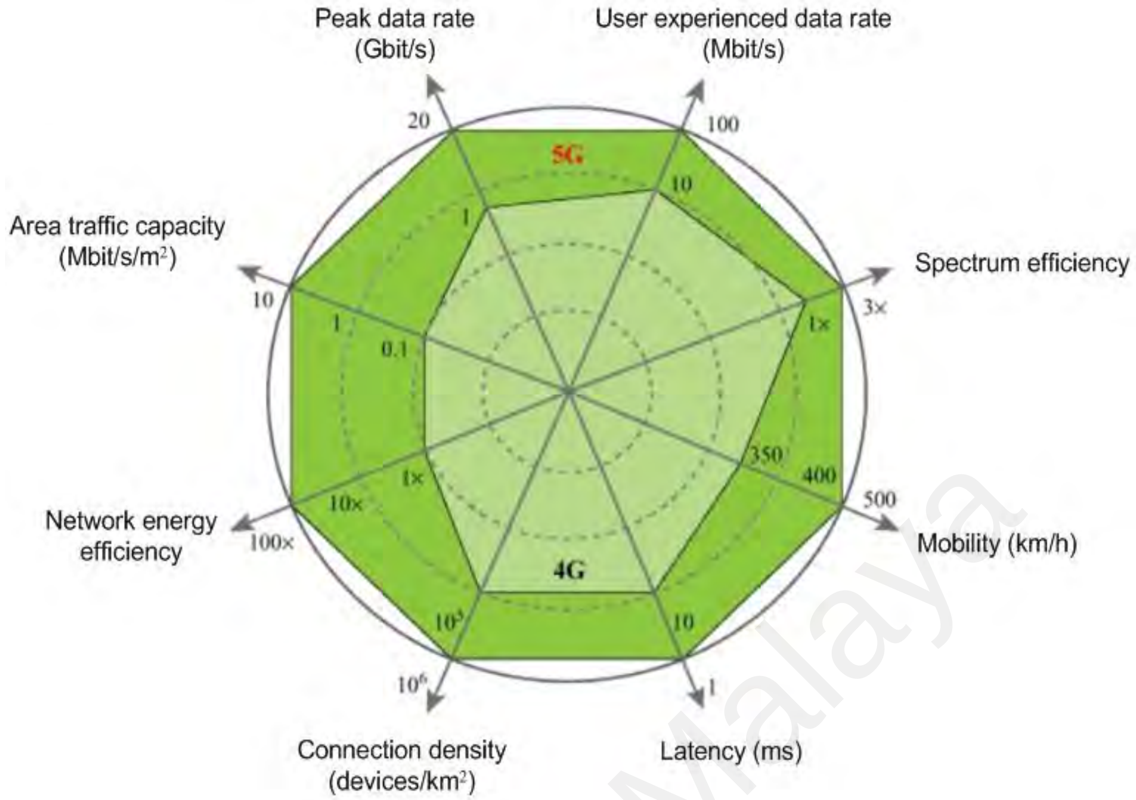

Figure 2.2: Key requirements of the 5G mobile communication system (Mumtaz et al., 2017)

2.3 Base Station Antennas

A base station antenna contributes significantly to the mobile communication system to establish a radio transmission line between radio stations. There are two types of communication such as communications between the base station and mobile users as well as communications between base stations. The radio wave energy should be radiated using a base station antenna within the defined coverage area to establish these communications. The size of the coverage area is dependent on the types of the base station antenna (Kyohei & James, 2008).

In the 1G mobile communication system, the type of base station antenna is omnidirectional, as illustrated in Figure 2.3. It provides a uniform radiation pattern in the horizontal plane around the base station. The base station antenna has a high gain that can support long-distance communications with a cell radius of hundreds of kilometers (Andrews et al., 2014). The type of antenna that is commonly used in the base station is a printed dipole antenna. However, the main drawback of an omnidirectional base station antenna is poor coverage, especially near or below the base station. This is due to the narrow radiation pattern in the vertical plane. Although an omnidirectional base station antenna provides radiation uniformly, only a small amount of total energy is received by mobile users (Stutzman & Thiele, 2012). Therefore, this type of base station antenna can cater only for the low capacity of mobile users. It is usually used in rural and private areas (Balanis, 2005; Kyohei & James, 2008; Stutzman & Thiele, 2012).

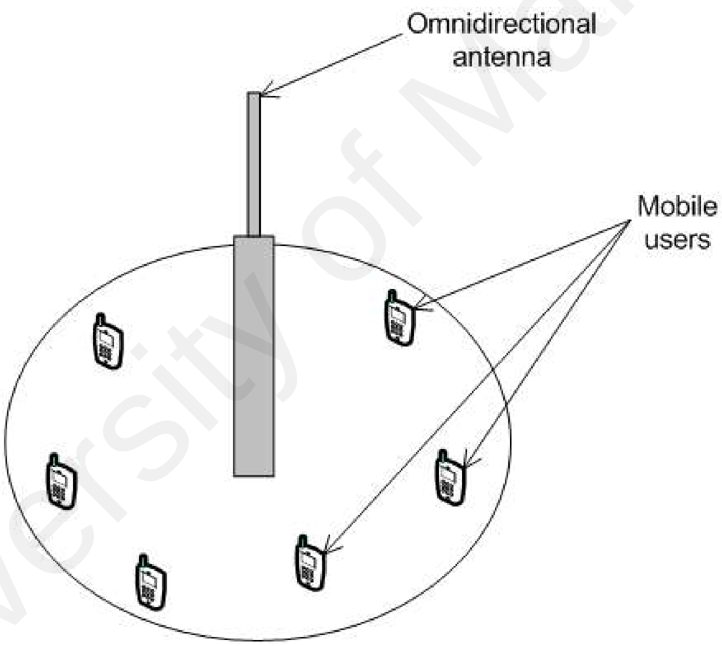

Figure 2.3: Omnidirectional base station antenna

A sector base station antenna is the most common type that has been implemented in mobile communication systems. The development of a sector base station antenna is to enhance the system capacity and network coverage. Therefore, an omnidirectional base station antenna was replaced by a sector base station antenna (Kyohei & James, 2008). A sector base station is capable of producing a number of radiation patterns within the defined coverage area. Figure 2.4 shows a three sectored base station. This base station is commonly used during the 2G and 3G mobile communication systems. As illustrated in Figure 2.4, three base station antennas of a vertical antenna array are used and each base station antenna covers one sector of 120° in the horizontal plane. The base station antenna for a three sectored base station has a beamwidth of 65° or 90°. There are several types of antenna that are used in the base stations such as dipoles, patch antennas, and log periodic antennas (Kyohei & James, 2008). In the current 4G mobile communication system, a six sectored base station is used in which, each sector covers 60° in the horizontal plane and the beamwidth is about 30° (Stutzman & Thiele, 2012). The sector base station uses both mechanical and electrical down tilt techniques to tilt the radiation patterns for long distance communications and reduce interference between base stations (Kyohei & James, 2008; Stutzman & Thiele, 2012). The base station has a cell radius of hundreds of meters to tens of kilometers (Bates, Gallon, Bocci, Walker, & Taylor, 2006).

Furthermore, the dual-band panel antennas were invented since the 2G mobile communication system to reduce the installation space and cost. These panel antennas consist of two antenna elements in which, one antenna element is operated at low frequency band and another antenna element is operated at high frequency band (Kyohei & James, 2008). The dual-polarized antennas had been implemented in the three sectored base station. The vertical and horizontal polarized antennas are placed alternately. The most common configuration is the dual orthogonal slant 45° linear polarizations. In addition, the down tilt angle is achieved using the electrical down tilt technique. In this technique, the phase shifters are employed by changing the length of the feed lines (Stutzman & Thiele, 2012). Besides that, the triple-band antenna was introduced in 2003 during the 3G mobile communication system. This antenna is operated at frequencies of 0.9 GHz, 1.5 GHz, and 2 GHz. Besides that, the adaptive antennas are utilized to increase the antenna gain at the desired direction and suppress interference at the undesired directions (Kyohei & James, 2008).

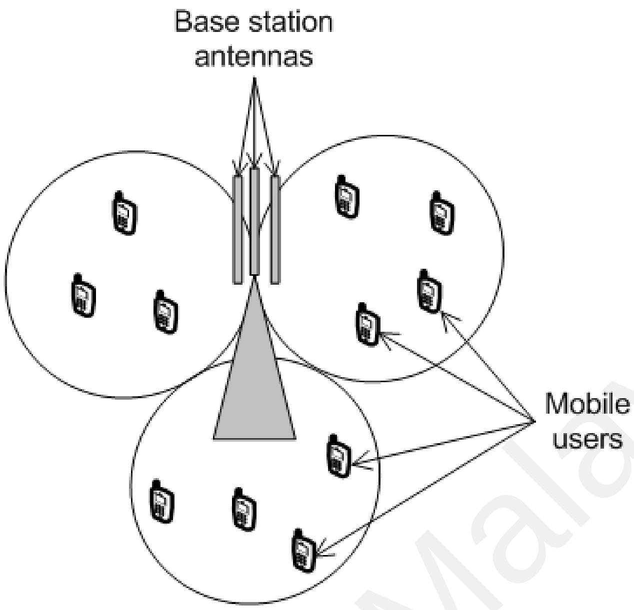

Figure 2.4: Three sectored base station antenna

In the current 4G mobile communication system, the multiple frequency band antennas were implemented at the base stations. These antennas are operated at frequencies of 0.9 GHz, 1.5 GHz, 2 GHz, and 2.6 GHz. Figure 2.5 shows the structure of the 4G base station antenna. These antennas are placed on the vertical plane. A feeding network is used to feed the antennas. However, the drawbacks of using these antennas are high side lobe levels and the appearance of the grating lobes at higher frequencies. Moreover, the implementation of an electrical beam tilt circuit degrades the radiation characteristics (Yamada & Rahman, 2016). Furthermore, the limitation of the 4G mobile communication system is a high co-channel interference between the base stations (Nam, Bai, Lee, & Kang, 2014; Panwar, Sharma, & Singh, 2016). Therefore, a new base station will be developed in the 5G mobile communication system to overcome these issues. Table 2.1 shows the summary of base station antennas from the 1G to the 4G mobile communication systems.

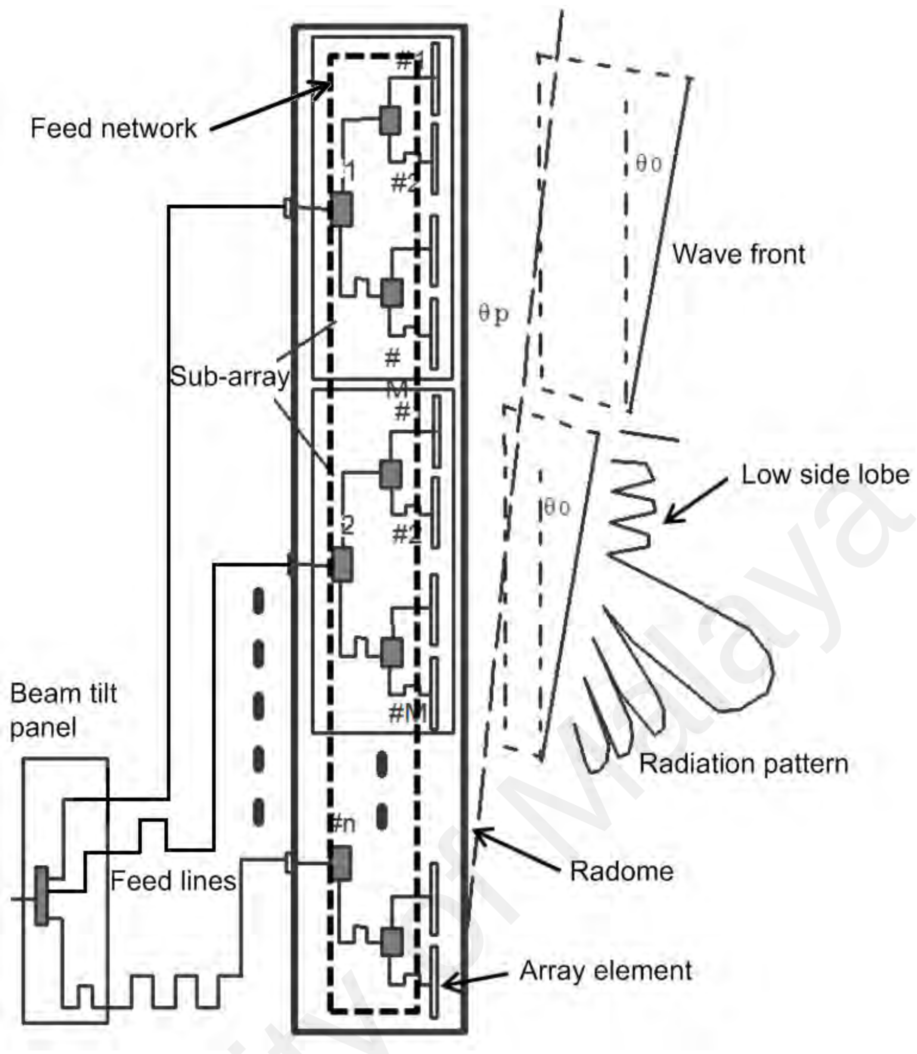

Figure 2.5: Structure of the 4G base station antenna (Yamada & Rahman, 2016)

Table 2.1: Summary of base station antennas from 1G to 4G

Mobile Communication System	**1G**	**2G**	**3G**	**4G**
Type of base station antenna	Omnidirectional	Sector	Sector	Sector
Frequency	900 MHz	900 MHz and 1.5 GHz	900 MHz, 1.5 GHz, and 2 GHz	900 MHz, 1.5 GHz, 2 GHz, and 2.6 GHz
Key feature	High gain, uniform radiation pattern, and analog system	Three sectors, beam tilting technique, dual-polarized antenna, and digital system	Triple frequency band antenna and adaptive antenna	Six sectors and multiple frequency band antenna

2.4 Millimeter Wave

Presently, the frequencies between 300 MHz and 3 GHz are fully utilized for commercial radio communications such as satellite communications, AM/FM radio, wireless fidelity, global positioning system, high definition television, and cellular (Alsharif & Nordin, 2017; Pi & Khan, 2012). Due to this, researchers have to explore new frequency bands in millimeter waves for more channel capacity and bandwidth for the 5G mobile communication system. By referring to Shannon-Harley theorem, the equation can be written as shown in Equation (2.1) (Sheikh & Lempiäinen, 2016):

$$C = B\log_2\left(1 + \frac{S}{N}\right) \tag{2.1}$$

where *C* is the channel capacity, *B* is the bandwidth of the channel, and *S/N* is the signal-to-noise ratio. Based on Equation (2.1), the channel capacity is proportional to the channel bandwidth and signal-to-noise ratio. Therefore, increasing the channel bandwidth will result in increasing the channel capacity of the mobile communication system.

According to the Friis transmission equations, the free space omnidirectional propagation loss will increase proportionally to the frequency and distance. The Friis transmission equations are shown in Equation (2.2) and Equation (2.3) (Rangan, Rappaport, & Erkip, 2014; Stutzman & Thiele, 2012; J. Zhang, Ge, Li, Guizani, & Zhang, 2017):

$$P_R = \frac{P_T A_{er} G_t \cos^2\phi}{4\pi r^2} \tag{2.2}$$

and

$$G_t = \varepsilon_{ap} D_t = \frac{k4\pi S_{area}}{\lambda^2} \tag{2.3}$$

where P_R and P_T are received and transmitted power, respectively, A_{er} is the effective aperture of receiving antenna, G_t is the antenna array gain, $cos^2 \phi$ is the polarization loss factor, r is the distance between the transmit antenna and the receive antenna, ε_{ap} is the aperture efficiency, D_t is the directivity of beam shaped by the antenna array, S_{area} is the area of the antenna array, and λ is the wavelength.

The millimeter wave communications can be affected by atmospheric conditions such as rain along with atmospheric and molecular absorption (Kourogiorgas, Sagkriotis, & Panagopoulos, 2015; Niu et al., 2015). During heavy rainfall, the system performance will be degraded as the frequency increases. In addition, the atmospheric and molecular absorption is significant at certain frequencies, which is not suitable for communication in an outdoor environment (Narekar & Bhalerao, 2015). The attenuation is more severe at frequencies between 57 GHz and 64 GHz due to oxygen absorption in the atmosphere. Moreover, high attenuation is observed at frequencies between 164 GHz and 200 GHz caused by water vapor absorption (Bae, Kim, & Chung, 2014).

The Federal Communications Commission (FCC) has defined a frequency band of 28 GHz to be utilized in the 5G mobile communication system (FCC, 2020; Hong et al., 2017). Therefore, studies have been conducted by Rappaport et al. (2013) to observe the rain attenuation and atmospheric absorption at 28 GHz in an urban environment with a cell radius of 200 m. The rain attenuation at different rainfall rates and atmospheric absorption in millimeter wave frequencies are presented in Figure 2.6 and Figure 2.7. The results showed that the rain attenuation is about 7 dB/km with a rainfall rate of 25 mm/h. Therefore, the attenuation is around 1.4 dB for a cell radius of 200 m. Meanwhile, the atmospheric absorption is about 0.012 dB for a cell radius of 200 m. It can be concluded that the attenuation caused by the rain and atmospheric absorption does not give any significant effect on the propagation for a cell radius of 200 m at 28

GHz (Niu et al., 2015). Based on these studies, the cell radius of a base station for the 5G mobile communication system must be less than 200 m at 28 GHz to ensure highly reliable signal connectivity for mobile users within the coverage area.

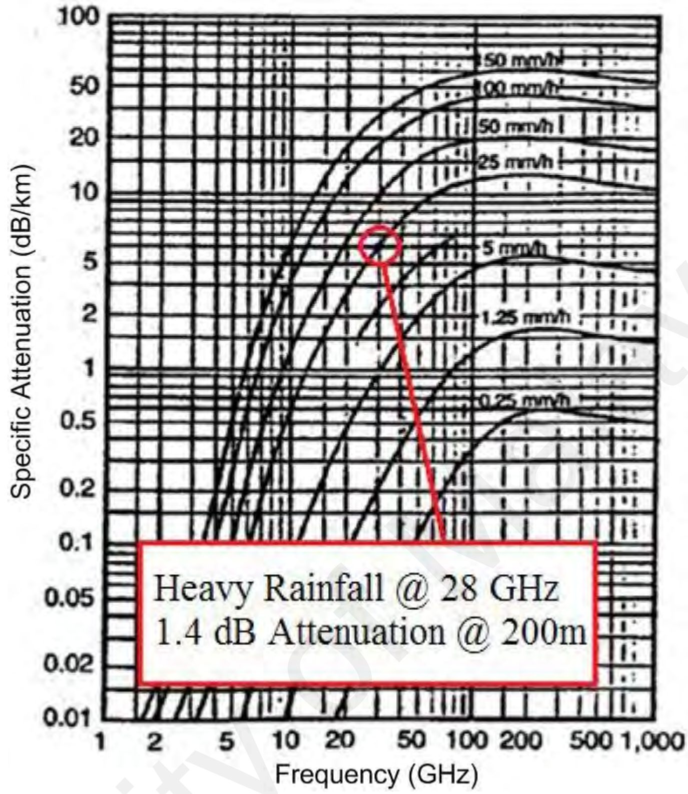

Figure 2.6: Rain attenuation across frequency at various rainfall rate (Rappaport et al., 2013)

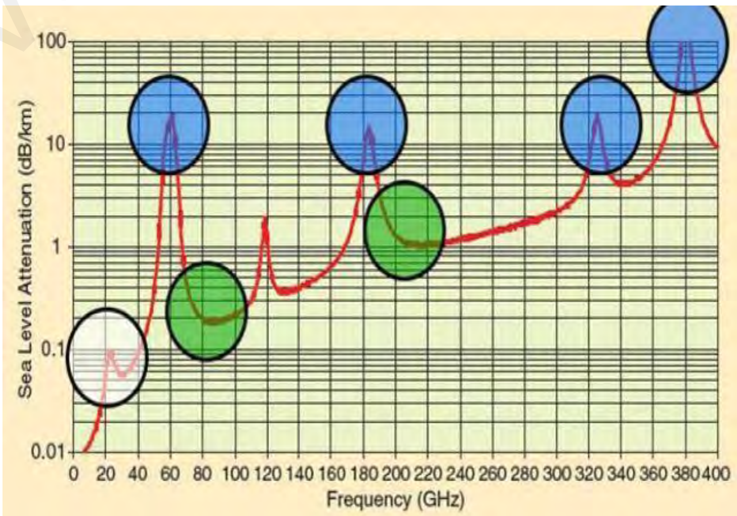

Figure 2.7: Atmospheric absorption in millimeter wave frequencies (Rappaport et al., 2013)

In addition, the free space path loss is dependent on the carrier frequency as the size of the antennas is kept constant and the wavelength is c/f, where c is the speed of light in vacuum and f is the carrier frequency. The wavelength of an antenna is decreased as the frequency increases. Based on Equation (2.2) and Equation (2.3), the effective aperture of the antenna increases with a factor of $\lambda^2/4$ and the size of the antenna is reduced as the frequency increases. The free space path loss between the transmitter and the receiver are increased with a factor of f^2 (Rangan et al., 2014; Swindlehurst, Ayanoglu, Heydari, & Capolino, 2014). On the other hand, the free space path loss remains unchanged if the effective aperture of the antenna at one end of either transmitter or receiver is kept constant. Moreover, the free space path loss decreases with a factor of f^2 if the effective aperture of the antenna at both transmitter and receiver are kept constant (Andrews et al., 2014; Gupta & Jha, 2015). Therefore, multiple antennas can be employed at the base station and the mobile terminal to reduce the free space path loss.

2.5 Multibeam Antennas for Base Station in the 5G Mobile Communication System

As mentioned in Section 2.4, the millimeter wave communications suffer from severe propagation loss, which affects the signal-to-interference-plus-noise ratio. The multibeam antennas are the most promising solution for base station in the 5G mobile communication system to overcome this issue. These antennas are capable of producing multiple beams in different directions within the defined cell area. The radiated beams have narrow beamwidth and high antenna gains. The advantages of employing the multibeam antennas at the base station are to enhance system capacity and improve network coverage as well as to reduce co-channel interference (Hong et al., 2017; P. Yang et al., 2014). There are three types of multibeam antennas that are suitable to be used at the base station such as reflector antennas, lens antennas, and array antennas. The basic principle of operation and the literature review of multibeam antennas are discussed in the following subsections.

2.5.1 Reflector Antennas

Reflector antennas are broadly utilized in the radar and satellite communication systems. There are three configurations of the reflector antennas such as plane, corner, and curved reflectors (Balanis, 2005). The principle of reflector antenna is based on the ray optics technique. The basic configurations of the center-fed reflector antenna are presented in Figure 2.8 (a). This antenna is formed by a dish reflector with diameter, D and focal length, F as well as feed antennas with antenna spacing, d. Multiple beams are produced in different directions, as the feed antennas are excited. The performance of a reflector antenna is depending on the shape of the reflectors, the feed antennas design as well as the positions of reflectors and feed antennas.

Studies on the reflector antennas have been actively conducted in the last few decades. The use of horn antennas as a feeding antenna can cause spill-over loss and polarization impurity, which degrades the system performance (Afifi, 1990; Hong et al., 2017). Therefore, many types of feeding antennas have been proposed such as electromagnetic bandgap antennas, leaky-wave slot arrays, and printed radiating elements (Kanso et al., 2011; Llombart, Neto, Gerini, Bonnedal, & Maagt, 2008; Mishra, Sood, & Kumar, 1998). Furthermore, the offset-fed reflectors have been implemented to reduce the distortion of the radiation pattern that was caused by the blockage of the feed antennas (Jorgensen, Balling, & English, 1985; Rudge, 1975). The configuration of the offset-fed reflector antenna is presented in Figure 2.8 (b). The shaped dual and triple reflectors along with the dual bifocal reflectors have been implemented to improve the aperture illumination for high aperture efficiency applications (Plastikov, 2016; Rao & Tang, 2006; Winter, 1971). Besides that, the planar reflectarrays have been developed to replace the dish reflector due to heavyweight, larger sized, and more expensive (Chahat et al., 2016; Monk & Clarricoats, 1994).

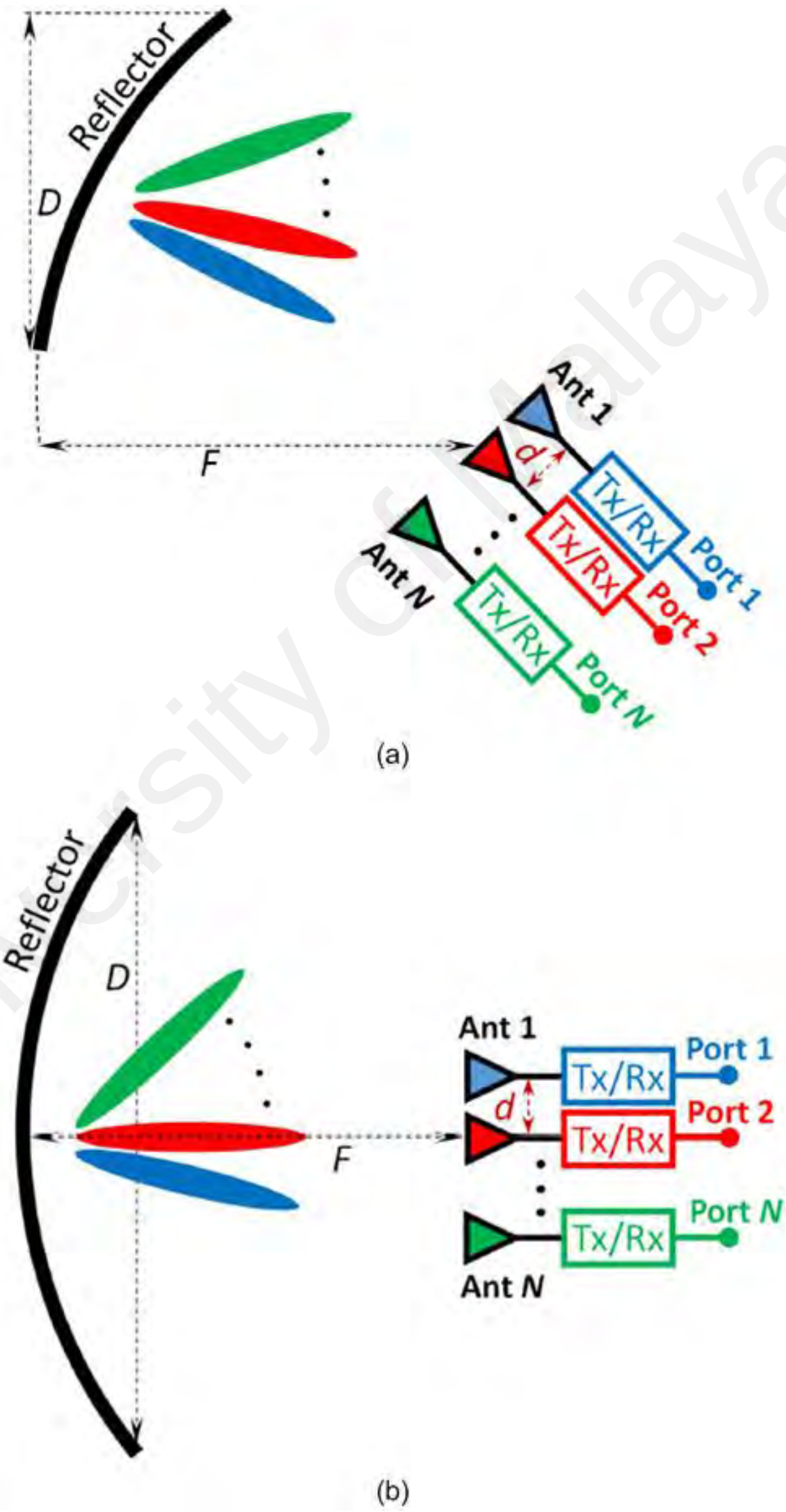

Figure 2.8: (a) Center-fed and (b) offset-fed reflector antenna (Hong et al., 2017)

There are many designs of center-fed and offset-fed reflector antennas that have been reported in millimeter waves (Dau-Chyrh & Ming-Chih, 1995; Han, Huang, & Kai, 2005; D. M. Pozar, Targonski, & Syrigos, 1997; Yu, Yang, Elsherbeni, Huang, & Kim, 2012). However, the reflector antennas have poor beam scanning along with distortion of the radiation patterns and reduction of the antenna gains due to blockage of feed antennas as well as high side lobe levels. The reflector antennas would almost be impossible to be implemented in a 5G base station due to these limitations.

2.5.2 Lens Antennas

The lens antennas are more compact and there is no blockage of the feed antenna in comparison to reflector antennas. Figure 2.9 illustrates a conventional lens antenna with diameter, *D* and focal length, *F* as well as feed antennas with antenna spacing, *d*. The multiple beams are produced on the surface of the lens when the feeding antennas are excited. The performance of the lens antenna is dependent on the geometry of the lens and properties of the lens material.

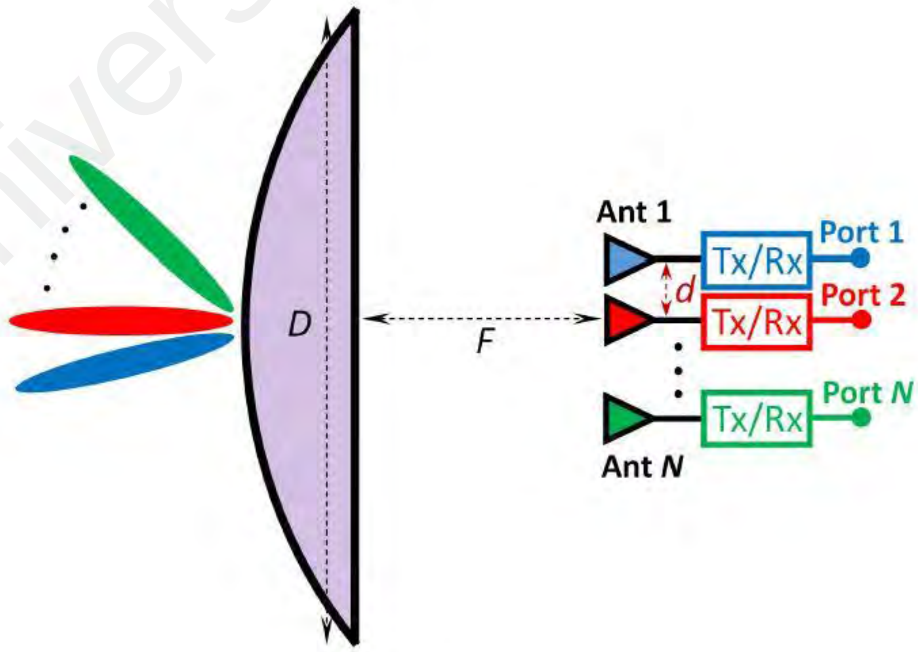

Figure 2.9: Lens antenna (Hong et al., 2017)

Many studies have been reported on the lens antennas to reduce the side lobe level of the radiated multiple beams and increase the antenna gain. There are many types of lenses antennas such as convex and concave lenses, bifocal lenses, spherical lenses as well as shaped lenses that have been developed (J. Lee & Carlise, 1983; Luh, Smith, & Scott, 1982; Maruyama, Yamamori, & Kuwahara, 2008; Peebles, 1988; Schoenlinner, Xidong, Ebling, Eleftheriades, & Rebeiz, 2002). The most popular lens antenna is the Luneburg lens, which has low scanning loss that can be achieved when the gradient-index lenses are fed by an array antenna conformal to the lens surface (Peeler & Coleman, 1958; Xue & Fusco, 2007). The Fresnel lenses have a low profile, however they suffer from high insertion loss due to shadow blockage and narrow bandwidth (Rotman, 1984). Extensive research has been conducted to reduce the weight and size of the lens antennas in recent years (Y. J. Cheng et al., 2008; Tekkouk, Ettorre, Coq, & Sauleau, 2016; Y. S. Zhang & Hong, 2012). The transmit arrays can be employed to produce multiple beams by using multi-layer printed metallic resonators or implementing delay lines between two surfaces of the lens (Boccardi et al., 2014; Nematollahi, Laurin, Page, & Encinar, 2015). Another type of lens antenna is the Rotman lens in which, the output faces of the lens are integrated with antenna elements. It has multiple focal points and it can be implemented using the bootlace concept. However, the Rotman lens suffers from high ohmic loss, high power loss within the lens, and high phase error across the aperture (Katagi et al., 1984; J. J. Lee & Valentine, 1996).

Although the lens antennas have improved the beam shaping techniques, the large structure of the lens antenna could lead to a phase error, especially for the beams that are pointing at directions from the broadside of the lens. Additionally, the positions of the feed antenna can cause mutual coupling, which can deform the radiation patterns and reduce the antenna gains (Hong et al., 2017). Therefore, lens antennas are not suitable to be utilized as a base station antenna in a 5G mobile communication system.

2.5.3 Array Antennas

Array antennas have received great interest among researchers and design engineers. These antennas are the most preferred solution in many wireless communication systems due to the ease of fabrication, as these antennas can be implemented on the flat surface as well as the cost-effectiveness for large-scale production. The array antennas are capable of producing multiple beams in different directions based on the phase distributions of the linear antenna array. Many types of beamforming circuits have been proposed, however, the most popular are the Blass matrix and the Butler matrix.

The Blass matrix consists of a number of rows and columns that are connected using transmission lines, as shown in Figure 2.10. Each column of the Blass matrix is integrated with an antenna element. The number of rows in the Blass matrix corresponds to the number of beams. A directional coupler is used at the crossing point between a column and a row. The phase shifters are implemented in the same row between two directional couplers (Mosca, Bilotti, Toscano, & Vegni, 2002). The Blass matrix is rarely used in any application due to its high loss characteristic, as the directional couplers with unity coupling values are required (P. Chen, Hong, Kuai, & Xu, 2009; Hong et al., 2017). Moreover, the Blass matrix has low efficiency due to its lossy network (Bhowmik et al., 2014). A technique of nonlinear multivariable programming was demonstrated to reduce the loss in the Blass matrix. The Blass matrix and microstrip antenna can be integrated using a single substrate. However, the results showed the appearance of minor spurious beams (Vetterlein & Hall, 1989).

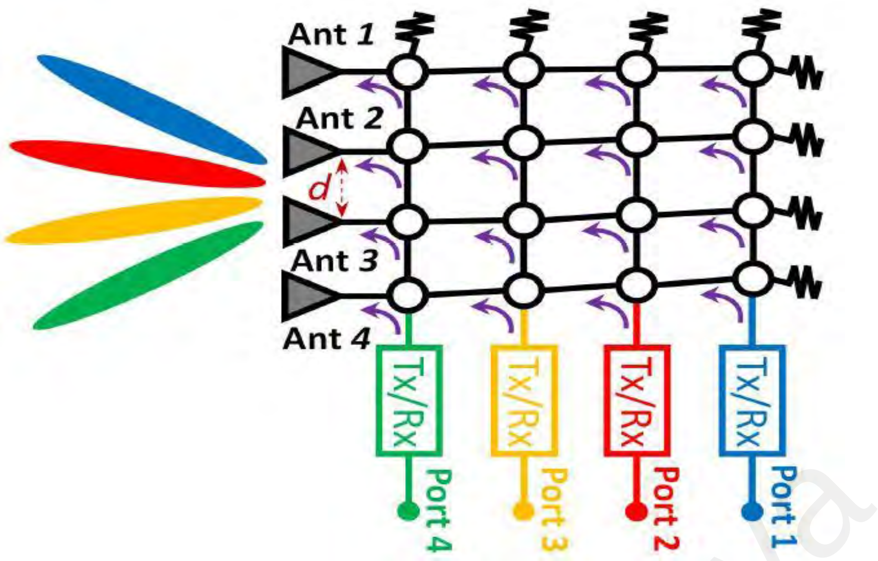

Figure 2.10: Structure of a 4 × 4 Blass matrix (Hong et al., 2017)

The most common beamforming circuit is the Butler Matrix since it was introduced by Butler (1960). The Butler matrix is broadly utilized in satellite and radar communication systems due to its design simplicity and low power dissipation. Figure 2.11 illustrates the structure of a 4 × 4 Butler matrix integrated with four antenna elements. The Butler matrix can be fabricated using advanced processes such as thick-film (Henry, Free, Izqueirdo, Batchelor, & Young, 2009) and low-temperature co-fired ceramic (Jong-Hoon, Pinel, Papapolymerou, Laskar, & Tentzeris, 2005). However, the standard printed circuit board (S. Cheng, Yousef, & Kratz, 2009) technology is preferred due to the cost-effectiveness for large-scale production (C. Chen & Chu, 2010). The structure of the Butler matrix is compact and it can be mounted easily at the base station. Furthermore, the Butler matrix has the ability of producing orthogonal beams, which improves the beam scanning coverage. Therefore, the Butler matrix is chosen as a beamforming circuit in this thesis. The previous research works on the designs of 4 × 4 and 8 × 8 Butler matrices are summarized in Table 2.2, along with the drawbacks. Table 2.3 lists the advantages and disadvantages of the multibeam antennas for base station in the 5G mobile communication system.

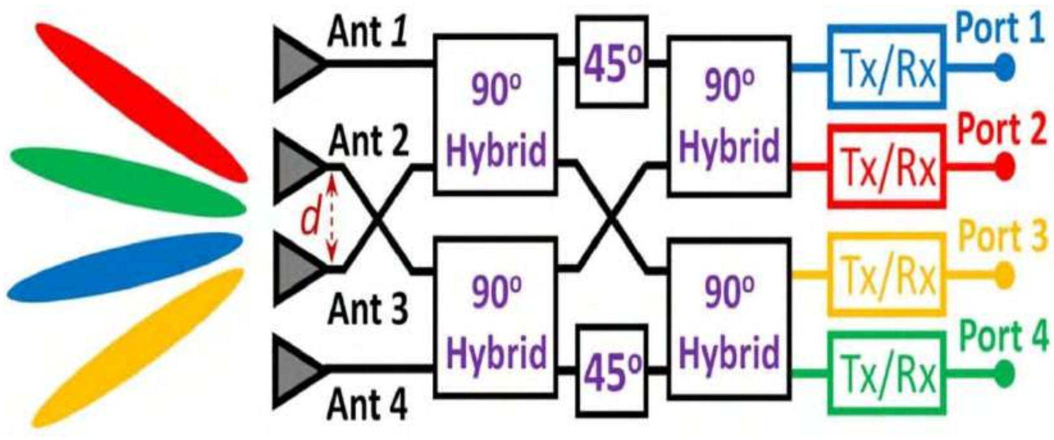

Figure 2.11: Structure of a 4 × 4 Butler matrix (Hong et al., 2017)

Table 2.2: Previous research works on the 4 × 4 and 8 × 8 Butler matrices

<table>
<tr><th>Authors</th><th>Description</th><th>Drawback</th></tr>
<tr><td>Babale et al. (2018)</td><td>Designed a 4 × 4 Butler matrix using only quadrature hybrids at 6 GHz without the use of a phase shifter and a crossover.</td><td rowspan="3">These techniques are only valid for a 4 × 4 Butler matrix and are not applicable for higher-order Butler matrices, which require a more complex structural design.</td></tr>
<tr><td>Tian et al. (2014)</td><td>Designed a 4 × 4 Butler matrix at 6 GHz using hybrid couplers and a crossover without the use of a phase shifter.</td></tr>
<tr><td>Ben Kilani et al. (2012)</td><td>Designed a 4 × 4 Butler matrix based on conductor-backed coplanar waveguide technology at 5.8 GHz using two directional elliptic couplers, two directional slot-coupled couplers, and two phase shifters.</td></tr>
<tr><td>Zhai et al. (2014)</td><td>Designed an 8 × 8 Butler matrix at 4.3 GHz using six quadrature hybrids and four phase shifters that are placed in the top and bottom layers, respectively.</td><td rowspan="2">The air gap between substrate layers can cause high insertion losses and high phase errors that degrade the performance of the Butler matrix.

The use of through-holes in multilayer technology increases the fabrication difficulties.</td></tr>
<tr><td>Zhong et al. (2017)</td><td>Designed a dual-layer substrate integrated waveguide 8 × 8 Butler matrix from 28 GHz to 31 GHz with additional four quadrature hybrids, as compared to the conventional configuration.</td></tr>
</table>

Table 2.3: Advantages and disadvantages of the multibeam antennas for base station in the 5G mobile communication system

Multibeam Antenna		Advantage	Disadvantage
Reflector		- Design simplicity - Design maturity	- Feed blockage - Poor beam scanning - High side lobe level
Lens		- No feed blockage - Good beam scanning	- Heavy - High phase error - High mutual coupling
Array	Blass matrix	- Flexible number of input and output ports - No crossover	- High loss - Low efficiency - Minor spurious beams
	Butler matrix	- Low power dissipation - Produce orthogonal beams - Ease of fabrication - Low cost and low profile	- High insertion loss and phase error, especially in higher-order matrices

2.6 Fundamental of the Butler Matrix

In this thesis, the Butler matrix is chosen as a beamforming circuit to feed the multibeam array antenna for base station in a 5G mobile communication system. The Butler matrix is a passive circuit of N inputs and N outputs connected to the antenna elements, where N is the power of 2 ($N = 2^n$). The $N \times N$ Butler matrix produces N beams in different directions. This circuit has equal amplitudes at the output ports when an input port is excited. Moreover, the phase differences between the output ports of the Butler matrix are constant for each input port.

The design procedure of the Butler matrix can be referred to in Moody (1964). A Butler matrix consists of circuit elements such as the quadrature hybrid, the crossover, and the phase shifter. The numbers of the quadrature hybrid and the phase shifter in a $N \times N$ Butler matrix can be determined using Equation (2.4) and Equation (2.5), respectively (Delaney, 1962):

$$\text{Number of quadrature hybrid} = \frac{N}{2}\log_2 N \qquad (2.4)$$

$$\text{Number of phase shifter} = \frac{N}{2}(\log_2(N) - 1) \tag{2.5}$$

Meanwhile, the number of the crossover in an $N \times N$ Butler matrix can be calculated using Equation (2.6) (Corona & Lancaster, 2003):

$$C_n = 2C_{n-1} + 2^{n-1}(2^{n-1} - 1) \tag{2.6}$$

where n should be more than 2, $C_1 = 1$ and $C_2 = 2$. The following subsections present detailed descriptions of the basic operation and the design principles of the quadrature hybrid, the crossover, and the phase shifter.

2.6.1 The Quadrature Hybrid

The quadrature hybrid is a 3 dB directional coupler with a 90° phase difference at the output ports of the circuit. It can be designed using a stripline line or a microstrip transmission (David M. Pozar, 2005). Figure 2.12 illustrates the geometry of the quadrature hybrid. The length and the characteristic impedance of the quadrature hybrid are $\lambda_g/4$ and Z_o, respectively, where λ_g is the wavelength in the microstrip transmission line. The design of this circuit is symmetrical in which, any port can be used as the input port. The output ports will be on the opposite side of the input port. Meanwhile, the isolated port will be on the same side as the input port.

When power enters at the input port, P1, the power is divided uniformly between the output ports, P2 and P3 with a 90° phase difference between these output ports if all ports are matched. There is no power coupled to P4, as the port is isolated. The scattering matrix of the quadrature hybrid is shown in Equation (2.7) as follows (David M. Pozar, 2005):

$$[S] = \frac{-1}{\sqrt{2}} \begin{bmatrix} 0 & j & 1 & 0 \\ j & 0 & 0 & 1 \\ 1 & 0 & 0 & j \\ 0 & 1 & j & 0 \end{bmatrix} \tag{2.7}$$

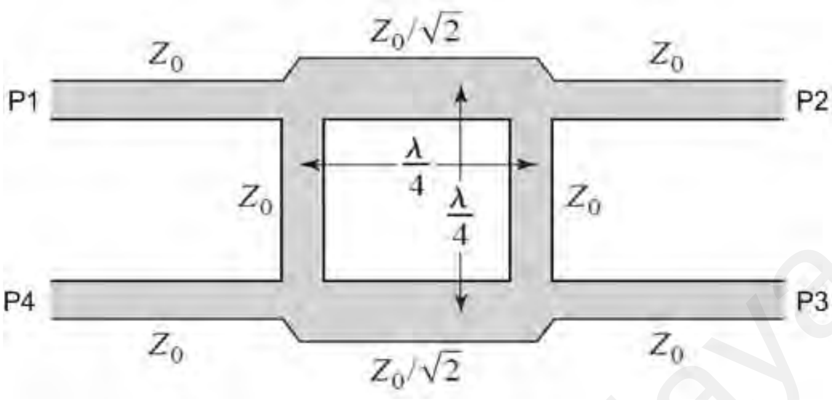

Figure 2.12 Geometry of the quadrature hybrid (David M. Pozar, 2005)

The quadrature hybrid can be analyzed using an even-odd mode decomposition technique. The normalized circuit of the quadrature hybrid is presented in Figure 2.13, where the wave of unit amplitude, $A_1 = 1$ is incident at port 1 and the characteristic impedance of a transmission line is normalized to Z_o. The normalized circuit of the quadrature hybrid in Figure 2.13 can be decomposed into the superposition of an even-mode excitation and an odd-mode excitation, as illustrated in Figure 2.14 and Figure 2.15, respectively.

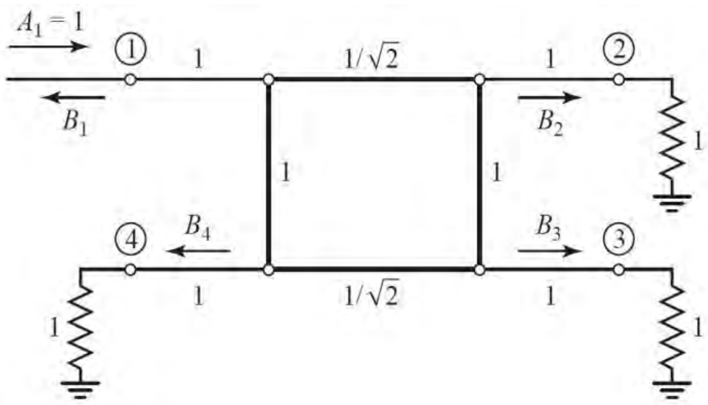

Figure 2.13: Normalized circuit of the quadrature hybrid (David M. Pozar, 2005)

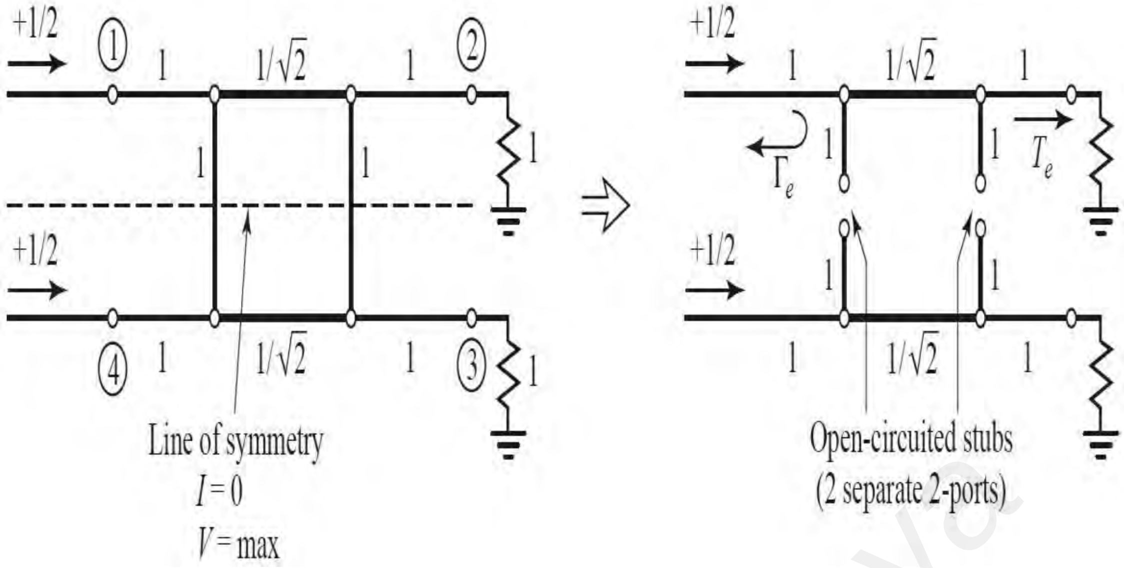

Figure 2.14: Decomposition of the quadrature hybrid into even-mode excitation (David M. Pozar, 2005)

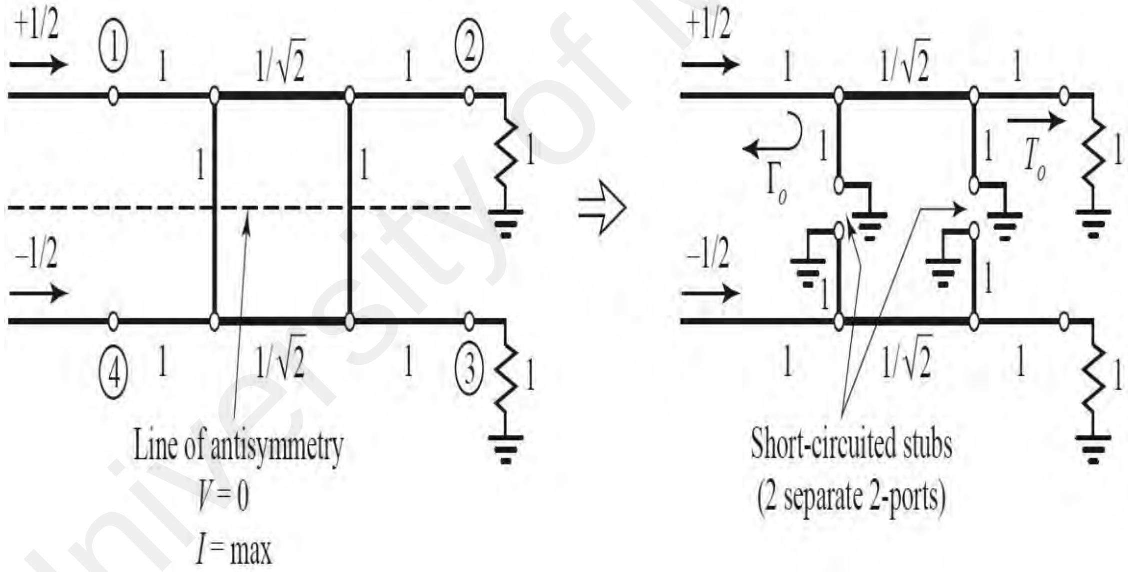

Figure 2.15: Decomposition of the quadrature hybrid into odd-mode excitation (David M. Pozar, 2005)

The actual response can be yielded from the sum of the responses to the even and odd excitations as the circuit is linear. The amplitudes of the incident waves for these two ports are +1/2 and −1/2. The amplitudes of the emerging wave at each port of the quadrature hybrid can be defined by Equation (2.8) to Equation (2.11) (David M. Pozar, 2005):

$$B_1 = \frac{1}{2}\Gamma_e + \frac{1}{2}\Gamma_o \tag{2.8}$$

$$B_2 = \frac{1}{2}T_e + \frac{1}{2}T_o \tag{2.9}$$

$$B_3 = \frac{1}{2}T_e - \frac{1}{2}T_o \tag{2.10}$$

$$B_4 = \frac{1}{2}\Gamma_e - \frac{1}{2}\Gamma_o \tag{2.11}$$

where Γ_e is the even-mode reflection coefficients, Γ_o is the odd-mode reflection coefficients, T_e is the even-mode transmission coefficients, and T_o is the odd-mode transmission coefficients. For even-mode two-port network, the calculations of Γ_e and T_e can be performed by multiplying the ABCD matrices of each cascade component in the circuit, as shown in Equation (2.12) (David M. Pozar, 2005):

$$\begin{bmatrix} A & B \\ C & D \end{bmatrix}_e = \underbrace{\begin{bmatrix} 1 & 0 \\ j & 1 \end{bmatrix}}_{\substack{\text{Shunt} \\ \text{Y=j}}} \underbrace{\begin{bmatrix} 0 & j/\sqrt{2} \\ j\sqrt{2} & 0 \end{bmatrix}}_{\substack{\lambda_g/4 \\ \text{Transmission} \\ \text{Line}}} \underbrace{\begin{bmatrix} 1 & 0 \\ j & 1 \end{bmatrix}}_{\substack{\text{Shunt} \\ \text{Y=j}}} = \frac{1}{\sqrt{2}}\begin{bmatrix} -1 & j \\ j & -1 \end{bmatrix} \tag{2.12}$$

The admittance of the shunt open-circuited $\lambda_g/8$ stubs can be expressed in Equation (2.13) (David M. Pozar, 2005):

$$Y = j\tan\beta l = j \tag{2.13}$$

where Y is the admittance, β is the phase constant, and l is the line length. The ABCD parameters can be converted to the S-parameters, which are equivalent to the reflection and transmission coefficients. The even-mode reflection and transmission coefficients can be defined by Equation (2.14) and Equation (2.15), respectively (David M. Pozar, 2005):

$$\Gamma_e = \frac{A+B-C-D}{A+B+C+D} = \frac{(-1+j-j+1)/\sqrt{2}}{(-1+j+j-1)/\sqrt{2}} = 0 \qquad (2.14)$$

$$T_e = \frac{2}{A+B+C+D} = \frac{2}{(-1+j+j-1)/\sqrt{2}} = \frac{-1}{\sqrt{2}}(1+j) \qquad (2.15)$$

For the odd-mode two-port network, the calculations of Γ_e and T_e can be performed by multiplying the ABCD matrices of each cascade component in the circuit. The matrix for odd-mode can be represented, as shown in Equation (2.16) (David M. Pozar, 2005):

$$\begin{bmatrix} A & B \\ C & D \end{bmatrix}_o = \frac{1}{\sqrt{2}} \begin{bmatrix} 1 & j \\ j & 1 \end{bmatrix} \qquad (2.16)$$

The ABCD parameters can be converted to the S-parameters, which are equivalent to the reflection and transmission coefficients. The odd-mode reflection and transmission coefficients can be expressed by Equation (2.17) and Equation (2.18), respectively (David M. Pozar, 2005):

$$\Gamma_o = 0 \qquad (2.17)$$

$$T_o = \frac{1}{\sqrt{2}}(1-j) \qquad (2.18)$$

Using Equation (2.14), Equation (2.15), Equation (2.17) and Equation (2.18) in Equation (2.8) to Equation (2.11), the amplitudes of the emerging wave for each port of the quadrature hybrid can be determined as written in Equation (2.19) to Equation (2.22) (David M. Pozar, 2005):

$$B_1 = 0 \quad \text{(Port 1 is matched)} \qquad (2.19)$$

$$B_2 = -\frac{j}{\sqrt{2}} \text{ (half power, } -90° \text{ phase shift from P1 to P2)} \qquad (2.20)$$

$$B_3 = -\frac{1}{\sqrt{2}} \text{ (half power, } -180° \text{ phase shift from P1 to P3)} \tag{2.21}$$

$$B_4 = 0 \qquad \text{(No power to P4)} \tag{2.22}$$

2.6.2 The Crossover

The crossover is a four-port network and it is also known as 0 dB coupler. This circuit allows the signal to flow to cross over to another port with high isolation. Figure 2.16 illustrates the geometry of the crossover. The crossover can be designed by cascading two quadrature hybrids using the microstrip transmission line (Wight, Chudobiak, & Makios, 1976).

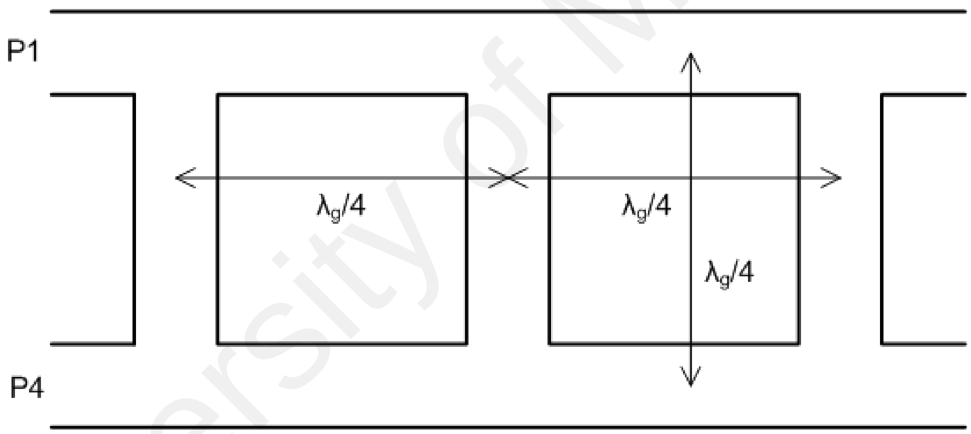

Figure 2.16: Geometry of the crossover (Khan, 2006)

As illustrated in Figure 2.16, the signal flows to port P3 when port P1 is excited. In contrast, the signal flows to port P2 when port P4 is excited. Theoretically, the insertion loss of the crossover should be zero. For instance, the output power of ports, P2 and P4 are zero as the signal flows from port P1 to port P3. The crossover can be analyzed using an even-odd mode decomposition technique that is similar to the technique that has been used for the quadrature hybrid, as explained in Section 2.6.1. The scattering matrix for the crossover can be expressed as written in Equation (2.23) (Khan, 2006):

$$S = \begin{bmatrix} 0 & 0 & j & 0 \\ 0 & 0 & 0 & j \\ j & 0 & 0 & 0 \\ 0 & j & 0 & 0 \end{bmatrix} \quad (2.23)$$

2.6.3 The Phase Shifter

The phase shifter is a two-port network. The use of a phase shifter is to change the phase of the signal that flows from one port to the other port. It can be designed using a microstrip transmission line. The length of the phase shifter corresponds to the phase shift. It can be defined using Equation (2.24) and Equation (2.25) as follows (Balanis, 2005):

$$L_{ps} = \frac{\phi \lambda_g}{360°} \quad (2.24)$$

and

$$\lambda_g = \frac{c}{f\sqrt{\varepsilon_{reff}}} \quad (2.25)$$

where L_{ps} is the length of the phase shifter, ϕ is the phase shift, λ_g is the wavelength in the microstrip transmission line, c is the speed of light in vacuum, f is the center frequency, and ε_{reff} is the effective dielectric constant.

2.7 Microstrip Discontinuity Compensation

The discontinuities at bends in the microstrip transmission line can degrade the performance of the designed circuit. These discontinuities introduce parasitic reactance that causes amplitude and phase errors, input and output mismatch as well as spurious coupling. Mitering or chambering the microstrip transmission line can reduce these effects. Several techniques are commonly used such as right-angle bend, swept bend, mitered bend, mitered step, and mitered T-junction (David M. Pozar, 2005). The right-angle bend technique is used in this thesis due to its design simplicity. Figure 2.17 illustrates the right-angle bend in the microstrip transmission line that has been compensated by mitering the corner.

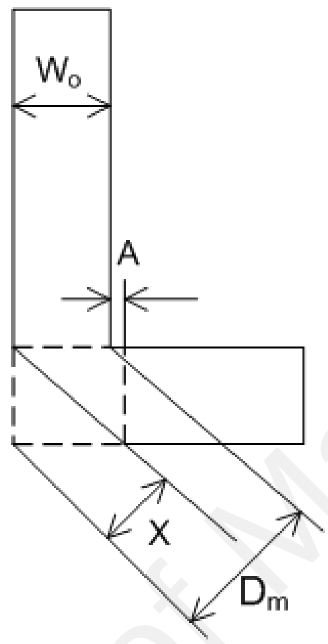

Figure 2.17: Mitered bend (Douville & James, 1978)

The mitered bend equations can be expressed as written in Equation (2.26) to Equation (2.28) (Douville & James, 1978):

$$D_m = W_o\sqrt{2} \tag{2.26}$$

$$X = D_m \times \left(0.52 + 0.65e^{-1.35\frac{W_o}{h_s}}\right) \tag{2.27}$$

$$A = X\sqrt{2} - W_o \tag{2.28}$$

where D_m is the diagonal length of the square miter, W_o is the width of the microstrip transmission line, X is the diagonal length of the optimum miter, h_s is the thickness of the substrate, and A is the compensated length for the optimal bend.

2.8 Rectangular Microstrip Antenna

Microstrip antennas are broadly utilized in wireless communication systems, especially in the base station applications. The microstrip antenna is chosen in this thesis due to its advantages of small size, simple in design, low profile, easy to integrate with the beamforming circuits using a single substrate, and cost-effectiveness for large-scale production. A microstrip antenna composes of a rectangular radiating element, a dielectric substrate, and a ground plane. The structure of the microstrip antenna is illustrated in Figure 2.18. This antenna is fed by a microstrip transmission line. The microstrip antenna can be designed using the Transmission-Line Model. This model is commonly used to obtain the width and length of the microstrip antenna.

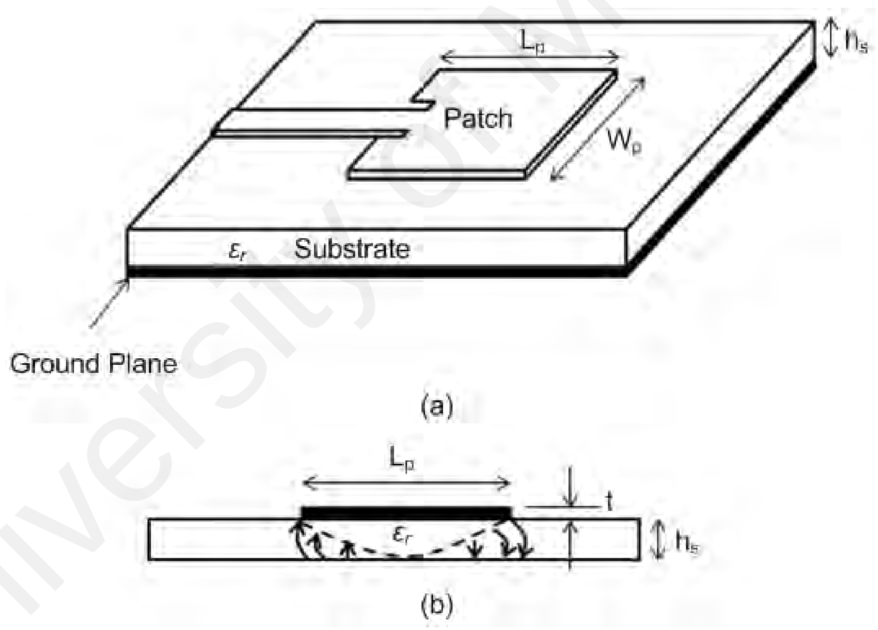

Figure 2.18: Microstrip antenna (a) Top view and (b) Side view (Balanis, 2005)

The width of the microstrip antenna can be determined from Equation (2.29) (Balanis, 2005):

$$W_p = \frac{c}{2f}\sqrt{\frac{2}{\varepsilon_r + 1}} \quad (2.29)$$

where W_p is the width of the microstrip antenna, c is the speed of light in vacuum, f is the center frequency, and ε_r is the dielectric constant of the substrate. Since the propagation wave travels not entirely in the substrate but fringes into the air, the effective dielectric constant can be calculated using Equation (2.30) (Balanis, 2005):

$$\varepsilon_{reff} = \left(\frac{\varepsilon_r + 1}{2}\right) + \left(\frac{\varepsilon_r - 1}{2}\right)\sqrt{1 + \frac{12h_s}{W_p}} \tag{2.30}$$

where ε_{reff} is the effective dielectric constant and h_s is the thickness of the substrate. The fields at the edges of the microstrip antenna experience fringing, as illustrated in Figure 2.18(b). The effect of a fringing field can cause the length of the radiating element to be greater than its physical dimension. Therefore, the extended length on both ends of the microstrip antenna is considered and it can be defined by Equation (2.31) (Balanis, 2005):

$$\Delta L_p = 0.412h_s\left(\frac{\varepsilon_{reff} + 0.3}{\varepsilon_{reff} - 0.258}\right)\left(\frac{\frac{W_p}{h_s}0.264}{\frac{W_p}{h_s} + 0.8}\right) \tag{2.31}$$

The actual length of the microstrip antenna can be expressed by Equation (2.32) (Balanis, 2005):

$$L_p = \frac{c}{2f\sqrt{\varepsilon_{reff}}} - 2\Delta L \tag{2.32}$$

The effective length of the microstrip antenna can be defined as written in Equation (2.33) (Balanis, 2005):

$$L_{eff} = L_p + 2\Delta L \tag{2.33}$$

2.9 Array Antenna Configuration

In the development of a 5G base station antenna, one of the essential requirements of the base station antenna is high antenna gain to overcome the high propagation loss in the millimeter wave frequencies. As a single-element antenna provides a broad radiation pattern with low antenna gain, it is insufficient to be utilized at the base station. Therefore, the antenna gain should be increased by enlarging the electrical size of the antenna in an array configuration that has more than two antenna elements. There are a few geometrical configurations of array antenna such as linear, rectangular, and circular. These geometrical configurations determine the radiation pattern of an array antenna (Balanis, 2005).

The geometrical configuration of the array antenna is linear in this research. Linear array antenna is the most common configuration that has been used in many wireless communication systems. Figure 2.19 illustrates the configuration of a linear array antenna. The linear array antenna has equal antenna spacing, *d* with uniform amplitudes and constant phase differences between antenna elements. The total field of linear array antenna is the product of the field of a single-element antenna pattern and the array factor of the array antenna. The array factor is a function of the number of antenna elements, the antenna spacing, the geometrical configuration of array antenna as well as the relative amplitudes and phases in which, the radiation pattern of the array antenna can be changed (Balanis, 2005). The array factor of *N* element linear array can be defined as written in Equation (2.34) to Equation (2.36) (Balanis, 2005):

$$AF = 1 + e^{+j\psi} + e^{+j2\psi} + \cdots + e^{j(N-1)\psi} = \sum_{n=1}^{N} e^{j(n-1)\psi} \tag{2.34}$$

$$\psi = kd\sin\theta + \beta \tag{2.35}$$

$$k = \frac{2\pi}{\lambda} \tag{2.36}$$

where AF is the array factor, N is the number of antenna elements, ψ is the phase difference between adjacent antenna elements, k is the wave number, d is the antenna spacing, θ is the angle relative to the normal to the array, β is the phase difference of excitation current between adjacent antenna elements, and λ is the wavelength. By multiplying $e^{j\psi}$ at both sides of Equation (2.34), the expression can be written as shown in Equation (2.37) (Balanis, 2005):

$$(AF)e^{j\psi} = e^{j\psi} + e^{j2\psi} + e^{j3\psi} + \cdots + e^{j(N-1)\psi} + e^{jN\psi} \tag{2.37}$$

By subtracting Equation (2.34) from (2.37), the equation can be expressed as defined in Equation (2.38) (Balanis, 2005):

$$\begin{aligned} AF &= \left[\frac{e^{jN\psi} - 1}{e^{j\psi} - 1}\right] \\ &= e^{j\left[\frac{(N-1)}{2}\right]\psi}\left[\frac{e^{j\left(\frac{N}{2}\right)\psi} - e^{-j\left(\frac{N}{2}\right)\psi}}{e^{j(1/2)\psi} - e^{-j\left(\frac{1}{2}\right)\psi}}\right] \\ &= e^{j[(N-1)/2]\psi}\left[\frac{\sin\left(\frac{N}{2}\psi\right)}{\sin\left(\frac{1}{2}\psi\right)}\right] \end{aligned} \tag{2.38}$$

The array factor in Equation (2.38) can be simplified, as shown in Equation (2.39) if the reference point is at the center of the array antenna (Balanis, 2005):

$$AF = \left[\frac{\sin\left(\frac{N\psi}{2}\right)}{\sin\frac{\psi}{2}}\right] \tag{2.39}$$

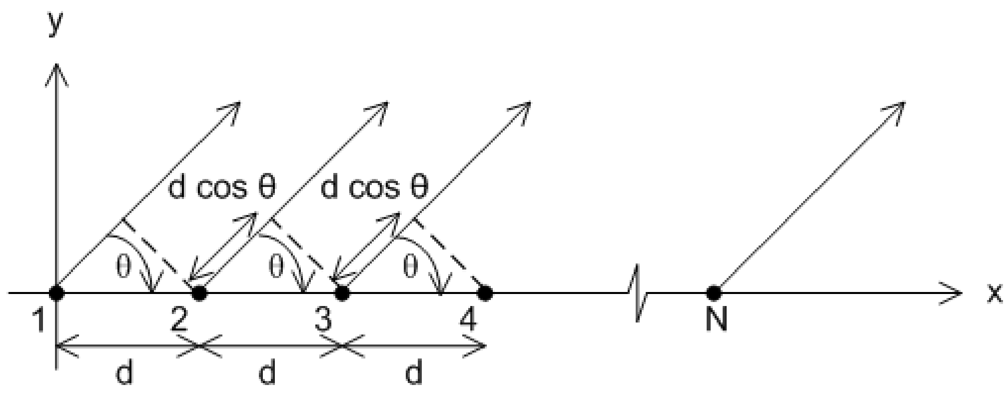

Figure 2.19: Linear array antenna

2.10 Summary

A brief overview of each generation from the first-generation to the current fourth-generation of the mobile communication system is presented in this chapter. The concepts and technical requirements of the 5G mobile communication system are addressed. Various types of antenna that have been used in the base station are demonstrated. Besides that, the characteristics of millimeter wave are explained and the limitations of millimeter wave communications are highlighted. Detailed descriptions of the multibeam antennas for the 5G base station are also presented. Apart from that, the fundamental of a Butler matrix including the basic operation as well as the design principles of the circuit elements such as the quadrature hybrid, the crossover, and the phase shifter are explained in detail. The rectangular microstrip antenna and the configuration of the linear array antenna are also described. The next chapter will present the research methodology.

CHAPTER 3: METHODOLOGY

3.1 Introduction

The research methodology of designing a multibeam array antenna for base station in a fifth-generation (5G) mobile communication system is described in this chapter. The research methodology is explained briefly with an illustration of a flowchart. The main requirements of a base station antenna for the 5G mobile communication system are addressed. Besides that, a three-dimensional electromagnetic simulation software used for antenna design is also described. Apart from that, the antenna fabrication and measurements are presented in detail.

3.2 Methodology

The flowchart of the research methodology that describes the design of a multibeam array antenna for base station in a 5G mobile communication system is illustrated in Figure 3.1. This research is divided into three main parts, which are designing a Butler matrix, designing a multibeam array antenna, and designing multibeam base station antennas. The research work began with the literature review on the 5G mobile communication systems such as the concepts and technical requirements. Moreover, studies were performed on several types of multibeam antennas that are considered for the development of a base station antenna for the 5G mobile communication system. In this thesis, beamforming circuit of a Butler matrix and microstrip antenna were considered in designing a base station antenna. Therefore, the basic circuit operation and the fundamental designs of the Butler matrix together with microstrip antenna were studied in detail.

The first part of this thesis is to design a Butler matrix to feed a multibeam array antenna. The Butler matrix consists of circuit elements such as the crossover, the quadrature hybrid, and the phase shifters using microstrip technology. The dimensions of these circuit elements were calculated using the design equations. These circuit elements were simulated and optimized to obtain the required circuit performance. The circuit elements were integrated to form an 8 × 8 Butler matrix. The simulation and optimization of the 8 × 8 Butler matrix were performed to achieve a low-loss and low phase error characteristic. Subsequently, the 8 × 8 Butler matrix was fabricated and measurements of scattering parameters such as return losses, isolations, transmission amplitudes, and transmission phases for input ports of the Butler matrix were conducted. Then, the simulation and measurement results were observed and analyzed.

The second part of this thesis is to design a multibeam array antenna. The first step was to design a single-element microstrip antenna. The dimensions of the microstrip antenna were calculated using the design equations. This antenna was simulated and optimized to obtain the desired antenna performance. Then, the output ports of the 8 × 8 Butler matrix were integrated with the microstrip antenna and the simulations were performed with different antenna spacing of 0.6λ to 0.8λ to study the beam coverage in the vertical plane. The radiation characteristics of the different antenna spacing for input ports were observed and analyzed. The best configuration of antenna spacing for the base station was identified. The multibeam array antenna was fabricated and measurements were conducted. Then, the simulation and measurement results were observed and analyzed.

The last part of this thesis is the proposed design concept of multibeam base station antennas for the 5G mobile communication system. The configuration of the multibeam base station antennas based on the designed multibeam array antenna was presented. Moreover, the design of the multibeam base station antennas to achieve a 360° coverage area in the horizontal plane was done using three-dimensional electromagnetic simulation software. The relevant parameters for the beam coverage designs were identified. The analyses of the beam coverage designs in the horizontal and vertical sectorizations were performed.

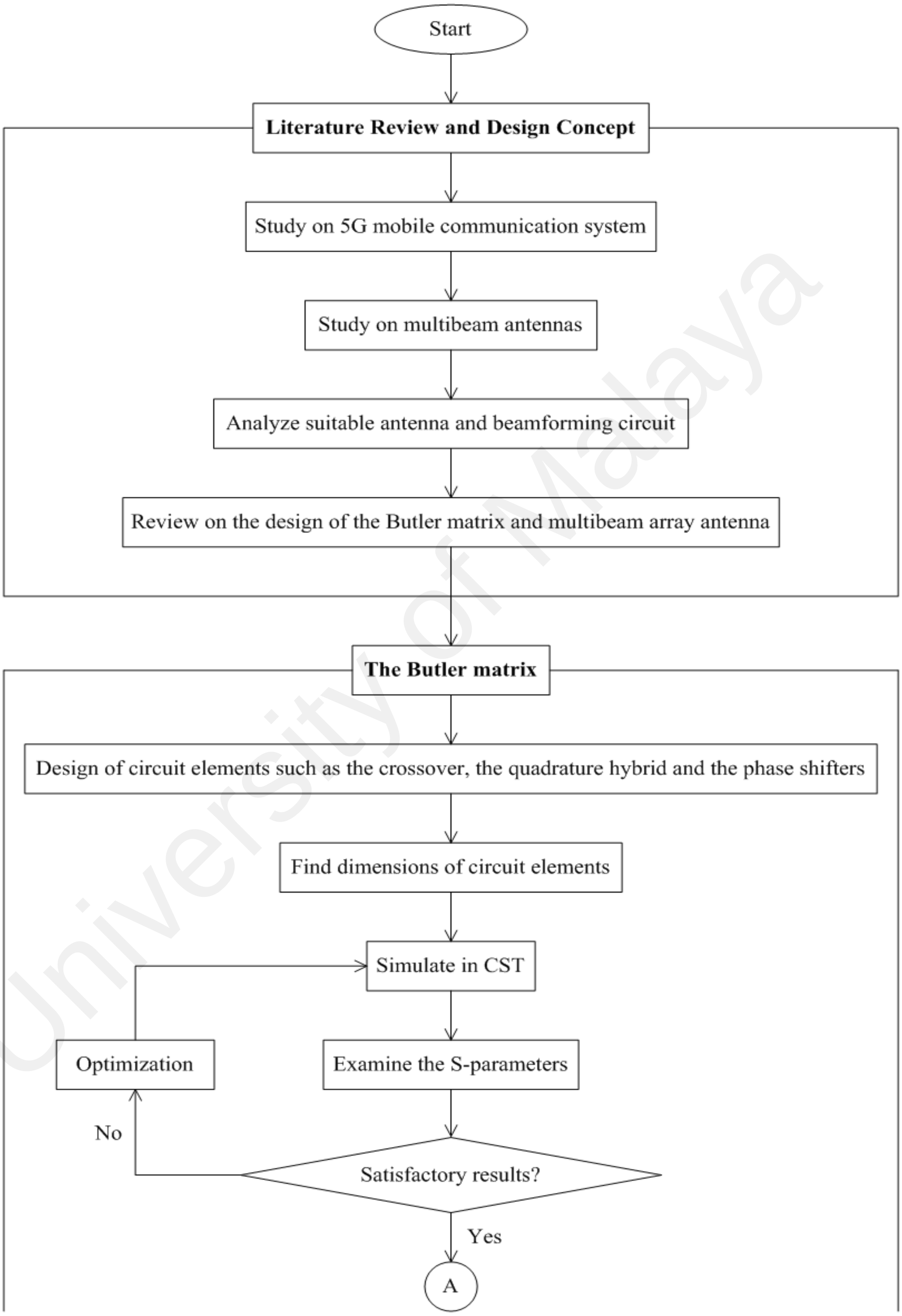

Figure 3.1, continued

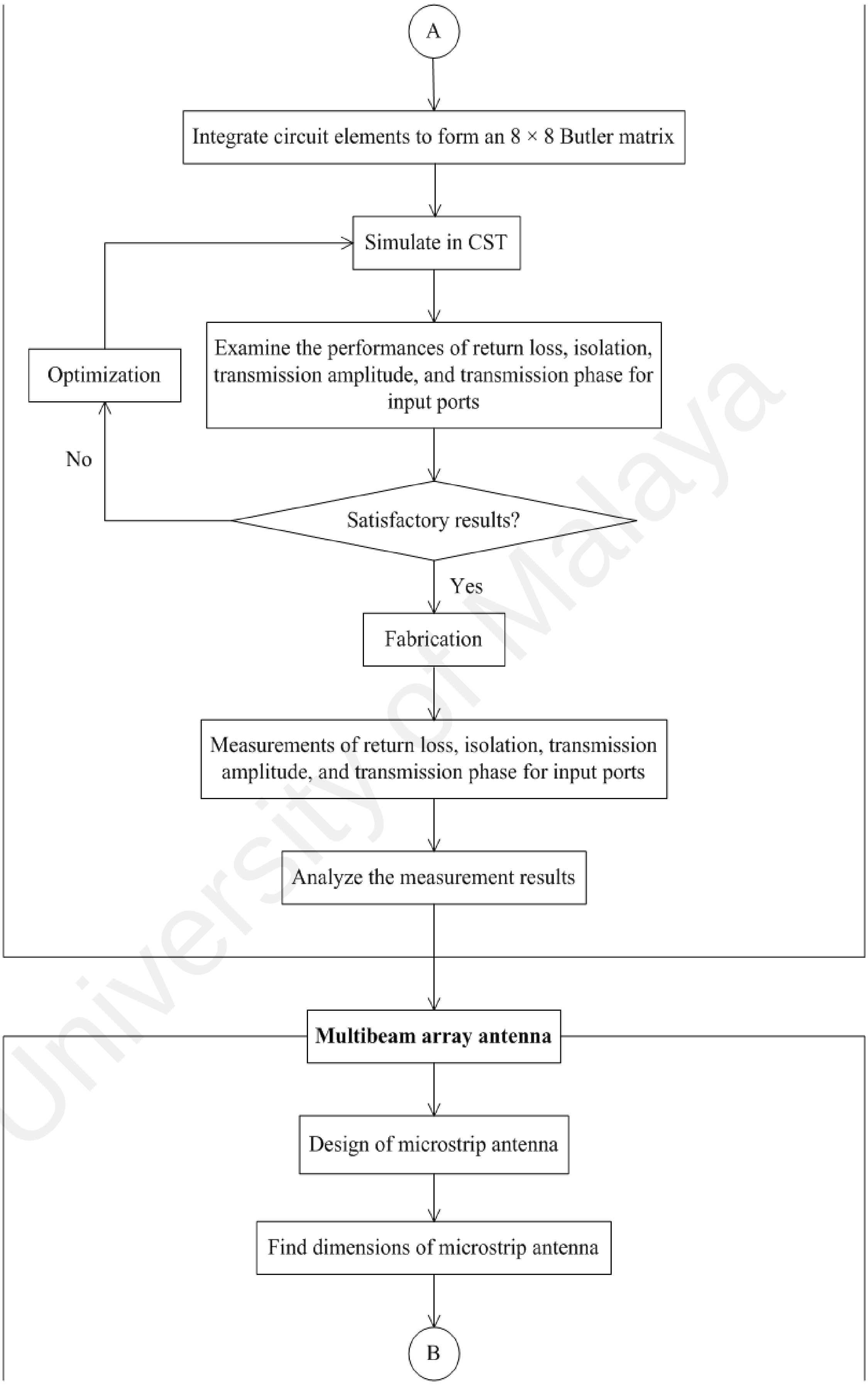

Figure 3.1, continued

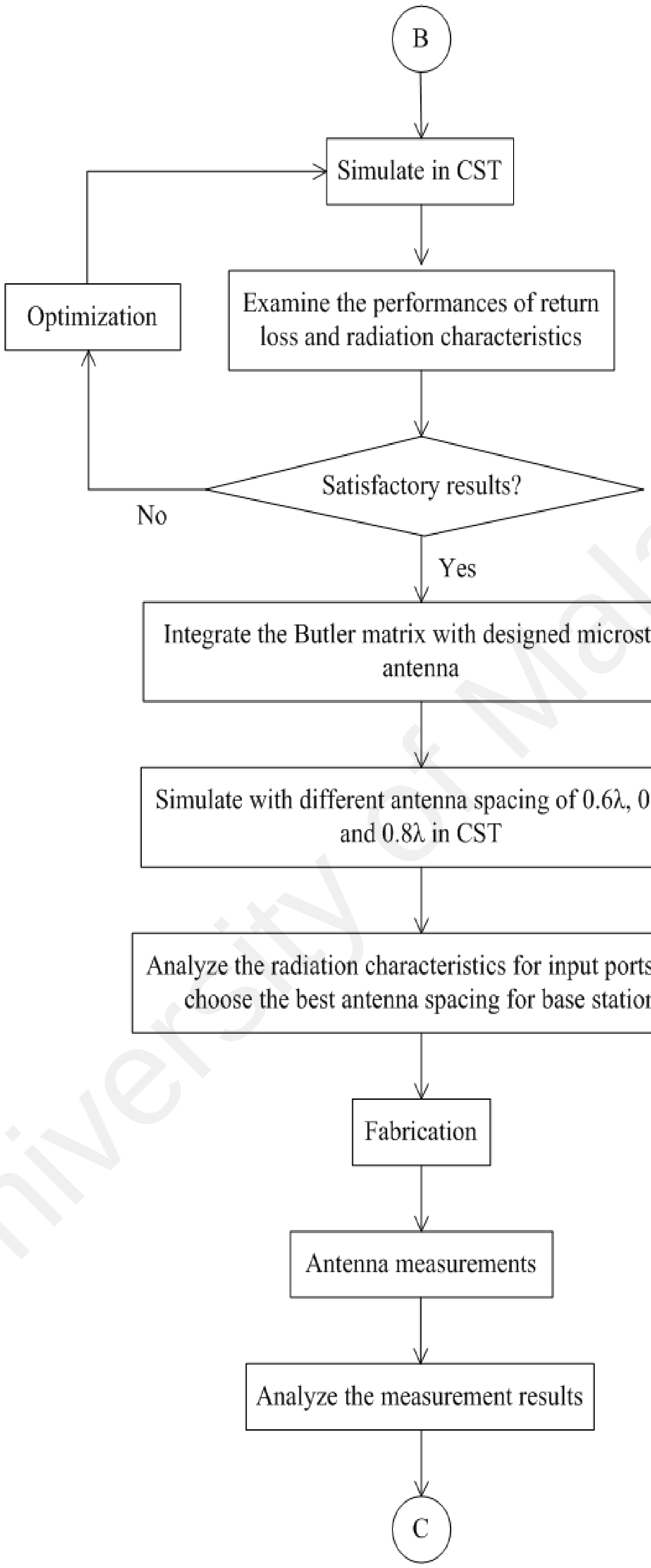

Figure 3.1, continued

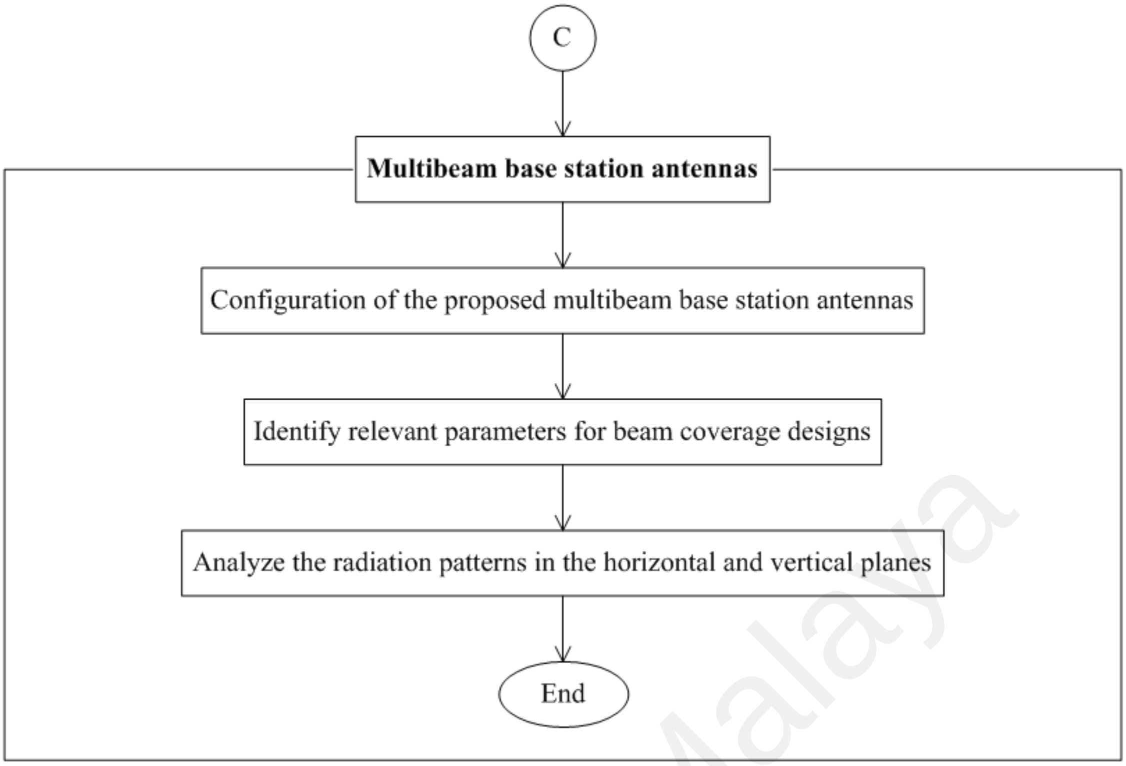

Figure 3.1: Flowchart of designing a multibeam array antenna for base station in the 5G mobile communication system

3.3 Main Requirements of a Base Station Antenna in the 5G Mobile Communication System

The development of a base station antenna is challenging since the requirements of the mobile communication system has become more stringent. A base station antenna with an efficient performance is required, especially for the outdoor environment to overcome the multipath effects and high propagation loss in the millimeter wave frequencies. Hence, extensive studies have been conducted by researchers to propose new system requirements for base station antenna in the 5G mobile communication system.

In this thesis, the proposed base station antenna for the 5G mobile communication system is designed to operate at the frequency band of 28 GHz, as defined by the Federal Communications Commission (FCC). The cell radius of the base station is less than 200 m to ensure continuous signal connectivity within the defined coverage area. Thus, it is expected that the deployment of the base station will be dense in the 5G mobile network. Besides that, the base station produces multiple beams in different directions. To achieve multibeam characteristics, a beamforming circuit is required to feed the base station antenna and the Butler matrix is considered in this research. Moreover, the antenna gain is more than 8 dBi and the input impedance of the base station antenna is 50 Ω. The base station consists of several base station antennas to provide a total beam coverage area of 360° in the horizontal plane. The beam coverage of each base station antenna in the horizontal plane is between 60° and 120°. Meanwhile, the beam coverage of the base station antenna in the vertical planes is more than 60°. Furthermore, the beam tilt angle of the base station antenna is less than 20°. Table 3.1 summarizes the main requirements of a base station antenna in the 5G mobile communication system.

Table 3.1: Main requirements of a base station antenna in the 5G mobile communication system

Requirement	Detail
Operating frequency	28 GHz
Cell radius	< 200 m
Type of beam	Multiple beams
Beamforming circuit	Butler matrix
Gain	> 8 dBi
Input impedance	50 Ω
Beam coverage in the horizontal plane	60° to 120°
Beam coverage in the vertical plane	> 60°
Beam tilt angle	< 20°

The proposed design concept of multibeam base station antennas for the 5G mobile communication system is presented in Figure 3.2. The multibeam base station antennas employ several base station antennas that are arranged in the vertical planes. Moreover, the base station antennas produce multiple beams and each beam is dedicated to one particular mobile user, as shown in Figure 3.2. The advantages of employing multibeam base station antennas in the mobile network are to reduce co-channel interference by controlling the beam directions, increase system capacity, and improve network coverage.

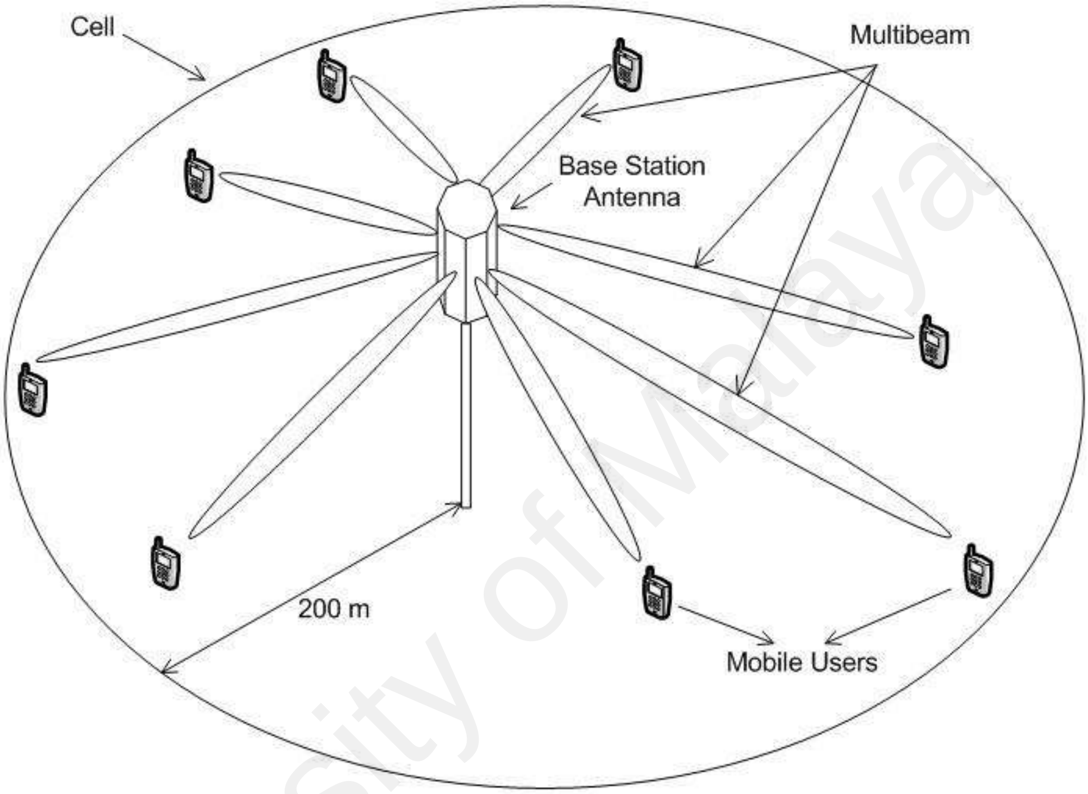

Figure 3.2: Multibeam base station antennas for the 5G mobile communication system

3.4 Electromagnetic Simulation Software

The three-dimensional electromagnetic simulation software is widely used among design engineers and researchers in various fields such as electronics, communication, aerospace, automotive, healthcare, energy, and defense. This software provides computation solutions for electromagnetic designs to obtain a high accuracy analysis. Furthermore, the software helps the users to analyze and improve the design performance with the shorter design process as well as to reduce costs by minimizing the physical prototypes. There are many commercial electromagnetic simulation software currently available in the market such as Computer Simulation Technology (CST, 2019), Advanced Design System (Keysight, 2019), Altair Feko (Altair, 2019), ANSYS HFSS (Ansoft, 2019), Microwave Office (AWR, 2019), and Sonnet Suites (Sonnet, 2019).

In this research, Computer Simulation Technology (CST) Microwave Studio software was used for the circuit and antenna designs. The CST Microwave Studio software is a high performance three-dimensional electromagnetic analysis software package used for designing, optimizing, along with analyzing electromagnetic components and systems in high frequencies. Additionally, the software has various simulation techniques such as time domain solver, frequency domain solver, multilayer solver, integral equation solver, eigenmode solver, and asymptotic solver that can be used for various design applications. In fact, these solvers are based on a finite integration technique that solves Maxwell's equations (Hirtenfelder, 2007). The time domain solver is chosen in this research for the simulation to yield the entire broadband frequency behavior of the designed Butler matrix and multibeam array antenna with one calculation run. Notably, the software supports hexahedral grids with the Perfect Boundary Approximation method for an efficient meshing process. This method increases the accuracy by improving the geometry description of the designed structures (Weiland, Timm, & Munteanu, 2008).

The post-processing tools that are available in this software enable the users to further analyze the simulation results of the designed structures. The characteristics such as scattering parameters, antenna gain, radiation efficiency, current distribution, and antenna radiation patterns can be obtained. These characteristics are observed and analyzed to ensure the design specifications are met before the fabrications of these structures are performed.

3.5 Antenna Fabrication

The designed Butler matrix and multibeam array antenna were fabricated using a photo etching process. The substrate material used in this research was NPC-F220A from Nippon Pillar Packing Co. Ltd. This substrate material is a double-sided printed circuit board with the design structure at the top layer and the ground at the bottom layer. The datasheet of the substrate material is appended in Appendix A. The chemical etching process was performed to etch the unwanted area of the copper clad so that the intended design pattern was obtained. Finally, the 2.92 mm coaxial connectors were soldered at the input and output ports of the fabrication boards for measurement purposes. The datasheet of the 2.92 mm coaxial connector is appended in Appendix B.

3.6 Measurements

Measurements such as return loss, transmission coefficients, isolation, radiation pattern, and antenna gain were performed in this research. The setups for the measurement are explained in the following subsections.

3.6.1 Return loss, Transmission Coefficients, and Isolation Measurements

The return loss measurement is a one-port network measurement that is used to measure the impedance matching at the input and output ports of the Butler matrix. Figure 3.3 illustrates the measurement setup for the return loss of the Butler matrix. Port 1 of the vector network analyzer is connected to the input port of the Butler matrix to measure the return loss of the Butler matrix at the input port. After that, to measure the return loss at the output port of the Butler matrix, port 1 of the vector network analyzer is connected to the output port of the Butler matrix.

The transmission coefficients measurement is a two-port network measurement that is used to measure the amplitude and phase between the input and output ports of the

Butler matrix. The measurement setup for the transmission coefficient of the Butler matrix is shown in Figure 3.4. Port 1 of the vector network analyzer is connected to the input port of the Butler matrix and port 2 of the vector network analyzer is connected to the output port of the Butler matrix. There are magnitude and phase selections in the setting of the vector network analyzer. These selections are used to measure the amplitude and phase between the input and output ports of the Butler matrix, respectively.

Moreover, the isolation measurement is also a two-port measurement that is used to measure the leakage or feedthrough from one port to another. Figure 3.5 presents the measurement setup for the isolation of the Butler matrix. To measure the isolation at the input ports of the Butler matrix, port 1 of the vector network analyzer is connected to the input port of the Butler matrix while port 2 of the vector network analyzer is connected to another input port of the Butler matrix. Then, to measure the isolation at the output ports of the Butler matrix, port 1 of the vector network analyzer is connected to the output port of the Butler matrix and port 2 of the vector network analyzer is connected to another output port of the Butler matrix.

The return loss, transmission coefficients, and isolation measurements are performed using a vector network analyzer of the N5224A PNA Microwave Analyzer by Keysight Technologies. The vector network analyzer is calibrated by eliminating the systematic errors before the measurements are conducted to ensure accurate measurement data. To calibrate the network analyzer, the Keysight Calibration Kit is used. There are four basic standards of calibration such as short, open, load, and through. The photograph of the one-port network measurement setup for the return loss of the Butler matrix and the photograph of the two-port network measurement setup of the transmission coefficient of the Butler matrix are illustrated in Figure 3.6 and Figure 3.7, respectively.

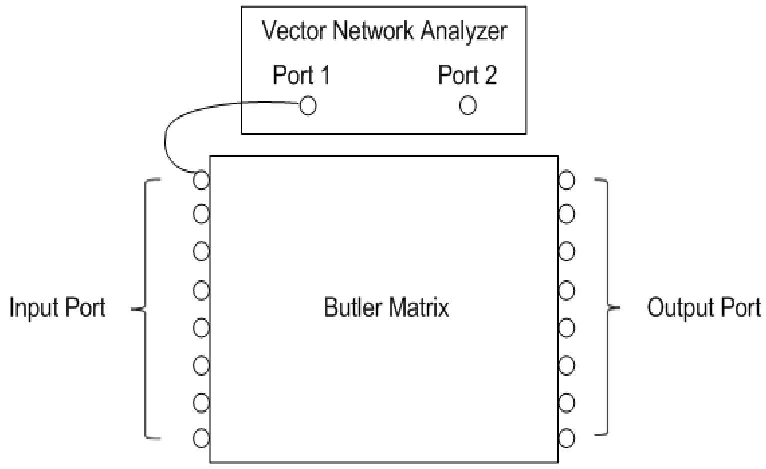

Figure 3.3: Measurement setup for the return loss of the Butler matrix

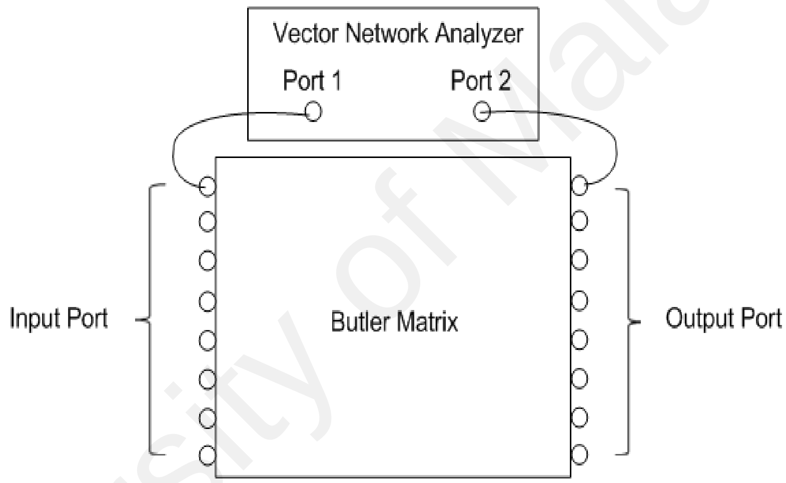

Figure 3.4: Measurement setup for the transmission coefficient of the Butler matrix

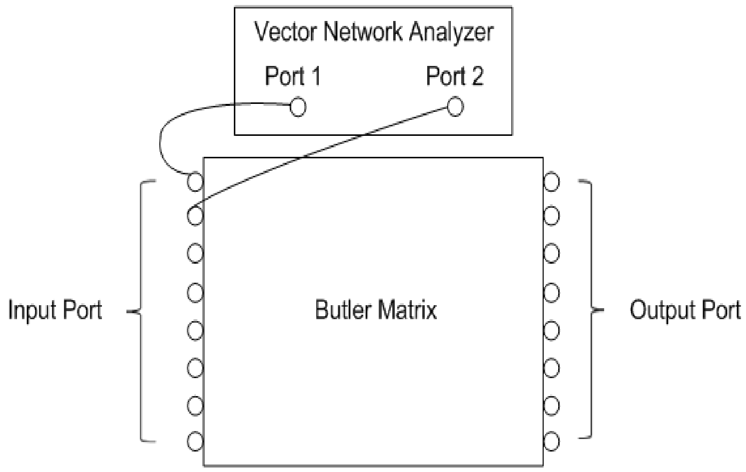

Figure 3.5: Measurement setup for the isolation of the Butler matrix

Figure 3.6: Photograph of the one-port network measurement setup for the return loss of the Butler matrix

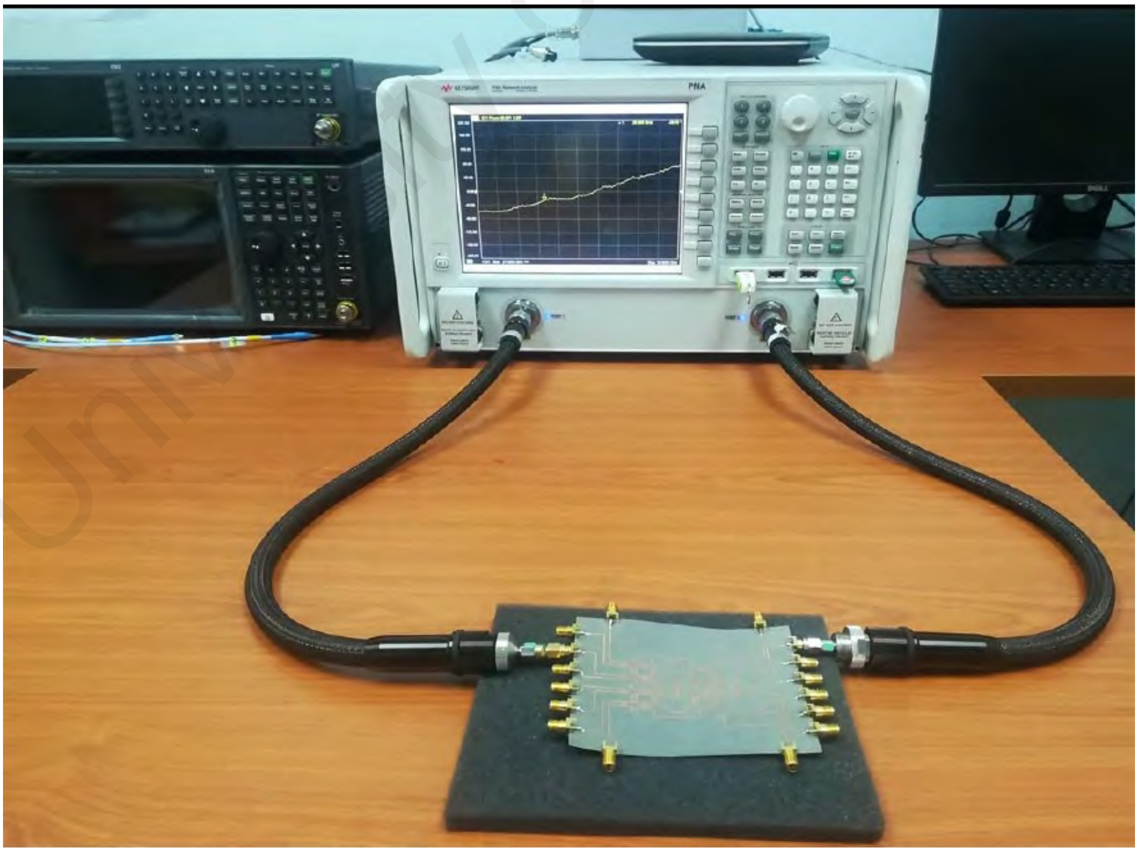

Figure 3.7: Photograph of the two-port network measurement setup for the transmission coefficient of the Butler matrix

3.6.2 Radiation Pattern Measurement

The radiation pattern measurement is performed in an anechoic chamber to reduce electromagnetic interferences. The distance for a far field radiation pattern measurement can be determined using Equation (3.1) (Balanis, 2005):

$$R = \frac{2D^2}{\lambda} \tag{3.1}$$

where D is the largest dimension of the antenna and λ is the wavelength. Figure 3.8 illustrates the measurement setup for the radiation pattern of the antenna under test. The distance between the reference antenna and the antenna under test is determined using Equation (3.1). Both the reference antenna and antenna under test are placed aligning with each other. The antenna under test is fixed on the turntable to enable the 360° rotation. A vector network analyzer of the N5224A PNA Microwave Analyzer is used to measure the signal level. Port 1 of the vector network analyzer is connected to the reference antenna with defined input power and port 2 of the vector network analyzer is connected to the antenna under test to measure the received signal of the antenna. The reference antenna used in this research is a standard gain horn antenna by A-INFO Inc. The datasheet of the horn antenna is appended in Appendix C. Figure 3.9 shows the photograph of the measurement setup for the radiation pattern of the antenna under test.

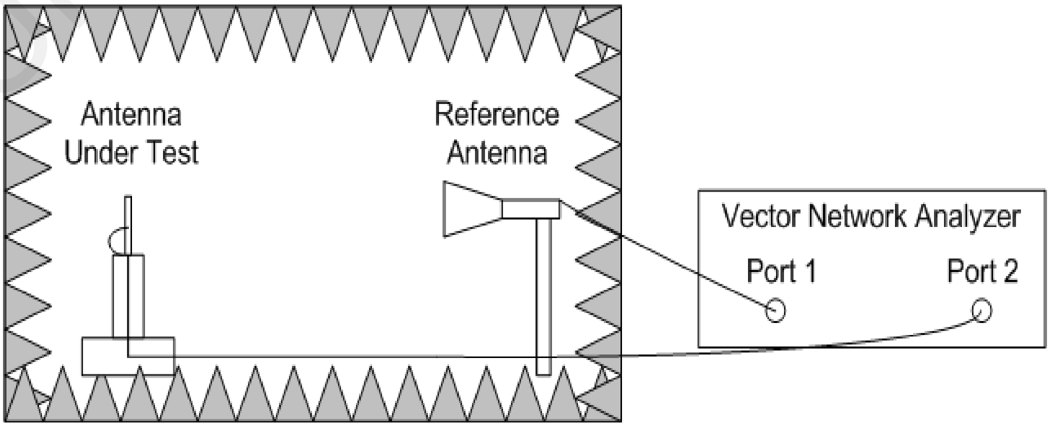

Figure 3.8: Measurement setup for the radiation pattern of the antenna under test

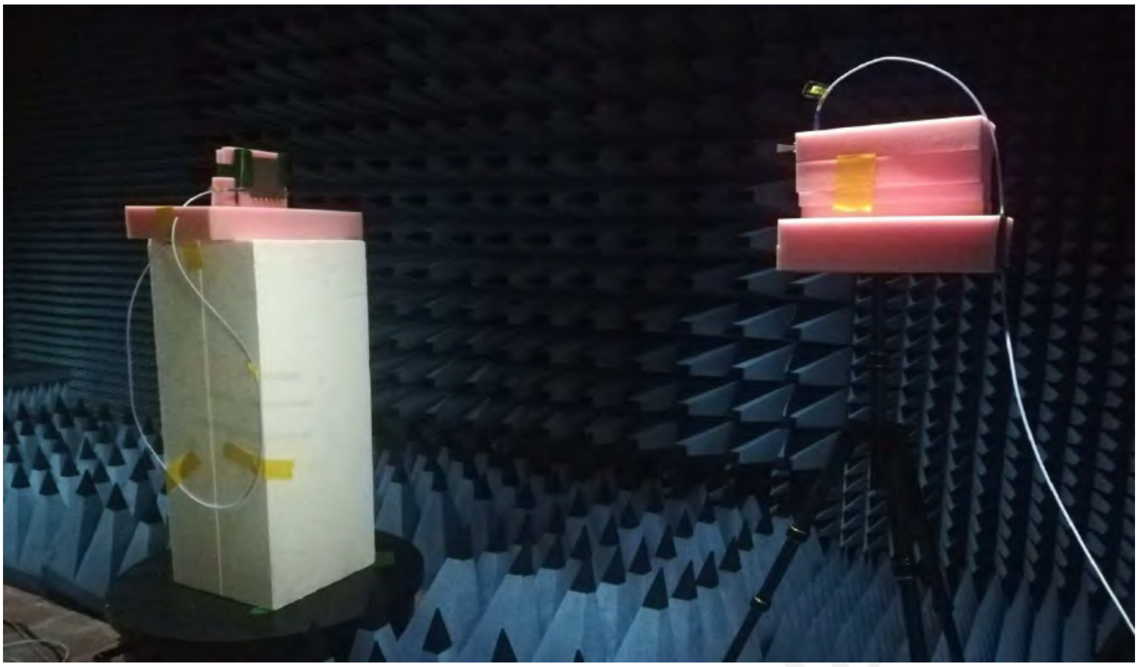

Figure 3.9: Photograph of the measurement setup for the radiation pattern of the antenna under test

3.6.3 Antenna Gain Measurement

The antenna gain measurement is also performed in an anechoic chamber. Two reference antennas and an antenna under test are required in this measurement. The reference antenna used in this measurement is the same as the reference antenna used in the radiation pattern measurement, which is a standard gain horn antenna. Firstly, two reference antennas are connected to a vector network analyzer, as shown in Figure 3.10. The distance between the reference antenna and antenna under test is determined using Equation (3.1). The maximum value of the received signal is measured, and this value is referred to as the reference level. Then, one of the reference antennas is replaced with the antenna under test, as shown in Figure 3.10. The value of the received signal is measured, and this value is referred to as the measured level. Therefore, the antenna gain for the antenna under test can be calculated, as defined in Equation (3.2):

$$\textit{Gain (dBi)} = \textit{Reference Gain} + (\textit{Measured Level} - \textit{Reference Level}) \quad (3.2)$$

where reference gain is the gain of the horn antenna in the datasheet, as appended in Appendix C, the measured level is the received signal measured by the reference antenna and antenna under test, and the reference level is the received signal measured by the two reference antennas. The photograph of the measurement setup for the radiation pattern of the antenna under test is presented in Figure 3.11.

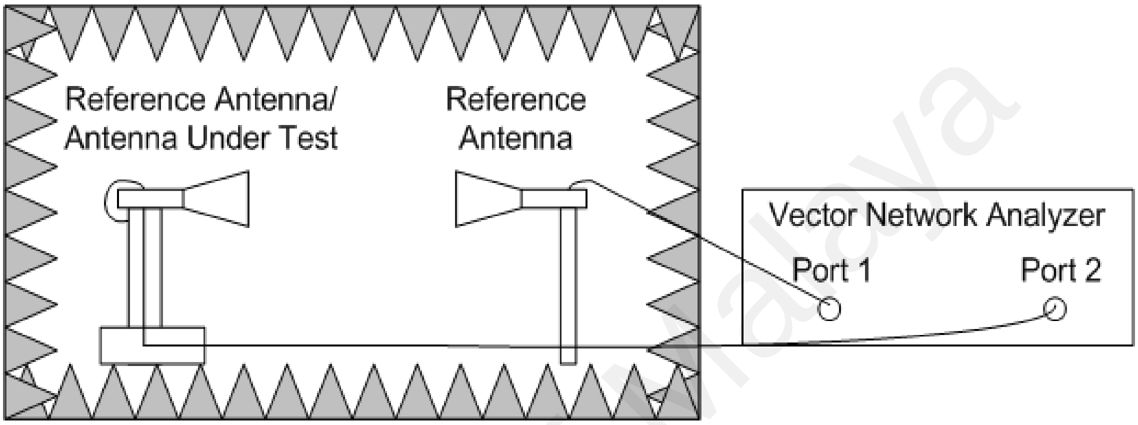

Figure 3.10: Measurement setup for the antenna gain of the antenna under test

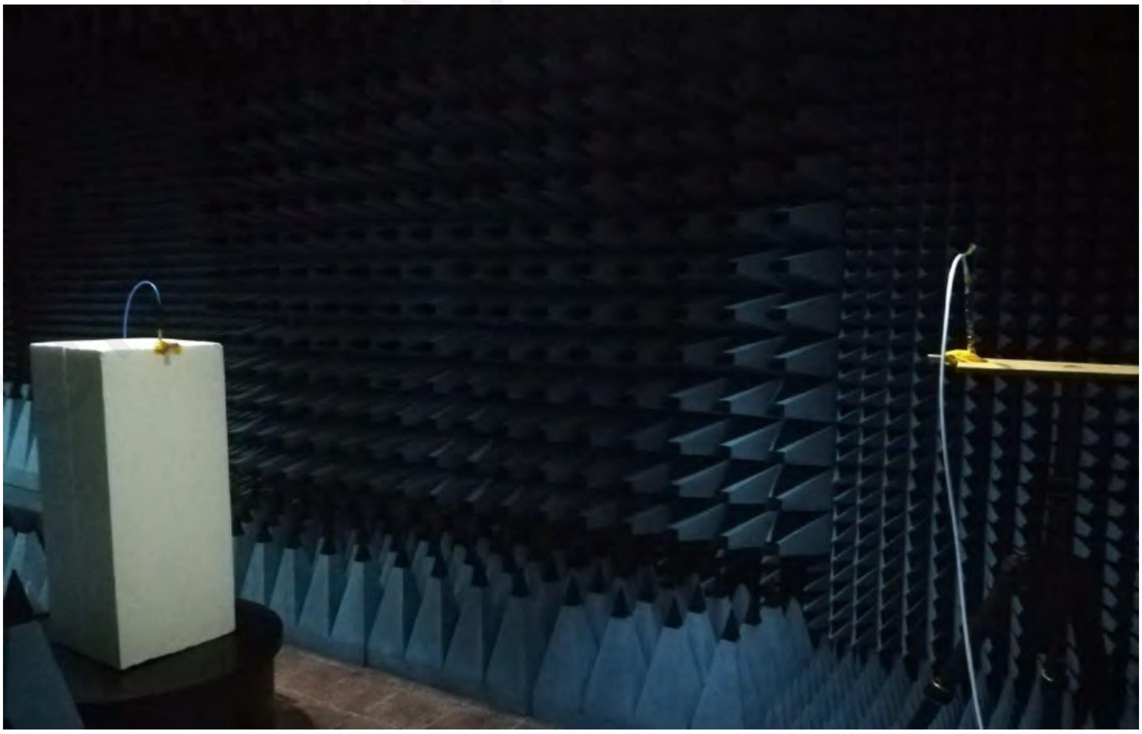

Figure 3.11: Photograph of the measurement setup for the antenna gain of the antenna under test

3.7 Summary

The research methodology of designing a multibeam array antenna for base station in the 5G mobile communication system is presented in this chapter. The detailed methodology processes of the literature review, design of a Butler matrix, design of a multibeam array antenna, and design of multibeam base station antennas are explained accordingly. Moreover, the three-dimensional electromagnetic simulation software used for the circuit and antenna designs is described. Apart from that, the antenna fabrication and measurements are demonstrated. The design of a Butler matrix will present in the following chapter.

CHAPTER 4: DESIGN OF THE BUTLER MATRIX

4.1 Introduction

As mentioned in Chapter 3, the Butler matrix is considered in this research as a beamforming circuit to feed a multibeam array antenna due to its advantages of low profile, low power dissipation, design simplicity, and cost-effectiveness for large-scale production. Moreover, the Butler matrix has the ability of producing orthogonal beams, which improves the beam scanning coverage. This chapter presents the detailed design methodology to obtain the required electrical performance of a single-layer Butler matrix operating at 28 GHz. The Butler matrix consists of circuit elements such as the crossover, the quadrature hybrid, and the phase shifters. The most important mathematical equations to obtain the dimensions of the circuit elements are given in this chapter. The circuit elements were designed and optimized using three-dimensional electromagnetic simulation software. The parametric studies of the circuit elements and the correlations of the parameters are also demonstrated in detail. The designed Butler matrix was fabricated via a photo etching process. Measurements were conducted to ensure the actual performance of the fabricated Butler matrix. The simulation and measurement results of the Butler matrix were analyzed and discussed.

4.2 Design of the Butler Matrix

In this research, an 8 × 8 Butler matrix with eight inputs (Pi) and eight outputs (Oi) was designed, where $i = 1, 2, \ldots, N$ and N is the power of two ($N = 2^n$). The Butler matrix has equal amplitude at its output port when the input port is excited. Meanwhile, the phase differences between the output ports of the Butler matrix are constant. The phase differences between the output ports of the 8 × 8 Butler matrix can be determined using Equation (4.1):

$$\phi_p = \pm \frac{2p-1}{N} \times 180° \quad (4.1)$$

where N = 8, n = 3, and p = 1, 2, …, (n + 1). Table 4.1 lists the phase differences between the output ports of the 8 × 8 Butler matrix, which correspond to Equation (4.1).

Table 4.1: Phase differences, ϕ_p between the output ports of the 8 × 8 Butler matrix

p	ϕ_p
1	± 22.5
2	± 157.5
3	± 112.5
4	± 67.5

The structure of the 8 × 8 Butler matrix is illustrated in Figure 4.1. The Butler matrix consists of sixteen crossovers, twelve quadrature hybrids, and eight phase shifters. There are three values of the phase shifters that are required in designing an 8 × 8 Butler matrix, which are 22.5°, 45°, and 67.5°. The circuit elements were designed using a microstrip transmission line. The ideal output phases of the 8 × 8 Butler matrix for the input ports is presented in Figure 4.2. The phase differences between the output ports of the Butler matrix for the input ports of P1, P2, P3, and P4 were similar with respect to the input ports of P8, P7, P6, and P5 but the polarities were opposite due to the symmetrical structure. As shown in the Figure 4.2, the minimum phase differences were produced by the input ports, P1 and P8 with phase differences of −22.5° and 22.5°, respectively. On the other hand, the maximum phase differences were produced by the input ports, P2 and P7 with phase differences of 157.5° and −157.5°, respectively. Table 4.2 lists the design specifications of an 8 × 8 Butler matrix for each circuit element such as the crossover, the quadrature hybrid, the phase shifters along with the complete structure of an 8 × 8 Butler matrix. These design specifications are required to be met to ensure the designed 8 × 8 Butler matrix achieves a low-loss and low phase error characteristic.

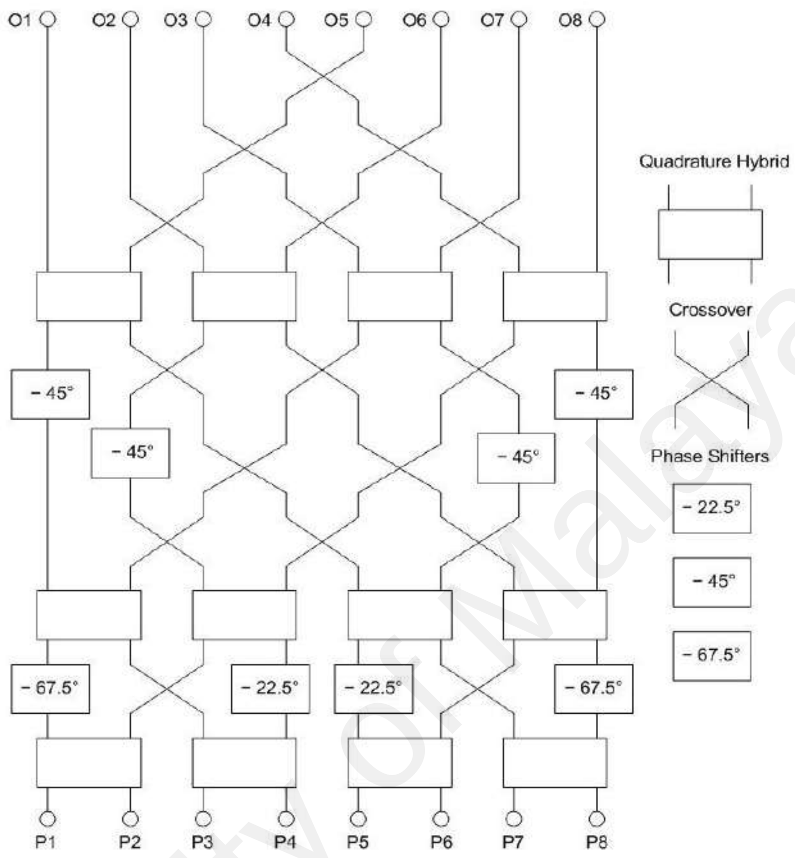

Figure 4.1: Structure of the 8 × 8 Butler matrix

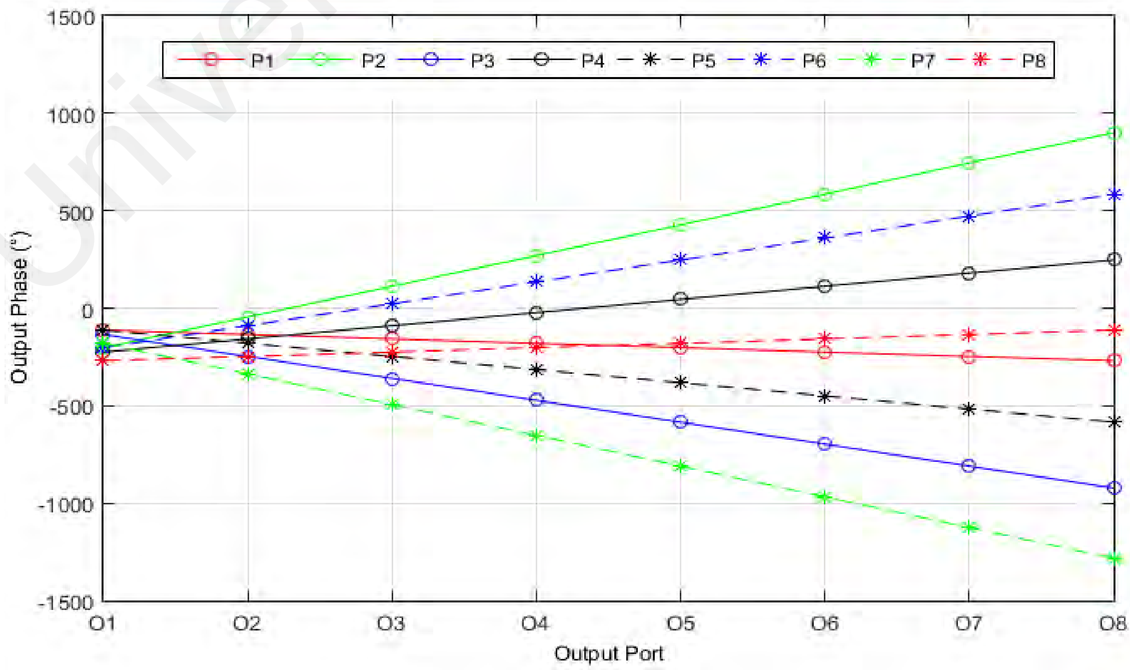

Figure 4.2: Ideal output phases of the 8 × 8 Butler matrix for the input ports

Table 4.2: Design specifications of the crossover, the quadrature hybrid, the phase shifters, and the 8 × 8 Butler matrix

Circuit Element	Design Specification	Value
Crossover	S_{11}	≤ −10 dB
	S_{31}	0 dB
Quadrature hybrid	S_{11}	≤ −10 dB
	S_{21}	−3 dB
	S_{31}	−3 dB
	S_{41}	≤ −10 dB
	Phase (S_{21}) – Phase (S_{11})	90°
22.5° phase shifter	S_{11}	≤ −10 dB
	Phase (S_{21}) – Phase (S_{11})	22.5°
45° phase shifter	S_{11}	≤ −10 dB
	Phase (S_{21}) – Phase (S_{11})	45°
67.5° phase shifter	S_{11}	≤ −10 dB
	Phase (S_{21}) – Phase (S_{11})	67.5°
8 × 8 Butler matrix	S_{11}, S_{22}, S_{33}, S_{44}, S_{55}, S_{66}, S_{77}, S_{88}, S_{99}, S_{1010}, S_{1111}, S_{1212}, S_{1313}, S_{1414}, S_{1515}, S_{1616}	≤ −10 dB
	Transmission amplitude (S_{ij}) where i = 9, 10, 11, 12, 13, 14, 15, 16 and j= 1, 2, 3, 4, 5, 6, 7, 8	≤ −10 dB
	Isolations ($S_{(j-1)i}$) where i = 1, 2, 3, 4, 5, 6, 7, 8, 9, 10, 11, 12, 13, 14, 15, 16 and j= 2, 3, 4, 5, 6, 7, 8, 9, 10, 11, 12, 13, 14, 15, 16	≤ −10 dB
	Phase ($S_{(i+1)j}$) – Phase (S_{ij}) where i = 9, 10, 11, 12, 13, 14, 15, 16 and j= 1	−22.5°
	Phase ($S_{(i+1)j}$) – Phase (S_{ij}) where i = 9, 10, 11, 12, 13, 14, 15, 16 and j= 2	157.5°
	Phase ($S_{(i+1)j}$) – Phase (S_{ij}) where i = 9, 10, 11, 12, 13, 14, 15, 16 and j= 3	−112.5°
	Phase ($S_{(i+1)j}$) – Phase (S_{ij}) where i = 9, 10, 11, 12, 13, 14, 15, 16 and j= 4	67.5°
	Phase ($S_{(i+1)j}$) – Phase (S_{ij}) where i = 9, 10, 11, 12, 13, 14, 15, 16 and j= 5	−67.5°
	Phase ($S_{(i+1)j}$) – Phase (S_{ij}) where i = 9, 10, 11, 12, 13, 14, 15, 16 and j= 6	112.5°
	Phase ($S_{(i+1)j}$) – Phase (S_{ij}) where i = 9, 10, 11, 12, 13, 14, 15, 16 and j= 7	−157.5°
	Phase ($S_{(i+1)j}$) – Phase (S_{ij}) where i = 9, 10, 11, 12, 13, 14, 15, 16 and j= 8	22.5°

4.2.1 Simulation Condition

The structure of the 8 × 8 Butler matrix was designed using three-dimensional electromagnetic (EM) simulation software called Computer Simulation Technology (CST) Microwave Studio. The substrate material used in this research was NPC-F220A from Nippon Pillar Packing Co. Ltd. The simulation parameters and the details of the substrate are summarized in Table 4.3.

Table 4.3: Simulation parameters and details of the substrate

Parameter	Detail/Value
EM simulation software	CST Microwave Studio
Frequency	28 GHz
Type of substrate	NPC-F220A (Nippon Pillar Packing Co. Ltd.)
Tan δ	0.0007
Dielectric constant	2.2
Substrate thickness	0.254 mm

4.2.2 Phase Delay and Loss of Microstrip Transmission Line

In a millimeter wave, it is crucial to ensure the dimensional accuracy of the circuit design. Therefore, the changes of phase in the microstrip transmission line were investigated to achieve a highly accurate circuit design. Figure 4.3 illustrates the model of the microstrip transmission line. The parameters of the microstrip transmission line are listed in Table 4.4.

Based on the simulation, the phase of S_{21} of the extended lines is presented in Figure 4.4. The wavelength in the microstrip transmission line was λ_g = 7.663 mm, which corresponds to a 360° phase change. Therefore, a 1° phase change corresponds to a line length of 0.02 mm. To achieve an accurate output phase at 28 GHz, very precise dimensions of the circuit elements are required. Besides that, the loss of the microstrip transmission line is shown in Figure 4.4, approximately 0.363 dB for a line length of 10 mm.

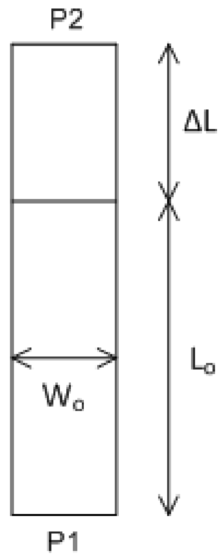

Figure 4.3: Model of the microstrip transmission line

Table 4.4: Parameters of the microstrip transmission line

Parameter	**Value**
L_o	7.7155 mm
W_o	0.7826 mm
Input impedance	50 Ω

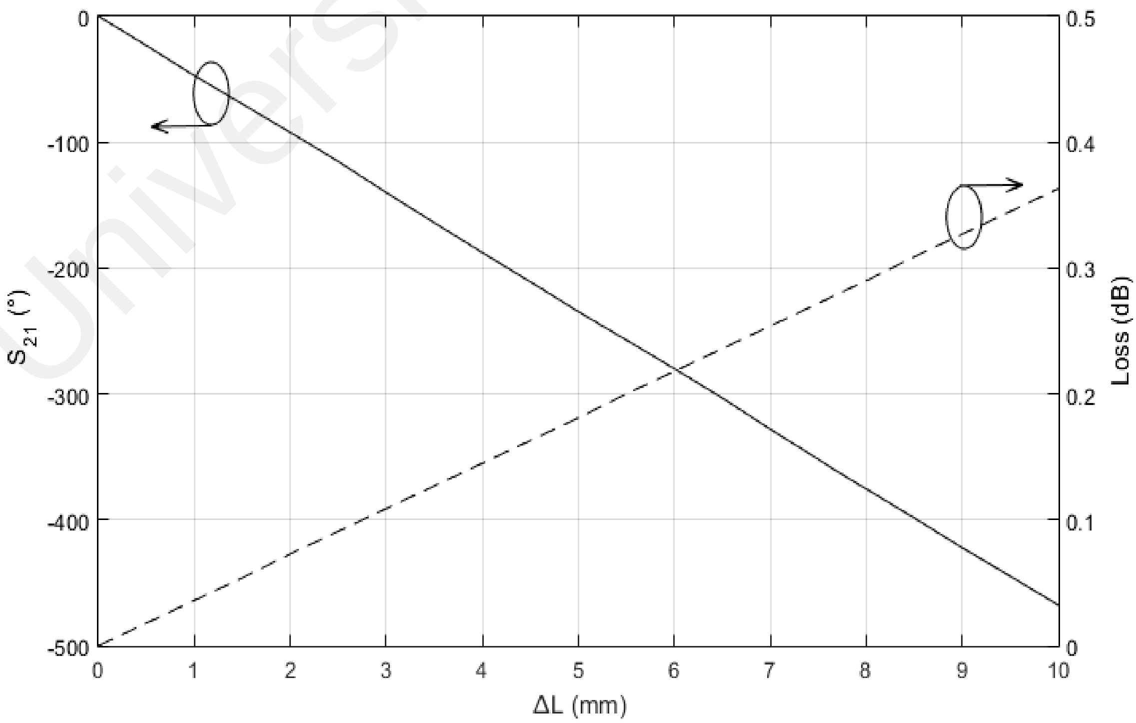

Figure 4.4: Phase of S_{21} and line loss of the microstrip transmission line

4.2.3 Design of the Crossover

The structure of the crossover as shown in Figure 2.16 was designed using a 50 Ω microstrip transmission line. The width of the crossover can be obtained using microstrip transmission line equations, as written in Equation (4.2) to Equation (4.4) (Gonzalez, 1996):

$$\frac{W_{zo}}{h_s} = \begin{Bmatrix} \dfrac{8e^A}{e^{2A}-2}; \qquad for\ \dfrac{W_{zo}}{h_s} < 2 \\ \dfrac{2}{\pi}\left[\begin{matrix} B - 1 - In(2B-1) + \\ \dfrac{\varepsilon_r - 1}{2\varepsilon_r}\left\{In(B-1) + 0.39 - \dfrac{0.61}{\varepsilon_r}\right\}; \end{matrix}\right] \\ for\ \dfrac{W_{zo}}{h_s} > 2 \end{Bmatrix} \tag{4.2}$$

$$A = \frac{Z_o}{60}\sqrt{\frac{\varepsilon_r + 1}{2}} + \frac{\varepsilon_r - 1}{\varepsilon_r + 1}\left(0.23 + \frac{0.11}{\varepsilon_r}\right) \tag{4.3}$$

$$B = \frac{377\pi}{2Z_o\sqrt{\varepsilon_r}} \tag{4.4}$$

where h_s is the substrate thickness, ε_r is the dielectric constant, and Z_o is the characteristic impedance. The length for the crossover can be determined using Equation (4.5) and Equation (4.6) (Balanis, 2005):

$$L_{zo} = \lambda_g/4 \tag{4.5}$$

and

$$\lambda_g = \frac{c}{f\sqrt{\varepsilon_{reff}}} \tag{4.6}$$

where L_{zo} is the length of the crossover, λ_g is the wavelength in the microstrip transmission line, c is the speed of light in vacuum, f is the frequency, and ε_{reff} is the effective dielectric constant. The calculated parameters of the crossover are presented in Table 4.5. These calculated parameters were used to design the crossover in CST Microwave Studio. The structure of the crossover is illustrated in Figure 4.5. As shown in Figure 4.5, the right-angle bends in the crossover at ports P1, P2, P3, and P4 were compensated by mitering the corner to reduce the effects of parasitic reactance that causes amplitude and phase errors, input and output mismatch as well as spurious coupling, as explained in Section 2.7.

Table 4.5: Calculated parameters of the crossover

Parameter	Value (mm)
L_{zo}	1.9581
W_{zo}	0.7826

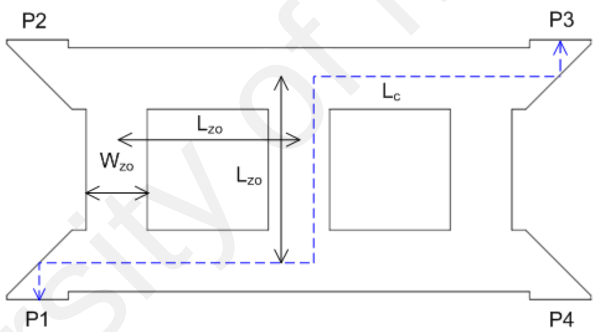

Figure 4.5: Structure of the crossover

To design a crossover with a low insertion loss at 28 GHz, parametric studies were conducted. The most important parameter was the total length of the crossover from P1 to P3, which was labeled as L_c, as shown in Figure 4.5. The length of L_c is three times of the length of L_{zo} and the extended lengths to ports, P1 and P3. The length of L_c was varied and the optimum length was obtained via simulation. Figure 4.6 presents the effects of L_c on the return loss, S_{11} and insertion loss, S_{21}. As shown in Figure 4.6, the return loss and insertion loss were sensitive to slight changes in L_c. For L_c = 7.020 mm and 7.035 mm, the return losses resonated at 28 GHz, but the return losses shifted to

28.2 GHz when L_c was decreased to 7.005 mm. The lowest insertion loss of −0.47 was achieved when L_c = 7.020 mm.

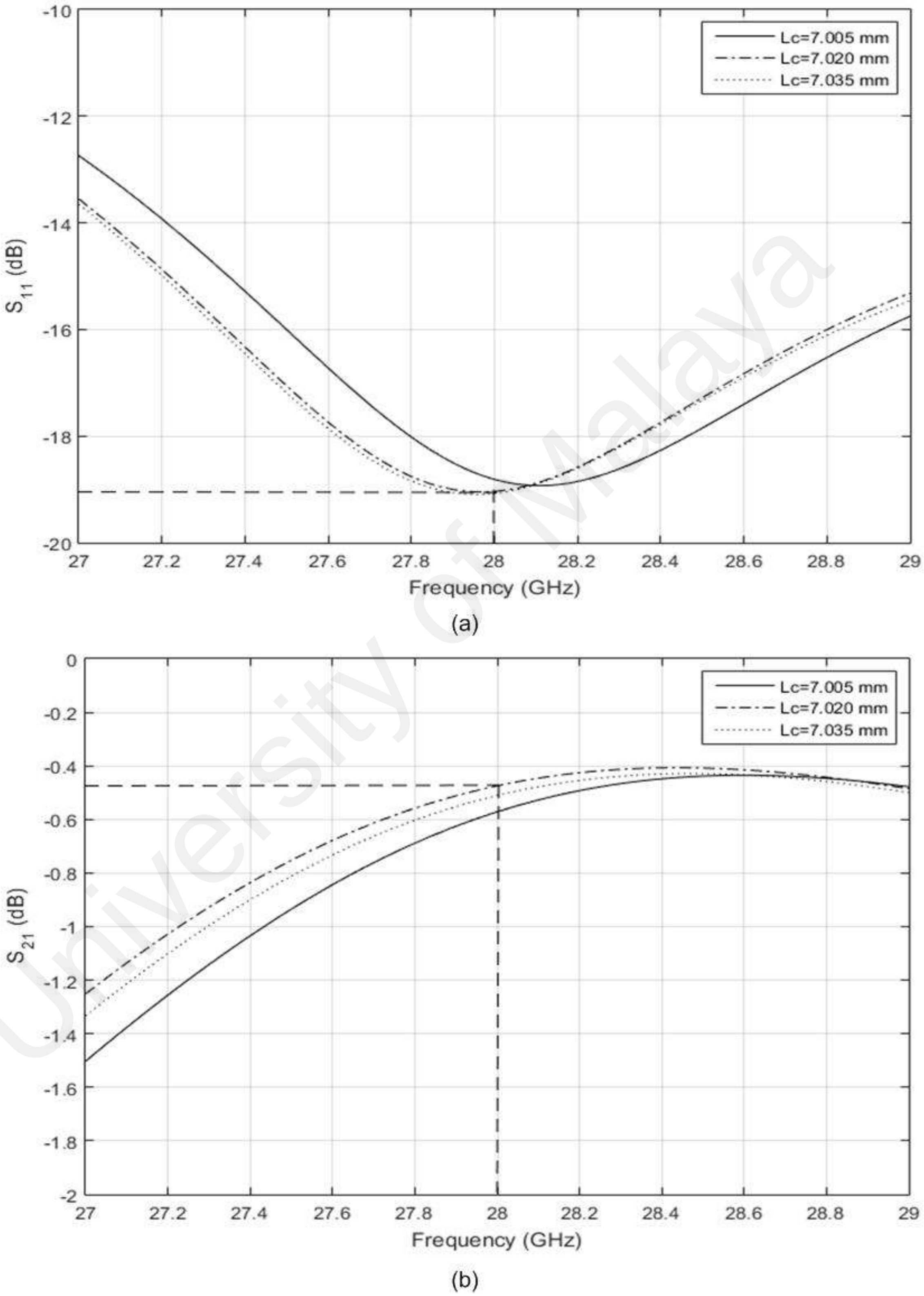

Figure 4.6: Effects of the total length, L_c of the crossover on (a) return loss and (b) insertion loss

Based on these parametric studies, the length of L_c = 7.020 mm was selected to simulate the crossover. The parameters of the crossover are listed in Table 4.6 and Figure 4.7 presents the amplitudes of the crossover. The amplitude of the insertion loss, S_{31} was −0.47 dB at 28 GHz. This excellent result shows that the crossover had a very good design. Figure 4.8 illustrates the power flow of the crossover when port 1 was excited. As shown in Figure 4.8, the power flowed from port 1 to port 3. Additionally, the amplitude of the return loss, S_{11} and the amplitude of the isolations, S_{21} and S_{41} of the crossover were less than −10 dB at 28 GHz, as presented in Figure 4.7. Therefore, less power was reflected to port 1 and most of the power flowed to port 3.

Table 4.6: Parameters of the crossover

Parameter	Values (mm)
L_{zo}	2.341
W_{zo}	0.7826

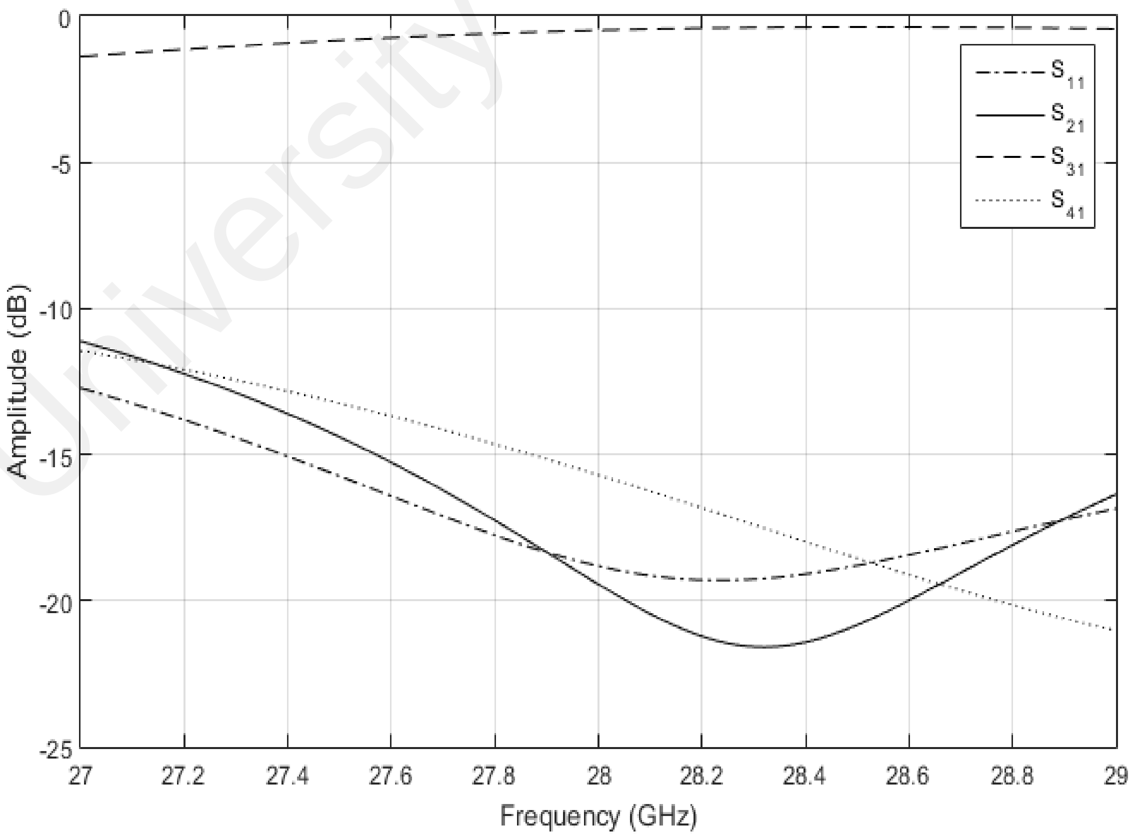

Figure 4.7: Simulated amplitudes of the crossover

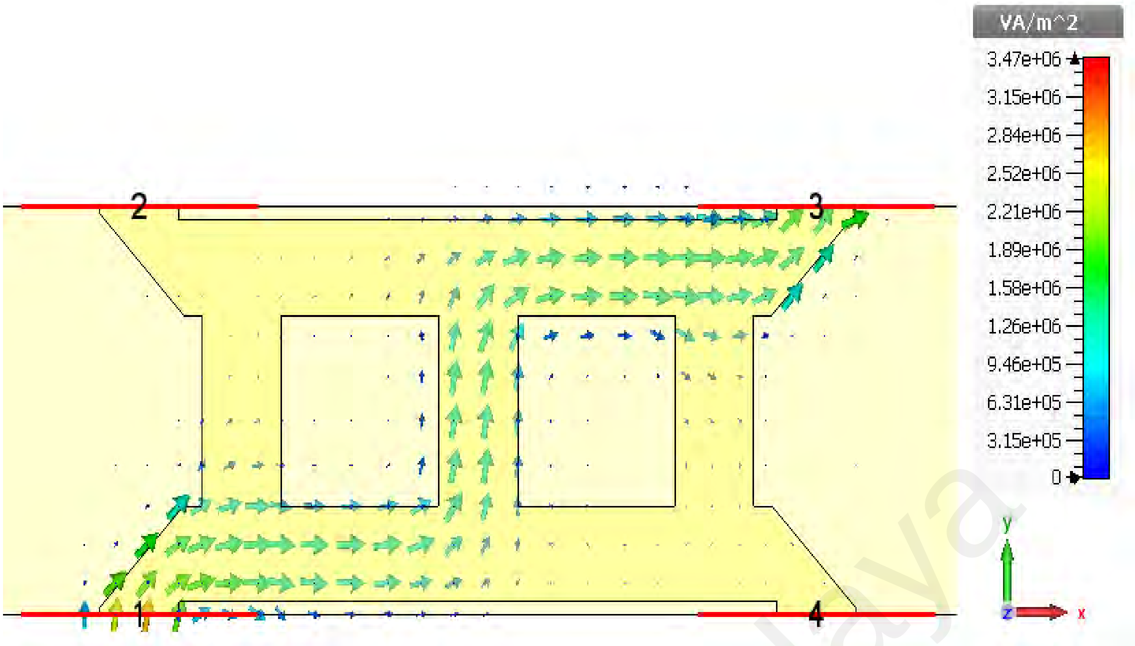

Figure 4.8: Power flow of the crossover when port 1 was excited

4.2.4 Design of the Quadrature Hybrid

The structure of the quadrature hybrid as shown in Figure 2.12 was designed with two different values of characteristic impedances, Z_o and $Z_o/\sqrt{2}$, which were 50 Ω and 35 Ω, respectively. The widths for both characteristic impedances of the quadrature hybrid, W_{zo} and W_z can be calculated using mathematical equations, as expressed in Equation (4.2) to Equation (4.4). Meanwhile, the lengths of the quadrature hybrid, L_{zo} and L_z can be obtained using Equation (4.5) and Equation (4.6). The values of W_{zo} and L_{zo} were the same values that were used in the crossover. Table 4.7 shows the calculated parameters of the quadrature hybrid.

Table 4.7: Calculated parameters of the quadrature hybrid

Parameter	Value (mm)
L_{zo}	1.9581
L_z	1.9301
W_{zo}	0.7826
W_z	1.2754

Based on these parameters, the most crucial design parameters were lengths of the quadrature hybrid, L_{zo} and L_z, which were required to achieve phase difference of 90° between the output ports, P2 and P3 when the input port, P1 was excited. The lengths of L_{zo} and L_z were almost one-quarter wavelength. Meanwhile, the widths of the quadrature hybrid, W_{zo} and W_z were used to achieve equal power ratios at the output ports, P2 and P3 along with good isolation at port P4. The calculated parameters listed in Table 4.7 were used to design the quadrature hybrid in CST Microwave Studio. The structure of the quadrature hybrid is illustrated in Figure 4.9.

To obtain good performance of a quadrature hybrid, parametric studies were conducted. The most important parameter was length of L_z, as shown in Figure 4.9. The length of L_z was varied and the optimum length was obtained via simulation. Figure 4.10 shows the effects of L_z on return loss, S_{11} and insertion losses, S_{21} and S_{31}. As shown in Figure 4.10(a), the return loss and insertion loss were not sensitive to slight changes of L_z. For L_z = 2 mm, 2.076 mm and 2.2 mm, the return losses resonated at 28 GHz. The insertion losses of −3 dB were achieved when L_z = 2.076 mm, as compared to the values of the insertion losses, S_{21} and S_{31}, as presented in Figure 4.10(b) and (c).

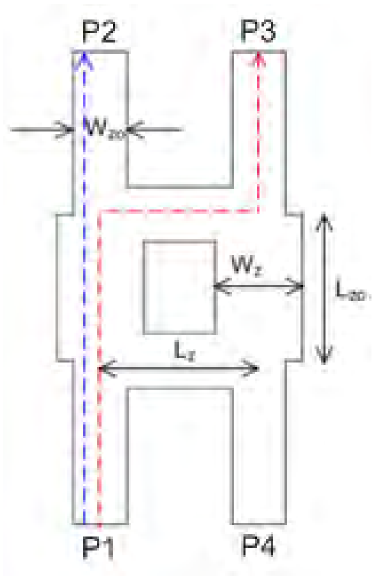

Figure 4.9: Structure of the quadrature hybrid

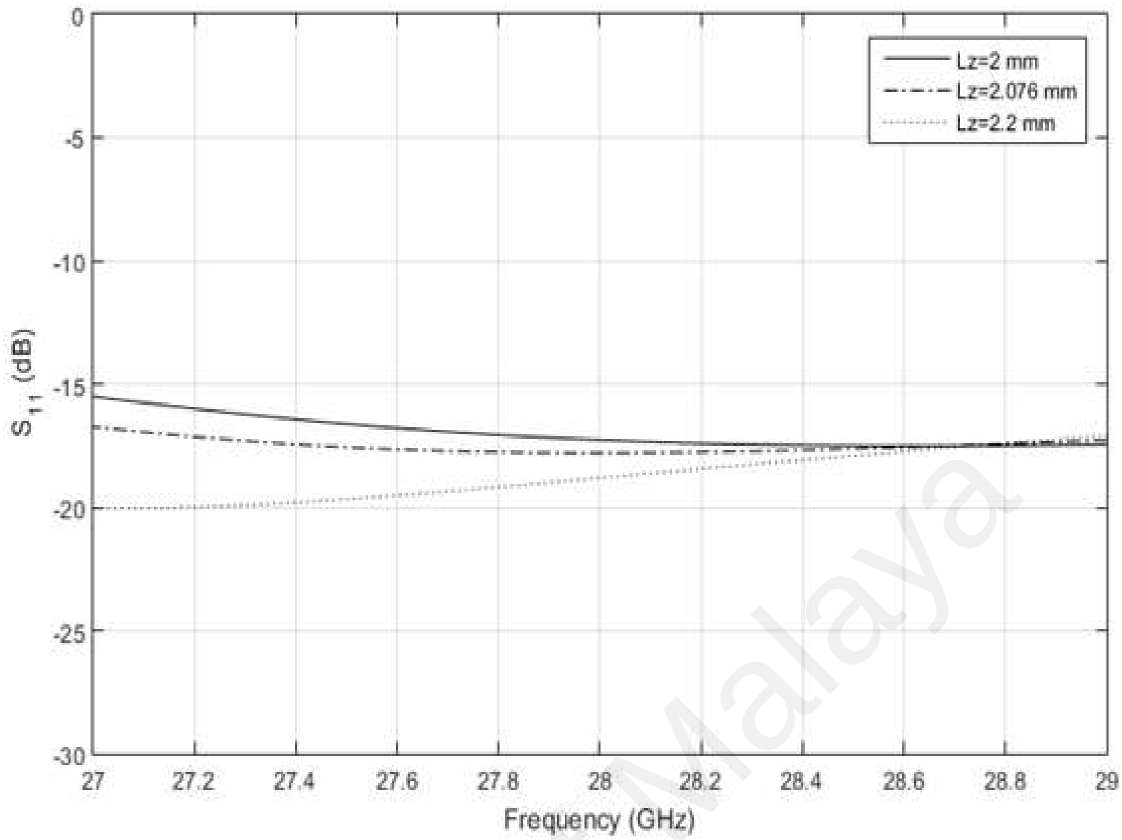

(a)

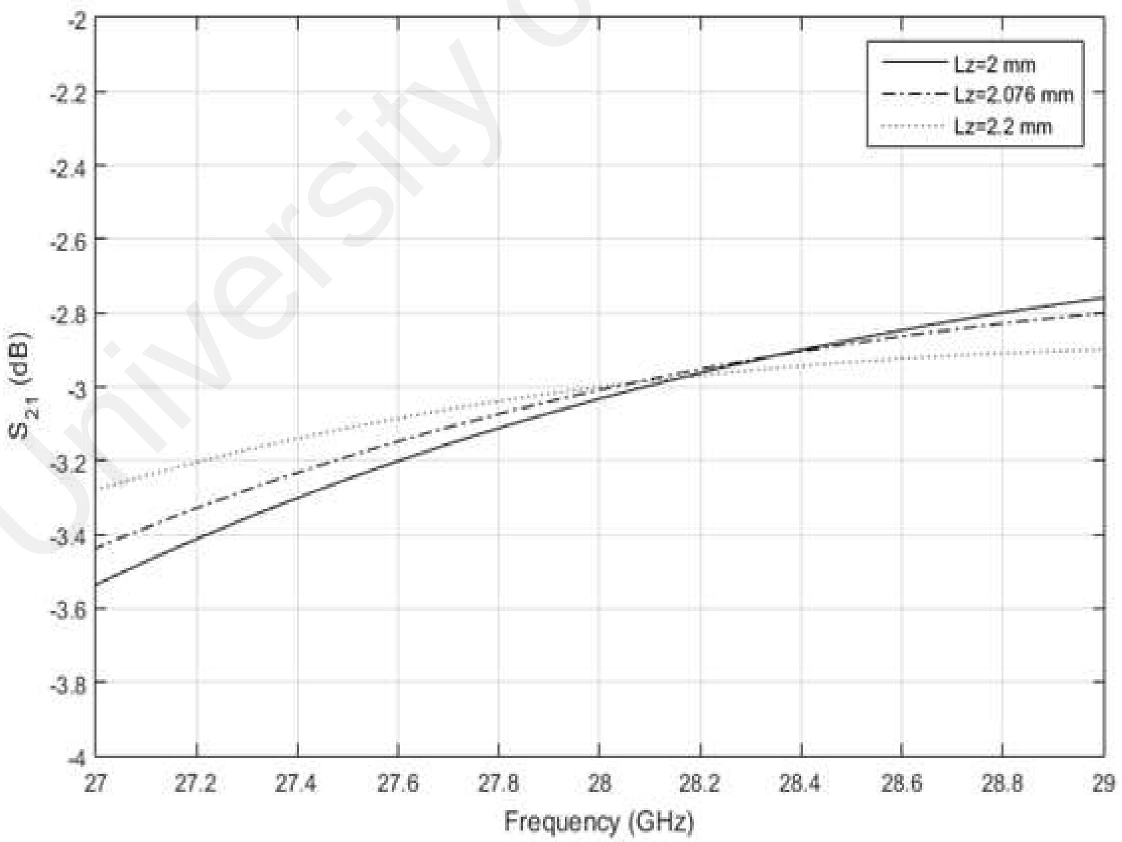

(b)

Figure 4.10, continued

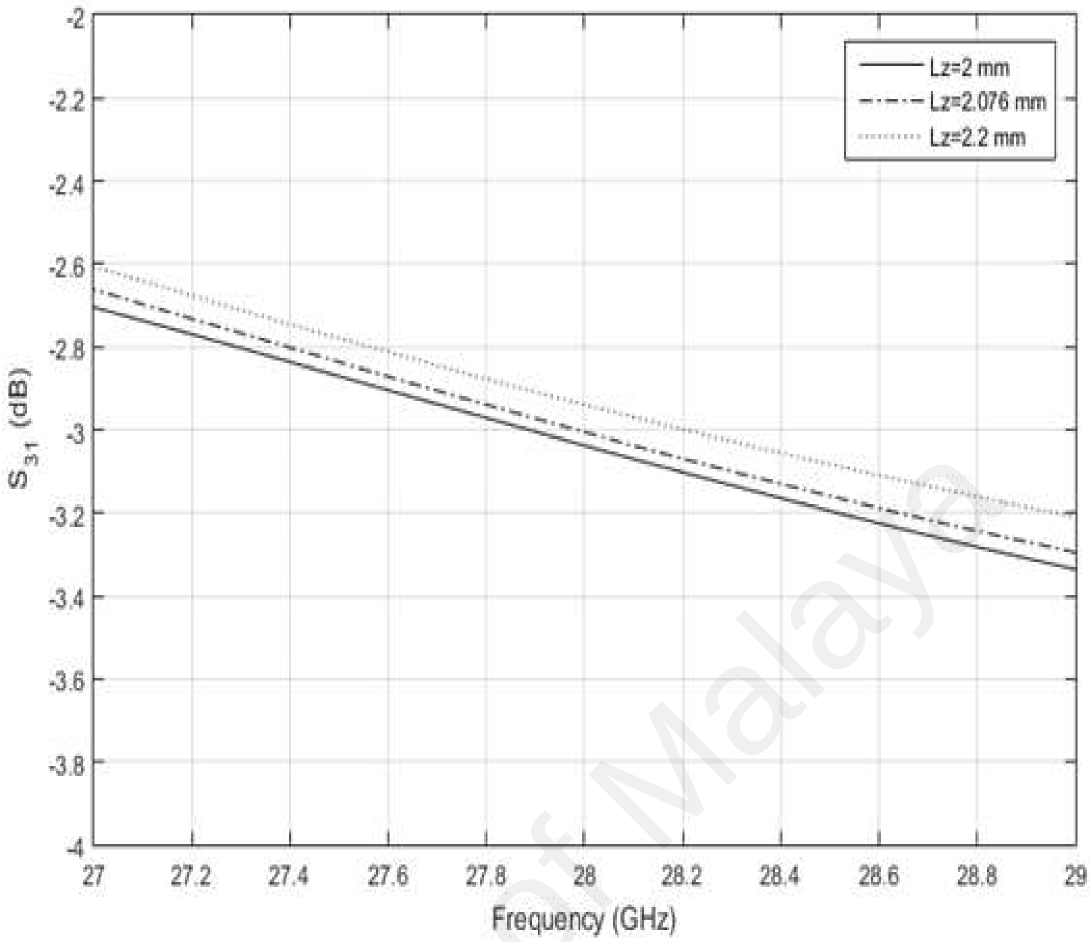

(c)

Figure 4.10: Effects of length, L_z of the quadrature hybrid on (a) return loss and insertion losses, (b) S_{21} and (c) S_{31}

Based on these parametric studies, the length of L_z = 2.076 mm was selected to simulate the quadrature hybrid. Table 4.8 lists the parameters of the quadrature hybrid and Figure 4.11 presents the amplitudes of the quadrature hybrid. The amplitude of insertion losses, S_{21} and S_{31} were −3 dB at 28 GHz. Good isolations of S_{11} and S_{41} were achieved with less than −20 dB from 27 GHz to 29 GHz. The excellent result shows that the quadrature hybrid had a very good design. Figure 4.12 illustrates the simulated output phases of ports, P2 and P3 when the input port, P1 was excited. The phase difference between ports P2 and P3 was 90° between 27 GHz and 29 GHz. The power flow of the quadrature hybrid when port 1 was excited is shown in Figure 4.13. As presented in Figure 4.13, the power flowed from port 1 to ports, 2 and 3. Furthermore, the amplitude of the return loss, S_{11} and the amplitude of the isolation, S_{41} of the quadrature hybrid were less than −10 dB at 28 GHz, as illustrated in Figure 4.11. Thus, less power was reflected to port 1 and most of the power flowed to ports, 2 and 3.

Table 4.8: Parameters of the quadrature hybrid

Parameter	Value (mm)
L_{zo}	2.341
L_z	2.076
W_{zo}	0.7826
W_z	1.2754

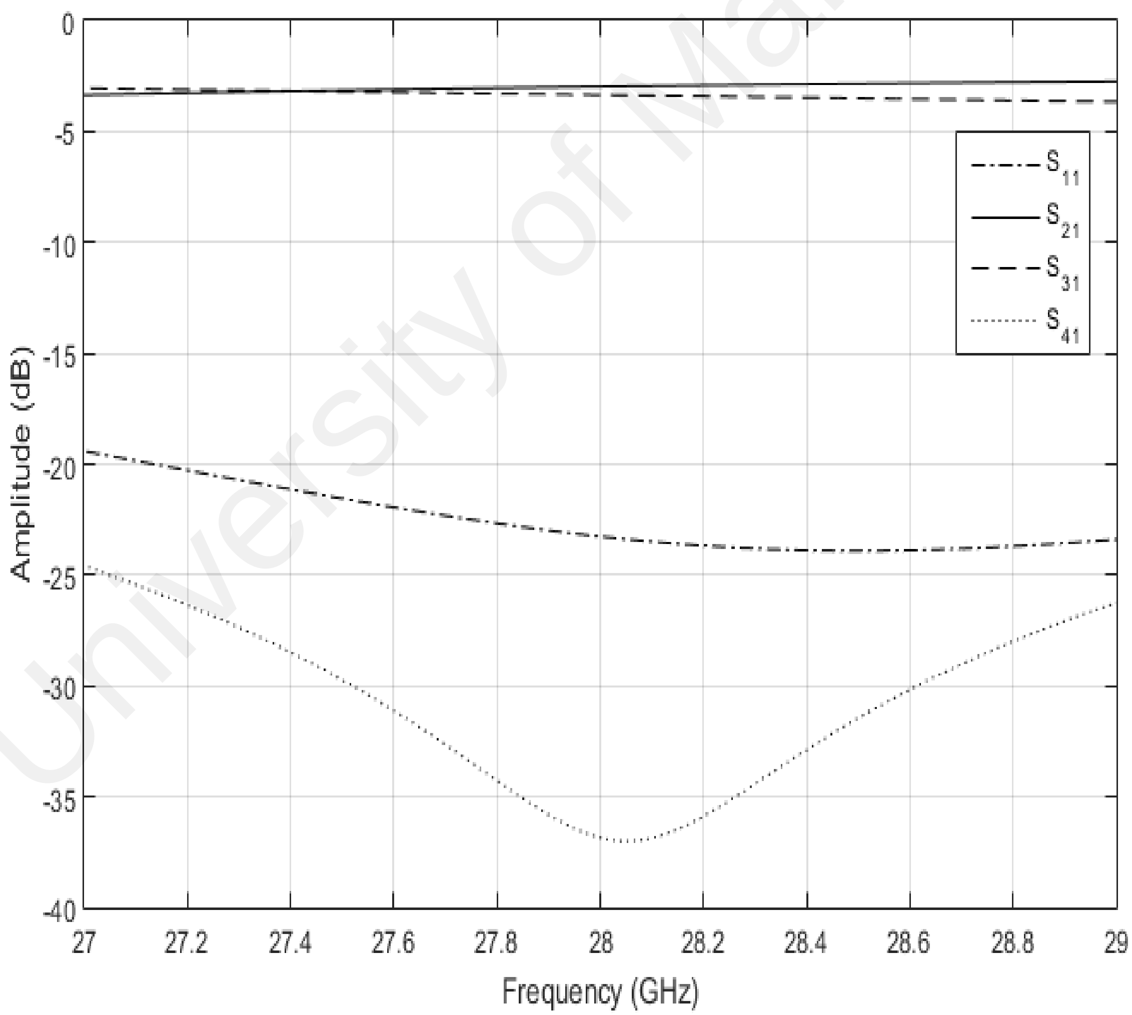

Figure 4.11: Simulated amplitudes of the quadrature hybrid

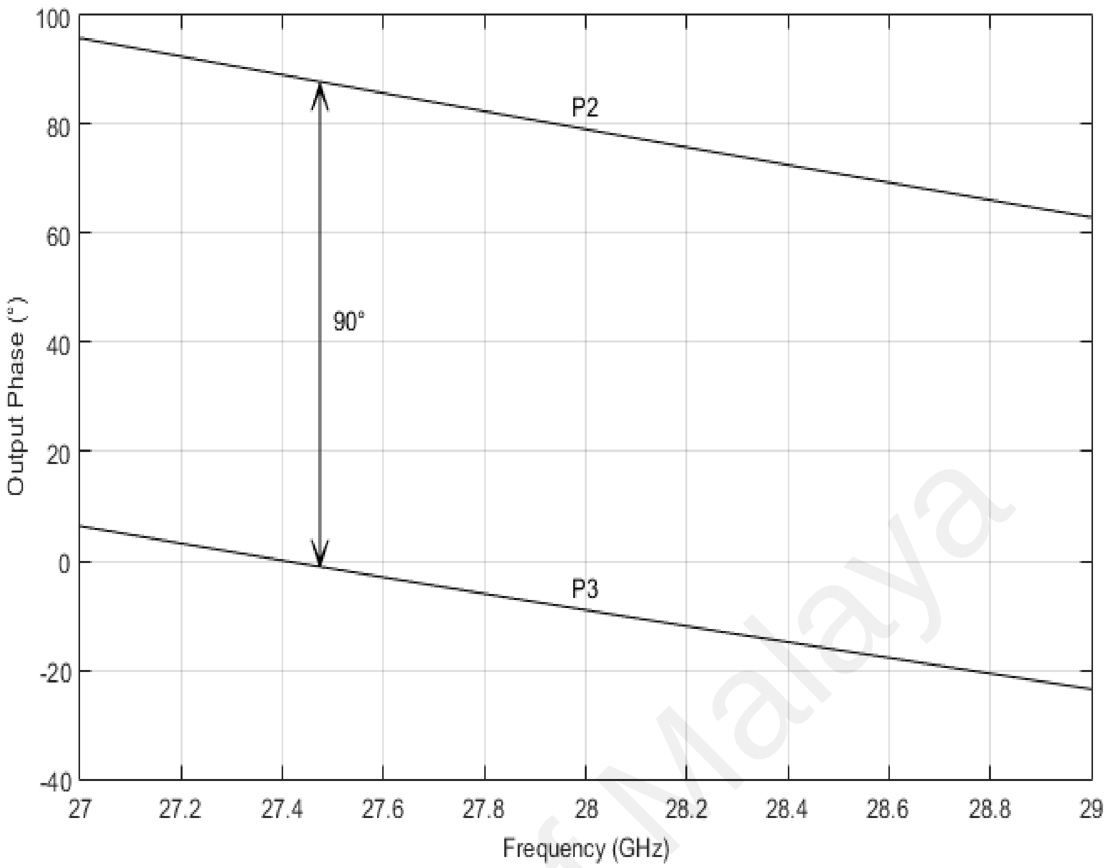

Figure 4.12: Simulated output phases of ports 2 and 3 when port 1 was excited

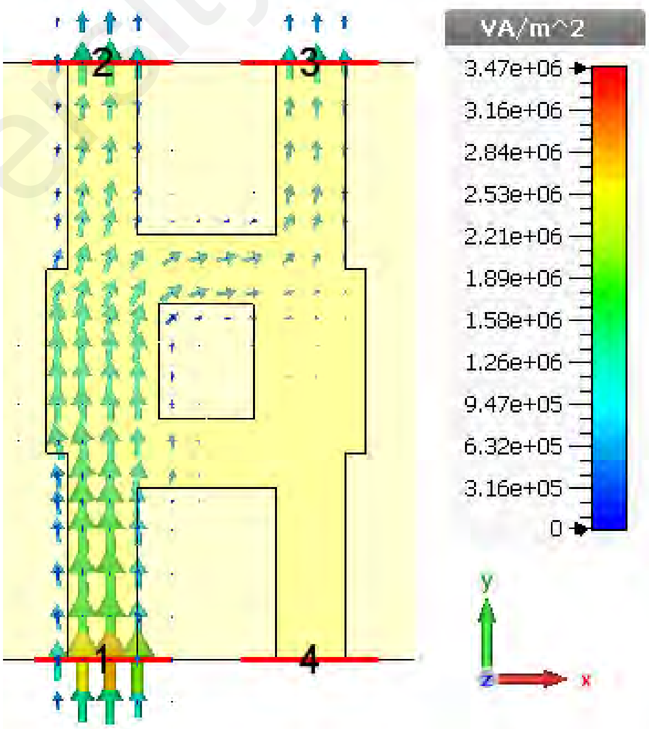

Figure 4.13: Power flow of the quadrature hybrid when port 1 was excited

4.2.5 Design of the Phase Shifters

Three phase shifters were required in the 8 × 8 Butler matrix that were 22.5°, 45°, and 67.5°, as mentioned in Section 4.2. The function of these phase shifters is to ensure the constant phase differences are achieved at the output ports of the Butler matrix. As a result, the produced main beams can be pointed at the desired directions. These phase shifters were designed using a 50 Ω microstrip transmission line. The widths of these phase shifters were the same as used in the quadrature hybrid and the crossover. The parameter can be calculated using mathematical equations, as expressed in Equation (4.2) to Equation (4.4). Meanwhile, the lengths of the phase shifters can be obtained using Equation (2.23) and Equation (2.24). The phase shifters had different lengths to achieve the desired phase differences of 22.5°, 45°, and 67.5°.

The structures of the 67.5° and 22.5° phase shifters, labeled as L_1 and L_2, are shown in Figure 4.14 and Figure 4.15, respectively. These 67.5° and 22.5° phase shifters were simulated and optimized using CST Microwave Studio to obtain the optimum results. Table 4.9 lists the optimized parameters of the phase shifters. Figure 4.16 and Figure 4.17 present the return losses and output phases of the 67.5° and the 22.5° phase shifters, respectively. The return losses were less than −10 dB from 27 GHz to 29 GHz for both phase shifters. Besides that, the phase differences of the 67.5° and 22.5° phase shifters were 67.5° and 22.5° at 28 GHz, respectively.

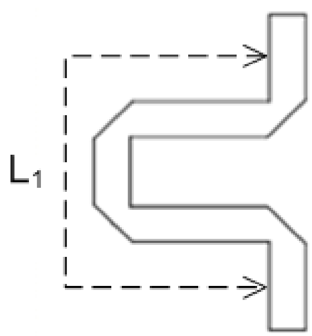

Figure 4.14: Structure of the 67.5° phase shifter

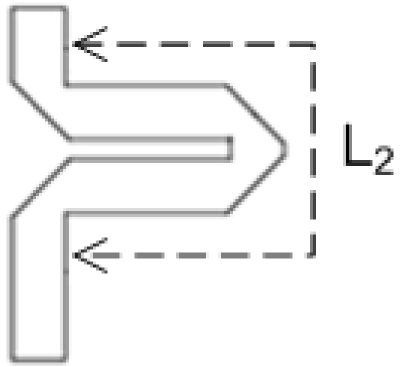

Figure 4.15: Structure of the 22.5° phase shifter

Table 4.9: Optimized parameters of the 67.5° and 22.5° phase shifters

Parameter	Values (mm)
L_1	11.9236
L_2	7.9652
W_{zo}	0.7826

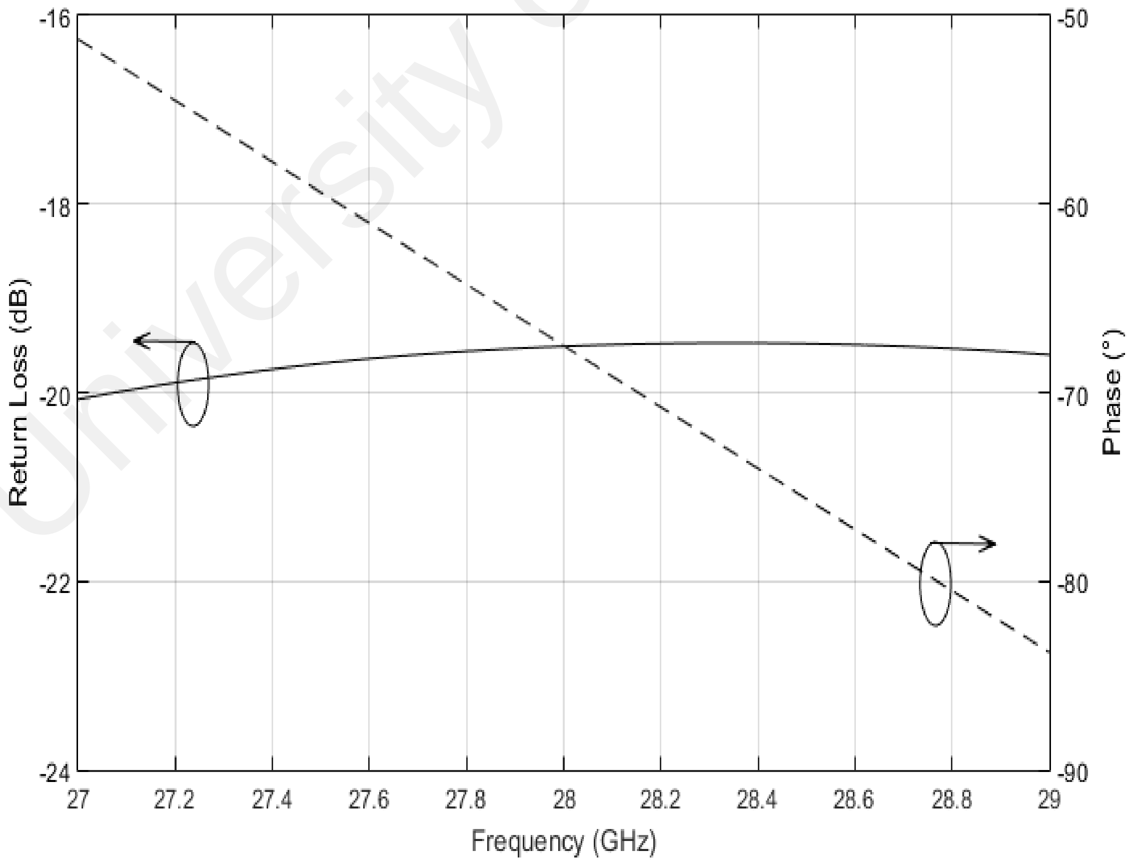

Figure 4.16: Return loss and output phase of the 67.5° phase shifter

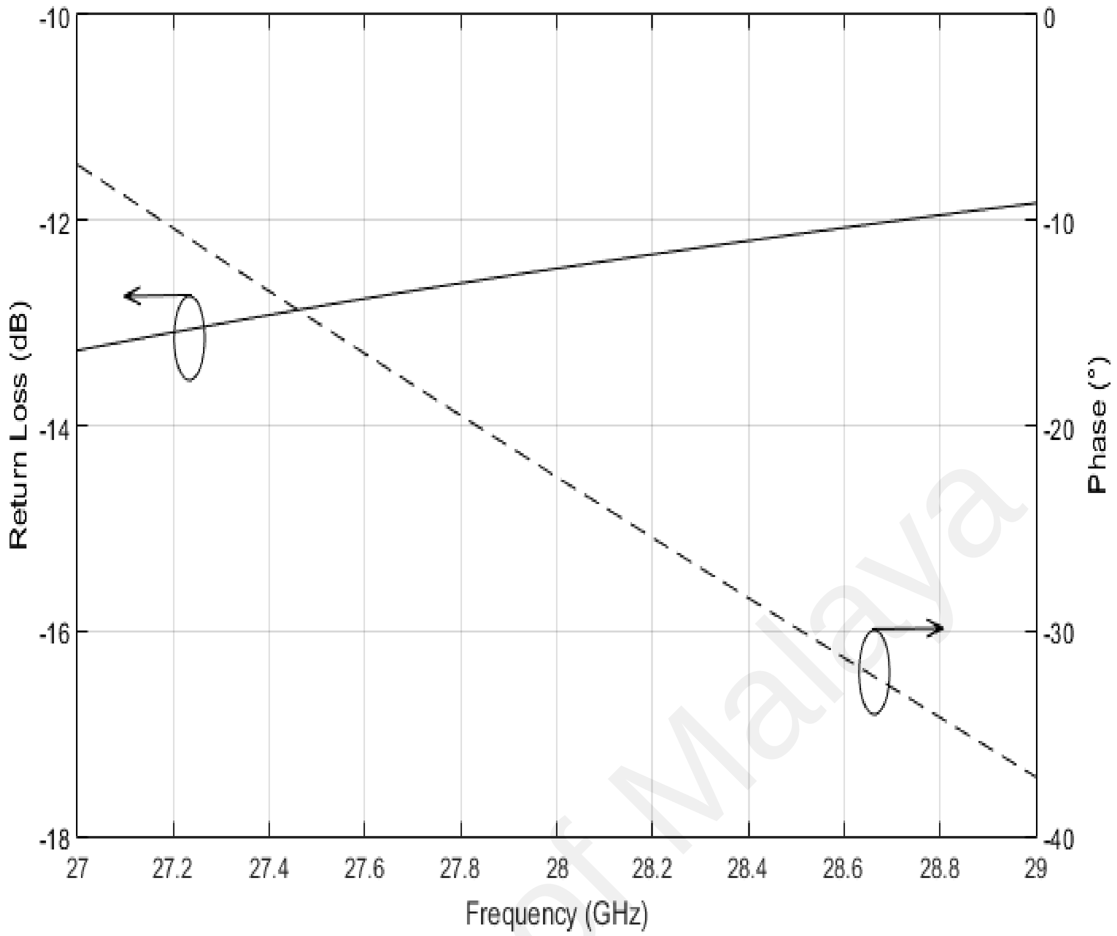

Figure 4.17: Return loss and output phase of the 22.5° phase shifter

Figure 4.18 illustrates the two phase shifters in the Butler matrix with phase differences of 67.5° and 22.5°, labeled as L_1 and L_2, respectively. As shown in Figure 4.18, the blue line presents the direction of the current flows to the output ports, O_1 and O_3 when the input port, P1 was excited. The red line presents the direction of the current flows to the output ports, O_2 and O_4 when the input port, P4 was excited. The phase differences can be obtained using Equation (4.7) and Equation (4.8) for the 67.5° and 22.5° phase shifters in the Butler matrix, respectively.

$$\phi_3 - \phi_1 = 22.5° \quad (4.7)$$

$$\phi_2 - \phi_4 = 67.5° \quad (4.8)$$

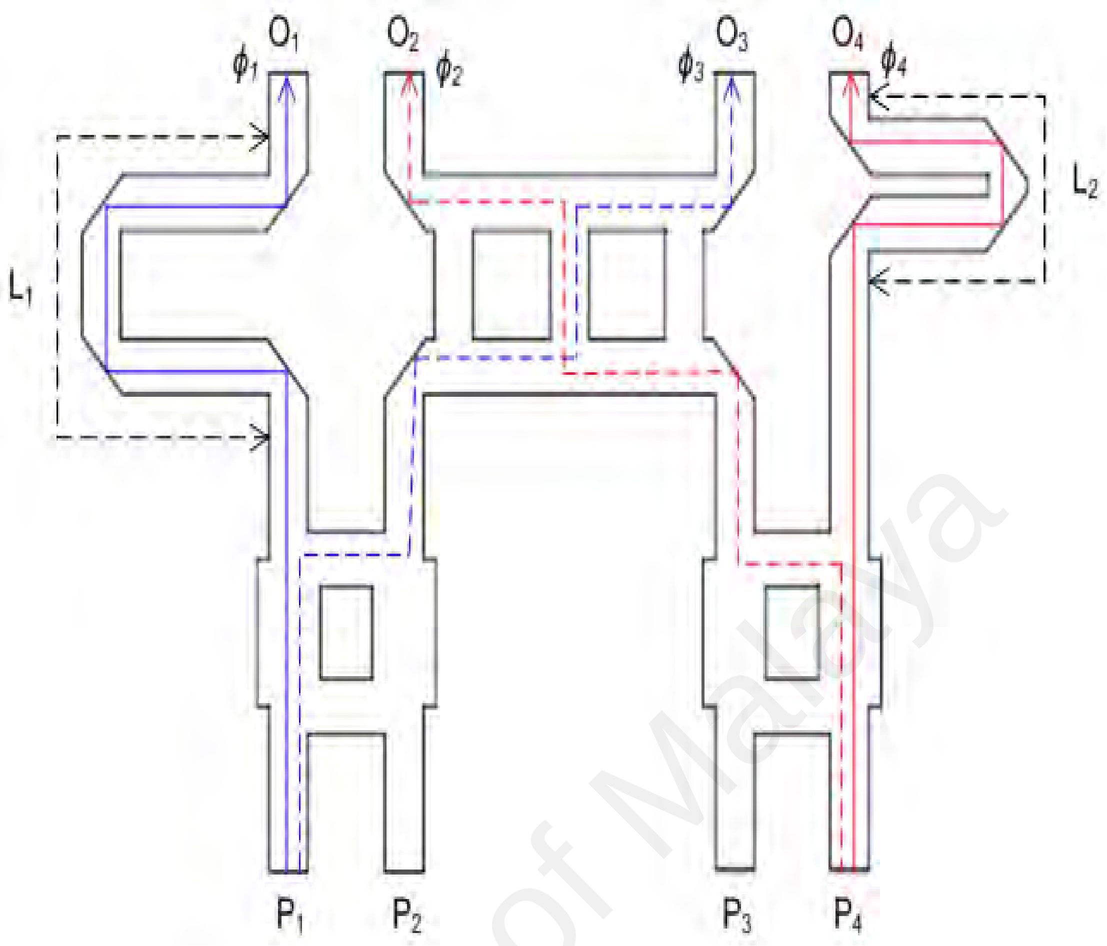

Figure 4.18: Structure of the 67.5° and 22.5° phase shifters in the 8 × 8 Butler matrix

The power flow in the 67.5° phase shifter when port 1 was excited is shown in Figure 4.19. As presented in Figure 4.19, the power flowed from port 1 to ports, 5 and 7 through the circuit elements such as the quadrature hybrid, the 67.5° phase shifter, and the crossover. Furthermore, these circuit elements were well designed and all ports of the circuit elements were matched. As shown in Figure 4.16, the return losses of the 67.5° phase shifter were less than −10 dB at 28 GHz. Therefore, less power was reflected to port 1 and most of the power flowed to ports, 5 and 7. The output phases of ϕ_1 to ϕ_4 at the output ports of the Butler matrix are illustrated in Figure 4.20. The output phase characteristics of ϕ_2 and ϕ_3 were similar due to the symmetrical structure. The phase differences of the phase shifters as shown in Figure 4.20 were correspond to Equation (4.7) and Equation (4.8).

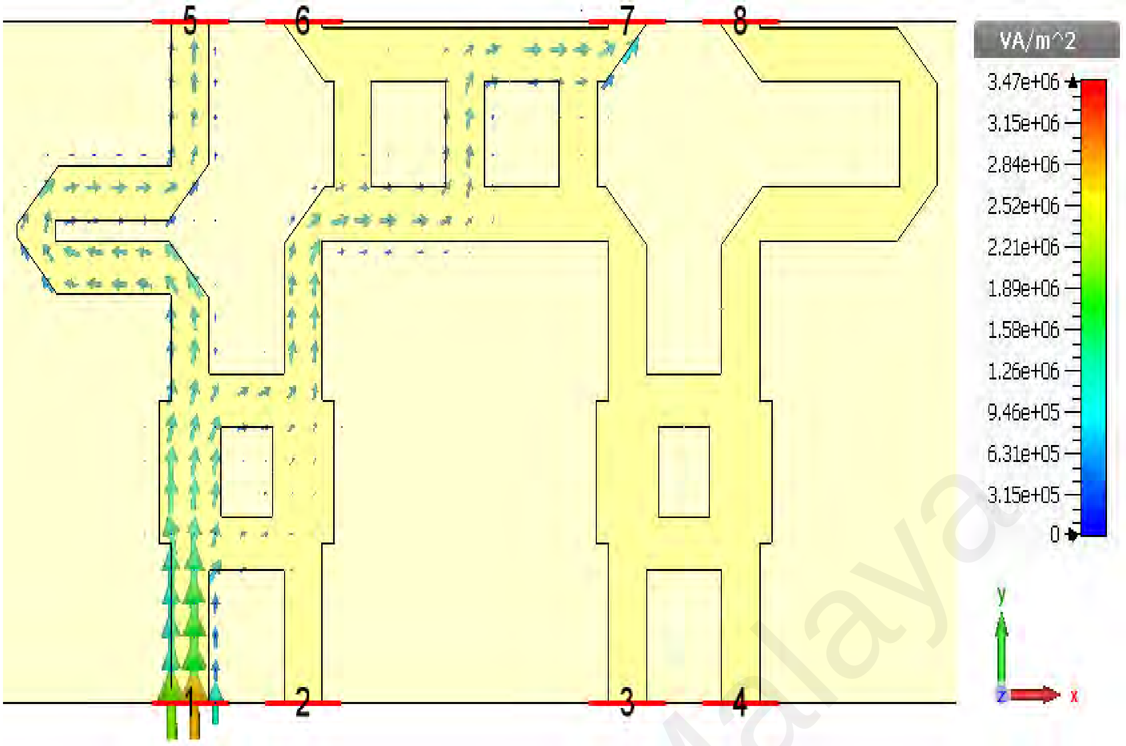

Figure 4.19: Power flow in the 67.5° phase shifters in the Butler matrix when port 1 was excited

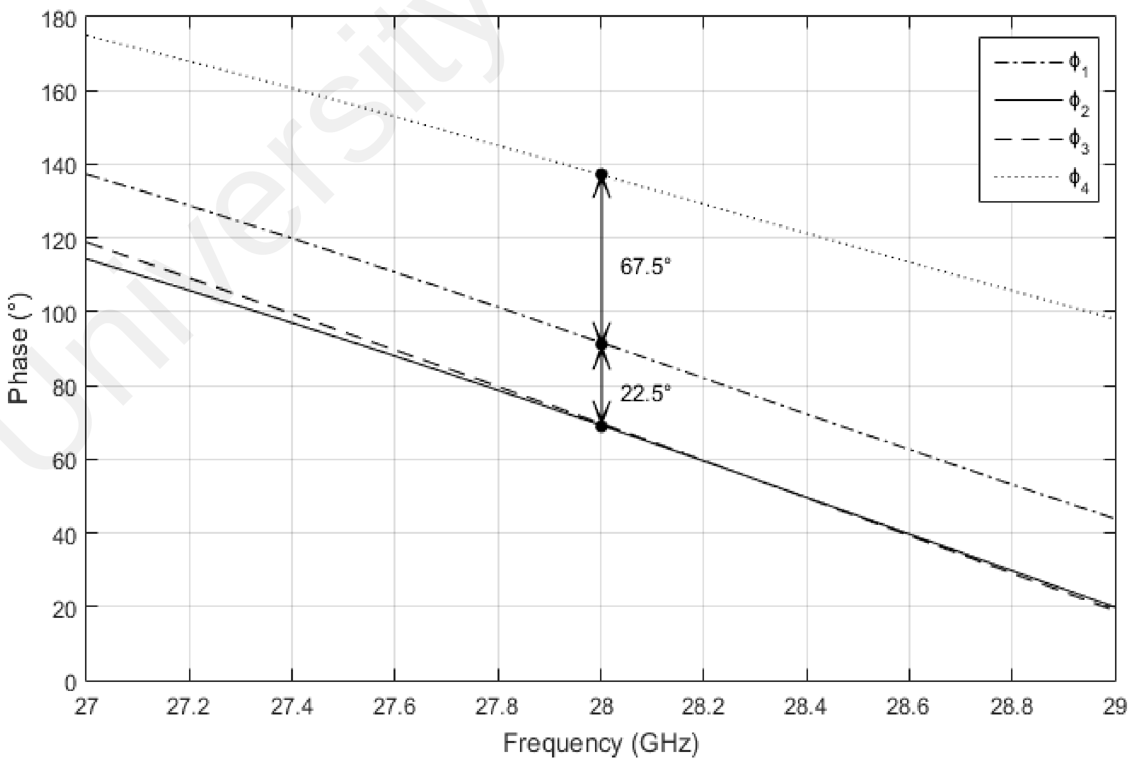

Figure 4.20: Phases of ϕ_1 to ϕ_4 at the output ports of phase shifters in the Butler matrix

As referred to in Figure 4.1, there were two types of 45° phase shifters. The first 45° phase shifter was located at the outer part of the 8 × 8 Butler matrix. The second 45° phase shifter was located beside the first 45° phase shifter. Figure 4.21 and Figure 4.22 show the structures of the first and the second 45° phase shifters labeled as L_3 and L_4, respectively. These structures of the phase shifters were simulated and optimized using CST Microwave Studio to obtain the optimum results. The optimized parameters of these phase shifters are shown in Table 4.10.

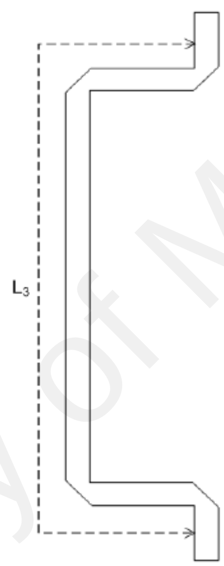

Figure 4.21: Structure of the first 45° phase shifter

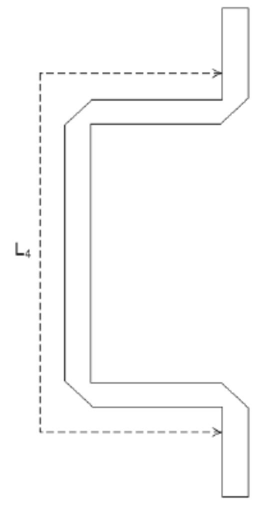

Figure 4.22: Structure of the second 45° phase shifter

Table 4.10: Optimized parameters of 45° phase shifters

Parameter	Values (mm)
L_3	34.6571
L_4	25.6446
W_{zo}	0.7826

Figure 4.23 and Figure 4.24 present the return losses and the output phases of the first and the second 45° phase shifters, respectively. The return losses were less than −10 dB from 27 GHz to 29 GHz for both 45° phase shifters. The phase differences for both 45° phase shifters were 45° at 28 GHz. Figure 4.25 shows the phase shifters in the Butler matrix and Figure 4.26 presents the power flow of the phase shifters in the Butler matrix when port 1 was excited. As illustrated in Figure 4.26, the power flowed from port 1 to ports, 9, 11, 13 and 15 through the circuit elements such as the quadrature hybrids, the crossovers, and the 67.5° phase shifters together with the first and the second 45° phase shifters. As shown in Figure 4.23 and Figure 4.24, the return losses of the first and second 45° phase shifters were less than −10 dB at 28 GHz. Thus, less power was reflected to port 1 and most of the power flowed to ports, 9, 11, 13 and 15.

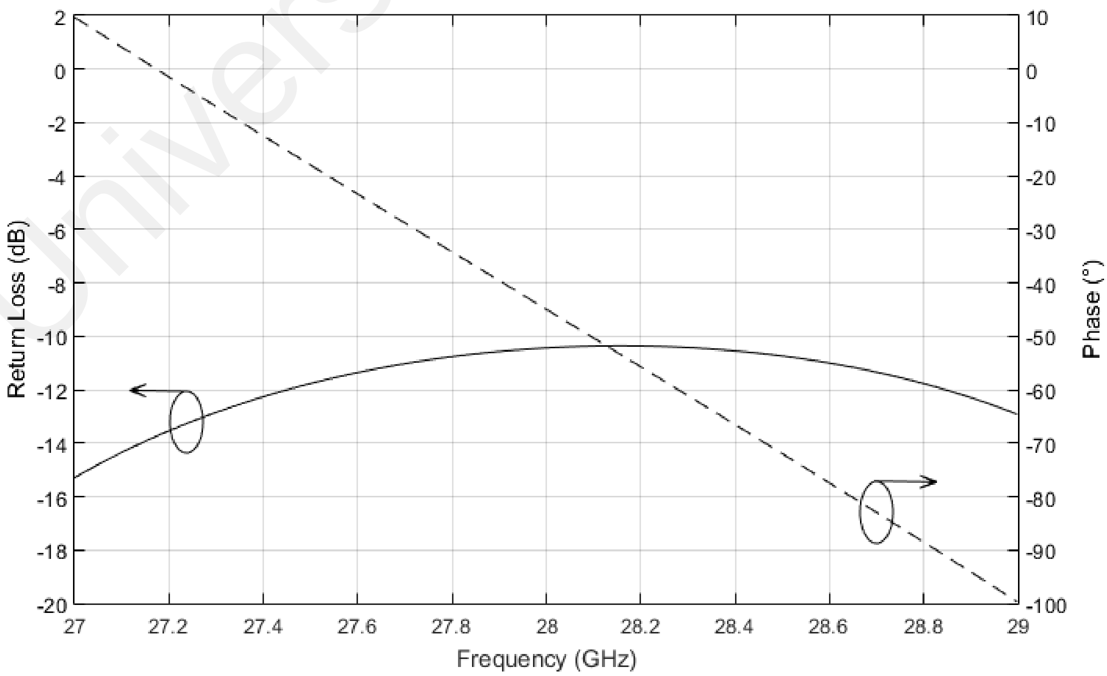

Figure 4.23: Return loss and output phase of the first 45° phase shifter

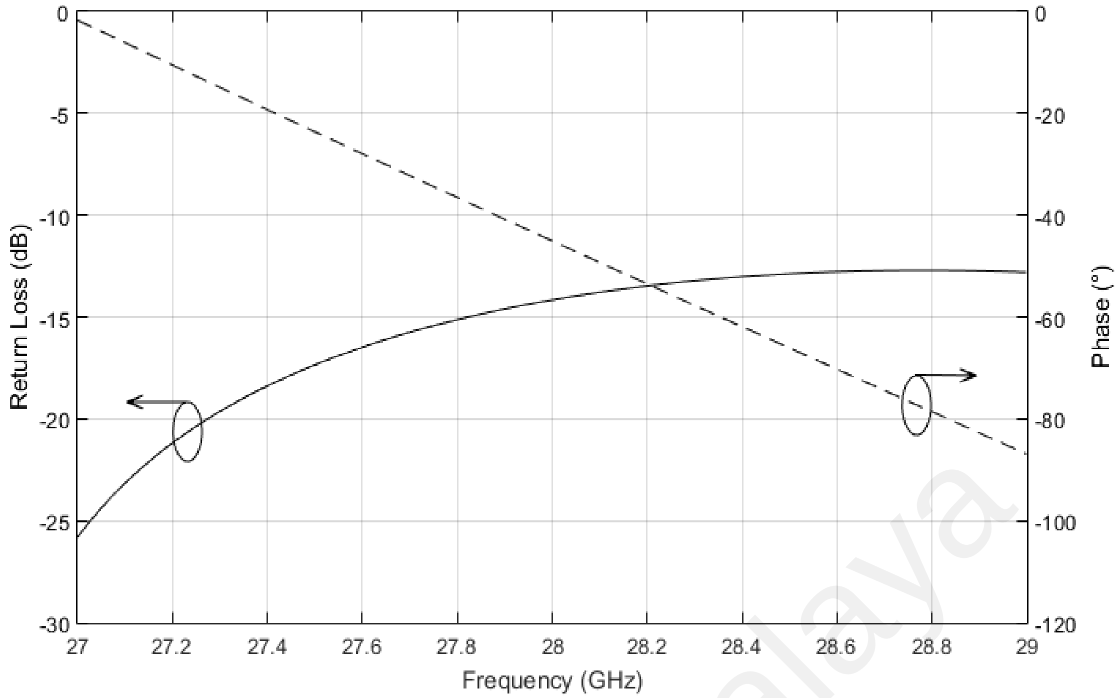

Figure 4.24: Return loss and output phase of the second 45° phase shifter

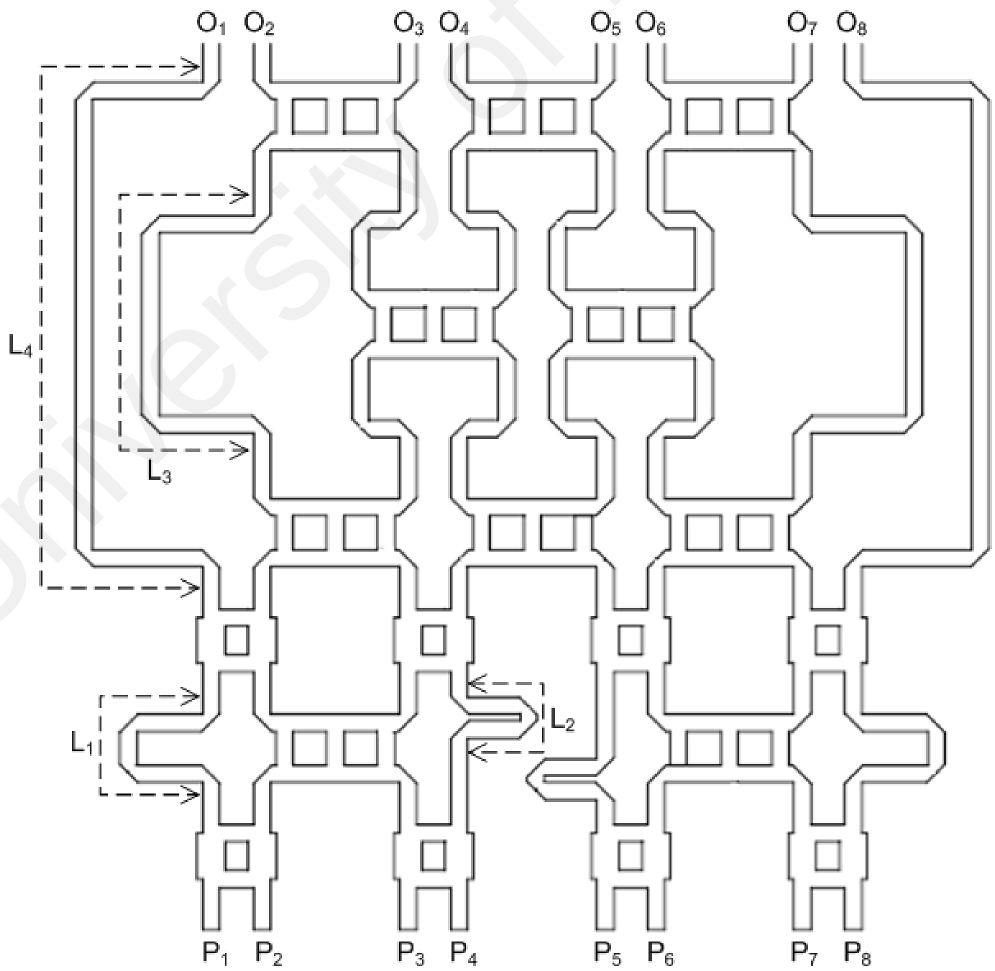

Figure 4.25: Structure of the 45° phase shifters in the 8 × 8 Butler matrix

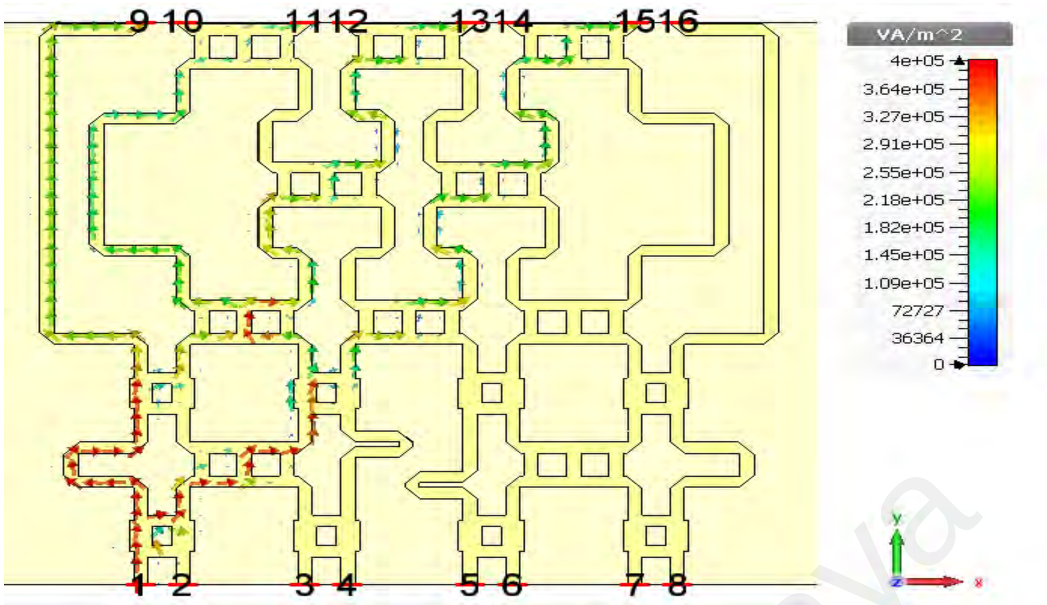

Figure 4.26: Power flow in the 45° phase shifters in the Butler matrix when port 1 was excited

4.2.6 Design of the 8 × 8 Butler Matrix

The circuit elements that were designed in Section 4.2.3 to Section 4.2.5 were integrated to form the complete design structure of an 8 × 8 Butler matrix, as illustrated in Figure 4.27. The 8 × 8 Butler matrix had eight input ports (P1 to P8) and eight output ports (O1 to O8) that were connected through sixteen crossovers, twelve quadrature hybrids, and eight phase shifters. Extended lines were designed at the input and output ports of the 8 × 8 Butler matrix to allow the implementation of coaxial connectors for measurement purposes. Figure 4.28 shows the power flow of the 8 × 8 Butler matrix when the input port, P1 was excited. As illustrated in Figure 4.28, the power flowed from the input port, P1 to the output ports, O1 to O8. Furthermore, the circuit elements were well designed and all ports were well matched. The return losses and the isolations of the circuit elements were less than −10 dB at 28 GHz, as presented in Figure 4.7, Figure 4.11, Figure 4.16, Figure 4.17, Figure 4.23, and Figure 4.24. Therefore, less power reflected to the input port, P1 and most of the power flowed to the output ports, O1 to O8.

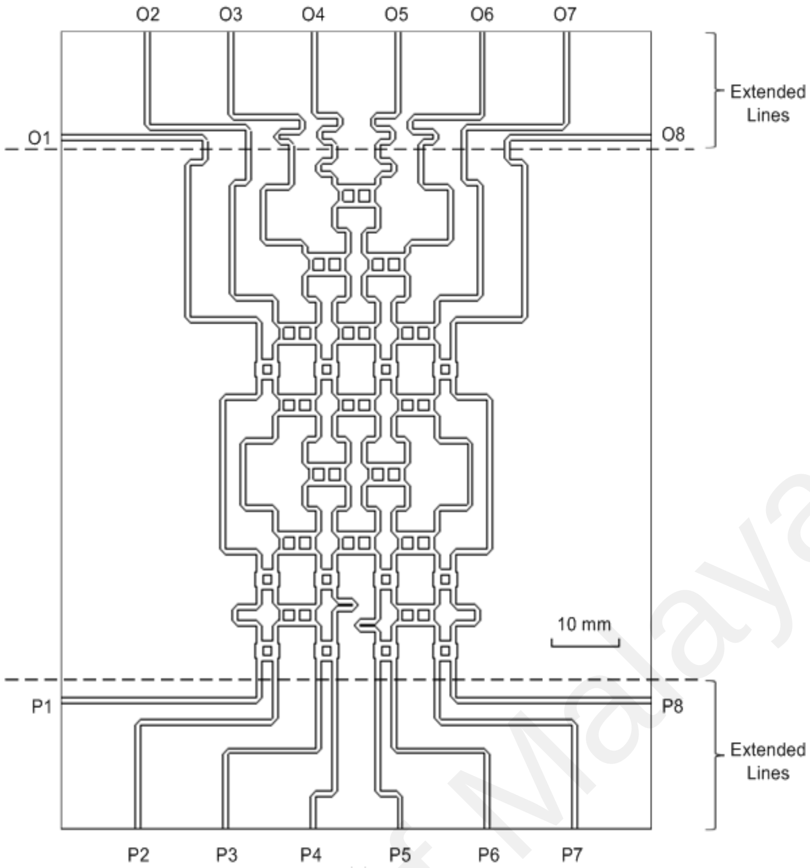

Figure 4.27: Designed structure of the 8 × 8 Butler matrix

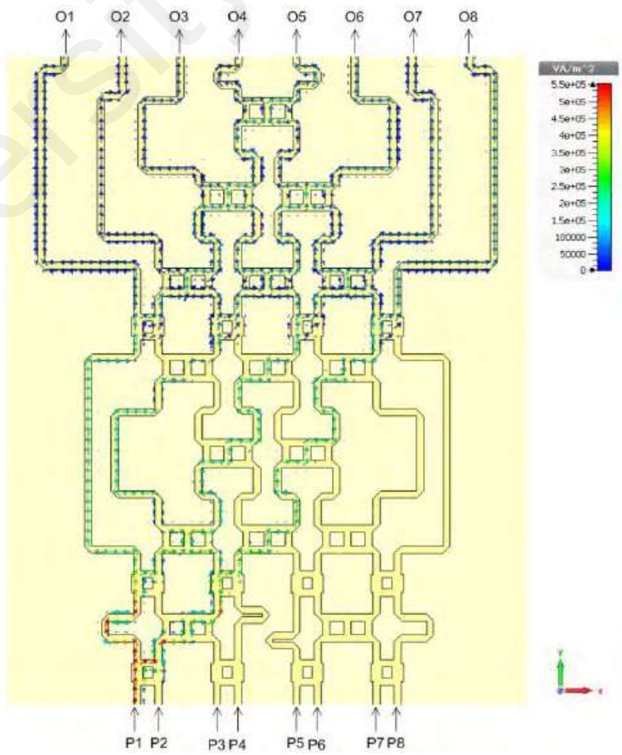

Figure 4.28: Power flow of the 8 × 8 Butler matrix when input port, P1 was excited

4.3 Fabrication and Measurement

The designed structure of the 8 × 8 Butler matrix as shown in Figure 4.27 was fabricated using a substrate material of NPC-220A via a photo etching process. Figure 4.29 shows a photograph of the fabricated 8 × 8 Butler matrix. The 2.92 mm coaxial connectors were soldered at the input and output ports of the 8 × 8 Butler matrix. The size of the fabricated board was 110 mm × 88 mm.

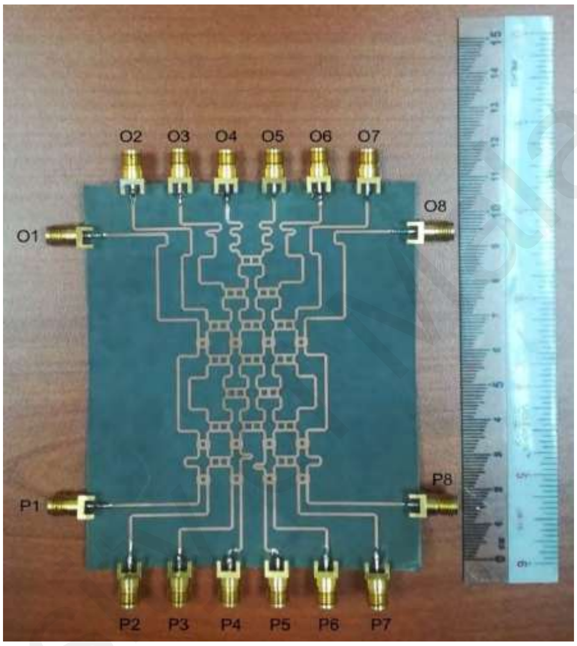

Figure 4.29: Photograph of the fabricated 8 × 8 Butler matrix

4.4 Results and Discussion

The simulation and measurement results of the 8 × 8 Butler matrix are presented in the following subsections. The results are also discussed in these subsections.

4.4.1 Return Loss and Isolation

Figure 4.30 and Figure 4.31 illustrate the simulated and measured return losses at the input ports of the 8 × 8 Butler matrix, respectively. As shown in Figure 4.30, the simulated return losses at the input ports of the 8 × 8 Butler matrix at 28 GHz were −13.17 dB, −12.59 dB, −28.97 dB, −13.87 dB, −15.54 dB, −14.31 dB, −12.59 dB, and

−13.17 dB for S_{11}, S_{22}, S_{33}, S_{44}, S_{55}, S_{66}, S_{77}, and S_{88}, respectively. The return losses of S_{11} and S_{88} together with S_{22} and S_{77} were equal. However, the return losses of S_{33} and S_{66} along with S_{44} and S_{66} were slightly different due to the reflections of the 22.5° phase shifters in the 8 × 8 Butler matrix, as illustrated in Figure 4.27. Meanwhile, the measured return losses at the input ports of the 8 × 8 Butler matrix at 28 GHz were −13.75 dB, −22.19 dB, −12.94 dB, −12.70 dB, −13.76 dB, −16.02 dB, −17.07 dB, and −12.74 dB for S_{11}, S_{22}, S_{33}, S_{44}, S_{55}, S_{66}, S_{77}, and S_{88}, respectively, as presented in Figure 4.31. Both simulated and measured return losses at the input ports of the 8 × 8 Butler matrix were less than −10 dB, in wide frequency range of 27 GHz to 29 GHz. The simulated and measured return losses at the output ports of the 8 × 8 Butler matrix are illustrated in Figure 4.32 and Figure 4.33, respectively. As shown in Figure 4.32, the simulated return losses at the output ports of the 8 × 8 Butler matrix at 28 GHz were −11.35 dB, −18 dB, −20.46 dB, −15.40 dB, −15.86 dB, −19.38 dB, −20.17 dB, and −12.52 dB for S_{99}, S_{1010}, S_{1111}, S_{1212}, S_{1313}, S_{1414}, S_{1515}, and S_{1616}, respectively. The return losses of S_{99} and S_{1616}, S_{1010} and S_{1515}, S_{1111} and S_{1414}, together with S_{1212} and S_{1313} were approximately same. Meanwhile, the measured return losses at the output ports of the 8 × 8 Butler matrix at 28 GHz were −15.45 dB, −12.07 dB, −24.49 dB, −24.49 dB, −15.44 dB, −16.92 dB, −12.92 dB, and −25.22 dB for S_{99}, S_{1010}, S_{1111}, S_{1212}, S_{1313}, S_{1414}, S_{1515}, and S_{1616}, respectively, as presented in Figure 4.33. Both simulated and measured return losses at the output ports of the 8 × 8 Butler matrix were less than −10 dB, in the wide frequency range of 27 GHz to 29 GHz. However, it can be observed that the measured results were slightly different from the simulation results due to the fabrication tolerance. As explained in Section 4.2.2, slight extended lengths of the microstrip transmission line in the fabricated 8 × 8 Butler matrix could cause losses. Moreover, the variations in the substrate properties and the effect of the coaxial connectors due to soldering might also induce additional losses.

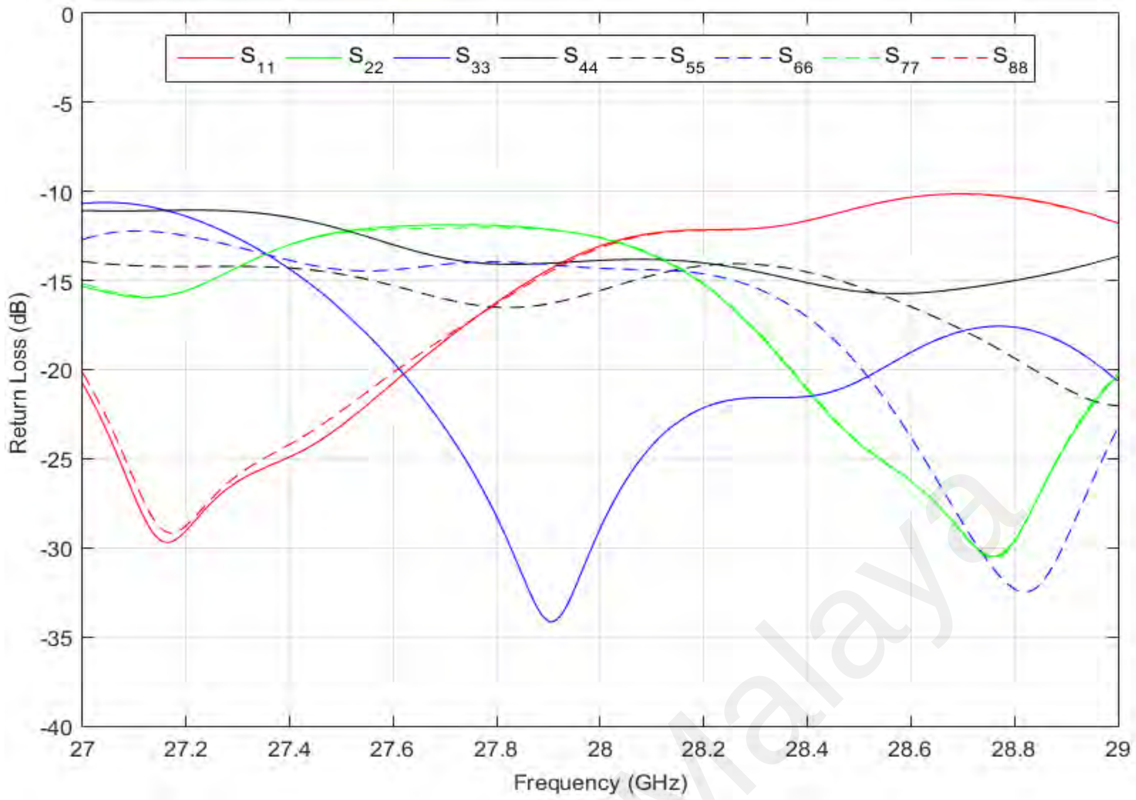

Figure 4.30: Simulated return losses at the input ports of the 8 × 8 Butler matrix

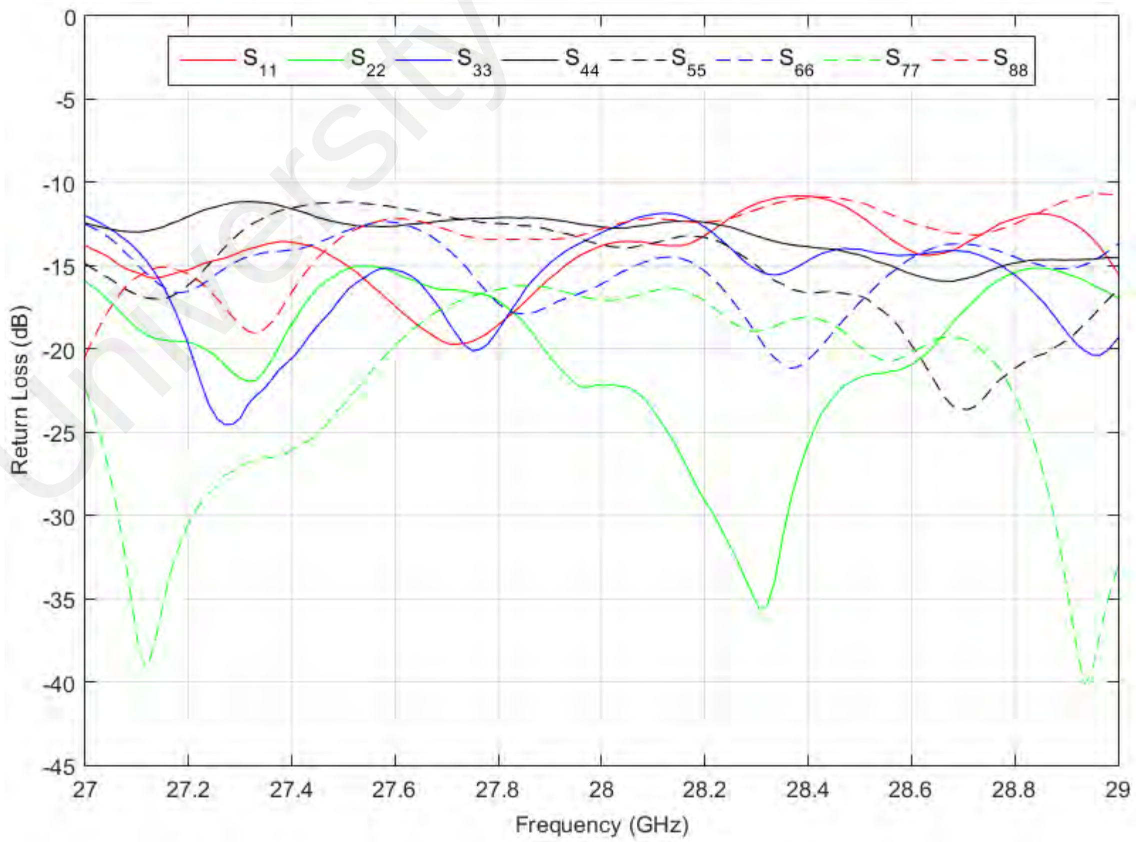

Figure 4.31: Measured return losses at the input ports of the 8 × 8 Butler matrix

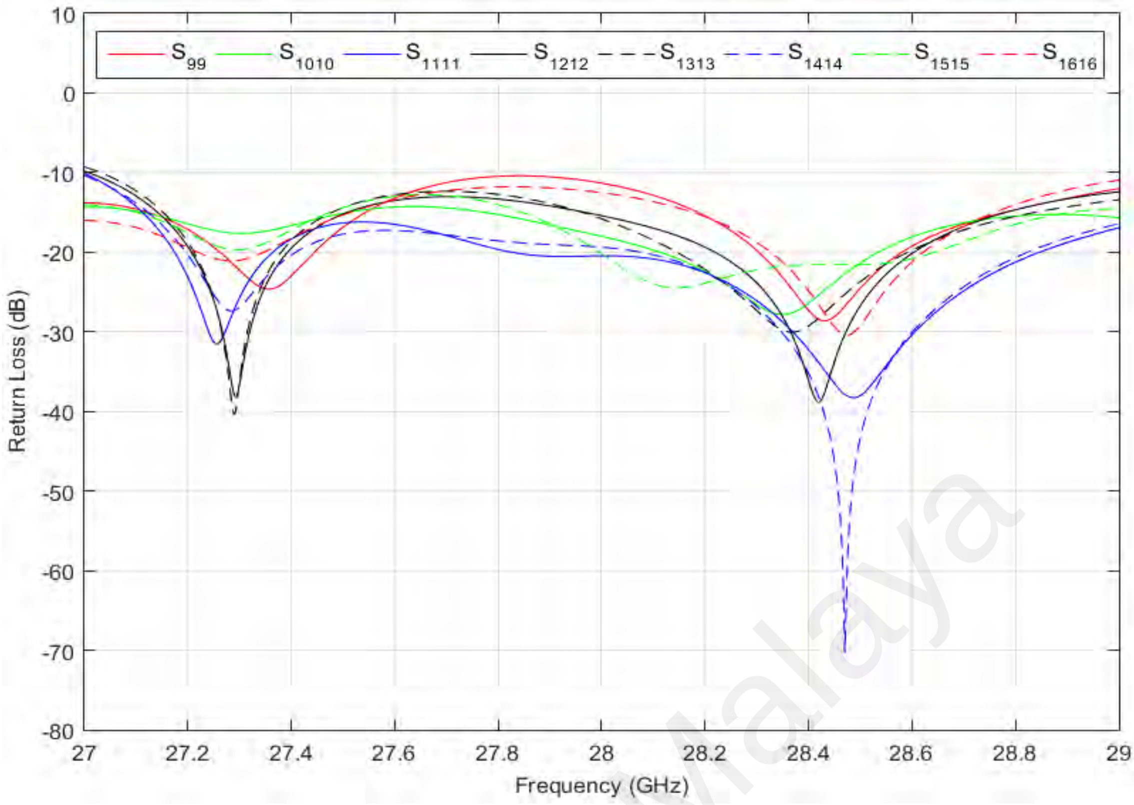

Figure 4.32: Simulated return losses at the output ports of the 8 × 8 Butler matrix

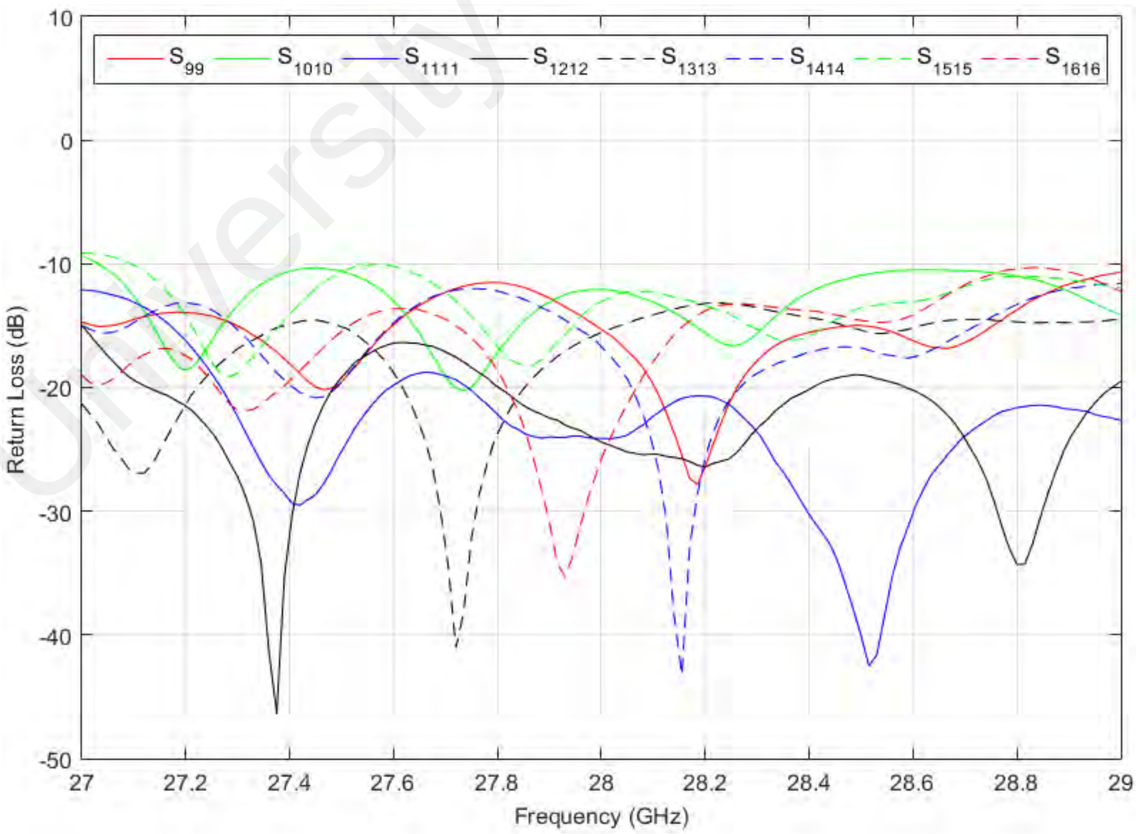

Figure 4.33: Measured return losses at the output ports of the 8 × 8 Butler matrix

The simulated and measured isolations between the input ports of the 8 × 8 Butler matrix are illustrated in Figure 4.34 and Figure 4.35, respectively. As shown in Figure 4.34, the simulated isolations between the input ports of the 8 × 8 Butler matrix were between −15 dB and −55 dB at 28 GHz. The measured isolations between the input ports of the 8 × 8 Butler matrix were from −20 dB and −50 dB at 28 GHz, as presented in Figure 4.35. Meanwhile, the simulated and measured isolations between the output ports of the 8 × 8 Butler matrix are shown in Figure 4.36 and Figure 4.37, respectively. As illustrated in Figure 4.36, the simulated isolations between output ports of the 8 × 8 Butler matrix were between −15 dB and −40 dB at 28 GHz. The measured isolations between output ports of the 8 × 8 Butler matrix were between −20 dB and −45 dB at 28 GHz, as presented in Figure 4.37. It can be observed that the measured results were slightly different from the simulation results due to the fabrication tolerance. Slight extended lengths of the microstrip transmission line in the fabricated 8 × 8 Butler matrix could cause losses, as explained in Section 4.2.2. The variations in the substrate properties and the effect of the coaxial connectors due to soldering might induce losses. However, the fabricated 8 × 8 Butler matrix was proven useful at the 28 GHz.

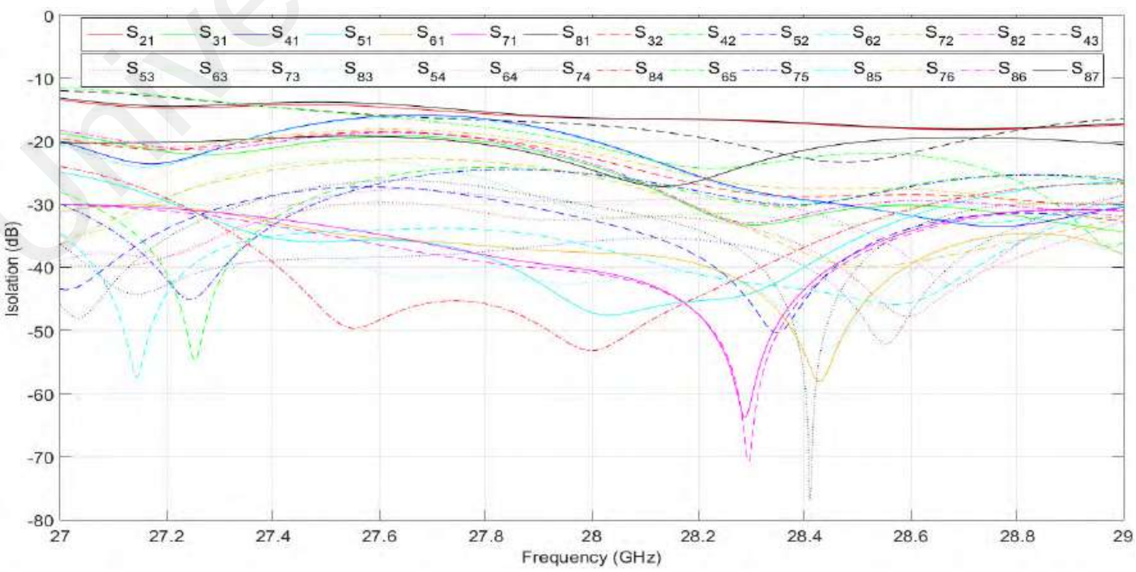

Figure 4.34: Simulated isolations between the input ports of the 8 × 8 Butler matrix

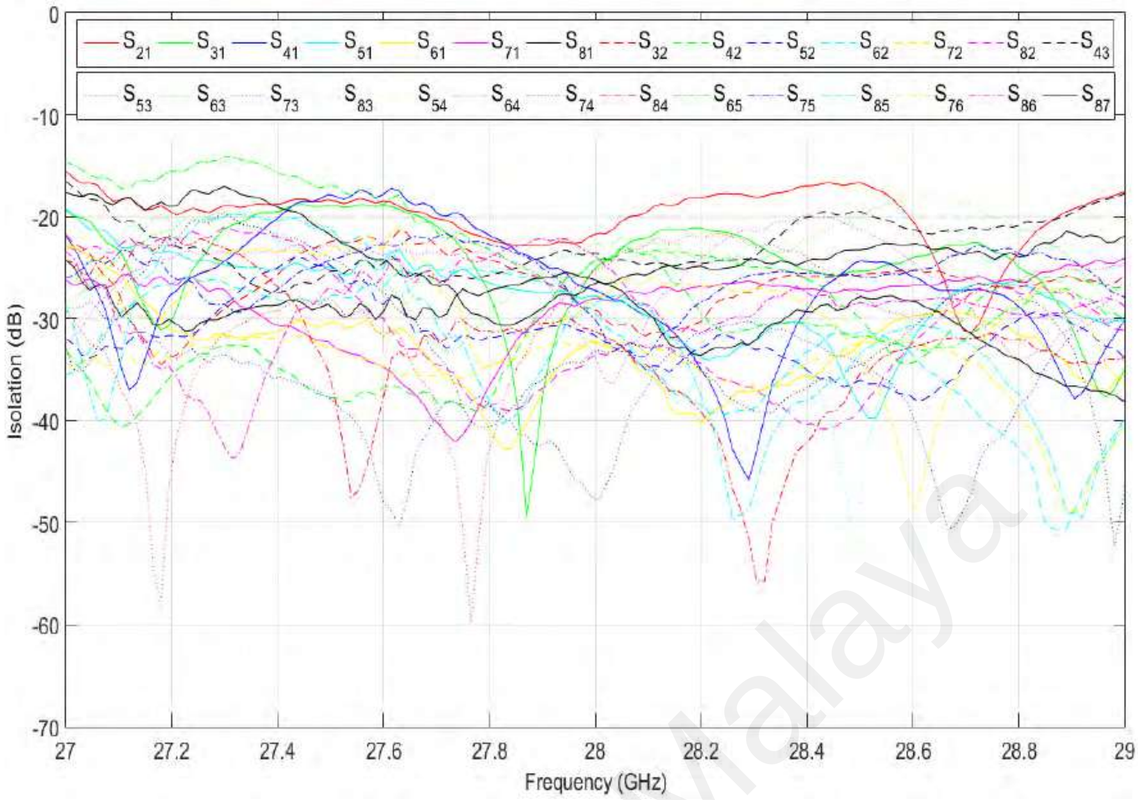

Figure 4.35: Measured isolations between the input ports of the 8 × 8 Butler matrix

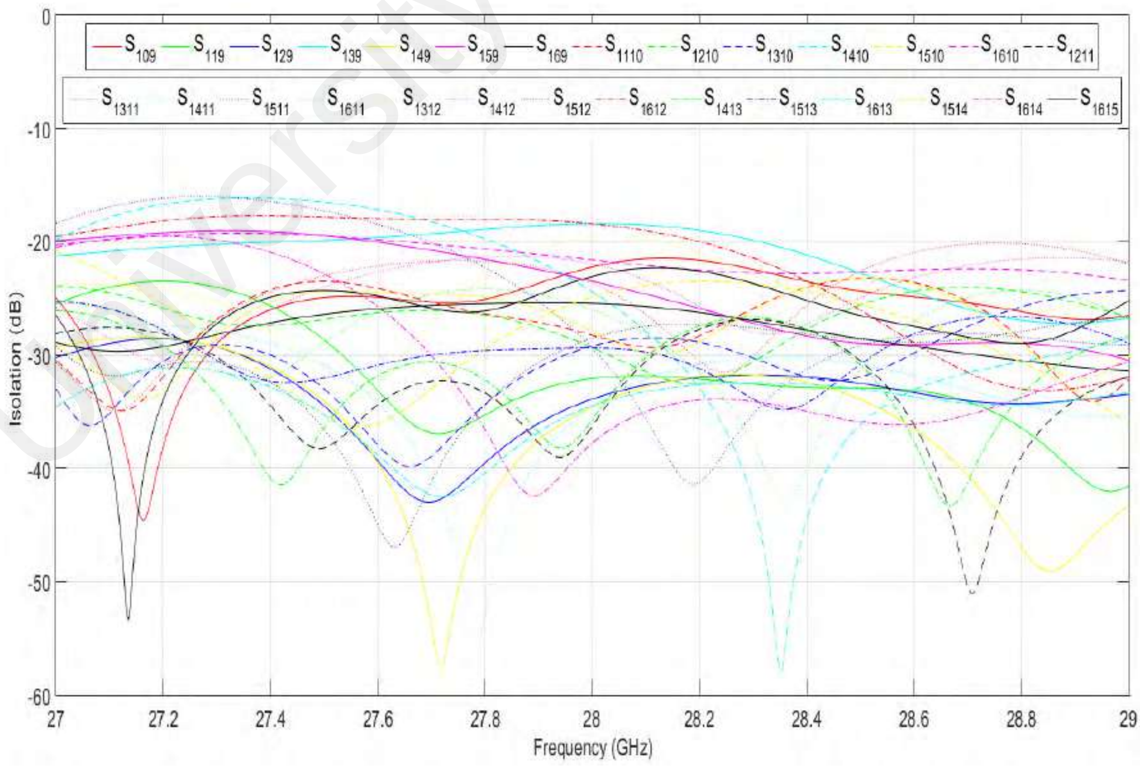

Figure 4.36: Simulated isolations between the output ports of the 8 × 8 Butler matrix

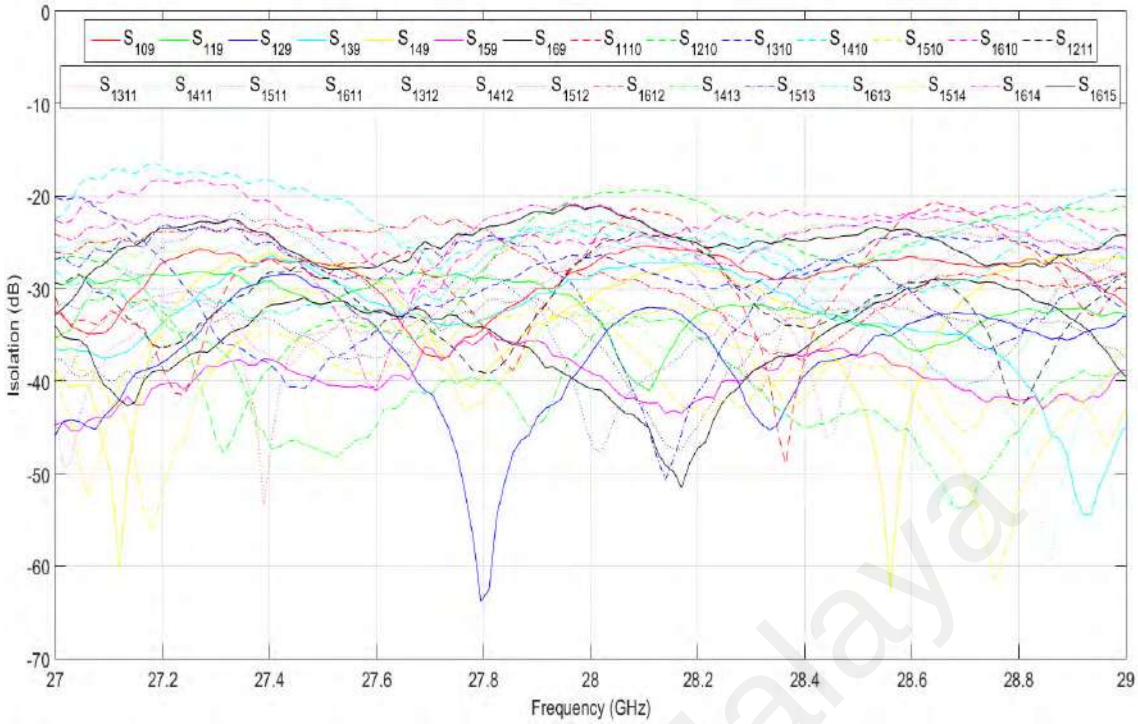

Figure 4.37: Measured isolations between the output ports of the 8 × 8 Butler matrix

4.4.2 Transmission Amplitude

Figure 4.38 and Figure 4.39 show the simulated and measured transmission amplitudes at the output ports of the 8 × 8 Butler matrix at 28 GHz, respectively. The transmission amplitude shows the ratio of the output power to the input power. Theoretically, the amplitude at each output port of the 8 × 8 Butler matrix should be −9 dB when the input power is excited. However, the simulated amplitude was approximately −14 dB and the difference of the amplitude was 5 dB. Using the line loss of the microstrip transmission line, as shown in Figure 4.4, the loss was revealed to be 5 dB for a line length of 150 mm, which was estimated from the configuration in Figure 4.27. The average deviation of ± 2 dB was due to the reflections in the 8 × 8 Butler matrix. For the measured transmission amplitudes, the average deviation of ± 2 dB was due to the fabrication tolerance. As explained in Section 4.2.2, slight extended lengths of the microstrip transmission line in the fabricated 8 × 8 Butler matrix could cause losses. Moreover, the variations in the substrate properties and the coaxial connectors due to soldering might also induce additional losses. Therefore, the average amplitudes were reduced from −15 dB to −17 dB.

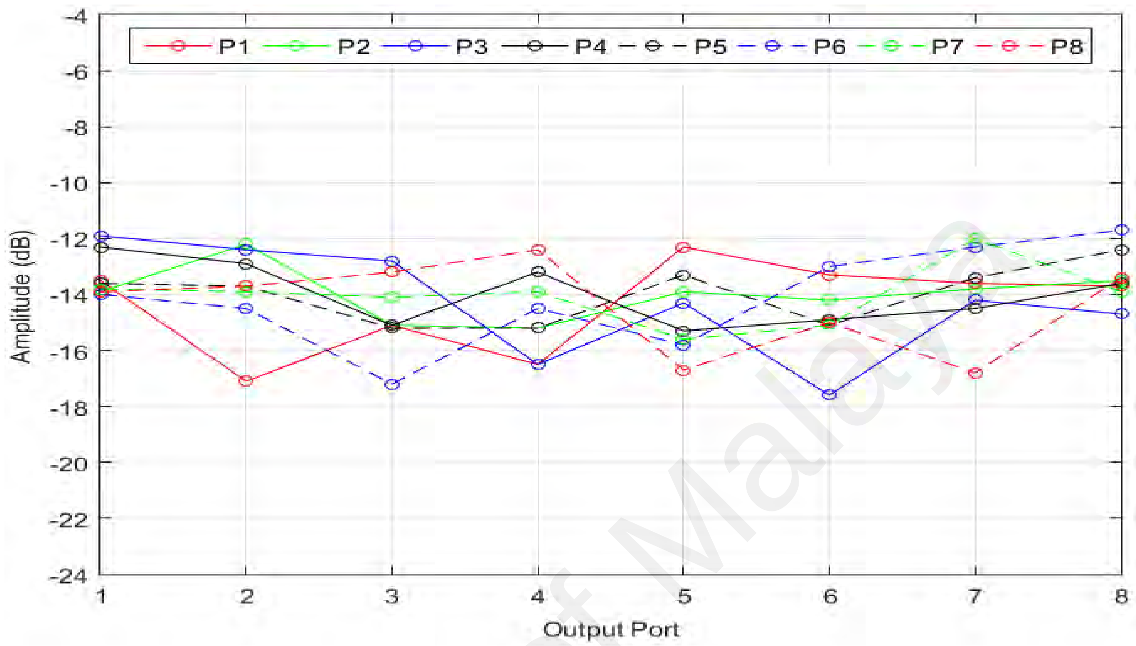

Figure 4.38: Simulated transmission amplitudes at the output ports of the 8 × 8 Butler matrix at 28 GHz

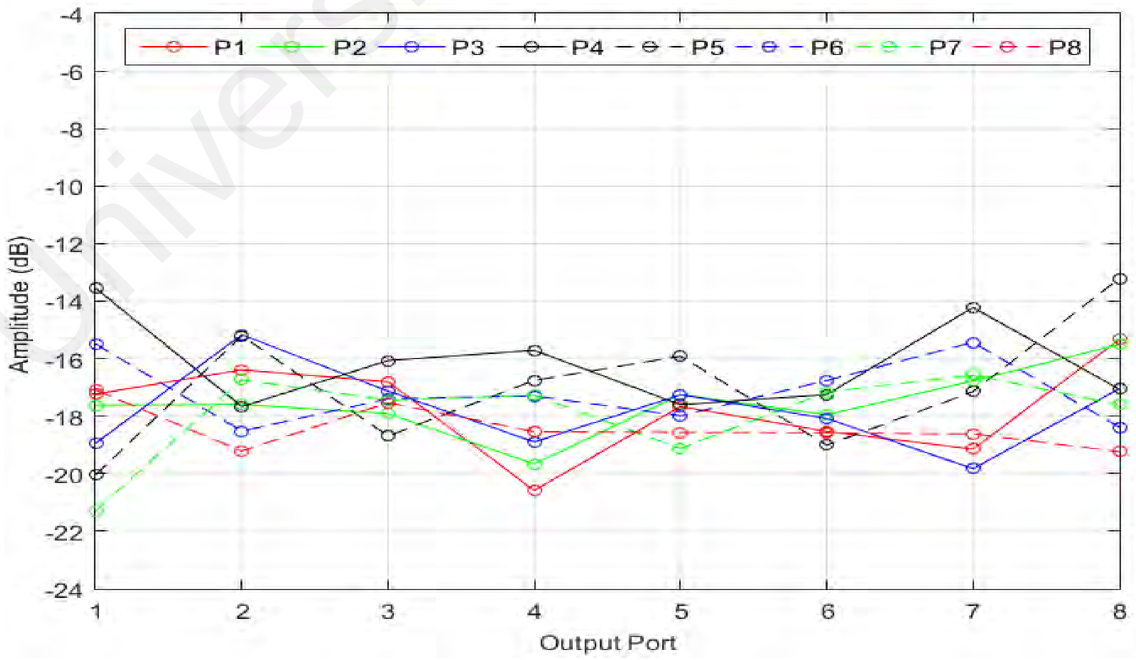

Figure 4.39: Measured transmission amplitudes at the output ports of the 8 × 8 Butler matrix at 28 GHz

4.4.3 Transmission Phase

The simulated and measured output phases for the input ports of the 8 × 8 Butler matrix at 28 GHz are shown in Figure 4.40. The phase differences for the input ports of P1, P2, P3, P4, P5, P6, P7, and P8 of the 8 × 8 Butler matrix were −22.5°, 157.5°, −112.5°, 67.5°, −67.5°, 112.5°, −157.5°, and 22.5°, respectively. Based on Figure 4.40, the simulated and measured output phases of the 8 × 8 Butler matrix showed linear characteristics. The simulated and measured output phases were validated via comparison with the ideal output phases of the 8 × 8 Butler matrix, as presented in Figure 4.2. A good agreement was achieved between the measured and simulated output phases with an average phase error of ± 10° due to the fabrication tolerance. Slight extended lengths of the microstrip transmission line in the fabricated 8 × 8 Butler matrix could cause losses, as explained in Section 4.2.2. Besides, the variations in the substrate properties and effects of the coaxial connectors due to soldering might induce additional losses.

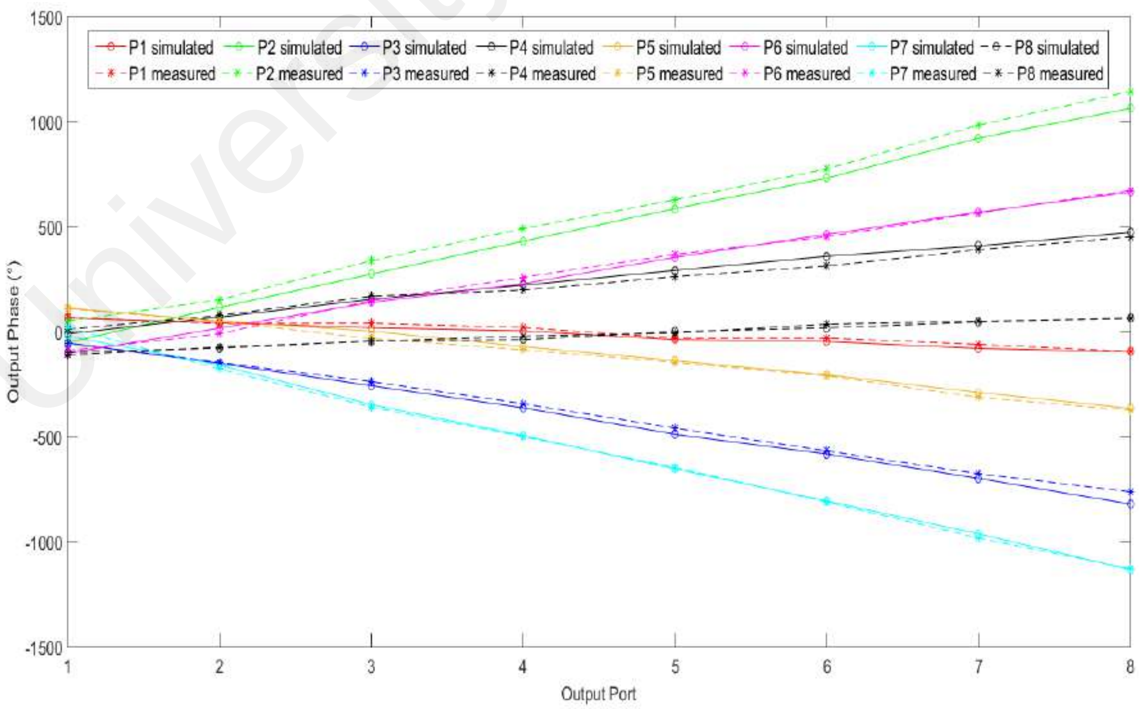

Figure 4.40: Simulated and measured output phases for the input ports of the 8 × 8 Butler matrix at 28 GHz

4.5 Summary

This chapter presents the design of a single-layer 8 × 8 Butler matrix at 28 GHz. The Butler matrix consisted of sixteen crossovers, twelve quadrature hybrids, and eight phase shifters. The circuit elements were designed using CST Microwave Studio with highly accurate dimensions. Moreover, the optimum designs of the circuit elements are demonstrated in detail in this chapter. The electrical performances of the circuit elements were observed and analyzed. Based on the satisfactory results of the circuit elements, these circuit elements were integrated to form an 8 × 8 Butler matrix. The designed 8 × 8 Butler matrix was fabricated using a substrate material named NPC-F220A. The structure of the Butler matrix was compact with a dimension of 88 × 110 × 0.253 mm^3. In addition, measurements were conducted and the performance of the Butler matrix was observed and analyzed. The return losses of the Butler matrix were less than −10 dB from 27 GHz to 29 GHz. Meanwhile, the isolations of the Butler matrix were less than −15 dB at 28 GHz. Besides that, the average values of insertion loss and phase error of the Butler matrix at 28 GHz were ± 2 dB and ± 10°, respectively. A good agreement between the measured and simulated results was obtained in this research. Table 4.11 summarizes the comparison between the proposed 8 × 8 Butler matrix with previous works reported in the literature. Compared with the previous works, the insertion loss obtained in this study is almost the same. It is not difficult to achieve a low insertion loss at lower frequencies of 1.9 GHz and 4.3 GHz, as reported by Adamidis, Vardiambasis, Ioannidou, and Kapetanakis (2019) and Zhong et al. (2017), respectively because the wavelength is larger. Besides that, Zhai et al. (2014) reported an 8 × 8 Butler matrix based on a dual-layer structure and the layers were connected via through-holes. The 8 × 8 Butler matrix obtained a simulated insertion loss of ± 2 dB at 29.5 GHz. However, the overall losses of the fabricated board are not clarified. In this thesis, the proposed 8 × 8 Butler matrix is a single-layer structure using printed circuit board technology, which is simple to design, more cost-effective and easy to fabricate. Additionally, the proposed structure is compact and it can be used to feed a multibeam array antenna for a spaced-constrained base station. Furthermore, it can be clearly observed that the proposed 8 × 8 Butler matrix yielded the least phase error of ± 10°, as shown in Table 4.11. The next chapter will present the design of a multibeam array antenna fed by the 8 × 8 Butler matrix.

Table 4.11: A comparison between the designed 8 × 8 Butler matrix and previous works

Authors	Technology	Number of layer	Frequency (GHz)	Circuit size (mm^2)	Insertion Loss	Phase error
Adamidis et al. (2019)	Printed circuit board	1	1.9	250 × 220	1.5 dB	± 12°
Zhong et al. (2017)	Printed circuit board	2	4.3	155 × 155	2.5 dB	± 15°
Zhai et al. (2014)	Substrate integrated waveguide	2	29.5	103 × 41	* 2 dB	* 15°
This work	Printed circuit board	1	28	110 × 88	± 2 dB	± 10°

*Simulation results

CHAPTER 5: DESIGN OF A MULTIBEAM ARRAY ANTENNA

5.1 Introduction

This chapter presents the design of a multibeam array antenna for base station in the fifth-generation mobile communication system. Firstly, a single-element microstrip antenna was designed and optimized using three-dimensional electromagnetic simulation software. The performance of the single-element microstrip antenna was observed and analyzed. Then, the design of the multibeam array antenna was fed by an 8×8 Butler matrix, which had been designed in Chapter 4. The microstrip antenna was integrated at the output ports of the 8×8 Butler matrix. To investigate the beam coverage in the vertical plane, the antenna spacing of the multibeam array antenna was varied. The best antenna spacing for the beam coverage was identified. Furthermore, the performance of the multibeam array antenna was observed and analyzed. The designed multibeam array antenna was fabricated via a photo etching process. Measurements were conducted to ensure the actual performance of the fabricated multibeam array antenna. The simulation and measurement results of the multibeam array antenna were analyzed and discussed.

5.2 Design of a Single-element Microstrip Antenna

The microstrip antenna was designed at 28 GHz using a substrate material named NPC-F220A from Nippon Pillar Packaging Co. Ltd, which is the same substrate material used to design an 8×8 Butler matrix, as mentioned in Chapter 4. Figure 5.1 illustrates the geometry of the microstrip antenna. This antenna is fed by a 50 Ω microstrip transmission line via a quarter wave transformer. The purpose of using a quarter wave transformer is to provide a good impedance matching between the microstrip transmission line and the microstrip antenna.

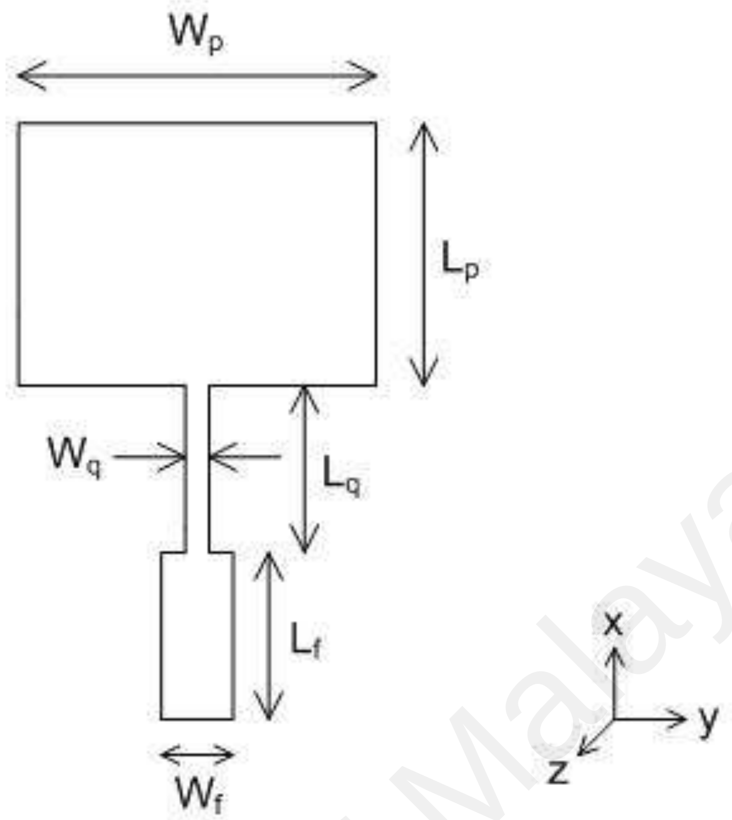

Figure 5.1: Geometry of the microstrip antenna

The dimensions of the microstrip antenna were determined using the fundamental microstrip antenna design equations, as presented in Section 2.8. The width of the 50 Ω microstrip transmission line was calculated using mathematical equations as expressed in Equation (4.1) to Equation (4.3). Meanwhile, the length of the 50 Ω microstrip transmission line was obtained using Equation (4.4) and Equation (4.5). The calculated parameters of the microstrip antenna are listed in Table 5.1.

Table 5.1: Calculated parameters for the microstrip antenna

Parameter	Value
Width of patch, W_p	4.2352 mm
Effective dielectric constant, ε_{reff}	2.0575
Extended length, ΔL_p	0.1329 mm
Actual length of patch, L_p	3.4689 mm
Effective length, L_{eff}	3.7347 mm
Width of 50 Ω microstrip transmission line, W_f	0.7826 mm
Length of 50 Ω microstrip transmission line, L_f	1.9581 mm

The impedance of the quarter wave transformer is determined using Equation (5.1) (David M. Pozar, 2005):

$$Z_q = \sqrt{Z_a Z_f} \tag{5.1}$$

where Z_q is the impedance of the quarter wave transformer, Z_a is the input impedance at the center of the microstrip antenna, and Z_f is the impedance of the microstrip transmission line. The input impedance at the center of the microstrip antenna should be determined from the simulation to obtain an accurate impedance of the quarter wave transformer. This step is very important, especially at high frequency to reduce the impedance mismatch between the quarter wave transformer and the microstrip antenna. Figure 5.2 presents the simulated input impedance at the center of the microstrip antenna.

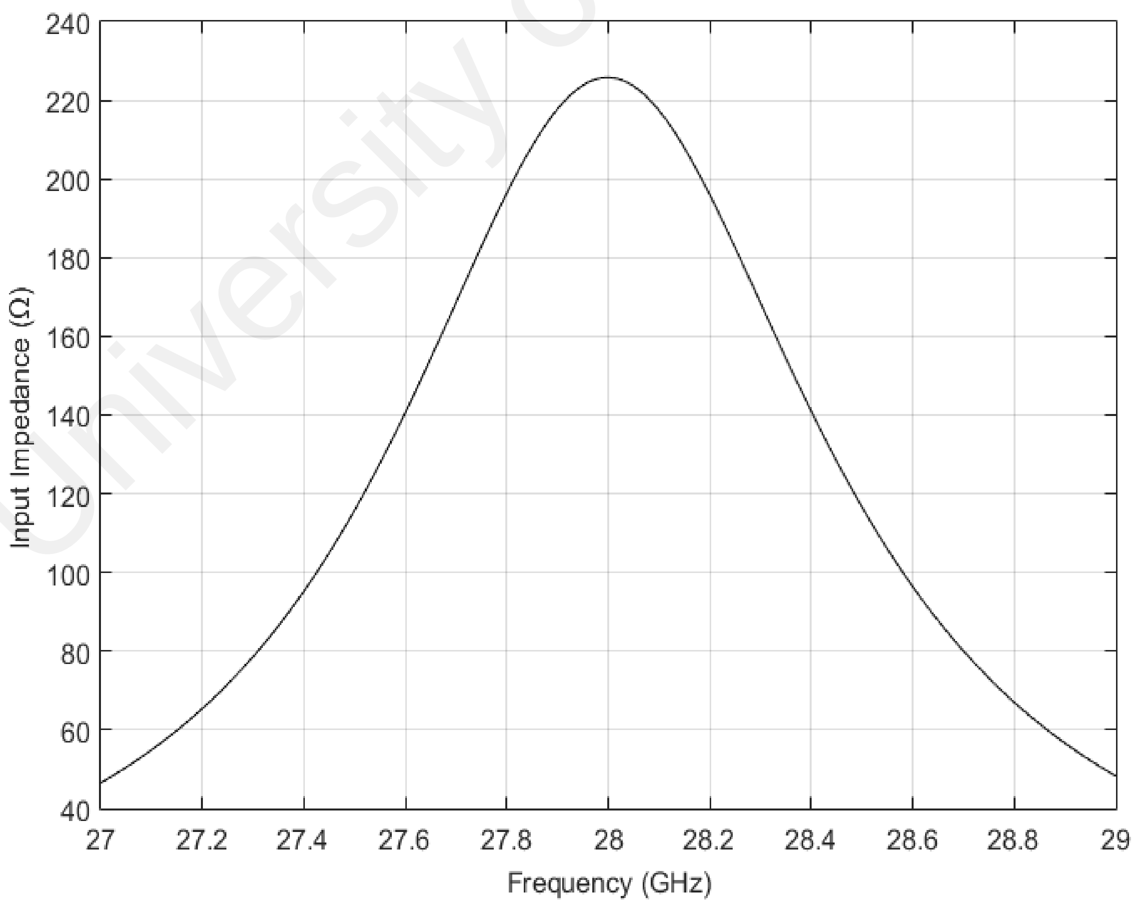

Figure 5.2: Input impedance of the microstrip patch edge, Z_a

Based on Figure 5.2, the simulated input impedance, Z_a had a maximum value of 225.79 Ω at 28 GHz. Using the Equation (5.1), the impedance of the microstrip transmission line was 50 Ω and therefore, the calculated impedance of the quarter wave transformer was 106.25 Ω. The width of the quarter wave transformer, W_q was determined using mathematical equations as expressed in Equation (4.1) to Equation (4.3). Meanwhile, the length of the quarter wave transformer, L_q was calculated using Equation (4.4) and Equation (4.5). Table 5.2 lists the parameters of the microstrip antenna and the quarter wave transformer.

Table 5.2: Parameters of the microstrip antenna and the quadrature wave transformer

Parameter	Value
Z_a	225.79 Ω
Z_f	50 Ω
Z_q	106.25 Ω
L_q	2.0251 mm
W_q	0.1984 mm

The parameters as listed in Table 5.1 and Table 5.2 were used to design the microstrip antenna in Computer Simulation Technology (CST) Microwave Studio. The microstrip antenna was simulated and optimized to obtain the optimum results. Table 5.3 lists the optimized parameters and the characteristics of the microstrip antenna. The simulated return loss of the microstrip antenna is illustrated in Figure 5.3. It can be observed that the return loss of the microstrip antenna was less than −10 dB between 27.65 GHz and 28.37 GHz. Meanwhile, the radiation patterns of the microstrip antenna at 28 GHz for Phi = 0° and Phi = 90° are presented in Figure 5.4(a) and (b), respectively. Based on Figure 5.4, the radiation patterns of the microstrip antenna showed a good symmetry at the boresight with an antenna gain of 7 dBi.

Table 5.3: Optimized parameters and the characteristics of the microstrip antenna

Structure	Parameter	Value (mm)	Characteristic
Patch	L_p	3.2529	Gain, G_p = 7 dBi
	W_p	4.2352	
Quarter wave transformer	L_q	2.0251	Z_q = 106 Ω
	W_q	0.1984	
Microstrip feed line	L_f	1.9581	Z_f = 50 Ω
	W_f	0.7826	

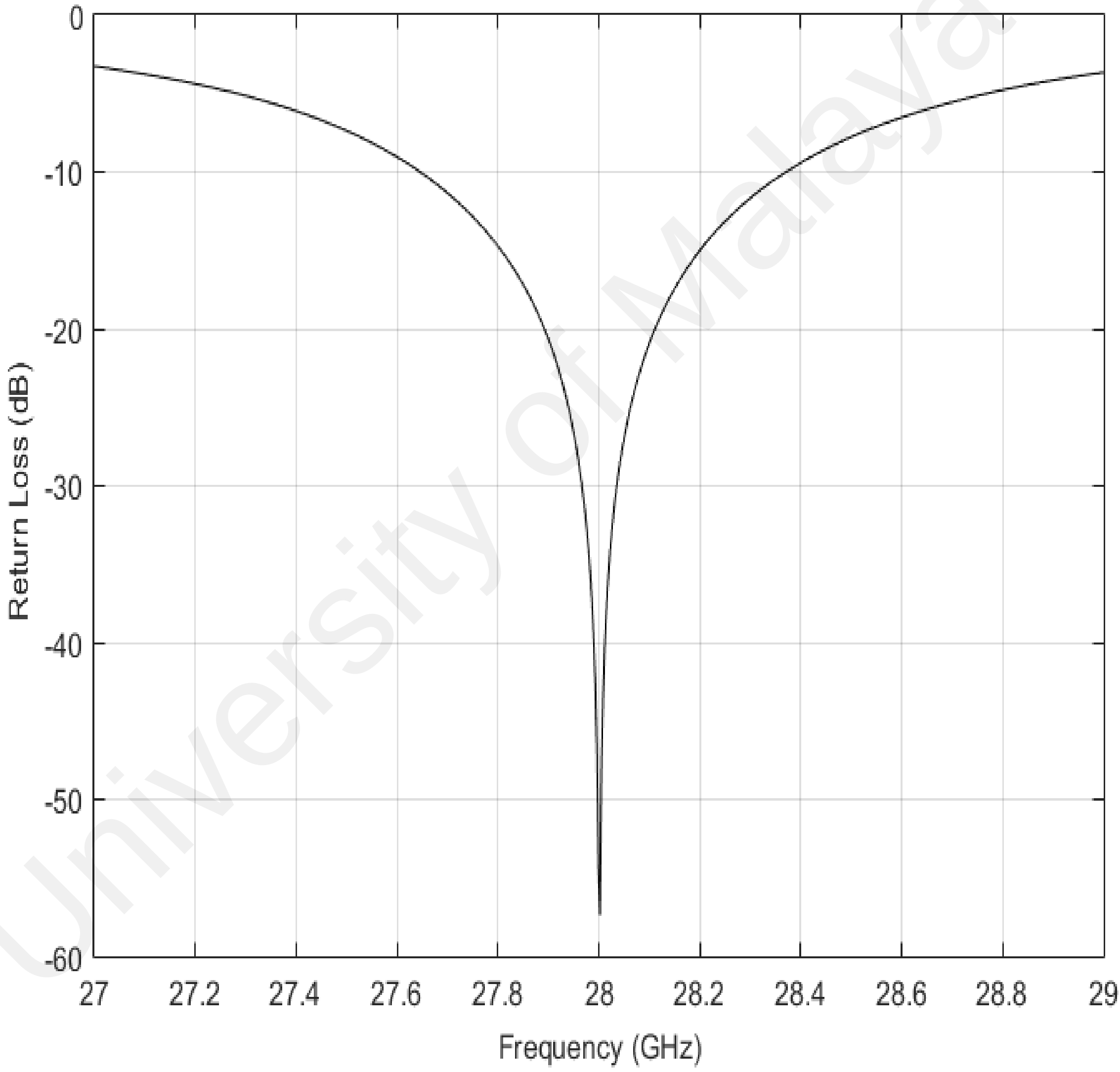

Figure 5.3: Simulated return loss of the microstrip antenna

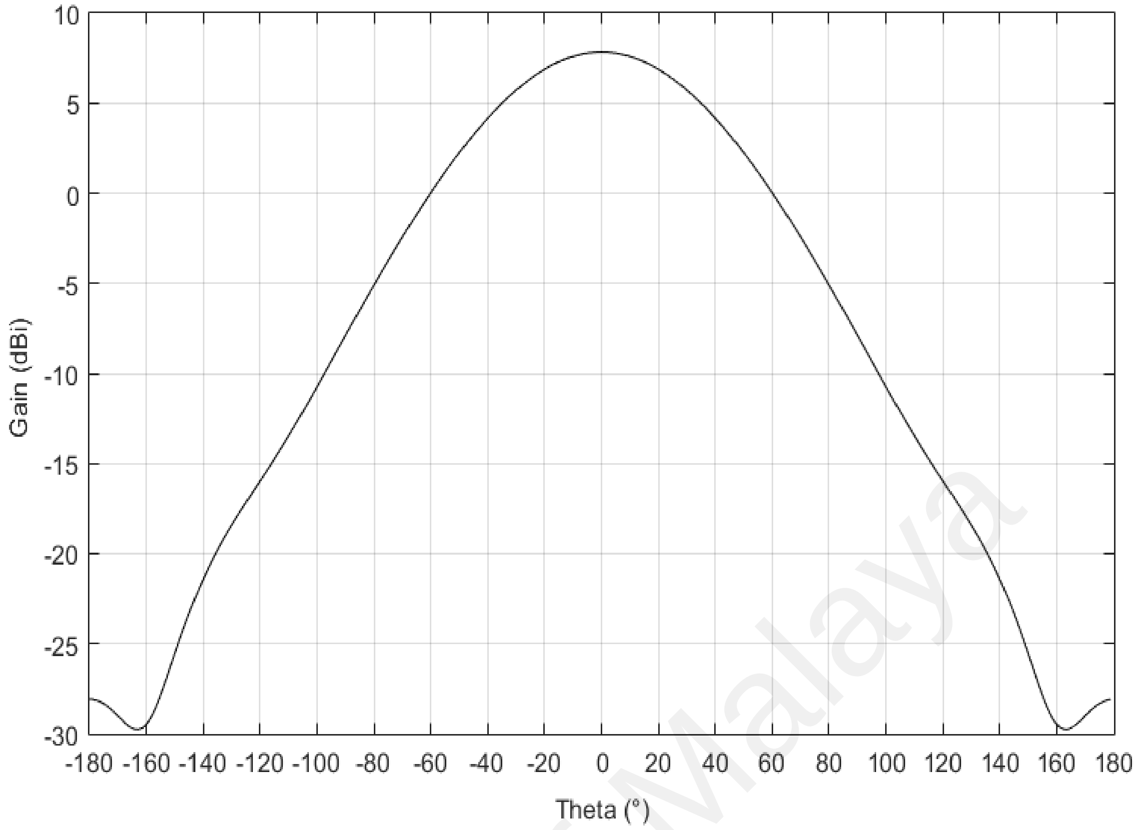

(a)

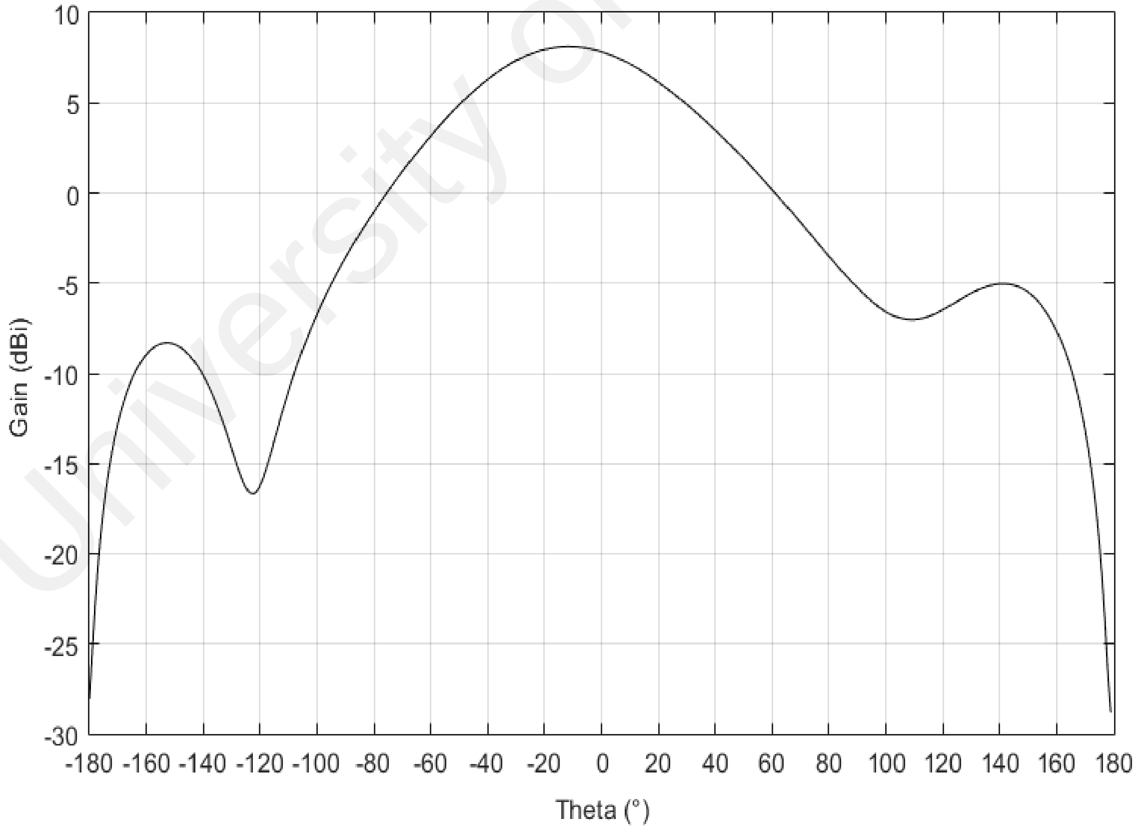

(b)

Figure 5.4: Simulated radiation patterns of the microstrip antenna at 28 GHz for (a) Phi = 0° and (b) Phi = 90°

5.3 Design of a Multibeam Array Antenna

This section presents a detailed design of a multibeam array antenna fed by an 8 × 8 Butler matrix. Furthermore, the beam coverages in the vertical plane were evaluated using mathematical equation by varying the antenna spacing of the multibeam array antenna. Electromagnetic simulation was performed for the multibeam array antenna with different antenna spacing to validate the theoretical results. The radiation patterns of the multibeam array antenna were observed and analyzed.

5.3.1 Design Concept

The multibeam array antenna fed by an 8 × 8 Butler matrix was designed and operated at 28 GHz. Figure 5.5 illustrates the configuration of the multibeam array antenna in which, the microstrip antenna that had been designed in Section 5.2 was integrated at the output ports, O1 to O8 of the 8 × 8 Butler matrix. Eight antenna elements were required for the multibeam array antenna.

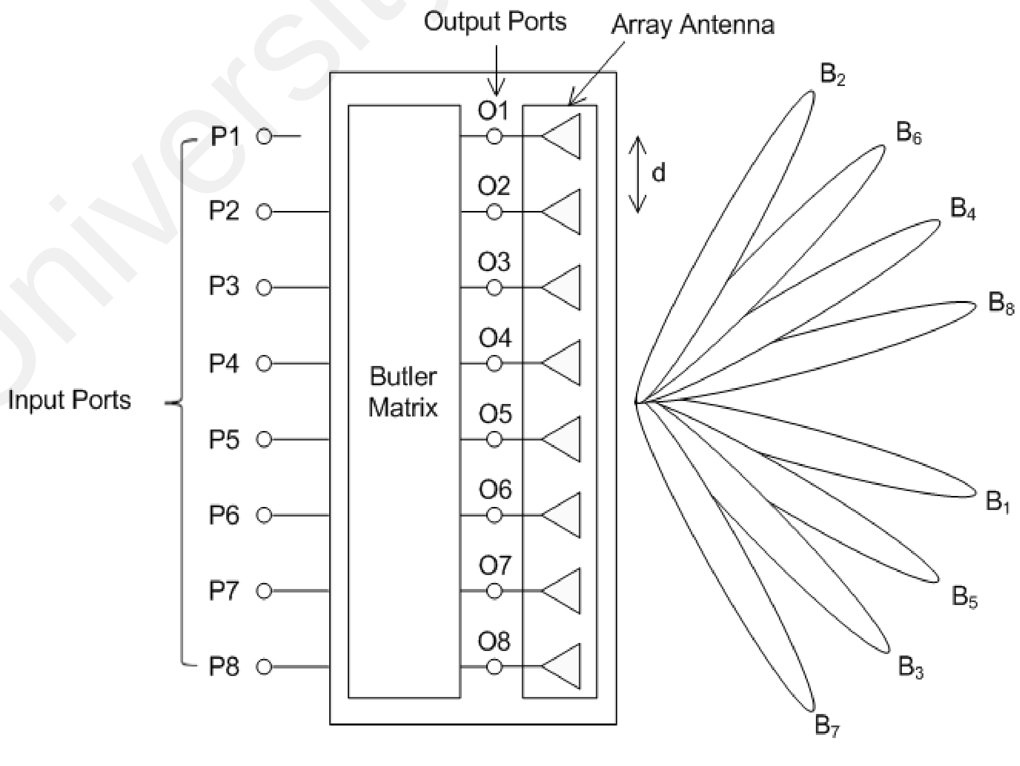

Figure 5.5: Configuration of the multibeam array antenna

The proposed multibeam array antenna produced eight beams (B_i) at eight different directions when the input ports were fed, as shown in the Figure 5.5. The main beam angles can be expressed, as shown in Equation (5.2) (Néron & Delisle, 2005):

$$sin\,\theta_p = \pm\frac{\lambda}{d}\frac{\phi_p}{360°} \tag{5.2}$$

where λ is the wavelength, ϕ_p is the phase difference between the output ports of the Butler matrix, and d is the antenna spacing. Table 5.4 lists the design specifications of the multibeam array antenna.

Table 5.4: Design specifications of the multibeam array antenna

Parameter	Value
Frequency	28 GHz
S_{11}	≤ -10 dB
Antenna gain	> 8 dBi
Beam coverage in the vertical plane	> 60°
Beamforming circuit	Butler matrix
Number of antenna elements	8

5.3.2 Beam Coverage

As referred to Equation (5.2), the main beam angle corresponds to the antenna spacing. Therefore, the effect of the multibeam array antenna with different antenna spacing was analyzed to control the beam coverage in the vertical plane. It is very important to ensure mobile users receive the good signal quality. The beam coverage of the multibeam array antenna with antenna spacing of 0.6λ to 0.8λ were observed and evaluated in this research, as there is an effect of mutual coupling between the antenna elements when the antenna spacing is less than 0.5λ. This mutual coupling effect can cause inaccurate beam directions and deform the radiation patterns. The main beam angles for phase differences between the output ports of the 8 × 8 Butler matrix with antenna spacing of 0.6λ to 0.8λ were calculated using Equation (5.2) and listed in Table

5.5. As shown in Table 5.5, the multibeam array antenna with an antenna spacing of 0.6λ steered the main beams from -47° to 47°. Meanwhile, the multibeam array antenna with an antenna spacing of 0.7λ steered the main beams from -39° to 39°. For the multibeam array antenna with an antenna spacing of 0.8λ, the main beams steered from -33° to 33°. Hence, the beam coverages in the vertical plane for the multibeam array antenna with antenna spacing of 0.6λ, 0.7λ, and 0.8λ were 94°, 78°, and 66°, respectively. It can be concluded that the beam coverage was reduced when the antenna spacing of the multibeam array antenna was increased.

Table 5.5: Calculated main beam angles, θ_p for phase differences between the output ports of the 8 × 8 Butler matrix, ϕ_p with antenna spacing, d

Beam number, B_n	ϕ_p	θ_p		
		d = 0.6λ	d = 0.7λ	d = 0.8λ
1	-22.5°	6°	5°	4°
2	157.5°	-47°	-39°	-33°
3	-112.5°	31°	27°	23°
4	67.5°	-18°	-16°	-14°
5	-67.5°	18°	16°	14°
6	112.5°	-31°	-27°	-23°
7	-157.5°	47°	39°	33°
8	22.5°	-6°	-5°	-4°
Beam coverage		94°	78°	66°

5.3.3 Electromagnetic Simulations

The structure of the multibeam array antenna with antenna spacing, d is presented in Figure 5.6. The multibeam array antenna was fed by an 8 × 8 Butler matrix and each output port of the 8 × 8 Butler matrix was designed with the same spacing as the spacing of the antenna elements. The multibeam array antennas with antenna spacing of 0.6λ to 0.8λ were simulated and optimized using CST Microwave Studio. The simulated radiation patterns for the multibeam array antennas with antenna spacing of 0.6λ to 0.8λ are presented in Figure 5.7 to Figure 5.9, respectively. The simulated main beam angles of the multibeam array antennas for antenna spacing of 0.6λ to 0.8λ are listed in Table

5.6. The radiation patterns of the beams, B_2, B_4, B_6, and B_8 were similar with respect to the radiation patterns of the beams, B_7, B_5, B_3, and B_1 but the polarities were opposites due to the symmetrical structure of the 8 × 8 Butler matrix. Therefore, the radiation patterns of these beams were not presented in this thesis.

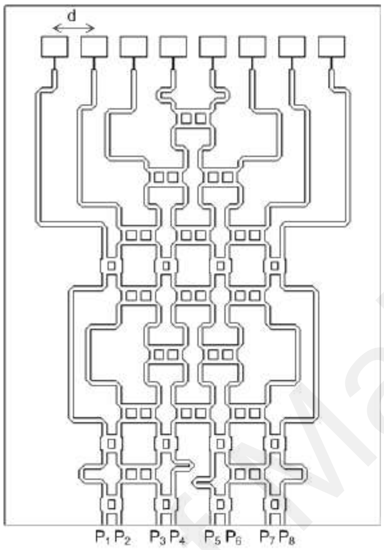

Figure 5.6: Structure of the multibeam array antenna with antenna spacing, *d*

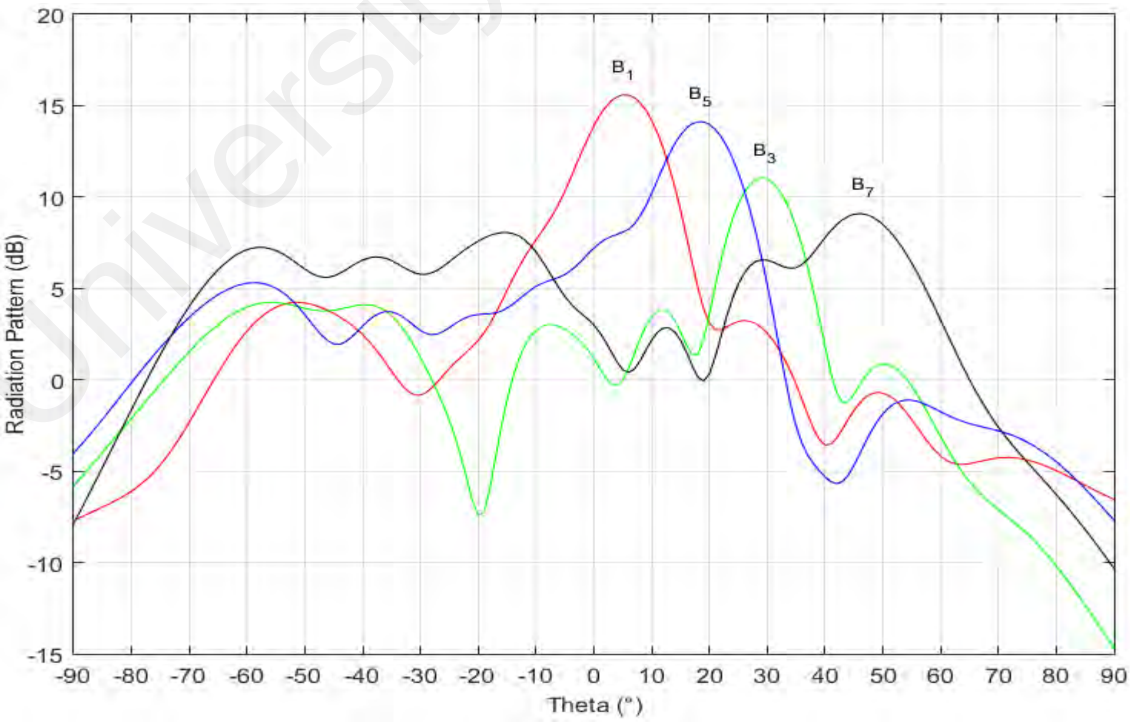

Figure 5.7: Simulated radiation patterns of the multibeam array antenna for beams, B_1, B_3, B_5, and B_7 with $d = 0.6\lambda$

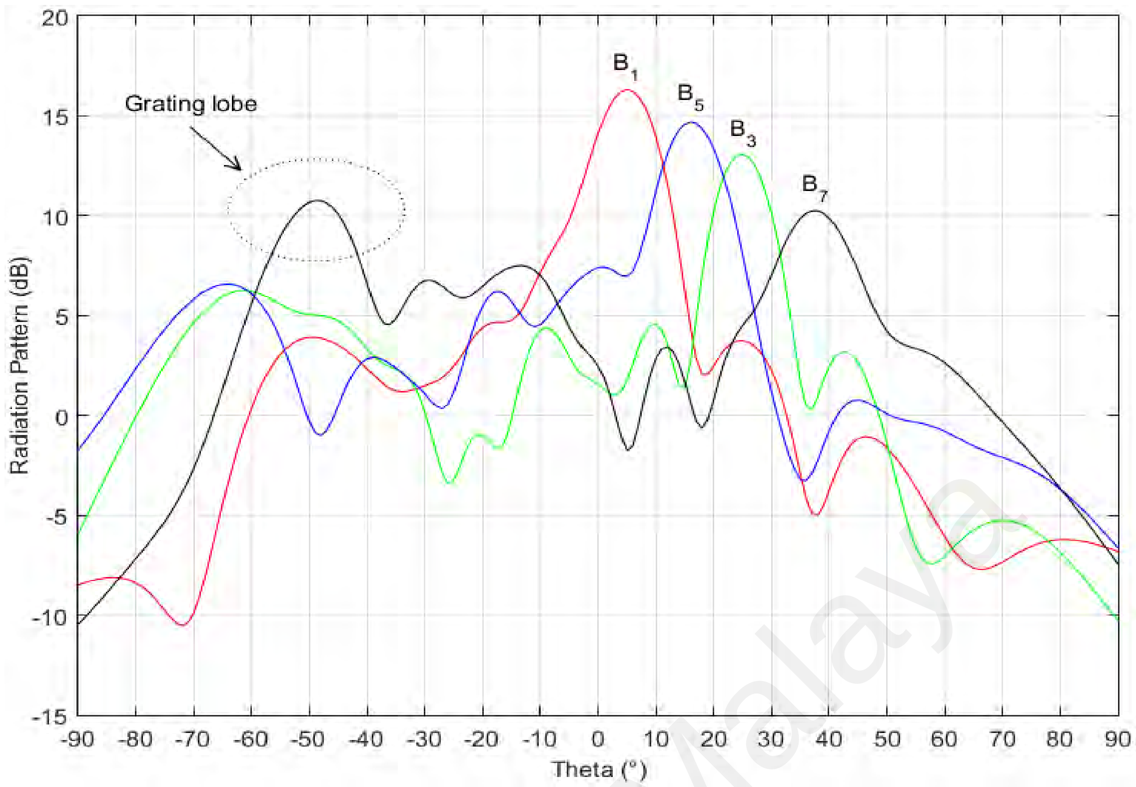

Figure 5.8: Simulated radiation patterns of the multibeam array antenna for beams, B_1, B_3, B_5, and B_7 with $d = 0.7\lambda$

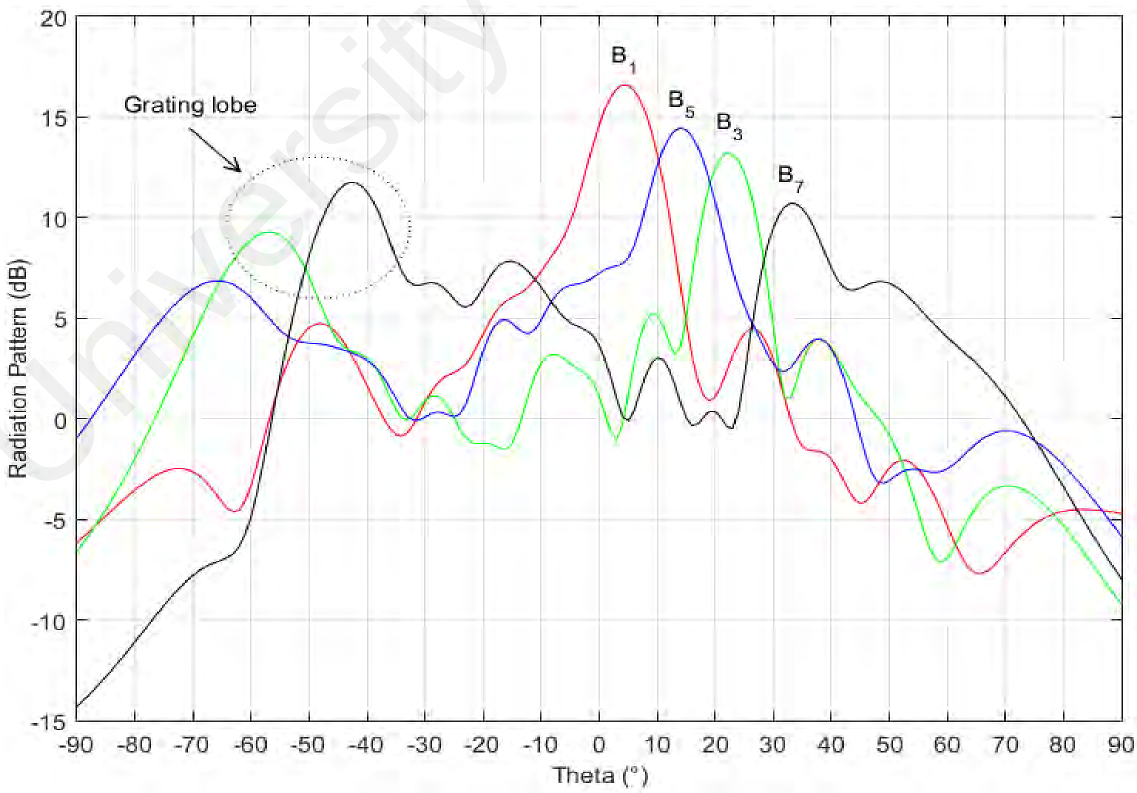

Figure 5.9: Simulated radiation patterns of the multibeam array antenna for beams, B_1, B_3, B_5, and B_7 with $d = 0.8\lambda$

Table 5.6: Simulated main beam angles of the multibeam array antenna with different antenna spacing, *d*

Beam number, B_n	Beam angle		
	d = 0.6λ	d = 0.7λ	d = 0.8λ
B_1	6°	5°	4°
B_3	31°	26°	23°
B_5	18°	15°	13°
B_7	45°	38°	33°

As shown in Figure 5.7 to Figure 5.9 and Table 5.6, the radiation patterns show that the beam coverage was reduced when the spacing of antenna was increased from 0.6λ to 0.8λ, which corresponded to the calculated values as listed in Table 5.5. However, the appearance of the grating lobe was observed at −49° for the multibeam array antenna with an antenna spacing of 0.7λ, as presented in Figure 5.8. For the multibeam array antenna with an antenna spacing of 0.8λ, the grating lobes were observed at −43° and −57°, as illustrated in Figure 5.9. These grating lobes can cause interference to the nearby base stations. The grating lobe angle can be calculated using Equation (5.3) and listed in Table 5.7:

$$\frac{\phi_p}{360°} - \frac{d}{\lambda}\sin\theta_G = 1 \tag{5.3}$$

Table 5.7: Grating lobe angles of the multibeam array antenna for different antenna spacing, *d*

B_p	d = 0.6λ		d = 0.7λ		d = 0.8λ	
	Equation (5.3)	CST	Equation (5.3)	CST	Equation (5.3)	CST
B_3	-	-	-	-	-59°	-57°
B_7	-	-	-53°	-49°	-45°	-43°

The simulated antenna gains of the multibeam array antennas for beams, B_1, B_3, B_5 and B_7 with antenna spacing of 0.6λ to 0.8λ are shown in Figure 5.10. The antenna gains were between 9 dBi and 17 dBi. It can be noticed that the appearance of the grating lobes could reduce the antenna gains at beams, B_3 and B_7. Furthermore, the deviations of transmission amplitude and phase in the 8 × 8 Butler matrix, as explained in Section 4.4.2 and Section 4.4.3 could also reduce the antenna gains.

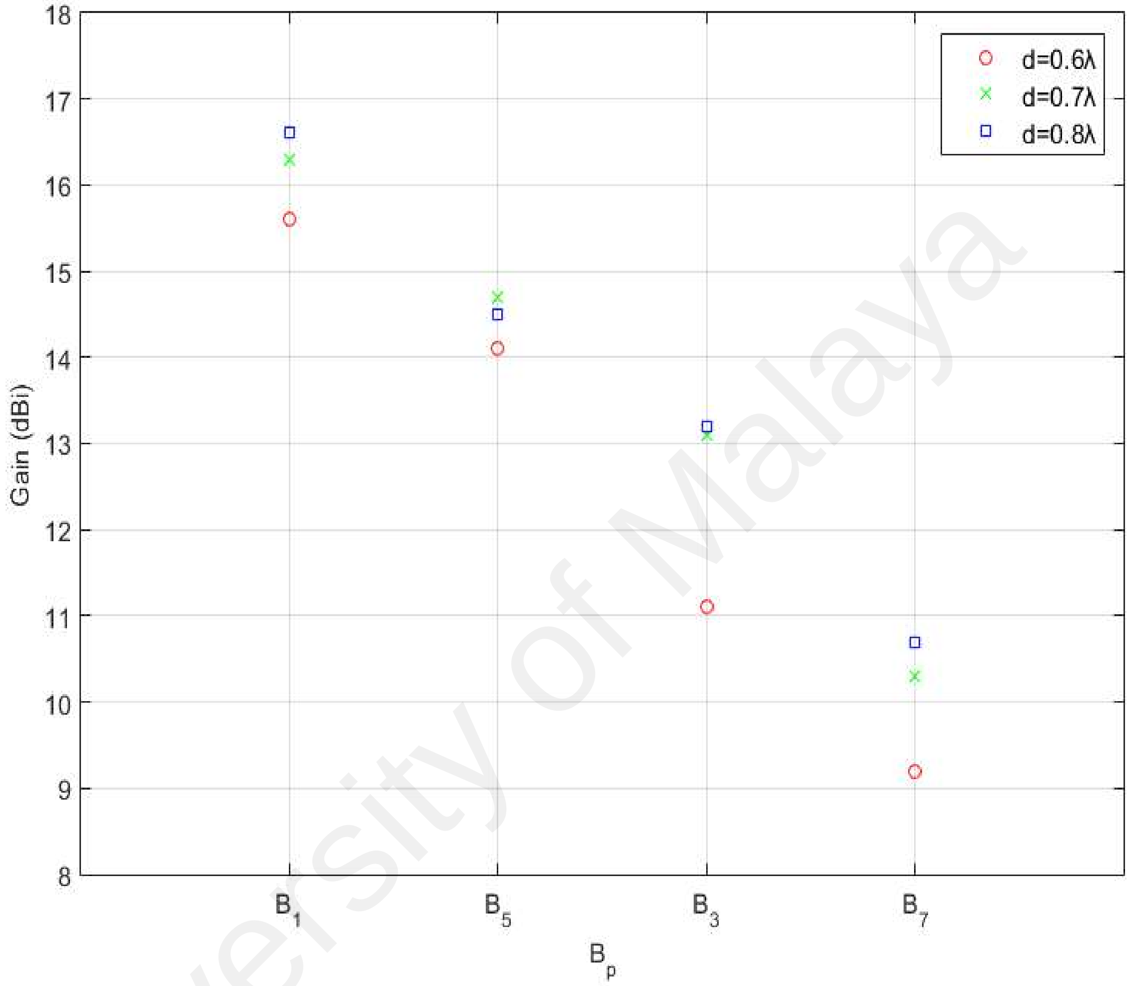

Figure 5.10: Simulated antenna gains of multibeam array antenna for antenna spacing of 0.6λ, 0.7λ, and 0.8λ

To avoid the appearances of the grating lobes, the design of the multibeam array antenna with an antenna spacing of 0.6λ was selected for fabrication. Figure 5.11 illustrates the complete structure of the multibeam array antenna, where extended lines were designed at the input ports of the multibeam array antenna to allow the implementation of coaxial connectors for measurement purposes. This structure was simulated and optimized using CST Microwave Studio.

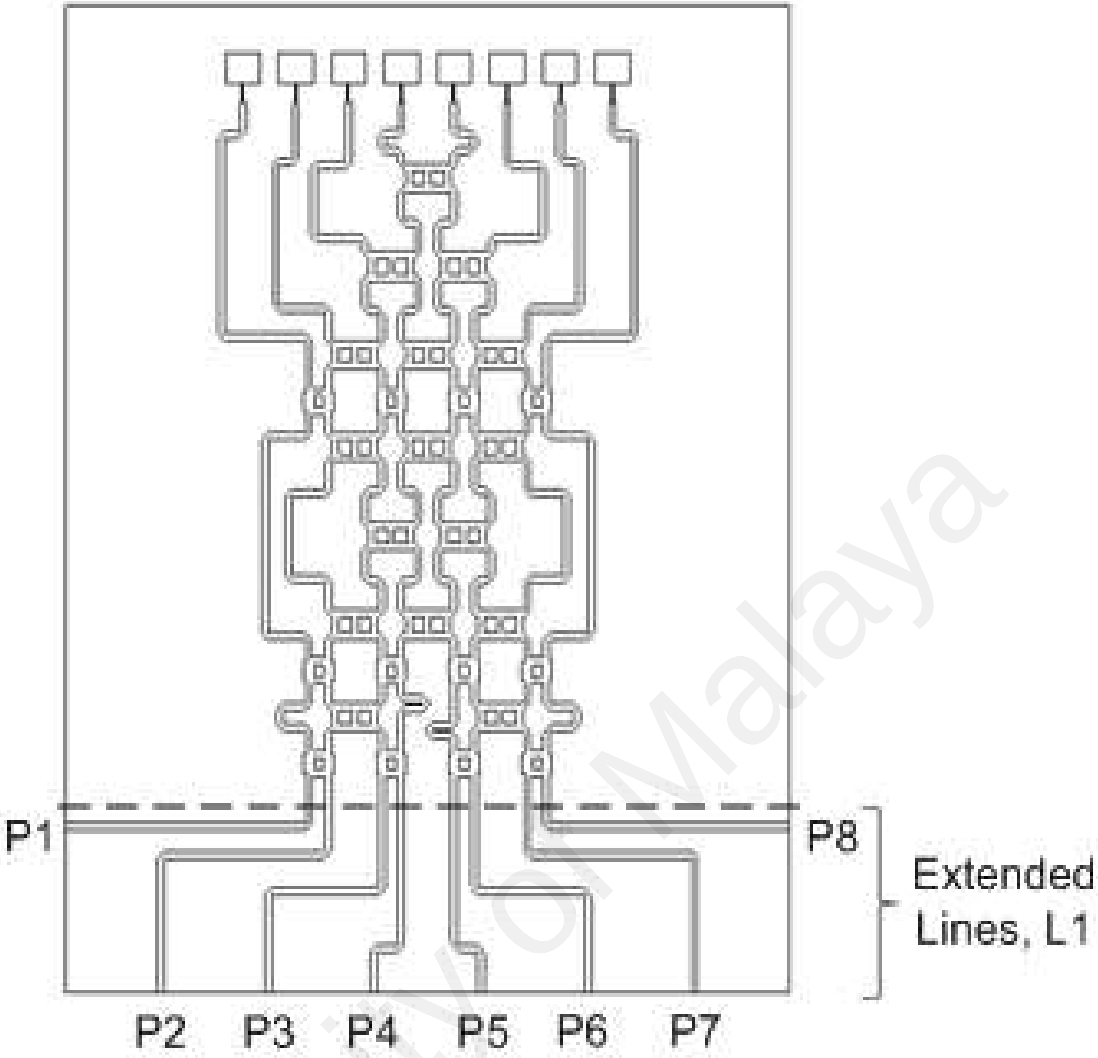

Figure 5.11: Structure of the multibeam array antenna with extended lines at the input ports

5.4 Fabrication and Measurement

Figure 5.12 shows a photograph of the fabricated multibeam array antenna. The 2.92 mm coaxial connectors were soldered at the input ports of the multibeam array antenna. The dimension of the fabricated multibeam array antenna was 88 mm × 106 mm. To validate the simulation results, the return losses of the fabricated multibeam array antenna were measured using a vector network analyzer (Keysight N5224A) and the radiation characteristics were performed in an anechoic chamber.

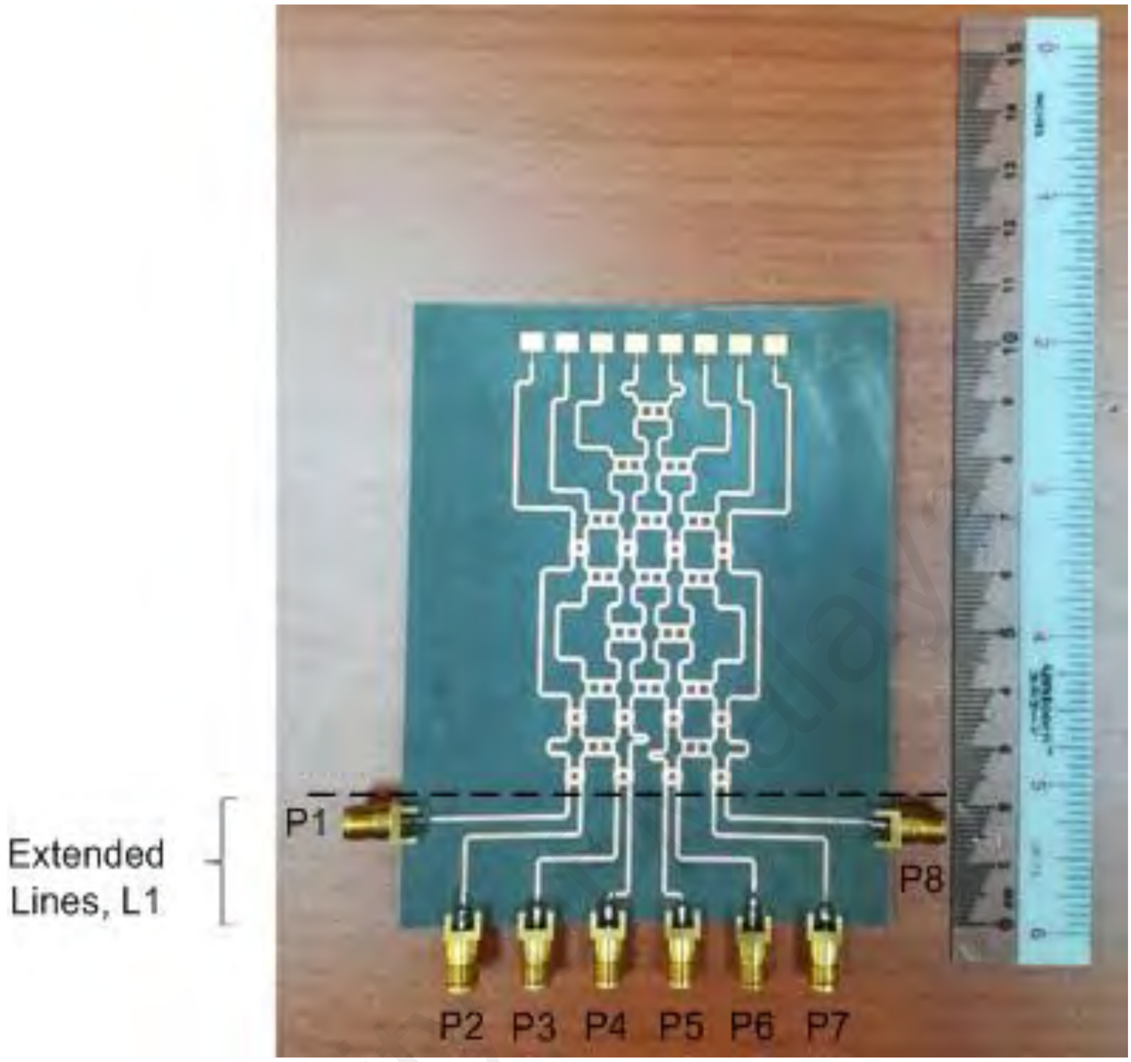

Figure 5.12: Photograph of the fabricated board

5.5 Results and Discussion

The following subsections discuss the simulation and measurement results of the multibeam array antenna such as return loss and radiation characteristics.

5.5.1 Return Loss

Figure 5.13 and Figure 5.14 show the simulated and measured return losses at the input ports of the multibeam array antenna, respectively. As illustrated in Figure 5.13, the simulated return losses at the input ports of the multibeam array antenna at 28 GHz were −13.04 dB, −26.65 dB, −18.22, −14.23 dB, −31.02 dB, −13.66 dB, −27.34 dB, and −13.2 dB for S_{11}, S_{22}, S_{33}, S_{44}, S_{55}, S_{66}, S_{77}, and S_{88}, respectively. Meanwhile, the measured return losses at the input ports of the multibeam array antenna at 28 GHz were −12.98 dB, −15.32 dB, −12.05 dB, −22.93 dB, −12.28 dB, −11.89 dB, −11.67 dB, and −12.75 dB for S_{11}, S_{22}, S_{33}, S_{44}, S_{55}, S_{66}, S_{77}, and S_{88}, respectively, as shown in Figure 5.14. Additionally, both simulated and measured return losses at the input ports of the multibeam array antenna were less than −10 dB, in wide frequency range of 27 GHz to 29 GHz. However, it can be observed that the measured results were slightly different from the simulation results due to the fabrication tolerance. As explained in Section 4.2.2, slight extended lengths of the microstrip transmission line in the fabricated 8 × 8 Butler matrix could cause losses. Moreover, the variations in the substrate properties and the effect of the coaxial connectors due to soldering might also induce additional losses.

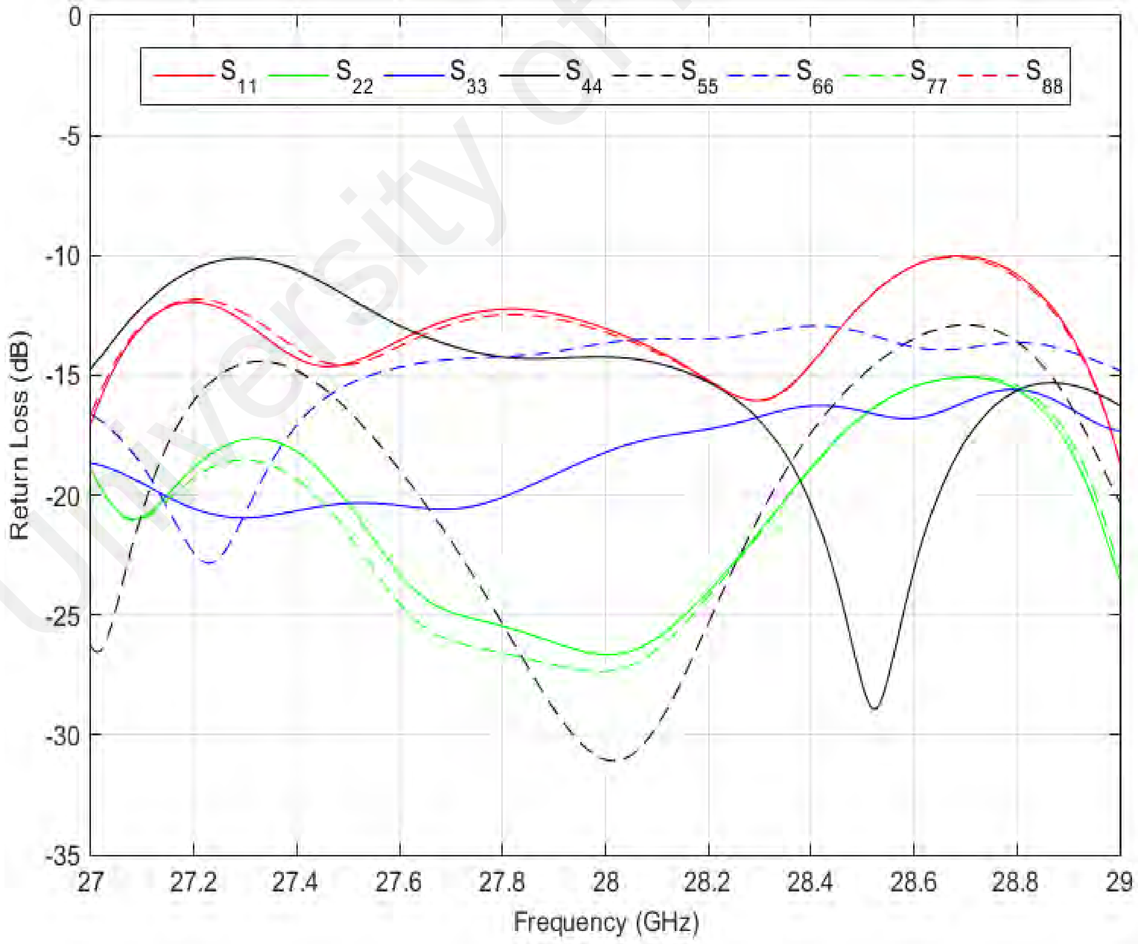

Figure 5.13: Simulated return losses at the input ports of the multibeam array antenna

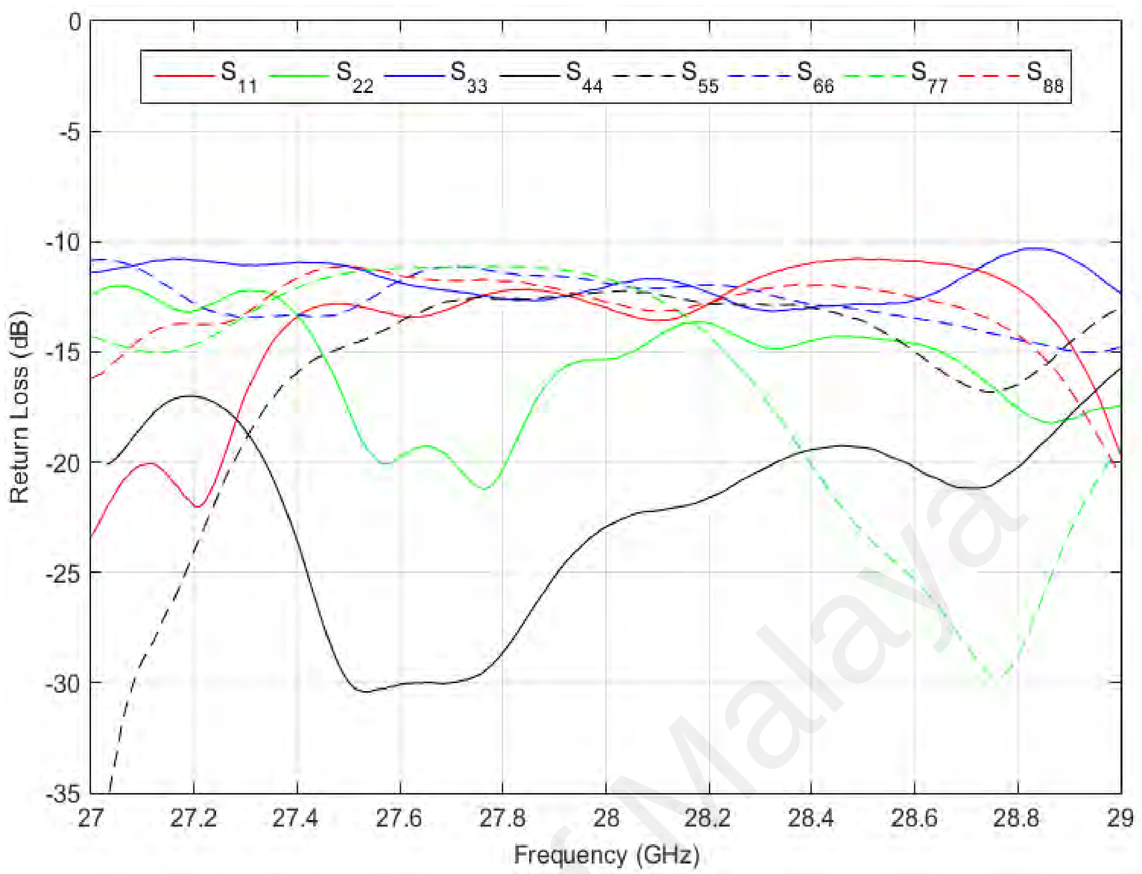

Figure 5.14: Measured return losses at the input ports of the multibeam array antenna

5.5.2 Radiation Characteristics

Figure 5.15 and Figure 5.16 present the simulated and measured radiation patterns for the input ports of the multibeam array antenna at 28 GHz, respectively. The simulated main beams were pointed at 5°, −46°, 29°, −19°, 19°, −29°, 46°, and −5° for the input ports, P1, P2, P3, P4, P5, P6, P7, and P8, respectively. Meanwhile, the measured main beams were pointed at 6°, −44°, 30°, −18°, 18°, −30°, 44°, and −6° for the input ports, P1, P2, P3, P4, P5, P6, P7, and P8, respectively. The simulated and measured main beam angles of the multibeam array antenna agreed very well with the theoretical values, as presented in Table 5.5. The simulated and measured beam coverages of the multibeam array antenna were 92° and 88°, respectively. In addition, the measured side lobe characteristics were in good agreement with the simulated results.

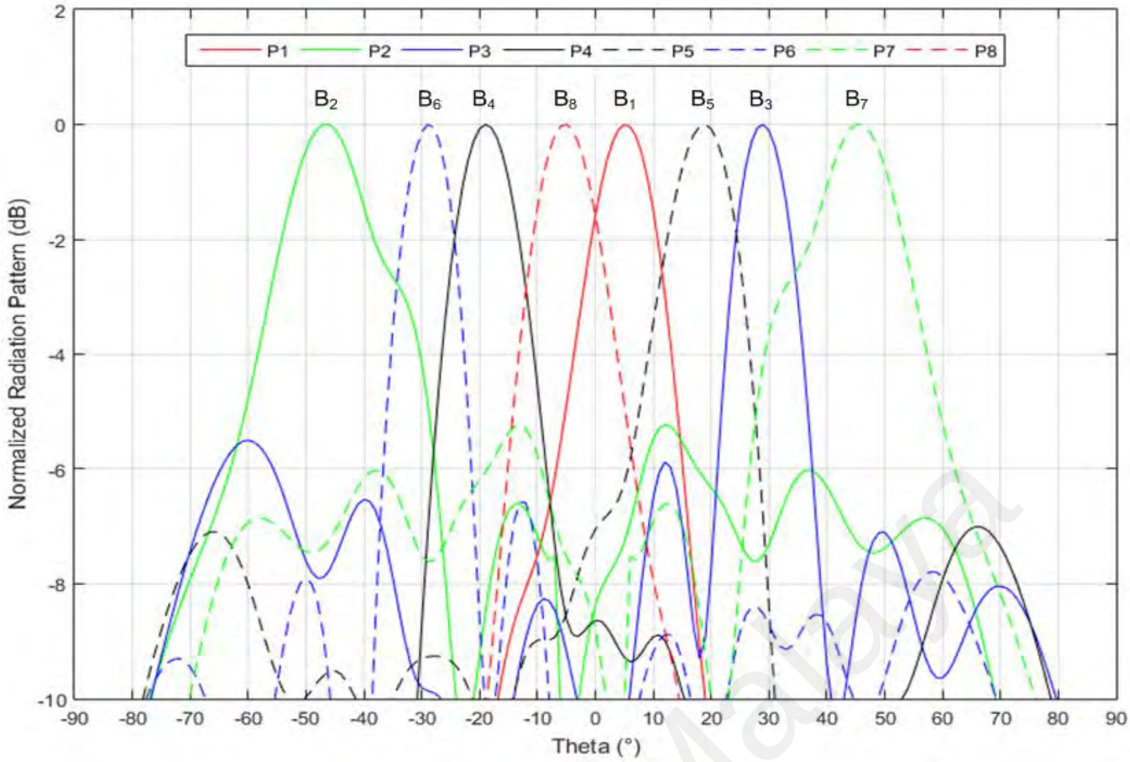

Figure 5.15: Simulated radiation patterns for the input ports of the multibeam array antenna at 28 GHz

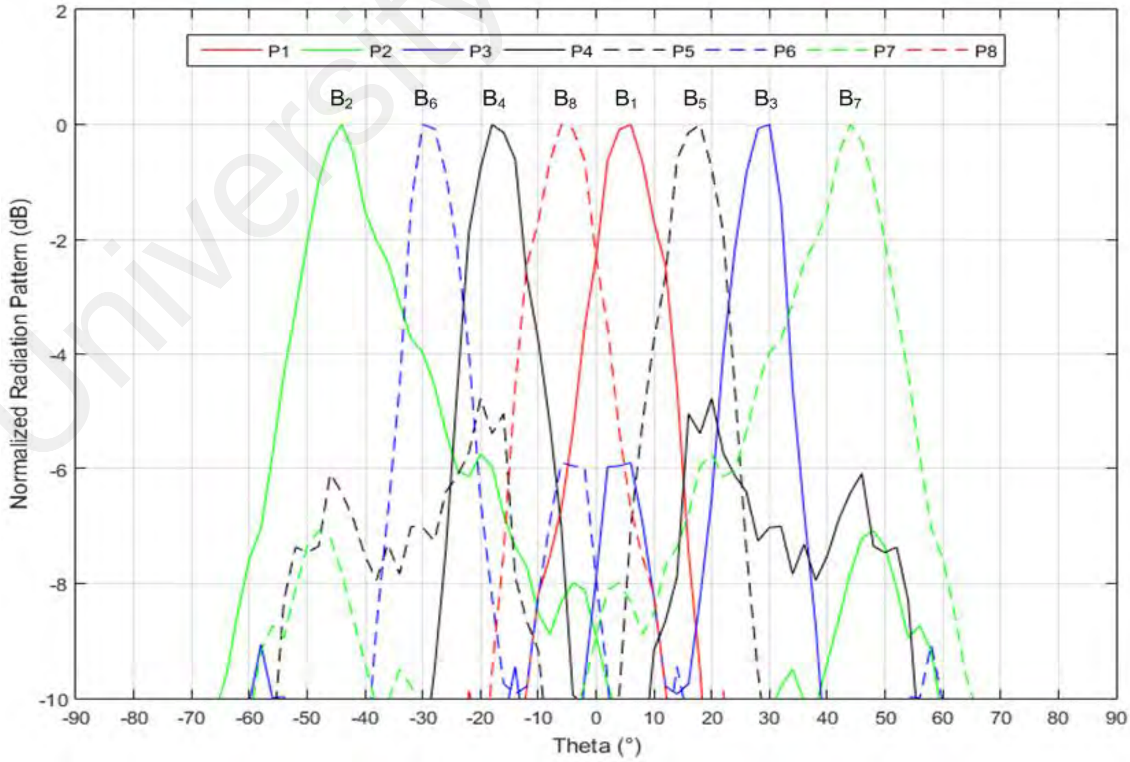

Figure 5.16: Measured radiation patterns for the input ports of the multibeam array antenna at 28 GHz

Figure 5.17 illustrates the simulated and measured antenna gains of the multibeam array antenna at 28 GHz for the beams, B_1 to B_8 and Table 5.8 lists the simulated and measured antenna gains of the multibeam array antenna at 28 GHz for the beams, B_1 to B_8. As presented in Figure 5.17 and Table 5.8, the simulated antenna gains of the multibeam array antenna at 28 GHz for the beams, B_1 to B_8 were between 9 dBi and 15 dBi. Meanwhile, the measured antenna gains of the multibeam array antenna at 28 GHz for the beams, B_1 to B_8 were between 9 dBi and 14 dBi. The differences between the simulated and measured antenna gains were around 1 dB. As explained in Section 4.4.2 and Section 4.4.3, the small deviation of transmission amplitude and phase in the 8 × 8 Butler matrix could reduce the antenna gains. Additionally, the reduction of antenna gains for beams, B_2, B_3, B_6, and B_7 were due to slightly increased level of the side lobes, as could be observed in Figure 5.15 and Figure 5.16. The simulated and measured gains were maximums for the center beams, B_1 and B_8, as shown in Figure 5.17. Both simulated and measured gains were gradually decreased as the beams were far from the center beams, B_1 and B_8, and the phase differences between the output ports of the 8 × 8 Butler matrix for the beams were also increased. A good agreement was obtained between simulated and measured antenna gains of the multibeam array antenna.

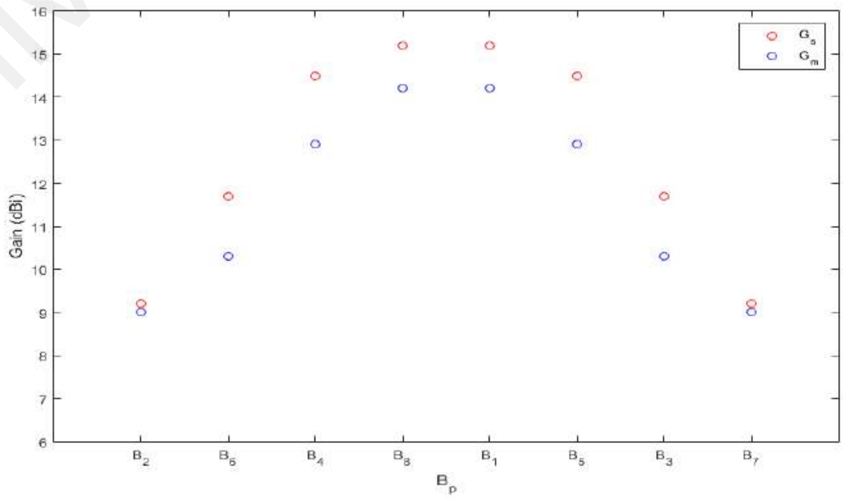

Figure 5.17: Simulated, G_s and measured, G_m antenna gains for the input ports of the multibeam array antenna at 28 GHz

Table 5.8: Simulated, G_s and measured, G_m antenna gains for the input ports of the multibeam array antenna at 28 GHz

Beam Number, B_p	B_1 (dBi)	B_2 (dBi)	B_3 (dBi)	B_4 (dBi)	B_5 (dBi)	B_6 (dBi)	B_7 (dBi)	B_8 (dBi)
G_s	15.2	9.2	11.7	14.5	14.5	11.7	9.2	15.2
G_m	14.2	9.0	10.3	12.9	12.9	10.3	9.0	14.2

5.6 Summary

This chapter presents the design of a single-layer multibeam array antenna at 28 GHz for base station in the 5G mobile communication system. The single-element microstrip antenna was designed and integrated at the output ports the 8 × 8 Butler matrix. The analysis of the multibeam array antenna with different antenna spacing was performed to control the beam coverage in the vertical plane. However, the appearances of grating lobes were observed when the antenna spacing is more than 0.7λ. Therefore, a multibeam array antenna with an antenna spacing of 0.6λ was selected for fabrication. The structure of the multibeam array antenna was compact with a dimension of 88 × 106 × 0.254 mm^3, which is suitable for a practical space-constrained base station. The performance of the multibeam array antenna was ensured via comprehensive electromagnetic simulation. The proposed multibeam array antenna was fabricated and measurements were conducted. The return losses of the multibeam array antenna for the input ports were less than −10 dB at 28 GHz. The radiation characteristics of the multibeam array antenna for the input ports showed good agreement with simulation results. The measured antenna gains were between 9 dBi and 14 dBi with beam coverage of 88°. Thus, the multibeam array antenna is adequate and suitable for base station in the 5G mobile communication system. The next chapter will present the proposed design concept of multibeam base station antennas for the 5G mobile communication system.

CHAPTER 6: DESIGN OF MULTIBEAM BASE STATION ANTENNAS

6.1 Introduction

This chapter describes the proposed concept of multibeam base station antennas for a fifth-generation (5G) mobile communication system using the multibeam array antenna that had been designed in Chapter 5. The design of multibeam base station antennas consists of several multibeam array antennas. The multibeam array antennas will be employed at the base station to deliver simultaneous horizontal and vertical sectorizations within a defined cell area. In this chapter, the configuration of a base station antenna is explained and the radiation patterns of the base station antenna in the horizontal and vertical planes are presented through graphical representations. Apart from that, the design of the multibeam base station antennas to achieve a 360° coverage area in the horizontal plane is demonstrated in detail. The analyses of beam coverage designs in the horizontal and vertical sectorizations were performed through electromagnetic simulation for better coverage solutions to mobile users within the defined cell area. The results of the three-dimensional radiation patterns were analyzed and discussed. Note that, only simulation results were presented in this chapter, as antenna measurements are impossible to perform in the antenna chamber due to the configuration of the multibeam array antennas. However, the actual performance of the multibeam array antenna was validated via measurements, as presented in Chapter 5. As a matter of fact, the multibeam base station antennas work independently to provide beam coverage to mobile users.

6.2 Concept of Multibeam Base Station Antennas

In the mobile communication system, a coverage area is divided into several cells and each cell is divided into several sectors. The number of sectors should be increased within the cell area to enhance system capacity and improve network coverage. To achieve this, the multibeam base station antennas are a promising solution for a 5G mobile communication system. The multibeam base station antennas produce multiple beams in different directions within a defined cell area and each beam is dedicated to a particular mobile user. The cell radius of the multibeam base station antennas is defined to be less than 200 m. The multibeam base station antennas can also reduce co-channel interference.

In the 5G mobile communication system, higher-order sectorization plays an important role to cater to the increasing demand for higher data traffic and higher data rates. The sectorization can be utilized in both horizontal and vertical planes within the cell area. Figure 6.1 illustrates the simultaneous horizontal and vertical sectorizations served by the multibeam base station antennas. As shown in Figure 6.1, a base station antenna provides beam coverage in the vertical plane and the base station antennas provide beam coverage in the horizontal plane.

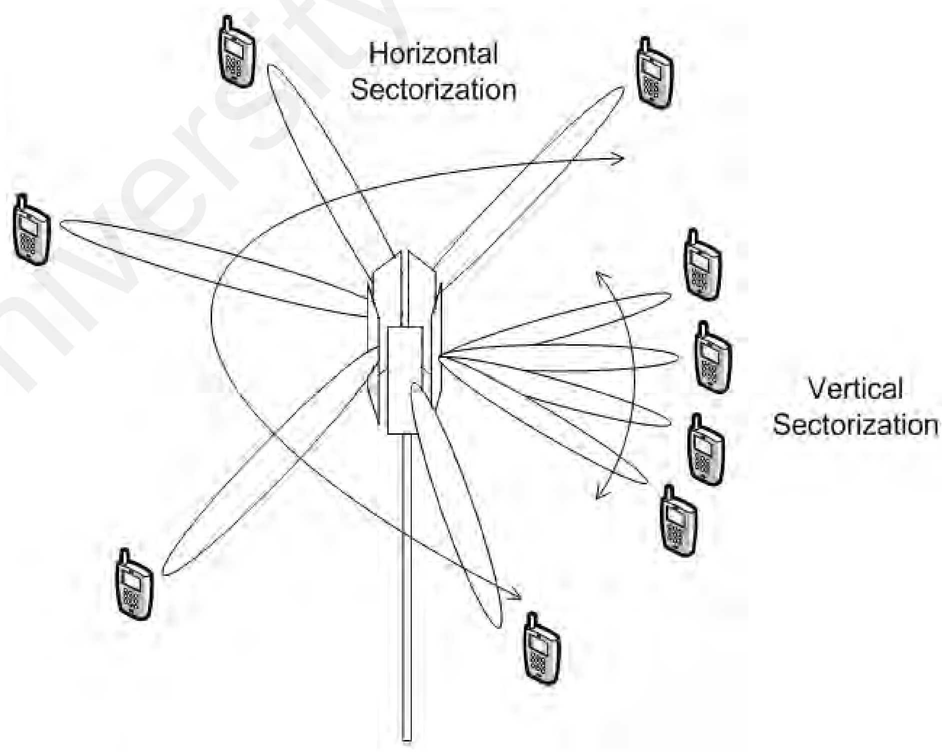

Figure 6.1: Simultaneous horizontal and vertical sectorizations of the multibeam base station antennas in the 5G mobile communication system

The advantages of the horizontal sectorization are to increase frequency reuse and improve system capacity. Meanwhile, the vertical sectorization is used to maximize network coverage and enhance system performance, especially for inner and outer cells, as shown in Figure 6.2. Furthermore, the vertical sectorization also provides better coverage solution to mobile users for high-rise building, as presented in Figure 6.3.

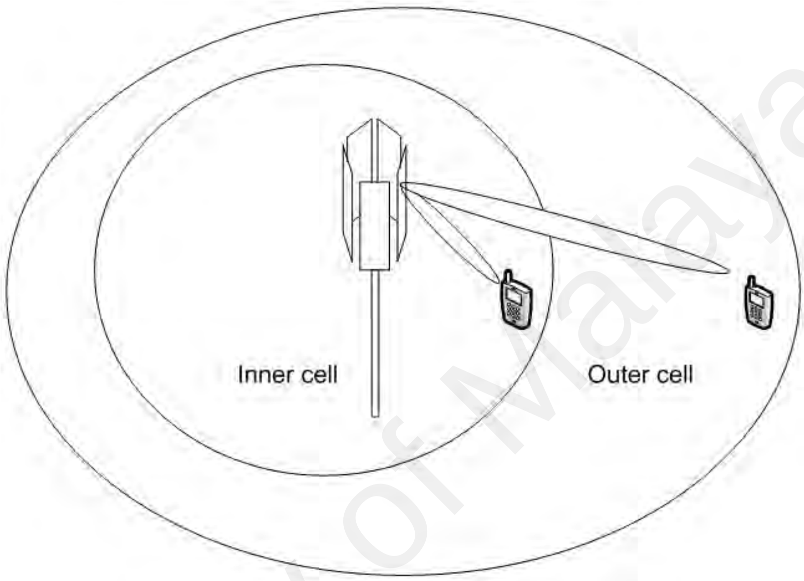

Figure 6.2: A multibeam base station antenna provides beam coverage to mobile users for inner and outer cells

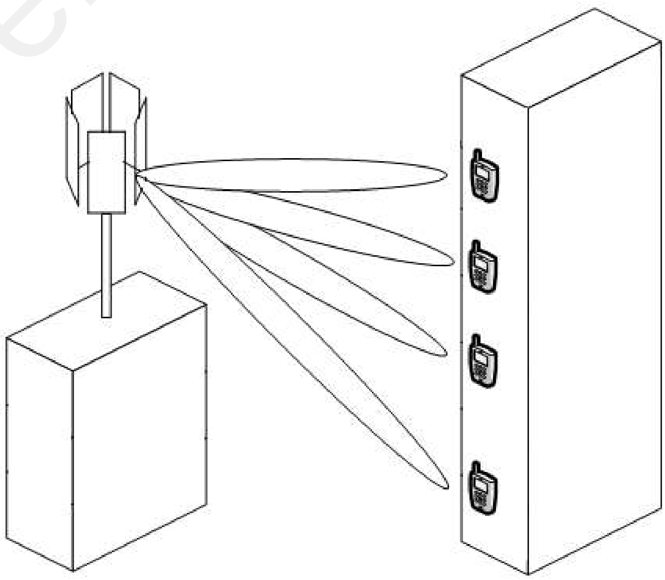

Figure 6.3: A multibeam base station antenna provides beam coverage to mobile users at different floors of high-rise building

6.3 Configuration of a Base Station Antenna

A base station antenna for the multibeam base station is developed using a multibeam array antenna, which consists of eight-element antennas fed by an 8 × 8 Butler matrix, as presented in Chapter 5. As the Butler matrix is a reciprocal network, it can be used to combine signals from an array antenna or to split an excited signal to input ports. In the transmitting mode, a radiation pattern will produce at a specific direction when the input port is excited. Meanwhile, the array antennas will receive the signal at a certain direction resulting in one of the input port having the most power of the signal in the receiving mode. Figure 6.4 illustrates the configuration of the base station antenna. The input ports of the Butler matrix will be integrated to a beam switching network. The use of a beam switching network is to switch an input port to produce a particular beam to a specific mobile user. The base station antenna will be placed in the vertical plane of the multibeam base station. Thus, the base station antenna produces beam coverage in the vertical plane.

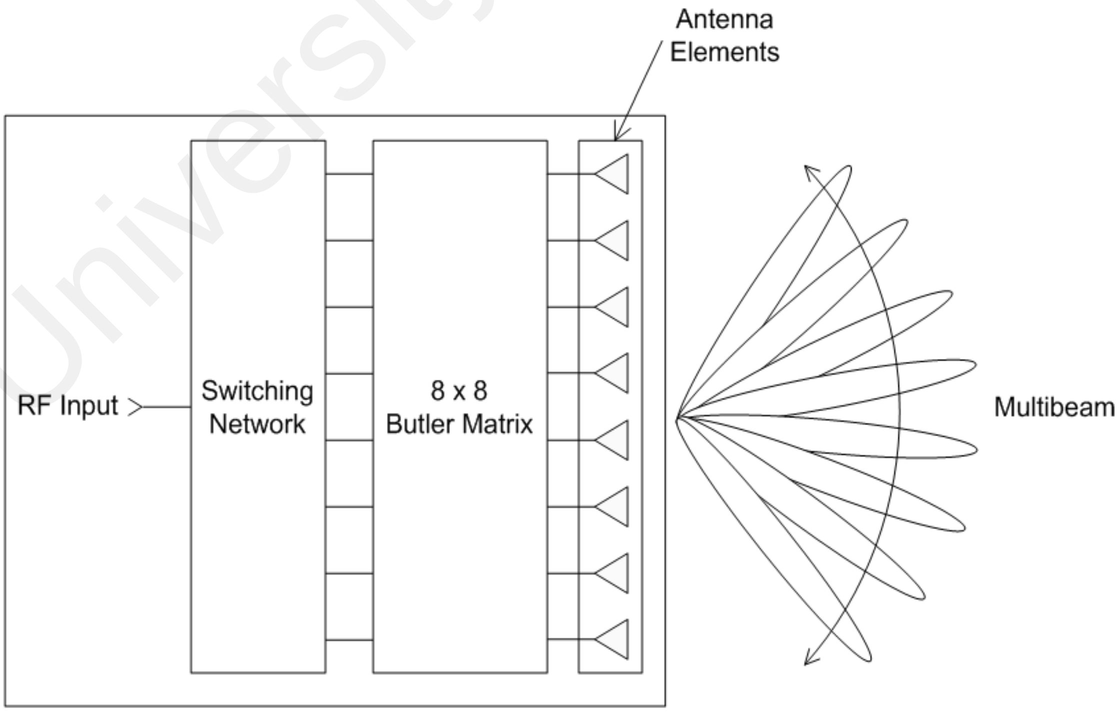

Figure 6.4: Configuration of the base station antenna with a beam switching network for the 5G multibeam base station antennas

Figure 6.5 presents the top view of the three-dimensional radiation pattern of the base station antenna when P1 was fed. Based on Figure 6.5, the 3-dB beamwidth of the base station antenna in the horizontal plane was 72°. The radiation patterns of the base station antenna in the horizontal plane for the input ports, P2, P3, P4, P5, P6, P7, and P8 were similar. Therefore, the radiation patterns of these input ports were not presented in this thesis. As presented in Chapter 5, the base station antenna was capable of producing eight beams at eight different directions when the input ports, P1 to P8 were fed. Figure 6.6 illustrates the side view of the three-dimensional radiation patterns of the base station antenna when the input ports, P1 to P8 were fed. The main beams of the radiation patterns for the base station antenna were pointed at −5°, 46°, −29°, 19°, −19°, 29°, −46°, and 5° when the input ports, P1, P2, P3, P4, P5, P6, P7, and P8 were fed, respectively. Based on these figures, the beam coverage of the base station antenna in the vertical plane was 94°.

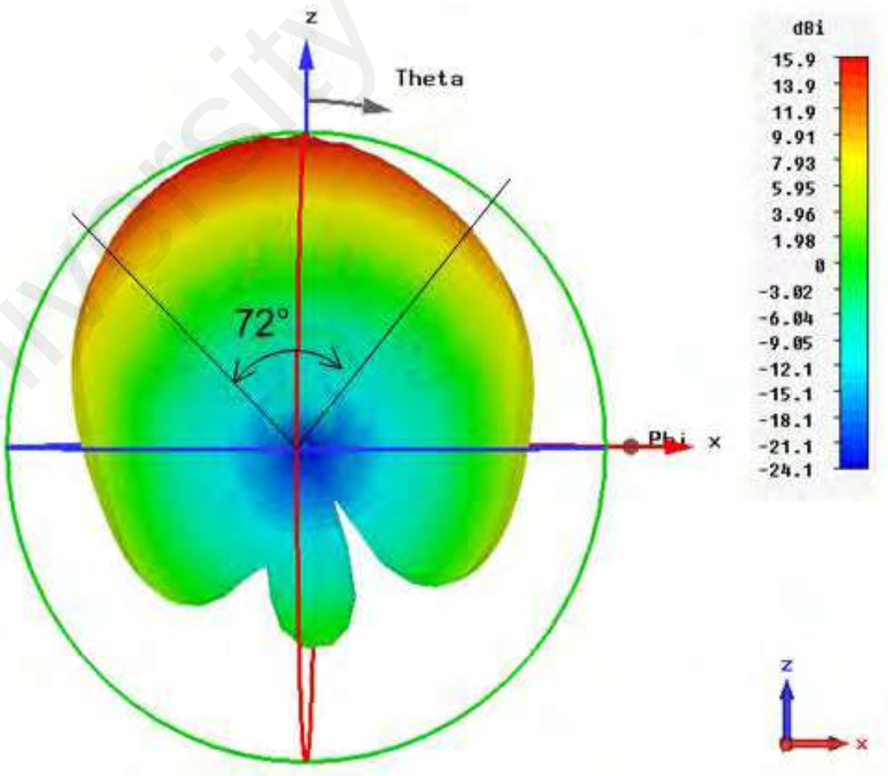

Figure 6.5: Top view of the three-dimensional radiation pattern of the base station antenna when P1 was fed

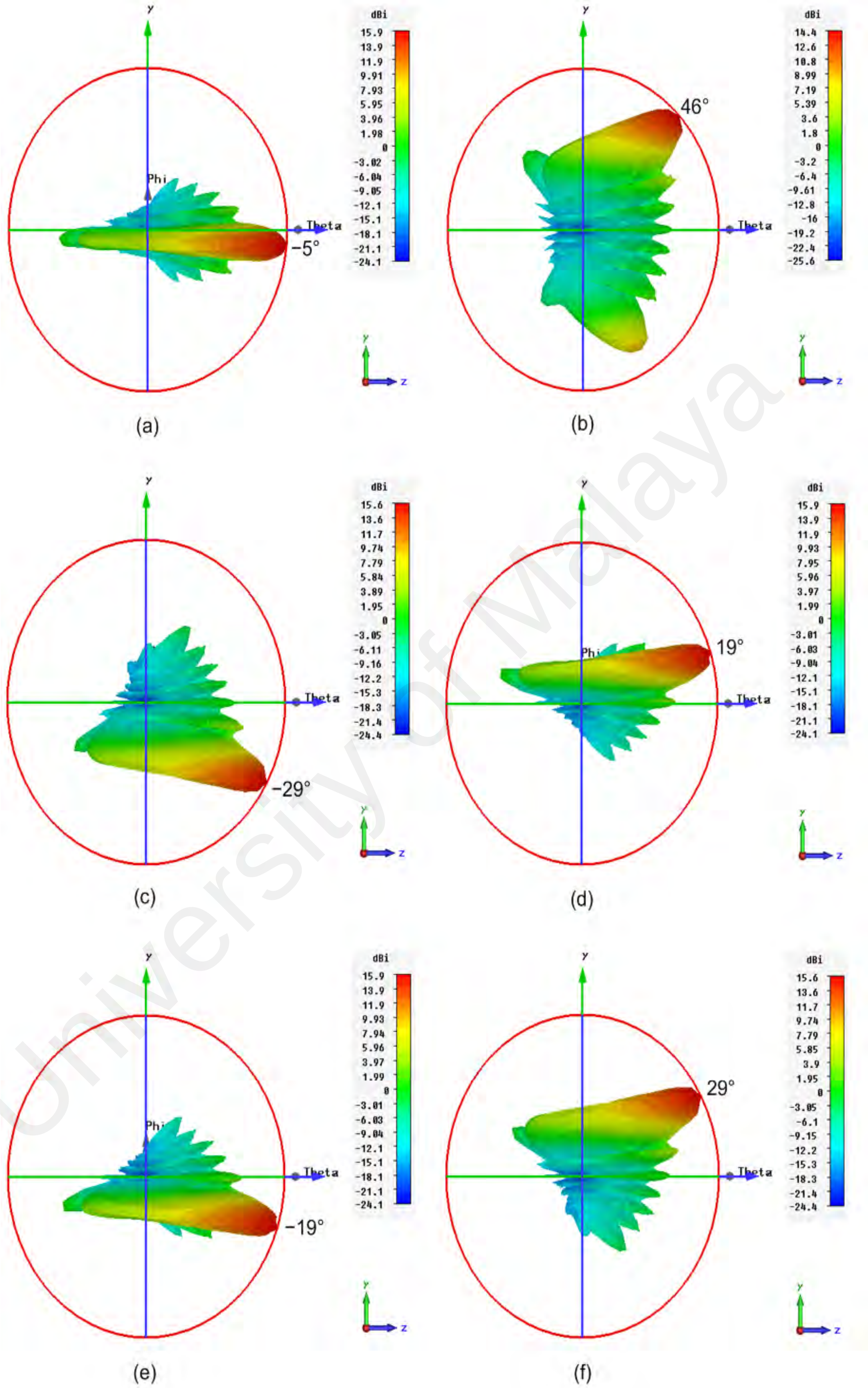

Figure 6.6, continued

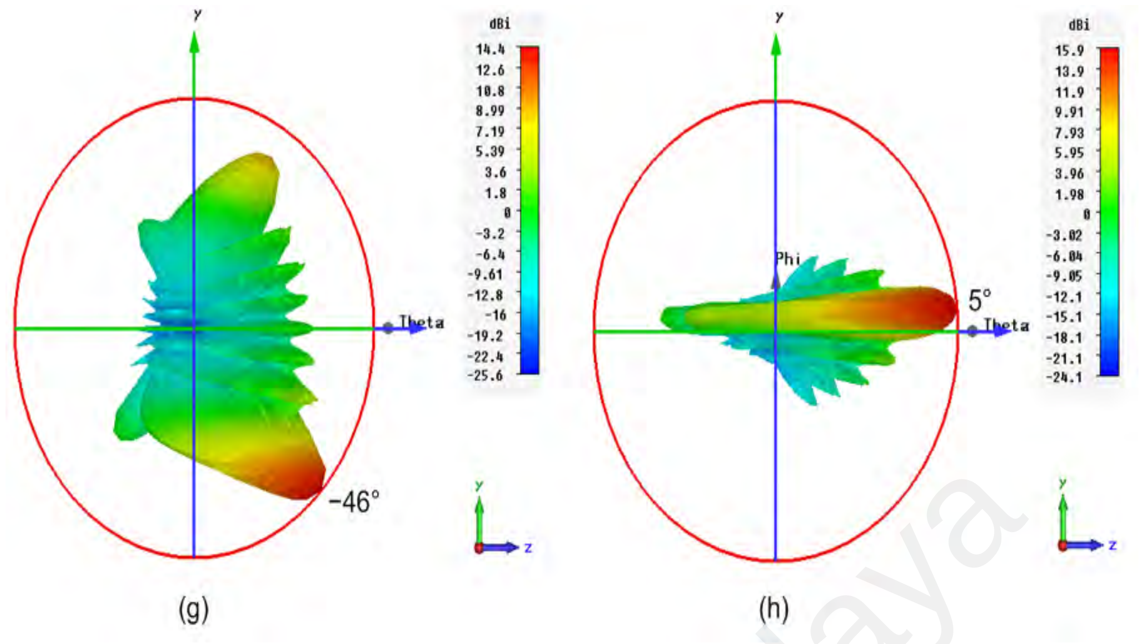

Figure 6.6: Side view of the three-dimensional radiation patterns of the base station antenna when (a) P1, (b) P2, (c) P3, (d) P4, (e) P5, (f) P6, (g) P7, and (h) P8 were fed

6.4 Beam Coverage Designs for the 5G Mobile Communication System

This section discusses the beam coverage designs of the multibeam base station antennas for the 5G mobile communication system. As the 5G mobile communication system provides higher data traffic and higher data rates, as well as massive connections to mobile users, it is very important to ensure that the multibeam base station antennas deliver simultaneous horizontal and vertical sectorizations within the defined cell area. The higher-order horizontal and vertical sectorizations play significant roles in designing the beam coverage within the defined cell area. In this thesis, the shape of the coverage area of each cell was determined by the radiation patterns of the multibeam base station antennas. To provide simultaneous horizontal and vertical sectorizations, the relevant parameters of the beam coverage designs were identified. The following subsections explain the beam coverage designs of the multibeam base station antennas for the horizontal and vertical sectorizations.

6.4.1 Horizontal Sectorization

In horizontal sectorization, the numbers of sectors in the cell area were determined by the radiation patterns of the base station antennas in the horizontal plane. As mentioned in Section 6.3, the 3-dB beamwidth of a base station antenna in the horizontal plane was 72°. Therefore, five base station antennas were required to provide a total coverage area of 360°, as shown in Figure 6.7. Each base station antenna provides beam coverage of a sector of 72°. Based on Figure 6.7, pentagon-shaped multibeam base station antennas model are proposed, as illustrated in Figure 6.8. The proposed pentagon-shaped multibeam base station antennas consist of five boards of base station antenna that were arranged in the vertical plane. The radiation patterns of the proposed pentagon-shaped multibeam base station antennas in the horizontal plane are presented in Figure 6.9. Five boards of base station antenna produce five radiation patterns in the horizontal plane and each base station antenna covers one sector. The proposed pentagon-shaped multibeam base station antennas will increase frequency reuse, improve system capacity, and enhance system coverage.

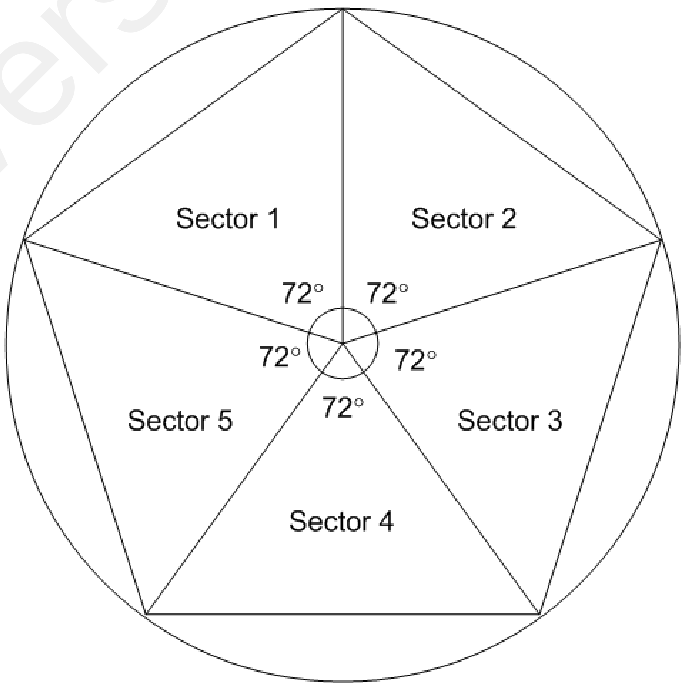

Figure 6.7: Horizontal sectorization of the multibeam base station antennas

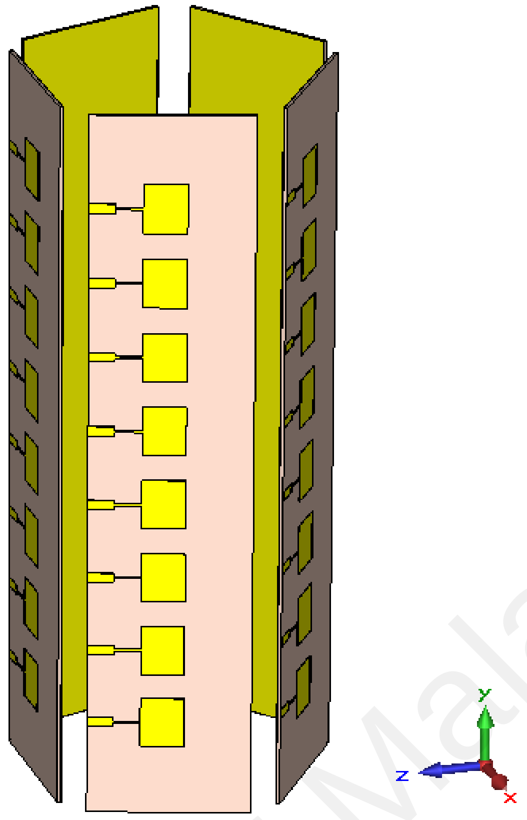

Figure 6.8: The proposed pentagon-shaped multibeam base station antennas

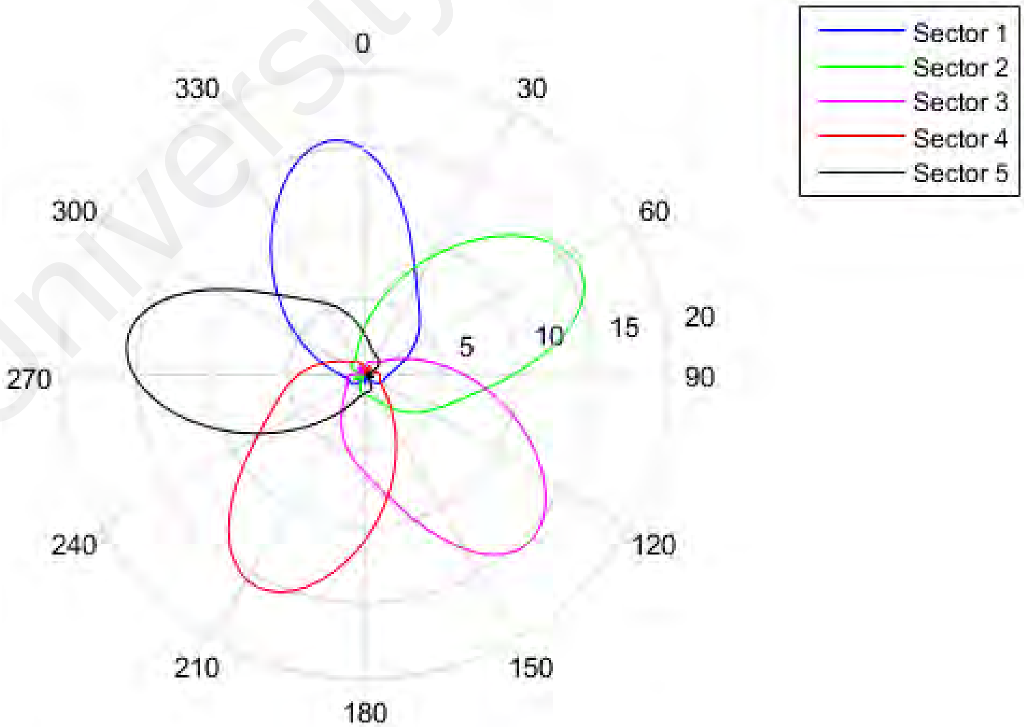

Figure 6.9: Radiation patterns of the multibeam base station antennas in the horizontal plane

6.4.2 Vertical Sectorization

In vertical sectorization, the number of the antenna elements determines the radiation pattern of the multibeam base station in the vertical plane. As explained in Section 6.3, a base station antenna was capable of producing eight beams at eight different directions. The radiation patterns in the vertical plane can be shaped depending on the operating environment. For example, the radiation patterns can provide beam coverage for inner and outer cells and beam coverage at different floors of a high-rise building. The most important design parameters in the beam shaping in the vertical sectorization are the cell radius, the height of the multibeam base station antennas, and the beam tilt angle of the base station antenna. The shaped beam of a multibeam base station antenna aims to provide beam coverage for inner and outer cells, as well as beam coverage at different floors for a high-rise building, as presented in Figure 6.10 and Figure 6.11, respectively. The beam tilt angle, θ_t can be calculated using Equation (6.1):

$$\tan\theta_t = \frac{r}{h} \tag{6.1}$$

where r is the cell radius and h is the height of the multibeam base station antennas.

In mobile communication system, the base station is fixed at a specific location. Therefore, the cell radius and the height of the multibeam base station antennas are fixed. Meanwhile, the beam tilt angle of the base station antenna can be adjusted according to the demand of the operating environment to provide continuous signal connectivity within a cell area. Therefore, the parametric studies of the beam tilt angle were conducted to observe the changes in the radiation patterns in the vertical plane. In these parametric studies, the beam tilt angle of the base station antenna was varied from 5° to 20° to ensure the antenna radiations in the horizontal planes are not deteriorated. The beam tilt angle was tilted clockwise from the positive y-axis.

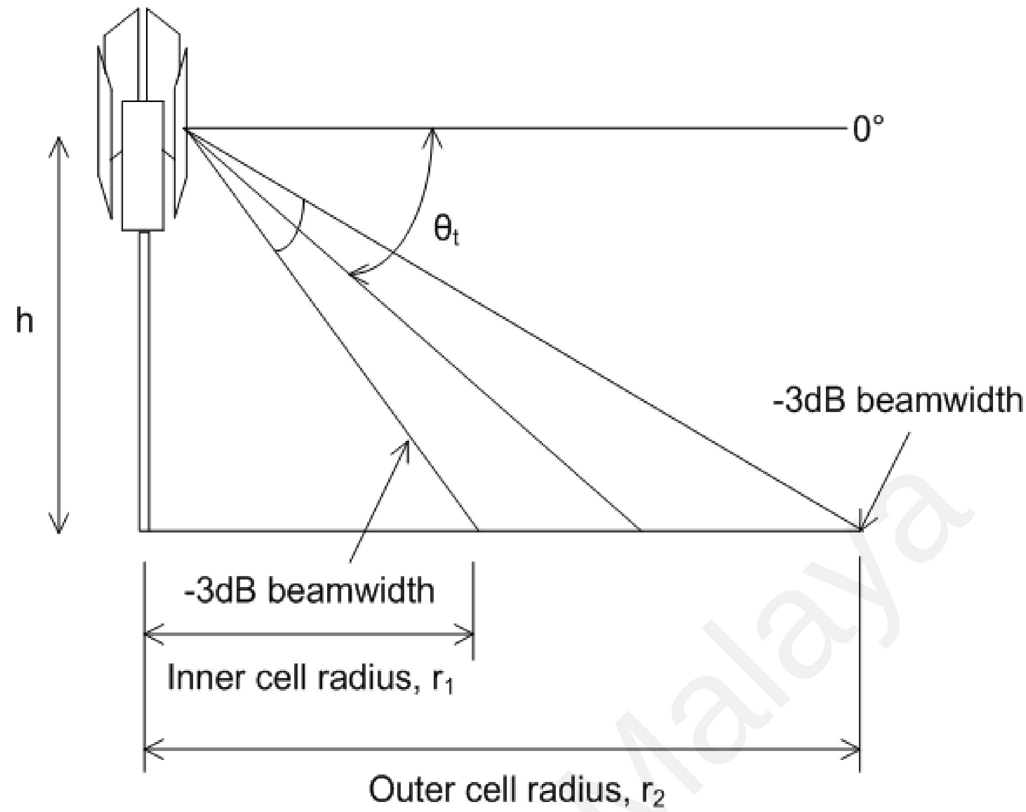

Figure 6.10: Shaped beam of a multibeam base station antenna to provide beam coverage for inner and outer cells

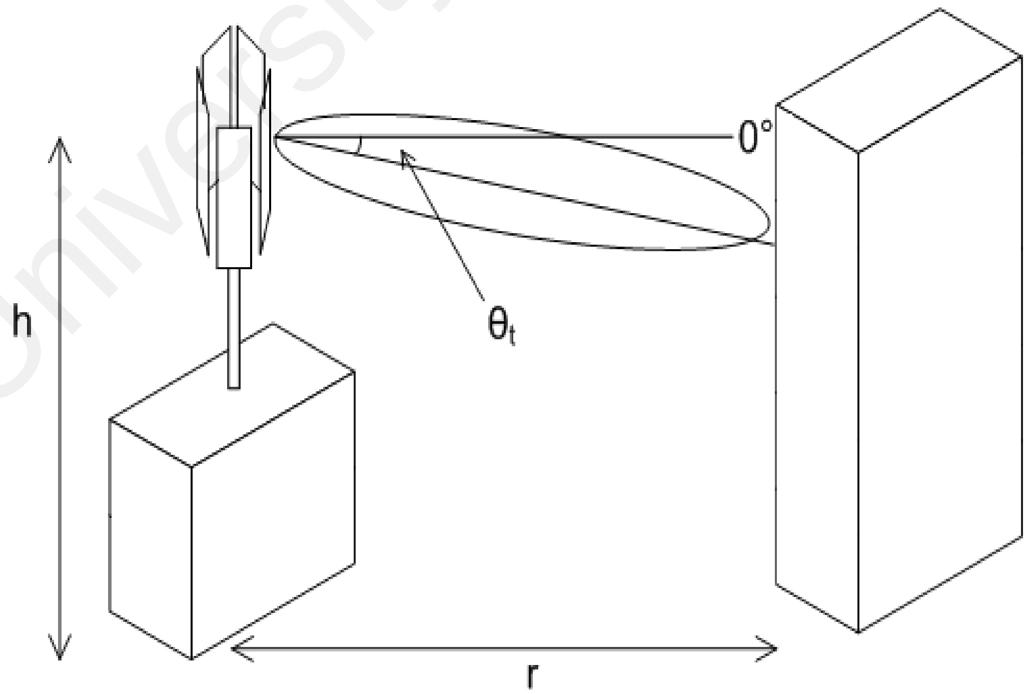

Figure 6.11: Shaped beam of a multibeam base station antenna to provide beam coverage at different floors for a high-rise building

Figure 6.12 to Figure 6.19 present the radiation patterns of the base station antenna in the horizontal and vertical planes when the beam tilt angle was tilted from 5° to 20°, respectively. The 3-dB beamwidth of the base station antenna in the horizontal plane was 72° for beam tilt angles of 5°, 10°, 15°, and 20°, as shown in Figure 6.12, Figure 6.14, Figure 6.16, and Figure 6.18, respectively. Only the radiation patterns of the base station antenna in the horizontal plane for the input port, P1 are shown, as the radiation patterns of the input ports, P2, P3, P4, P5, P6, P7, and P8 were similar. Therefore, the radiations for these input ports were not presented in this thesis. The coverage area of the base station antenna was between 39° and −49° when the beam tilt angle was tilted to 5°, as shown in Figure 6.13. Meanwhile, the coverage area of the base station antenna was between 35° and −55° when the beam tilt angle was tilted to 10°, as presented in Figure 6.15. The coverage area of the base station antenna was between 30° and −60° when the beam tilt angle was tilted to 15°, as illustrated in Figure 6.17. Furthermore, the coverage area of the base station antenna was between 25° and −65° when the beam tilt angle was tilted to 20°, as shown in Figure 6.19. The main beams of the base station antenna for the input ports are labeled in these figures. Table 6.1 summarizes the main beam angles of the base station antenna for different beam tilt angles.

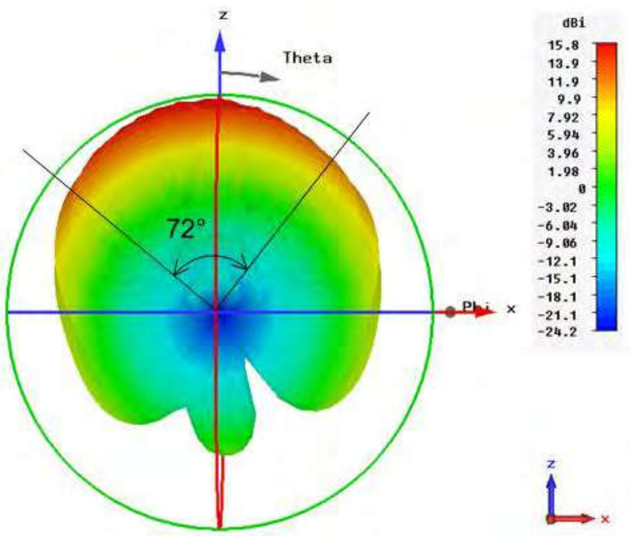

Figure 6.12: Top view of the three-dimensional radiation pattern of the base station antenna at θ_t = 5° when P1 was fed

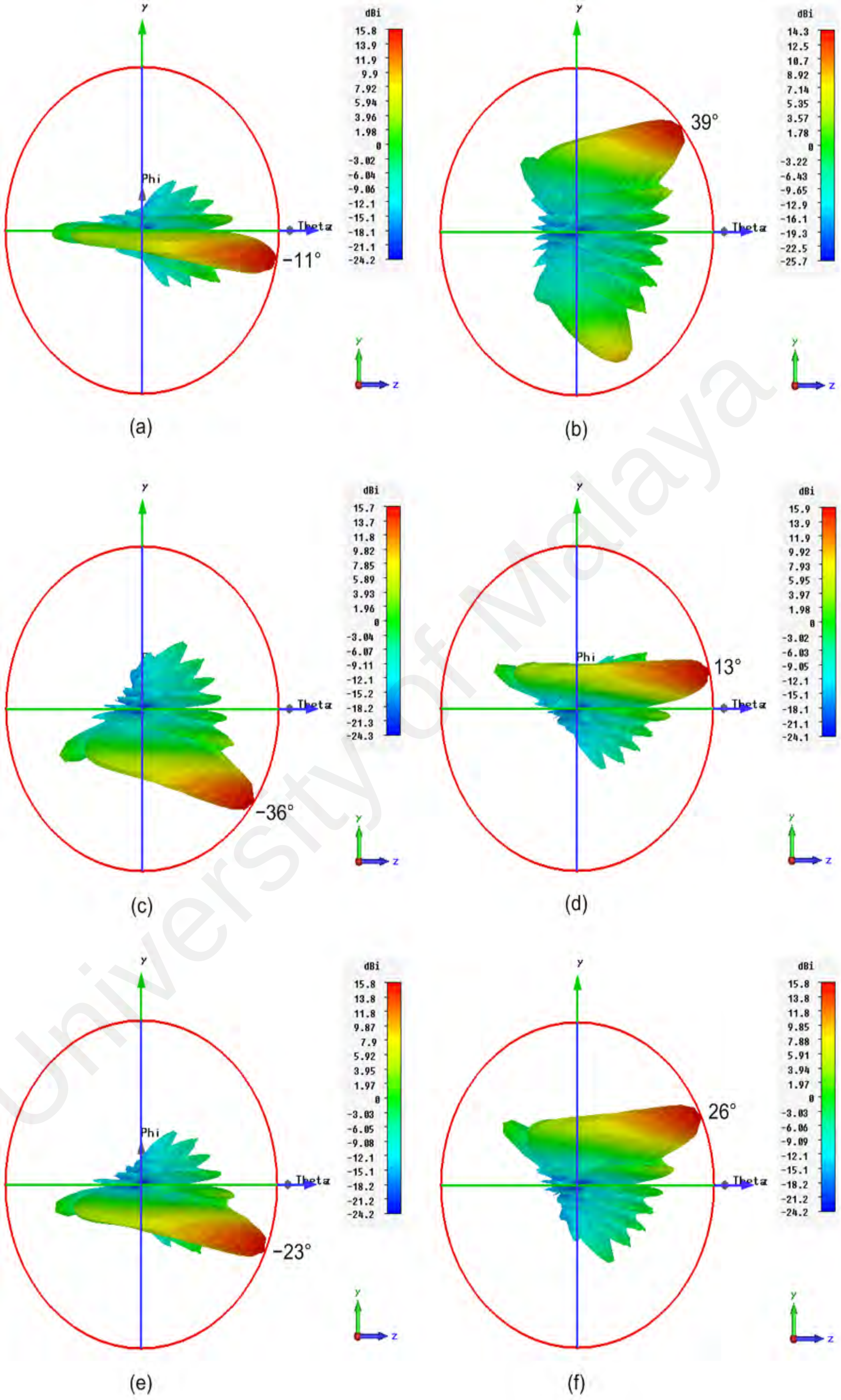

Figure 6.13, continued

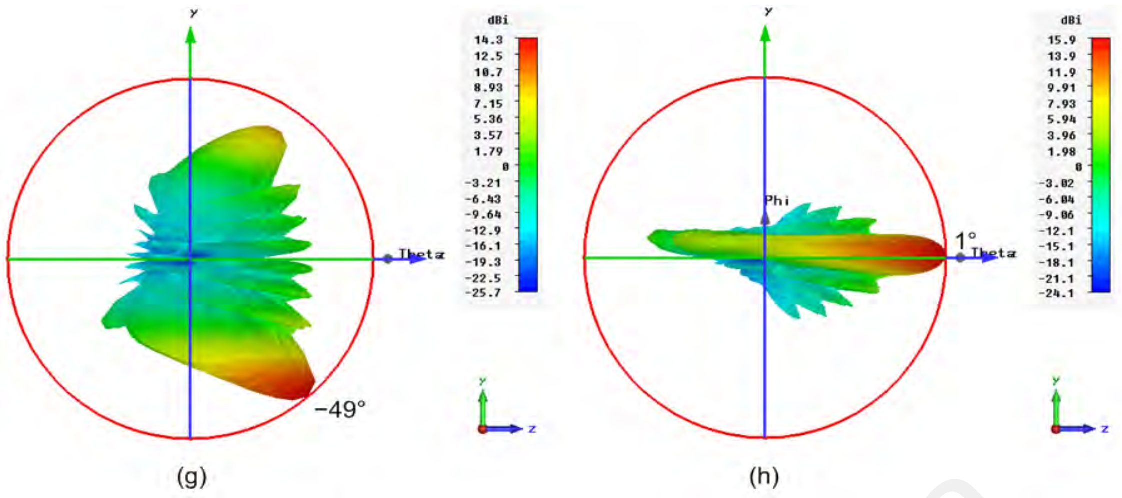

Figure 6.13: Side view of the three-dimensional radiation patterns of the base station antenna at θ_t = 5° when (a) P1, (b) P2, (c) P3, (d) P4, (e) P5, (f) P6, (g) P7, and (h) P8 were fed

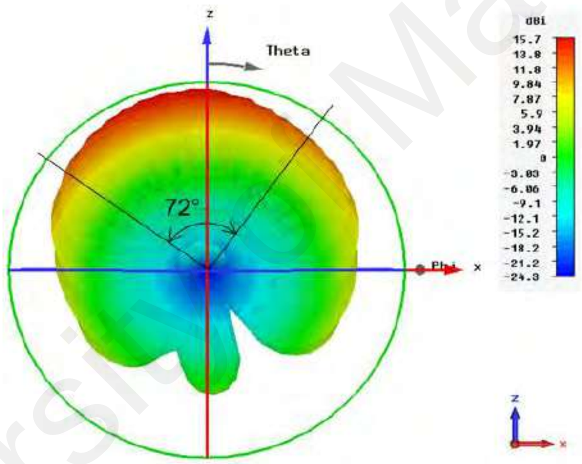

Figure 6.14: Top view of the three-dimensional radiation pattern of the base station antenna at θ_t = 10° when P1 was fed

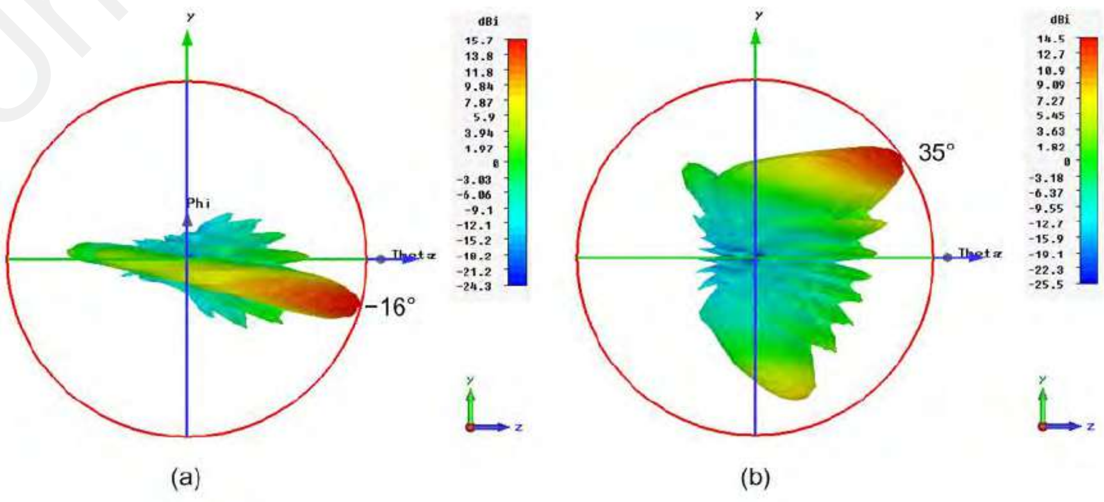

Figure 6.15, continued

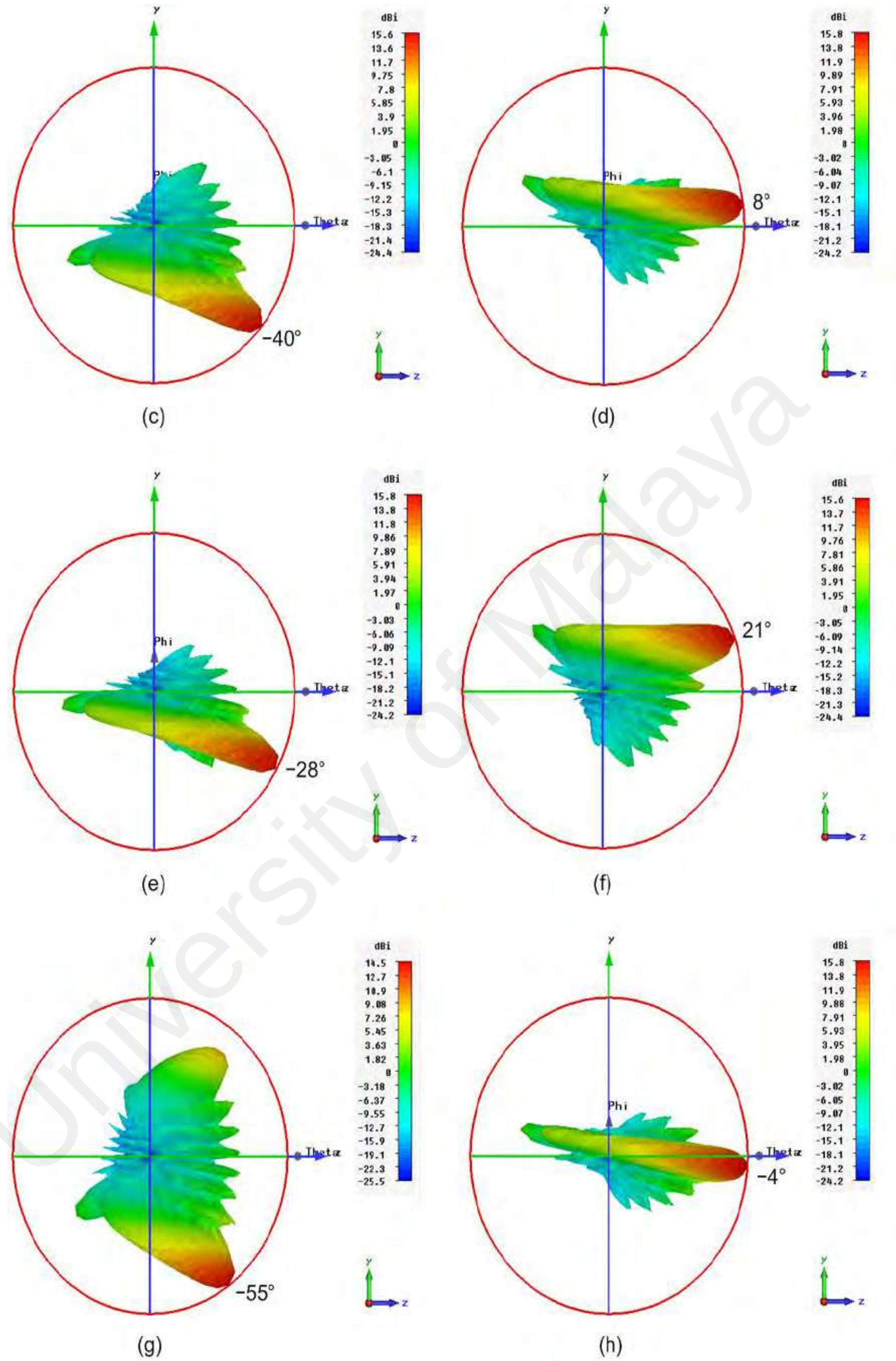

Figure 6.15: Side view of the three-dimensional radiation patterns of the base station antenna at θ_t = 10° when (a) P1, (b) P2, (c) P3, (d) P4, (e) P5, (f) P6, (g) P7, and (h) P8 were fed

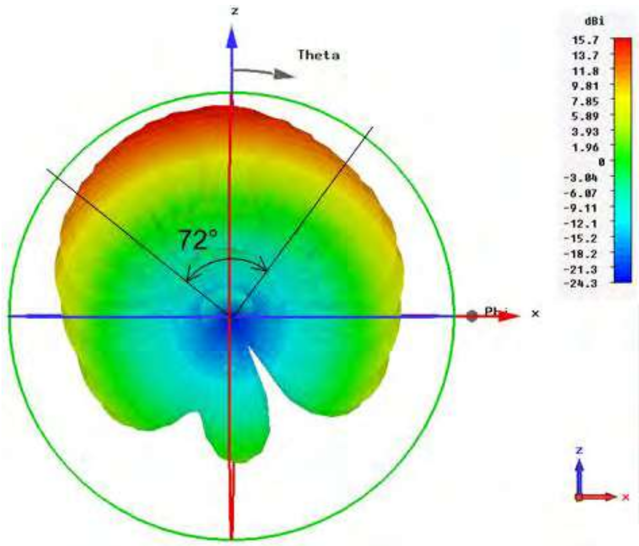

Figure 6.16: Top view of the three-dimensional radiation pattern of the base station antenna at θ_t = 15° when P1 was fed

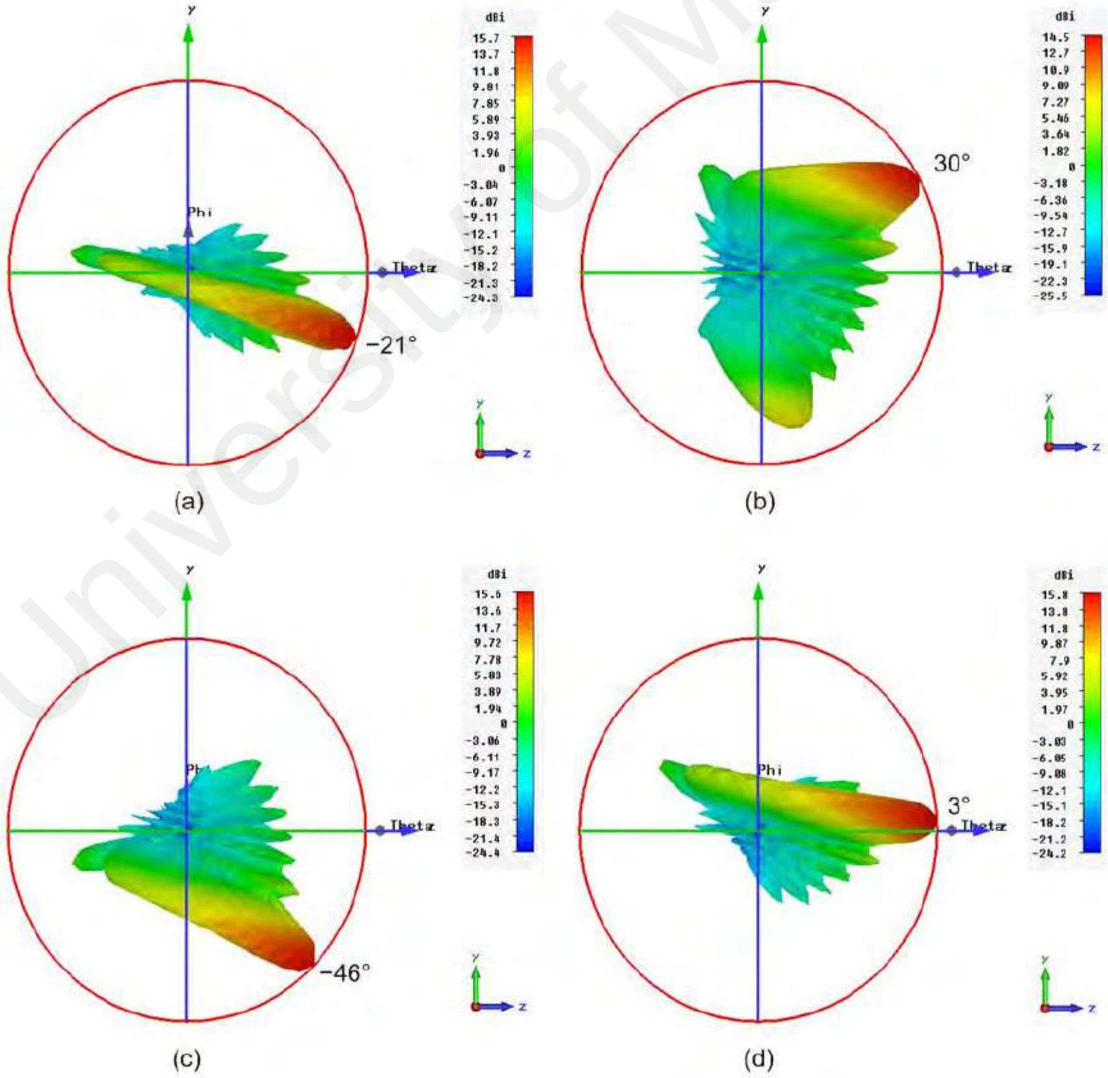

Figure 6.17, continued

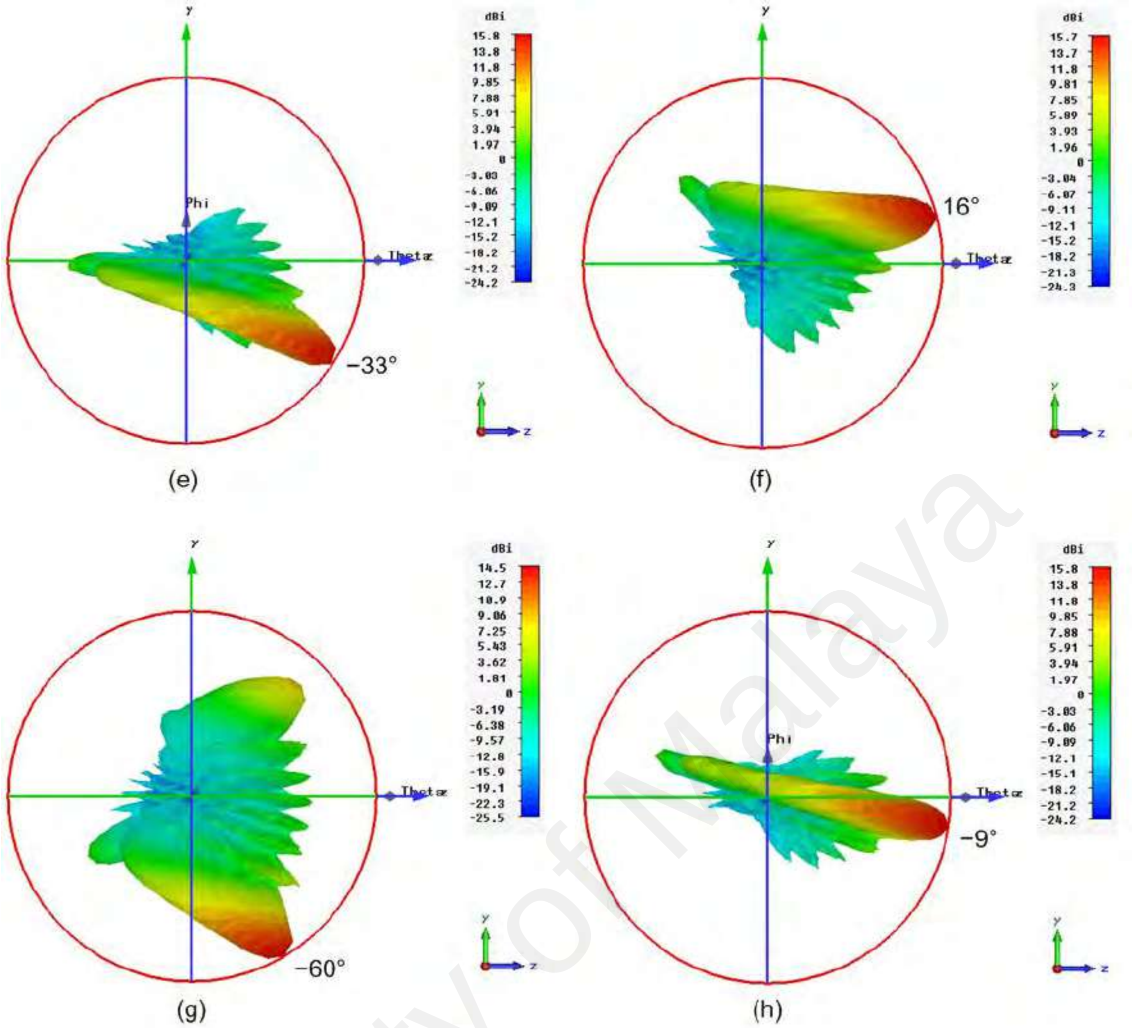

Figure 6.17: Side view of the three-dimensional radiation patterns of the base station antenna at θ_t = 15° when (a) P1, (b) P2, (c) P3, (d) P4, (e) P5, (f) P6, (g) P7, and (h) P8 were fed

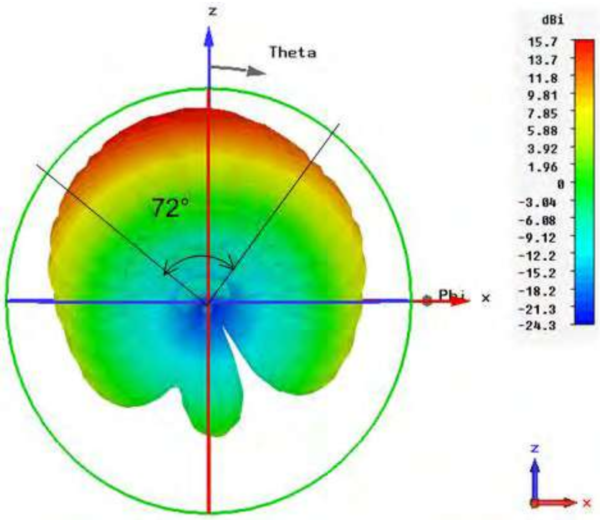

Figure 6.18: Top view of the three-dimensional radiation pattern of the base station antenna at θ_t = 20° when P1 was fed

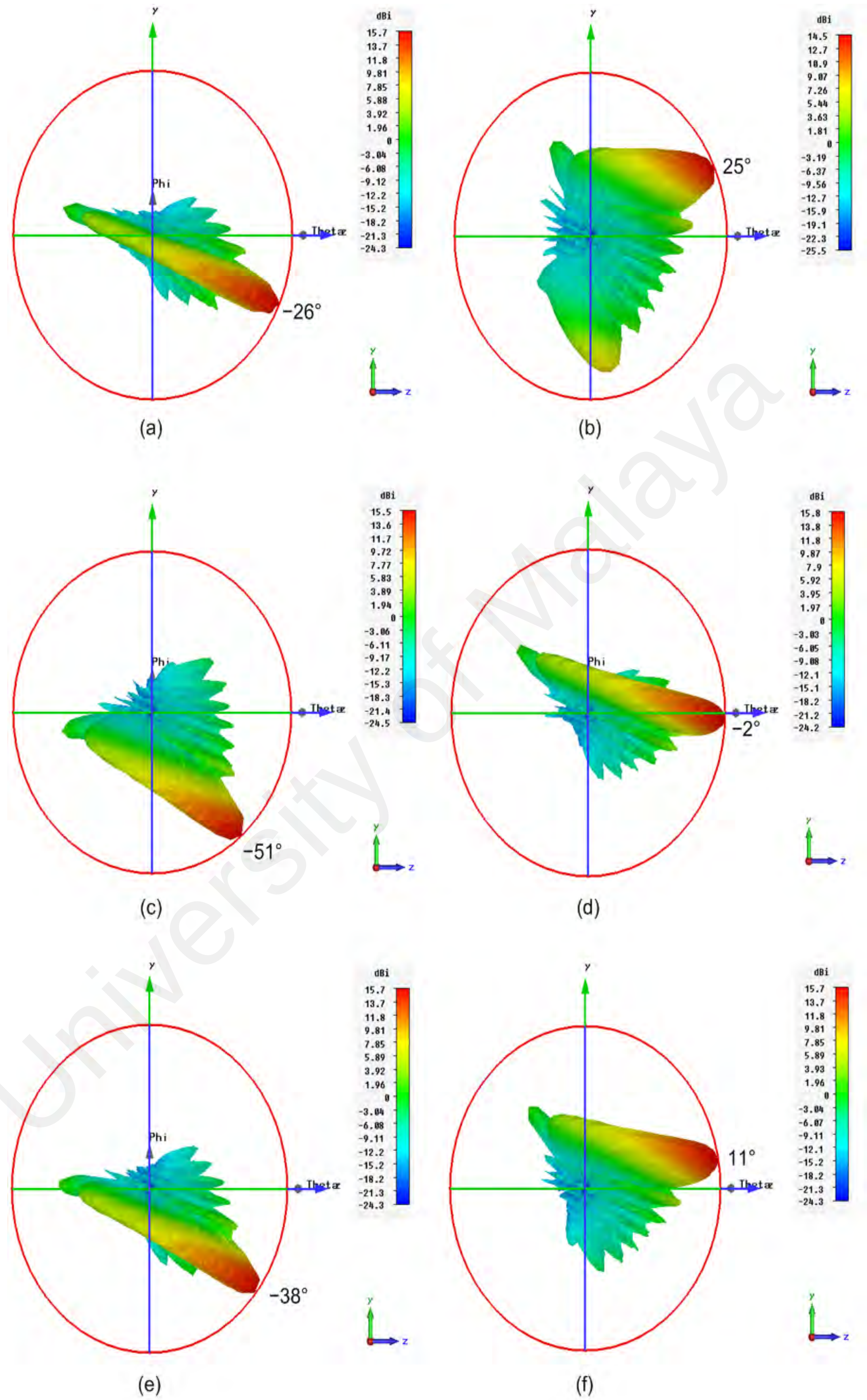

Figure 6.19, continued

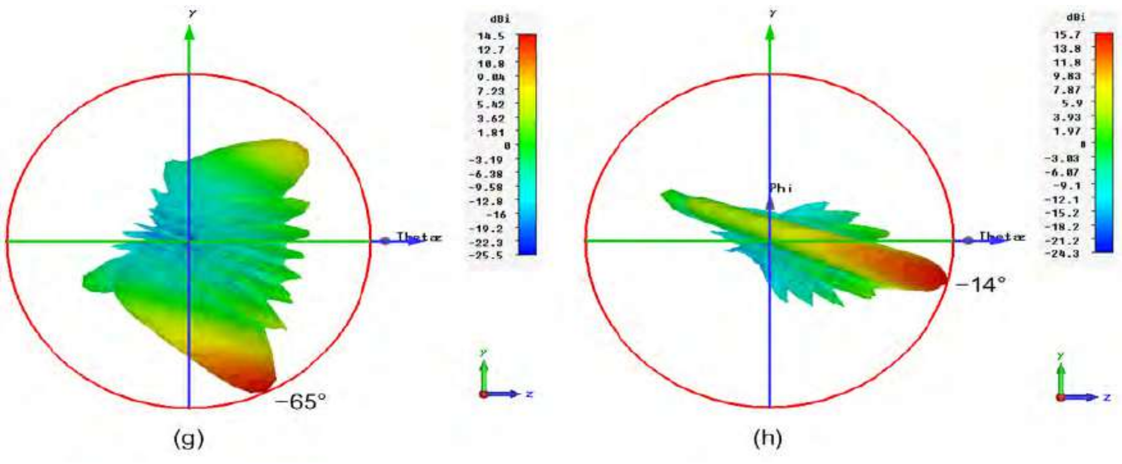

Figure 6.19: Side view of the three-dimensional radiation patterns of the base station antenna at θ_t = 20° when (a) P1, (b) P2, (c) P3, (d) P4, (e) P5, (f) P6, (g) P7, and (h) P8 were fed

Table 6.1: Main beam angles of the base station antenna at different beam tilt angles, θ_t

Beam number, B_n	θ_t = 5°	θ_t = 10°	θ_t = 15°	θ_t = 20°
1	-11°	-16°	-21°	-26°
2	39°	35°	30°	25°
3	-36°	-40°	-46°	-51°
4	13°	8°	3°	-2°
5	-23°	-28°	-33°	-38°
6	26°	21°	16°	11°
7	-49°	-55°	-60°	-65°
8	1°	-4°	-9°	-14°
Beam coverage	88°	88°	88°	88°

Based on Figure 6.12 to Figure 6.19 and Table 6.1, it can be observed that the main beam angles were shifted downward as the beam tilt angle was tilted from 5° to 20°. In addition, the beam coverage of the multibeam base station antenna in the vertical plane for the beam tilt angles remained the same, which was 88°. As shown in Figure 6.10, when the base station antenna was tilted from 5° to 10°, it could provide beam coverage to mobile users in the outer cells. On the other hand, when the base station antenna was tilted from 15° to 20°, it could provide beam coverage to mobile users in the inner cells. Furthermore, when the base station antenna was tilted from 5° to 10°, as shown in

Figure 6.11, it could provide beam coverage to mobile users at higher floors of the high-rise building. In contrast, when the base station antenna was tilted from 15° to 20°, it could provide beam coverage to mobile users at lower floors of the high-rise building. Therefore, the beam tilt technique proved useful for providing beam coverage to mobile users for the inner and outer cells, as well as beam coverage to mobile users at different floors of the high-rise building, provided that the multibeam base station were fixed at a specific location. By employing the beam tilt technique, the system capacity will be maximized and the network coverage will be improved in the 5G mobile communication system according to the demand of the operating environment.

6.5 Summary

This chapter proposed the design concept of the multibeam base station antennas for a 5G mobile communication system to deliver simultaneous horizontal and vertical sectorizations within a cell area. The configuration of a base station antenna was presented. Besides, the radiation patterns of the base station antenna in both horizontal and vertical planes were illustrated in graphical representations. The design of the multibeam base station antennas to achieve a 360° coverage area in the horizontal plane was discussed in detail. The analyses of beam coverage designs in the horizontal and vertical sectorizations were presented. Furthermore, the beam tilt technique was found to contribute significantly to the 5G mobile communication system to provide beam coverage to mobile users for the inner and outer cells, as well as beam coverage to mobile users at different floors of the high-rise building. By employing this technique at the multibeam base station antennas, the system capacity will be maximized and the network coverage will be improved according to the demand of the operating environment. The next chapter will conclude the research findings. Suggestions for future work will be also addressed.

CHAPTER 7: CONCLUSION

7.1 Conclusion

The mobile communication system evolved since the introduction of the first-generation mobile communication system to improve service quality. The design of a base station antenna becomes more challenging as the requirements of the mobile communication system become more stringent. The deployment of base stations in the fifth-generation (5G) mobile network is expected to deliver higher data traffic and higher data rates to mobile users within a defined cell area. To cater these demands, a base station antenna with an efficient performance is required.

In this research, a single-layer 8 × 8 Butler matrix operating at 28 GHz was designed as a beamforming circuit to feed a multibeam array antenna. The design methodology to achieve the required electrical performance of the 8 × 8 Butler matrix was demonstrated in detail. The circuit elements such as the crossover, the quadrature hybrid, and the phase shifters were designed and optimized. Furthermore, the parameter studies of the circuit elements were conducted and the correlations between the parameters were discussed. As a result, an 8 × 8 Butler matrix with precise dimensions was designed. The 8 × 8 Butler matrix was fabricated using a substrate material named NPC-F220A and measurements were performed to validate the simulation results. The structure of the 8 × 8 Butler matrix was compact with a dimension of 88 × 110 × 0.253 mm^3. The return losses of the 8 × 8 Butler matrix were less than −10 dB from 27 GHz to 29 GHz and the isolations of the 8 × 8 Butler matrix were less than −15 dB at 28 GHz. Furthermore, the insertion loss and the phase error of the 8 × 8 Butler matrix at 28 GHz were significantly improved, yielding values of ± 2 dB and ± 10°, respectively. Moreover, a good agreement between the measurement and simulation results was obtained.

Furthermore, a multibeam array antenna fed by an 8 × 8 Butler matrix based on a single-layer structure was designed at 28 GHz for base station. A study on the beam coverage of the multibeam array antenna in the vertical plane was conducted by varying the antenna spacing from 0.6λ to 0.8λ. The increase in the antenna spacing from 0.6λ to 0.8λ reduced the beam coverage of the multibeam array antenna. Moreover, the appearance of grating lobes could be seen when the antenna spacing was varied to more than 0.7λ. Therefore, the multibeam array antenna with an antenna spacing of 0.6λ was selected for fabrication. Measurements were conducted to validate the simulation results. The structure of the multibeam array antenna was compact with a dimension of 88 × 106 × 0.254 mm^3. The return losses of the multibeam array antenna were less than −10 dB at 28 GHz. The multibeam array antenna produced eight radiation patterns at eight different main beam angles with measured antenna gains between 9 dBi and 14 dBi. The beam coverage of the multibeam array antenna in the vertical plane was 88°. A good agreement between the measurement and simulation results was obtained. Thus, the developed multibeam array antenna was found to be adequate and suitable for a practical space-constrained base station, specifically in the 5G mobile communication system.

Besides that, this thesis presented the proposed design concept of multibeam base station antennas for the 5G mobile communication system. The configuration of a base station antenna was demonstrated and the radiation patterns were presented in both horizontal and vertical planes. Furthermore, the description for the design of the multibeam base station antennas was presented to achieve a 360° coverage area in the horizontal plane. Additionally, the beam coverage designs in the horizontal and vertical sectorizations were performed and analyzed. This ensured that simultaneous multiple beams in the horizontal and vertical planes were delivered to mobile users within the defined cell area. Moreover, the beam tilt technique played an important role in the vertical sectorization to provide beam coverage to mobile users for the inner and outer cells. This technique also provides beam coverage to mobile users at different floors in the high-rise building. Therefore, the proposed multibeam base station antennas presented in this thesis is a promising solution for the 5G mobile communication system. The following subsections highlighted the contributions of the thesis and recommendations for future work.

7.2 Contributions of the Thesis

The major contributions of this thesis are outlined as follows:

Firstly, a compact single-layer 8 × 8 Butler matrix with highly accurate dimensions was designed. During the design phase, the circuit elements such as the crossover, the quadrature hybrids, and the phase shifters were optimized to obtain optimum results. The circuit elements are then integrated to form an 8 × 8 Butler matrix. The designed 8 × 8 Butler matrix was fabricated and measurements were conducted. The simulation and measurement results were compared. The 8 × 8 Butler matrix achieved a low-loss and low phase error characteristic, which is sufficient to feed a multibeam array antenna.

Secondly, the best antenna spacing of the multibeam array antenna was identified without the appearance of the grating lobe and the beam coverage in the vertical plane is suitable for the base station. The multibeam array antenna was developed based on a single-layer structure, which operated at 28 GHz. The simulation and measurement results were compared. The return losses of the multibeam array antenna were less than −10 dB at 28 GHz. Moreover, the radiation characteristics are pointed at eight different directions with antenna gains between 9 dBi and 14 dBi. The structure of the multibeam array antenna was compact, which is suitable for base station in the 5G mobile communication system.

Finally, this thesis proposed the design concept of multibeam base station antennas in the 5G mobile communication system. The design of a 360° coverage area in the horizontal plane for the multibeam base station antennas was achieved. Moreover, the analyses of the beam coverage designs in the horizontal and vertical sectorizations were demonstrated. The results showed that the proposed multibeam base station antennas were capable of producing simultaneous horizontal and vertical sectorizations within the defined cell area. Additionally, the beam tilt technique is very useful to provide beam coverage to mobile users for inner and outer cells as well as to provide beam coverage to mobile users for high-rise buildings when the base station was fixed at a specific location. By employing this technique, the system capacity will be maximized and the network coverage will be improved. Thus, the proposed multibeam base station antennas were proven to be feasible for base station in the 5G mobile communication system.

7.3 Future Works

The research work presented in this thesis has showed promising results for base station in the 5G mobile communication system. Several aspects of the research works can be improved. The recommendations for further research are listed as follows:

i. The proposed base station antenna employs multibeam array antenna fed by an 8 × 8 Butler matrix produced eight radiation patterns at eight different main beam angles. A recommended solution is to increase the number of beams using higher-order Butler matrices. A base station antenna using higher-order Butler matrices will produce more beams to mobile users within a cell area, thus enhancing the system capacity.

ii. The designed multibeam array antenna suffered from losses due to the surface wave excitation, which degraded the radiation efficiency and increased the mutual coupling between the microstrip antennas. These issues can be solved by implementing electromagnetic band gap structure in the multibeam array antenna.

iii. The side lobes level of the multibeam array antenna can be reduced using tapered amplitude distribution technique. This technique can be realized by increasing the number of microstrip antennas and implementing unequal split power dividers or directional coupler at the output ports of the Butler matrix to produce unequal power distribution.

REFERENCES

Adamidis, G. A., Vardiambasis, I. O., Ioannidou, M. P., & Kapetanakis, T. N. (2019). Design and implementation of single-layer 4 × 4 and 8 × 8 Butler matrices for multibeam antenna arrays. *International Journal of Antennas and Propagation, 2019*, 12. doi:10.1155/2019/1645281

Afifi, M. S. (1990). Radiation and depolarization of multibeam offset reflectors fed by multimode pyramidal horns. *IEEE Transactions on Antennas and Propagation, 38*(8), 1213-1223. doi:10.1109/8.56957

Akyildiz, I. F., Kak, A., & Nie, S. (2020). 6G and Beyond: The Future of Wireless Communications Systems. *IEEE Access, 8*, 133995-134030. doi:10.1109/ACCESS.2020.3010896

Ali, A. A. M., Fonseca, N. J. G., Coccetti, F., & Aubert, H. (2011). Design and implementation of two-layer compact wideband Butler matrices in SIW technology for Ku-band applications. *IEEE Transactions on Antennas and Propagation, 59*(2), 503-512. doi:10.1109/TAP.2010.2093499

Alnoman, A., & Anpalagan, A. (2017). Towards the fulfillment of 5G network requirements: technologies and challenges. *Telecommunication Systems, 65*(1), 101-116. doi:10.1007/s11235-016-0216-9

Alsharif, M. H., Kelechi, A. H., Albreem, M. A., Chaudhry, S. A., Zia, M. S., & Kim, S. (2020). Sixth Generation (6G) Wireless Networks: Vision, Research Activities, Challenges and Potential Solutions. *Symmetry, 12*(4), 676.

Alsharif, M. H., & Nordin, R. (2017). Evolution towards fifth generation (5G) wireless networks: Current trends and challenges in the deployment of millimetre wave, massive MIMO, and small cells. *Telecommunication Systems, 64*(4), 617-637. doi:10.1007/s11235-016-0195-x

Altair. (2019). Altair-FEKO. Retrieved from https://altairhyperworks.com

Andrews, J. G., Buzzi, S., Wan, C., Hanly, S. V., Lozano, A., Soong, A. C. K., & Zhang, J. C. (2014). What will 5G be? *IEEE Journal on Selected Areas in Communications, 32*(6), 1065-1082. doi:10.1109/JSAC.2014.2328098

Ansoft. (2019). Ansys HFSS. Retrieved from https://www.ansys.com

AWR. (2019). Microwave Office. Retrieved from https://www.awrcorp.com

Babale, S. A., Rahim, S. K. A., Barro, O. A., Himdi, M., & Khalily, M. (2018). Single layered 4 × 4 Butler matrix without phase shifters and crossovers. *IEEE Access, 6*, 77289-77298. doi:10.1109/ACCESS.2018.2881605

Bae, E. S., Kim, J. S., & Chung, M. Y. (2014). *Radio resource management for multi-beam operating mobile communications.* Paper presented at the Asia-Pacific Conference on Communication (APCC2014), Pattaya, Thailand.

Balanis, C. A. (2005). *Antenna theory: Analysis and design* (3rd ed.). New Jersey: Wiley-Interscience.

Bantavis, P. I., Kolitsidas, C. I., Empliouk, T., Roy, M. L., Jonsson, B. L. G., & Kyriacou, G. A. (2018). A cost-effective wideband switched beam antenna system for a small cell base station. *IEEE Transactions on Antennas and Propagation, 66*(12), 6851-6861. doi:10.1109/TAP.2018.2874494

Bates, J., Gallon, C., Bocci, M., Walker, S., & Taylor, T. (2006). *Converged multimedia networks*: John Wiley & Sons.

Ben Kilani, M., Nedil, M., Kandil, N., & Denidni, T. (2012). Novel wideband multilayer Butler matrix using CB-CPW technology. *Progress In Electromagnetics Research C, 31*, 1-16. doi:10.2528/PIERC1205081

Bhowmik, W., Srivastava, S., & Prasad, L. (2014). Design of multiple beam forming antenna system using substrate integrated folded waveguide (SIFW) technology. *Progress In Electromagnetics Research B, 60*, 15-34. doi:10.2528/PIERB14022603

Blass, J. (1960). *Multidirectional antenna - A new approach to stacked beams.* Paper presented at the IRE International Convention Record, New York, USA.

Boccardi, F., Heath, R. W., Lozano, A., Marzetta, T. L., & Popovski, P. (2014). Five disruptive technology directions for 5G. *IEEE Commun. Mag, 52*. doi:10.1109/mcom.2014.6736746

Butler, J. L. (1960). *Multiple beam antennas*. Internal Memo RF-3849, Sanders Associates Nashua, N.H.

Chahat, N., Hodges, R. E., Sauder, J., Thomson, M., Peral, E., & Rahmat-Samii, Y. (2016). CubeSat deployable Ka-band mesh reflector antenna development for earth science missions. *IEEE Transactions on Antennas and Propagation, 64*(6), 2083-2093. doi:10.1109/TAP.2016.2546306

Chen, C., & Chu, T. (2010). Design of a 60-GHz substrate integrated waveguide Butler matrix—A systematic approach. *IEEE Transactions on Microwave Theory and Techniques, 58*(7), 1724-1733. doi:10.1109/TMTT.2010.2050097

Chen, P., Hong, W., Kuai, Z., & Xu, J. (2009). A double layer substrate integrated waveguide Blass matrix for beamforming applications. *IEEE Microwave and Wireless Components Letters, 19*(6), 374-376. doi:10.1109/LMWC.2009.2020020

Cheng, S., Yousef, H., & Kratz, H. (2009). 79 GHz Slot Antennas Based on Substrate Integrated Waveguides (SIW) in a Flexible Printed Circuit Board. *IEEE Transactions on Antennas and Propagation, 57*(1), 64-71. doi:10.1109/TAP.2008.2009708

Cheng, Y. J., Hong, W., Wu, K., Kuai, Z. Q., Yu, C., Chen, J. X., . . . Tang, H. J. (2008). Substrate integrated waveguide (SIW) Rotman lens and its Ka-band multibeam array antenna applications. *IEEE Transactions on Antennas and Propagation, 56*(8), 2504-2513. doi:10.1109/TAP.2008.927567

Cisco. (2017). Cisco Visual Networking Index: Global Mobile Data Traffic Forecast Update, 2017-2022. Retrieved from https://www.cisco.com/c/en/us/solutions/collateral/service-provider/visual-networking-index-vni/white-paper-c11-738429.html

Corona, A., & Lancaster, M. J. (2003). A high-temperature superconducting Butler matrix. *IEEE Transactions on Applied Superconductivity, 13*(4), 3867-3872. doi:10.1109/TASC.2003.820507

CST. (2019). CST Microwave Studio. Retrieved from https://www.cst.com

Dahlman, E., Parkvall, S., Astély, D., & Tullberg, H. (2014). *Advanced antenna solutions for 5G wireless access.* Paper presented at the Asilomar Conference on Signals, Systems and Computers.

Dau-Chyrh, C., & Ming-Chih, H. (1995). Multiple-polarization microstrip reflectarray antenna with high efficiency and low cross-polarization. *IEEE Transactions on Antennas and Propagation, 43*(8), 829-834. doi:10.1109/8.402202

Delaney, W. P. (1962). An RF multiple beam-forming technique. *IRE Transactions on Military Electronics, MIL-6*(2), 179-186. doi:10.1109/IRET-MIL.1962.5008426

Dogra, A., Jha, R. K., & Jain, S. (2020). A Survey on beyond 5G network with the advent of 6G: Architecture and Emerging Technologies. *IEEE Access*, 1-1. doi:10.1109/ACCESS.2020.3031234

Douville, R. J. P., & James, D. S. (1978). Experimental study of symmetric microstrip bends and their compensation. *IEEE Transactions on Microwave Theory and Techniques, 26*(3), 175-182. doi:10.1109/TMTT.1978.1129340

FCC. (2020). The FCC's 5G FAST Plan. Retrieved from https://www.fcc.gov/5G

Gavrilovska, L., Rakovic, V., & Atanasovski, V. (2016). Visions towards 5G: Technical requirements and potential enablers. *Wireless Personal Communications, 87*(3), 731-757. doi:10.1007/s11277-015-2632-7

Gonzalez, G. (1996). *Microwave transistor amplifiers: Analysis and design* (2nd ed.). Upper Saddle River, NJ, USA: Prentice-Hall, Inc.

Gupta, A., & Jha, R. K. (2015). A survey of 5G network: Architecture and emerging technologies. *IEEE Access, 3*, 1206-1232. doi:10.1109/ACCESS.2015.2461602

Han, C., Huang, J., & Kai, C. (2005). A high efficiency offset-fed X/Ka-dual-band reflectarray using thin membranes. *IEEE Transactions on Antennas and Propagation, 53*(9), 2792-2798. doi:10.1109/TAP.2005.854531

Henry, M., Free, C. E., Izqueirdo, B. S., Batchelor, J., & Young, P. (2009). Millimeter Wave Substrate Integrated Waveguide Antennas: Design and Fabrication Analysis. *IEEE Transactions on Advanced Packaging, 32*(1), 93-100. doi:10.1109/TADVP.2008.2011284

Hirtenfelder, F. (2007). *Effective Antenna Simulations using CST MICROWAVE STUDIO®.* Paper presented at the International ITG Conference on Antennas, Munich, Germany.

Hong, W., Jiang, Z. H., Yu, C., Zhou, J., Chen, P., Yu, Z., . . . He, S. (2017). Multibeam antenna technologies for 5G wireless communications. *IEEE Transactions on Antennas and Propagation, 65*(12), 6231-6249. doi:10.1109/TAP.2017.2712819

Hwang, R., Tsai, Y., & Hsiao, C. (2015, 19-24 July 2015). *An adaptive multi-beam massive array architecture for 5G wireless.* Paper presented at the 2015 IEEE International Symposium on Antennas and Propagation & USNC/URSI National Radio Science Meeting.

Jong-Hoon, L., Pinel, S., Papapolymerou, J., Laskar, J., & Tentzeris, M. M. (2005). Low-loss LTCC cavity filters using system-on-package technology at 60 GHz. *IEEE Transactions on Microwave Theory and Techniques, 53*(12), 3817-3824. doi:10.1109/TMTT.2005.859864

Jorgensen, R., Balling, P., & English, W. (1985). Dual offset reflector multibeam antenna for international communications satellite applications. *IEEE Transactions on Antennas and Propagation, 33*(12), 1304-1312. doi:10.1109/TAP.1985.1143523

Kanso, A., Chantalat, R., Naeem, U., Chreim, H., Thevenot, M., Bila, S., & Monediere, T. (2011). Multifeed EBG Dual-Band Antenna for Spatial Mission. *International Journal of Antennas and Propagation, 2011*, 14. doi:10.1155/2011/190358

Katagi, T., Mano, S., & Sato, S. (1984). An improved design method of Rotman lens antennas. *IEEE Transactions on Antennas and Propagation, 32*(5), 524-527. doi:10.1109/TAP.1984.1143353

Keysight. (2019). Advanced Design System (ADS). Retrieved from https://www.keysight.com

Khan, O. U. (2006). *Design of X-band 4 × 4 Butler matrix for microstrip patch antenna array.* Paper presented at the IEEE Region 10 Conference, Hong Kong, China.

Kim, S., Yoon, S., Lee, Y., & Shin, H. (2019). A Miniaturized Butler Matrix Based Switched Beamforming Antenna System in a Two-Layer Hybrid Stackup Substrate for 5G Applications. *Electronics, 8*(11), 1232.

Korhonen, J. (2014). *Introduction to 4G mobile communications*: Artech House, Inc.

Kourogiorgas, C., Sagkriotis, S., & Panagopoulos, A. D. (2015, 13-17 April 2015). *Coverage and outage capacity evaluation in 5G millimeter wave cellular systems: Impact of rain attenuation.* Paper presented at the 2015 9th European Conference on Antennas and Propagation (EuCAP).

Kyohei, F., & James, J. R. (2008). *Mobile antenna systems handbook* (3rd ed.): Artech House, Inc.

Le, L. B., Lau, V., Jorswieck, E., Dao, N.-D., Haghighat, A., Kim, D. I., & Le-Ngoc, T. (2015). Enabling 5G mobile wireless technologies. *EURASIP Journal on Wireless Communications and Networking, 2015*(1), 1-14. doi:10.1186/s13638-015-0452-9

Lee, J., & Carlise, R. (1983). A coma-corrected multibeam shaped lens antenna, part II: Experiments. *IEEE Transactions on Antennas and Propagation, 31*(1), 216-220. doi:10.1109/TAP.1983.1142992

Lee, J. J., & Valentine, G. W. (1996). *Multibeam array using Rotman lens and RF heterodyne.* Paper presented at the IEEE Antennas and Propagation Society International Symposium. 1996 Digest, Baltimore, MD, USA.

Llombart, N., Neto, A., Gerini, G., Bonnedal, M., & Maagt, P. D. (2008). Leaky wave enhanced feed arrays for the improvement of the edge of coverage gain in multibeam reflector antennas. *IEEE Transactions on Antennas and Propagation, 56*(5), 1280-1291. doi:10.1109/TAP.2008.922680

Luh, H., Smith, T., & Scott, W. (1982). A dual-band TEM lens for a multiple beam antenna system. *IEEE Transactions on Antennas and Propagation, 30*(2), 224-229. doi:10.1109/TAP.1982.1142773

Maruyama, T., Yamamori, K., & Kuwahara, Y. (2008). *Design of multibeam dielectric lens antennas by multi-objective optimization.* Paper presented at the European Microwave Conference, Amsterdam, Netherlands.

Mishra, A. R., Sood, K. K., & Kumar, A. (1998). Cavity backed microstrip patch array feed for multiple beam applications. *Electronics Letters, 34*(1), 4-6. doi:10.1049/el:19980076

Monk, A. D., & Clarricoats, P. J. B. (1994). Experimental demonstration of adaptive nulling using a mesh reflector antenna. *Electronics Letters, 30*(16), 1259-1261. doi:10.1049/el:19940874

Moody, H. (1964). The systematic design of the Butler matrix. *IEEE Transactions on Antennas and Propagation, 12*(6), 786-788. doi:10.1109/TAP.1964.1138319

Mosca, S., Bilotti, F., Toscano, A., & Vegni, L. (2002). A novel design method for Blass matrix beam-forming networks. *IEEE Transactions on Antennas and Propagation, 50*(2), 225-232. doi:10.1109/8.997999

Moubadir, M., Bayjja, M., Touhami, N. A., Aghoutane, M., & Tazon, A. (2015, 20-23 Oct. 2015). *Design and implementation of a technology planar 8 × 8 Butler matrix with square truncated edge-fed array antenna for WLAN networks application.* Paper presented at the International Conference on Wireless Networks and Mobile Communications (WINCOM), Marrakech, Morocco.

Mumtaz, S., Rodriguez, J., & Dai, L. (2017). *mmWave massive MIMO: A paradigm for 5G* (1st ed.): Academic Press.

Nam, W., Bai, D., Lee, J., & Kang, I. (2014). Advanced interference management for 5G cellular networks. *IEEE Communications Magazine, 52*(5), 52-60. doi:10.1109/MCOM.2014.6815893

Narekar, N. P., & Bhalerao, D. M. (2015, 2-4 April 2015). *A survey on obstacles for 5G communication.* Paper presented at the International Conference on Communications and Signal Processing (ICCSP), Melmaruvathur, India.

Nedil, M., Denidni, T. A., & Talbi, L. (2006). Novel butler matrix using CPW multilayer technology. *IEEE Transactions on Microwave Theory and Techniques, 54*(1), 499-507. doi:10.1109/TMTT.2005.860490

Nematollahi, H., Laurin, J., Page, J. E., & Encinar, J. A. (2015). Design of broadband transmitarray unit cells with comparative study of different numbers of layers. *IEEE Transactions on Antennas and Propagation, 63*(4), 1473-1481. doi:10.1109/TAP.2015.2402285

Néron, J.-S., & Delisle, G.-Y. (2005). Microstrip EHF Butler matrix design and realization. *ETRI Journal, 27*(6), 788-797. doi:10.4218/etrij.05.1005.0012

Niu, Y., Li, Y., Jin, D., Su, L., & Vasilakos, A. V. (2015). A survey of millimeter wave communications (mmWave) for 5G: Opportunities and challenges. *Wireless Networks, 21*(8), 2657-2676. doi:10.1007/s11276-015-0942-z

Panwar, N., Sharma, S., & Singh, A. K. (2016). A survey on 5G: The next generation of mobile communication. *Physical Communication, 18, Part 2*, 64-84. doi:10.1016/j.phycom.2015.10.006

Park, Y., & Adachi, F. (2007). *Enhanced radio access technologies for next generation mobile communication*. Dordrecht: Springer.

Peebles, A. L. (1988). A dielectric bifocal lens for multibeam antenna applications. *IEEE Transactions on Antennas and Propagation, 36*(5), 599-606. doi:10.1109/8.192135

Peeler, G., & Coleman, H. (1958). Microwave stepped-index luneberg lenses. *IRE Transactions on Antennas and Propagation, 6*(2), 202-207. doi:10.1109/TAP.1958.1144575

Pi, Z., & Khan, F. (2012, 4-7 Nov. 2012). *A millimeter-wave massive MIMO system for next generation mobile broadband.* Paper presented at the 2012 Conference Record of the Forty Sixth Asilomar Conference on Signals, Systems and Computers (ASILOMAR).

Plastikov, A. N. (2016). A high-gain multibeam bifocal reflector antenna with 40° field of view for satellite ground station applications. *IEEE Transactions on Antennas and Propagation, 64*(7), 3251-3254. doi:10.1109/TAP.2016.2560918

Pozar, D. M. (2005). *Microwave engineering* (3rd ed.). Hoboken, NJ :: J. Wiley.

Pozar, D. M., Targonski, S. D., & Syrigos, H. D. (1997). Design of millimeter wave microstrip reflectarrays. *IEEE Transactions on Antennas and Propagation, 45*(2), 287-296. doi:10.1109/8.560348

Ramírez-Arroyo, A., Zapata-Cano, P. H., Á, P.-C., Carmona-Murillo, J., Luna-Valero, F., & Valenzuela-Valdés, J. F. (2020). Multilayer Network Optimization for 5G & 6G. *IEEE Access, 8*, 204295-204308. doi:10.1109/ACCESS.2020.3036744

Rangan, S., Rappaport, T. S., & Erkip, E. (2014). Millimeter-wave cellular wireless networks: Potentials and challenges. *Proceedings of the IEEE, 102*(3), 366-385. doi:10.1109/JPROC.2014.2299397

Rao, S. K., & Tang, M. Q. (2006). Stepped-reflector antenna for dual-band multiple beam Satellite communications payloads. *IEEE Transactions on Antennas and Propagation, 54*(3), 801-811. doi:10.1109/TAP.2006.869938

Rappaport, T. S., Sun, S., Mayzus, R., Zhao, H., Azar, Y., Wang, K., . . . Gutierrez, F. (2013). Millimeter wave mobile communications for 5G Cellular: It will work! *IEEE Access, 1*, 335-349. doi:10.1109/ACCESS.2013.2260813

Rodriguez, J. (2015). *Fundamentals of 5G mobile networks* (1st ed.). Chichester: John Wiley & Sons Ltd.

Rotman, W. (1984). Analysis of an EHF aplanatic zoned dielectric lens antenna. *IEEE Transactions on Antennas and Propagation, 32*(6), 611-617. doi:10.1109/TAP.1984.1143379

Rotman, W., & Turner, R. (1963). Wide-angle microwave lens for line source applications. *IEEE Transactions on Antennas and Propagation, 11*(6), 623-632. doi:10.1109/TAP.1963.1138114

Rudge, A. (1975). Multiple-beam antennas: Offset reflectors with offset feeds. *IEEE Transactions on Antennas and Propagation, 23*(3), 317-322. doi:10.1109/TAP.1975.1141088

Saha, R. K. (2020). Licensed Countrywide Full-Spectrum Allocation: A New Paradigm for Millimeter-Wave Mobile Systems in 5G/6G Era. *IEEE Access, 8*, 166612-166629. doi:10.1109/ACCESS.2020.3023342

Schoenlinner, B., Xidong, W., Ebling, J. P., Eleftheriades, G. V., & Rebeiz, G. M. (2002). Wide-scan spherical-lens antennas for automotive radars. *IEEE*

Transactions on Microwave Theory and Techniques, 50(9), 2166-2175. doi:10.1109/TMTT.2002.802331

Shanzhi, C., & Jian, Z. (2014). The requirements, challenges, and technologies for 5G of terrestrial mobile telecommunication. *IEEE Communications Magazine, 52*(5), 36-43. doi:10.1109/MCOM.2014.6815891

Sheikh, M. U., & Lempiäinen, J. (2016). Macro cellular network transition from traditional frequency range to 28 GHz millimeter wave frequency band. *Wireless Networks*. doi:10.1007/s11276-016-1390-0

Sim, M. S., Lim, Y., Park, S. H., Dai, L., & Chae, C. (2020). Deep Learning-Based mmWave Beam Selection for 5G NR/6G With Sub-6 GHz Channel Information: Algorithms and Prototype Validation. *IEEE Access, 8*, 51634-51646. doi:10.1109/ACCESS.2020.2980285

Slomian, I., Wincza, K., Staszek, K., & Gruszczynski, S. (2017). Folded single-layer 8 × 8 Butler matrix. *Journal of Electromagnetic Waves and Applications, 31*(14), 1386-1398. doi:10.1080/09205071.2017.1348997

Sonnet. (2019). Sonnet Suites. Retrieved from http://www.sonnetsoftware.com

Stutzman, W. L., & Thiele, G. A. (2012). *Antenna theory and design* (3rd ed.): John Wiley & Sons.

Swindlehurst, A. L., Ayanoglu, E., Heydari, P., & Capolino, F. (2014). Millimeter-wave massive MIMO: The next wireless revolution? *IEEE Communications Magazine, 52*(9), 56-62. doi:10.1109/MCOM.2014.6894453

Tekkouk, K., Ettorre, M., Coq, L. L., & Sauleau, R. (2016). Multibeam SIW slotted waveguide antenna system fed by a compact dual-layer Rotman lens. *IEEE Transactions on Antennas and Propagation, 64*(2), 504-514. doi:10.1109/TAP.2015.2499752

Tian, G., Yang, J., & Wu, W. (2014). A novel compact Butler matrix without phase shifter. *IEEE Microwave and Wireless Components Letters, 24*(5), 306-308. doi:10.1109/LMWC.2014.2306898

Trinh-Van, S., Lee, J. M., Yang, Y., Lee, K., & Hwang, K. C. (2019). A sidelobe-reduced, four-beam array antenna fed by a modified 4 × 4 Butler matrix for 5G applications. *IEEE Transactions on Antennas and Propagation, 67*(7), 4528-4536. doi:10.1109/TAP.2019.2905783

Vallappil, A. K., Rahim, M. K. A., Khawaja, B. A., & Iqbal, M. N. (2020). Compact Metamaterial Based 4×4 Butler Matrix With Improved Bandwidth for 5G Applications. *IEEE Access, 8*, 13573-13583. doi:10.1109/ACCESS.2020.2966125

Vetterlein, S. J., & Hall, P. S. (1989). Novel multiple beam microstrip patch array with integrated beamformer. *Electronics Letters, 25*(17), 1149-1150. doi:10.1049/el:19890771

Weiland, T., Timm, M., & Munteanu, I. (2008). A practical guide to 3-D simulation. *IEEE Microwave Magazine, 9*(6), 62-75. doi:10.1109/MMM.2008.929772

Wight, J. S., Chudobiak, W. J., & Makios, V. (1976). A microstrip and stripline crossover structure. *IEEE Transactions on Microwave Theory and Techniques, 24*(5), 270-270. doi:10.1109/TMTT.1976.1128838

Winter, C. (1971). Dual vertical beam properties of doubly curved reflectors. *IEEE Transactions on Antennas and Propagation, 19*(2), 174-180. doi:10.1109/TAP.1971.1139903

Won-Cheol, L., Byung-Wook, M., Choul-Young, K., Jun Chul, K., & Jong-Min, Y. (2016). *A compact switched beam-forming network using silicon IPD technology for low-cost 5G communication.* Paper presented at the IEEE MTT-S International Microwave Symposium (IMS), San Francisco, CA, USA.

Xiang, W., Zheng, K., & Shen, X. S. (2016). *5G Mobile Communications*: Springer.

Xue, L., & Fusco, V. F. (2007). 24 GHz automotive radar planar Luneburg lens. *IET Microwaves, Antennas & Propagation, 1*(3), 624-628. doi:10.1049/iet-map:20050203

Yamada, Y., & Rahman, T. A. (2016). *Base station antenna technologies for 5G mobile system*. Paper presented at the International Conference on Advanced Technology and Applied Sciences, Kuala Lumpur, Malaysia.

Yang, P., Liu, D., & Zhang, Y. (2014). Performance analysis of joint base-station multiantenna multibeam and channel assignment scheme for hierarchical cellular system. *International Journal of Antennas and Propagation, 2014*, 9. doi:10.1155/2014/216890

Yang, Q., Ban, Y., Kang, K., Sim, C., & Wu, G. (2016). SIW multibeam array for 5G mobile devices. *IEEE Access, 4*, 2788-2796. doi:10.1109/ACCESS.2016.2578458

Yu, A., Yang, F., Elsherbeni, A. Z., Huang, J., & Kim, Y. (2012). An offset-fed X-band reflectarray antenna using a modified element rotation technique. *IEEE Transactions on Antennas and Propagation, 60*(3), 1619-1624. doi:10.1109/TAP.2011.2180299

Zhai, Y., Fang, X., Ding, K., & He, F. (2014). Miniaturization design for 8 × 8 Butler matrix based on back-to-back bilayer microstrip. *International Journal of Antennas and Propagation, 2014*, 7. doi:10.1155/2014/583903

Zhang, J., Ge, X., Li, Q., Guizani, M., & Zhang, Y. (2017). 5G millimeter-wave antenna array: Design and challenges. *IEEE Wireless Communications, 24*(2), 106-112. doi:10.1109/MWC.2016.1400374RP

Zhang, Y. S., & Hong, W. (2012). A millimeter-wave gain enhanced multi-beam antenna based on a coplanar cylindrical dielectric lens. *IEEE Transactions on Antennas and Propagation, 60*(7), 3485-3488. doi:10.1109/TAP.2012.2194646

Zhang, Z., Xiao, Y., Ma, Z., Xiao, M., Ding, Z., Lei, X., . . . Fan, P. (2019). 6G Wireless Networks: Vision, Requirements, Architecture, and Key Technologies. *IEEE Vehicular Technology Magazine, 14*(3), 28-41. doi:10.1109/MVT.2019.2921208

Zhong, L. H., Ban, Y. L., Lian, J. W., Yang, Q. L., Guo, J., & Yu, Z. F. (2017). Miniaturized SIW multibeam antenna array fed by dual-layer 8 × 8 Butler matrix. *IEEE Antennas and Wireless Propagation Letters, 16*, 3018-3021. doi:10.1109/LAWP.2017.2758373

Zhu, H., Sun, H., Ding, C., & Guo, Y. J. (2019). *Butler matrix based multi-beam base station antenna array.* Paper presented at the European Conference on Antennas and Propagation (EuCAP), Krakow, Poland.

LIST OF PUBLICATIONS AND PAPERS PRESENTED

A. Journals

1. **Intan Izafina Idrus**, Tarik Abdul Latef, Narendra Kumar Aridas, Mohamad Sofian Abu Talip, Yoshihide Yamada, Tengku Faiz Tengku Mohmed Noor Izam, and Tharek Abd Rahman. 2020. Design and characterization of a compact single-layer multibeam array antenna using an 8 × 8 Butler matrix for 5G base station applications. Turkish Journal of Electrical Engineering and Computer Sciences, 28 (2), 1121-1134. DOI: 10.3906/elk-1907-119.

2. **Intan Izafina Idrus**, Tarik Abdul Latef, Narendra Kumar Aridas, Mohamad Sofian Abu Talip, Yoshihide Yamada, Tharek Abd Rahman, Ismahayati Adam, and Mohd Najib Mohd Yasin. 2019. A low-loss and compact single-layer Butler matrix for a 5G base station antenna. PLoS ONE, 14 (12), 1-23. DOI: 10.1371/journal.pone.0226499.

B. Conferences

1. **Intan Izafina Idrus**, Tarik Abdul Latef, Yoshihide Yamada, Mohamad Sofian Abu Talip, Narendra Kumar Aridas, and Tharek Abd Rahman. Multibeam characteristics of an array antenna for 5G mobile base station. Paper presented at the IEEE International RF and Microwave Conference, 17-19 December 2018, Batu Feringgi, Penang.

2. Yoshihide Yamada, Kamelia M. Chatib Quzwain, **Intan Izafina Idrus**, Tarik Abd Latef, Farizah Ansarudin, Muhammad Kamran Ishfaq, and Tharek Abd Rahman. Base station antennas for the 5G mobile system.

Paper presented at the IEEE International RF and Microwave Conference, 17-19 December 2018, Batu Feringgi, Penang.

3. Yoshihide Yamada, Tharek Abd Rahman, and **Intan Izafina Idrus**. Multibeam array antennas for 5G mobile base station (CSN). Paper presented at the Malaysia-Japan Joint International Conference, 17-18 October 2018, Sepang, Negeri Sembilan.

4. Yoshihide Yamada, Chin Zhun Jing, Nurul Huda Abd Rahman, Kamilia Kamardin, **Intan Izafina Idrus**, Muhammad Rehan Ashraf, Tarik Abdul Latef, Tharek Abd Rahman, and Nyugen Quoc Dinh. Unequally element spacing array antenna with Butler matrix feed for 5G mobile base station. Paper presented at the International Conference on Telematics and Future Generation Networks, 24-26 July 2018, Kuching, Sarawak.